

Ultralow-Noise Silicon Nitride Trampoline Resonators for Sensing and Optomechanics

Christoph Reinhardt
Department of Physics
McGill University, Canada
August 2017



A thesis submitted to McGill University
in partial fulfillment of the requirements
of the degree of
Doctor of Philosophy

Abstract

In force sensing, optomechanics, and quantum motion experiments, it is typically advantageous to create lightweight, compliant mechanical elements with the lowest possible force noise. Here we report wafer-scale batch fabrication and characterization of nanogram-scale mechanical Si_3N_4 trampoline resonators having room temperature quality factors above 4×10^7 and ringdown times exceeding five minutes (1 mHz linewidth). We measure a thermally limited force noise sensitivity of $16.2 \pm 0.8 \text{ aN/Hz}^{1/2}$ at room temperature, with a spring constant ($\sim 1 \text{ N/m}$) 2-5 orders of magnitude larger than those of competing technologies. We also characterize the compatibility of these devices with a high-finesse cavity and their suitability for optomechanics applications, finding no evidence of surface or bulk optical losses from the processed nitride in a cavity achieving finesse 40,000. These parameters provide access to a single-photon cooperativity $C_0 \sim 8$ in the resolved-sideband limit, wherein a variety of outstanding optomechanics goals become feasible.

A characteristic of optomechanical systems with high cooperativities (e.g. $C_0 \gtrsim 1$) is, that they respond sensitively to smallest amounts of incident light. While generally desirable, this behavior poses certain technical challenges, most notably preventing our initial attempts to stabilize a laser's frequency to that of the cavity using traditional feedback techniques. This motivated developing a robust sideband laser locking technique ideally suited for applications requiring low probe power and heterodyne readout. By feeding back to a high-bandwidth voltage-controlled oscillator, we lock a first-order phase-modulation sideband to a high-finesse Fabry-Perot cavity in ambient conditions, achieving a closed-loop bandwidth of 3.5 MHz (with a single integrator) limited fundamentally by the signal delay. The measured transfer function of the closed loop agrees with a simple model based on ideal system components, and from this we suggest a modified design that should achieve a bandwidth exceeding 6 MHz with a near-causally limited feedback gain as high as 4×10^7 at 1 kHz. The off-resonance optical carrier enables alignment-free heterodyne readout, alleviating the need for additional lasers or optical modulators.

Abrégé

Dans les domaines de la détection de force, de l'optomécanique, et des expériences de mouvement quantique, il est typiquement avantageux de créer des éléments mécaniques légers et flexibles possédant un bruit de force minimal. Nous rapportons ici un procédé de fabrication à l'échelle d'une gaufrette, où des résonateurs mécaniques de type trampoline de Si_3N_4 de quelques nanogrammes sont fabriqués en lot, et la caractérisation de ces derniers montrant des facteurs de qualité de plus de 4×10^7 à température ambiante et des temps d'amortissement dépassant cinq minutes (largeur de résonance de 1 mHz). Nous mesurons une sensibilité du bruit de force de $16.2 \pm 0.8 \text{ aN/Hz}^{1/2}$, limitée par le bruit thermique à température ambiante, avec une raideur ($\sim 1 \text{ N/m}$) 2-5 ordres de grandeur plus élevée que celles des technologies concurrentes. Nous caractérisons également la compatibilité de ces dispositifs avec une cavité haute-finesse ainsi que leurs applications en optomécanique, ne trouvant aucune preuve de perte optique reliée à la surface ou au volume du nitrure traité en salle blanche, dans une cavité dont la finesse s'élève à 40,000. Ces paramètres donnent accès à une coopérativité à photon-unique $C_0 \sim 8$ dans le régime "sideband-resolved", où une variété d'objectifs courants du domaine de l'optomécanique deviennent réalisables.

Une des caractéristiques des systèmes optomécaniques à haute coopérativité ($C_0 \geq 1$) est qu'ils répondent sensiblement à de minuscules quantités de lumière incidente. Bien que généralement souhaitable, ce comportement pose certains défis techniques, empêchant notamment nos tentatives initiales de stabiliser la fréquence d'un laser à celle d'une cavité optique en utilisant des techniques de rétroaction traditionnelles. Cela a motivé le développement d'une technique robuste de rétroaction de la bande latérale d'un laser (sideband laser locking), idéale pour les applications nécessitant une faible puissance optique et une détection hétérodyne. En renvoyant à un oscillateur contrôlé par tension électrique avec une haute bande passante, on stabilise une bande latérale de modulation de phase de premier ordre à une cavité Fabry-Pérot haute-finesse dans des conditions ambiantes, atteignant une bande passante en boucle fermée de 3.5 MHz (avec un seul intégrateur), limitée fondamentalement par le retard du signal. La fonction de transfert mesurée en boucle fermée est en accord avec un modèle simple basé sur un système comprenant uniquement des composantes idéales. Nous proposons une modification qui devrait permettre d'atteindre une bande passante dé-

passant 6 MHz avec un gain de rétroaction quasiment causalement limité à 4×10^7 at 1 kHz. Le porteur optique hors resonance permet la détection hétérodyne sans alignement, enlevant ainsi la nécessité de lasers ou de modulateurs optiques supplémentaires

Acknowledgments

To Jack Sankey, thank you for giving me the opportunity to learn so many things in a great environment, for always having an open door and ear, and for your inspiring passion for science and teaching it to others; working with you has been a privilege. I also want to take the chance to express my admiration for your ability of wearing sweatbands with extraordinary grace and naturalness, while delivering supreme blues rock solos on your electric guitar (Eric Clapton would feel confirmation in his decision to concentrate on his singing career, if he could make it to one of the physics department barbecues).

To my other two PhD supervisory committee members Aashish Clerk and David Cooke, thank you for fruitful discussions of my project and your general career advice.

Thanks to my fellow lab mates, who contributed a great deal to making the last years as enjoyable as they have been: To Tina, for being great to work with; your sisyphian tenacity when we built our setup, and especially when you aligned the trampoline cavity was truly incentive. Thank you also for fun conversations over lunch and for enlightening me with the concept of marinating tofu (so much taste...). To Raphael, thank you for introducing me to the angular spectrum method and for discussions on electronics and MEMS. I am glad you took the role of the lab senior off my shoulders. To Simon, my oldest fellow lab mate, thank you for all the cleanroom and nitride resonator discussions, for keeping up with my snore at conference hotels, and for all the times you and your family hosted us with warm hospitality. To Vincent, thank you for the membrane-in-the-middle discussions, for your sophisticated humor, telling me about refrigerating jeans, introducing me to the Moroccan spiced pie, and much more. My time in Montreal wouldn't have been what it is, if you didn't join the group. Thanks to Simon, Vincent, and Raphael also for helping me with the French abstract of this dissertation. To Abeer, thank you for discussions of COMSOL, and for enriching conversations about different religions and cultures. To Max, I admire your dedication to your research, and thank you for discussions about interfacing lab hardware, and the times you and Andreas hosted barbecues or dinners. To Alexandre Bourassa, the guy who does backflips as well as he builds fiber interferometers; thank you for building a work horse of a setup, for passionate scientific discussions, and for coding help. To former undergraduate researchers of the Sankey Lab: Christopher McNally, Yishu Zhou, Vikramaditya Mathkar,

and Bogdan Piciu, thank you for being fun to work with, and your individual testing and coding help with the fiber interferometer.

Thanks to the Childress Lab members: To Erika, for discussions of laser frequency stabilization, telling me about the parasitic inductance, and for having a bubbly spirit. To Yannik, for sharing inventive workarounds for cryo stages and always being great to talk to. To Zack and Adrian, for patiently explaining spin resonances and coupling them to NV centers to us. To Zack, for presenting your research update as a play in three acts, and for conversations about many different topics. To Mark, for discussions of vacuum equipment and your sense of humor.

Thanks to other McGillians: To Peter Grütter, for fruitful discussions about force noise. To Dominic Ryan, for taking us on a field trip to the nuclear power plant of white river and the breakfasts at Bear's Den before. To Ilja and Yunning, for showing me around when I was new to the McGill cleanroom, and for discussions on various aspects of McGill life. Ilja, also for the occasional midnight poutine and many other activities outside the department. To Anja, for discussion of optomechanics and life in general. To the cleanroom staff at McGill: Matthieu, Lino, Zhao, Don, Jun, and Sasa, for your willingness to always help and share your insights. To John, James, Marc-Antoine, and Michel, for being welcoming when I joined McGill, and for creating an office atmosphere that made transitioning into a new environment a whole lot of fun. To Saeed, Hadi, Ahmed, and Mohammed, for good times in- and outside the department. To Benjamin, Felix, and Vincent for the occasional beer, scientific discussions, and cross-country skiing.

To researchers from outside McGill: Thanks to Christian Degen and Gary Steele for fruitful discussions about nanomechanical sensors. Thanks to John Teufel for a great viewpoint on our trampoline resonators (and the ones fabricated by Simon Groeblacher's lab at Delft). Thanks to Alexey Shkarin for performing the mechanical quality factor measurement of glued trampoline chips. Thanks to Scott Hoch for fabrication help.

I gratefully acknowledge additional funding from a Schulich Graduate Fellowship (2016-2017), a departmental scholarship (2013), and CMC Microsystems (nanofabrication expenses).

To my out-of-university friends and family: Thank you Johannes, Conrad, Klaus, Franz,

Till, and Lennart for visiting us in Montreal, meeting up somewhere in between, and keeping in touch. To Kim, I consider myself exceptionally lucky for having met you and for all the love and support you gave to me. Thank you. To my Dad, Andreas, my Mum Sybille, and my sister Bianka, I thank each of you for supporting me in your own ways and for always being there for me.

Statement of Originality

The work presented in this dissertation resulted in the publication of two articles as first author [1, 2]:

Ultralow-Noise SiN Trampoline Resonators for Sensing and Optomechanics

Christoph Reinhardt, Tina Müller, Alexandre Bourassa, and Jack C. Sankey

Physical Review X **6**, 021001 (2016)

Simple Delay-Limited Sideband Locking with Heterodyne Readout

Christoph Reinhardt, Tina Müller, and Jack C. Sankey

Optics Express **25**, 1582-1597 (2017).

Chapters 3 and 4 of this dissertation are based on Ref. [1] and Ch. 5 is based on Ref. [2].

The author, Christoph Reinhardt, claims the following elements of this dissertation to be considered original scholarship and distinct contribution to knowledge:

- Development of a silicon nitride (SiN) trampoline resonator fabrication protocol (Sec. 3.1, [1])
- Optimization of trampoline design with respect to force noise, resulting in lowest force noise among solid state mechanical sensors compatible with high-finesse optics (Sec. 3.3.2, [1])
- Incorporation of a SiN trampoline into a vacuum Fabry-Perot cavity and measurement of the resulting cavity finesse. The measured parameters correspond to a single-photon cooperativity ~ 10 in the resolved-sideband regime (Sec. 4.2.2, [1]). (The setup was designed by me and built together with Tina Müller, former Postdoc in the Sankey Lab. The measurement was performed by Tina Müller on a trampoline that I have fabricated.)
- Gluing a trampoline chip at three spots onto a metal support and measuring the effect on the mechanical quality factor of the fundamental out-of-plane mode. The resulting

decrease of 13% is modest compared to the reductions of one to two orders of magnitude, typically reported in the literature for extended square membranes (Sec. 3.3.3). (The measurement was performed by Alexey Shkarin, graduate student in the Harris Lab at Yale University. The measured devices were fabricated by me, including the development of the method for cleaving chips of eight trampolines into individual chips.)

- Simulation of the increase in mechanical quality factor of a SiN trampoline resonator when subjecting the trampoline to an optical trap with Gaussian mode profile. (Sec. 4.3)
- Design, implementation, and characterization of an optimized version of a delay limited sideband locking technique with heterodyne readout (I implemented the heterodyne readout capability, and the adjustable attenuator between voltage-controlled oscillator and electro-optic modulator (Chapter 5, [2]). Tina Müller, former Postdoc in the Sankey Lab, implemented the initial version of this setup, which served as a starting point for the optimized design).

Contribution of Co-Authors

The research carried out in this work was supervised by Jack C. Sankey.

This dissertation is based on two articles [1, 2], which were primarily co-written by Jack C. Sankey and me; Chapters 3-4 are based on Ref. [1] and Chapter 5 is based on Ref. [2]. Mentioned in the following are the contributions of other researchers and technicians to this work. Listed at the end are their affiliations and roles, at the time of the contribution.

- Chapter 2: Vincent Dumont provided Eq. 2.79 and contributed to Sec. 2.2.6 with discussions.
- Chapter 3: Alexandre Bourassa built the vacuum chamber and a previous version of the fiber interferometer that is employed in this chapter. For the presented measurements, I upgraded the fiber interferometer (replaced a homebuilt two-axis stage with a commercial one (closed-loop), assisted in interfacing it (python ctypes), designed and built a new support structure for the stage, replaced a fiber optical circulator with a four port fiber coupler, and added a preamplifier before the lock-in amplifier. Yishu Zhou, Vikramaditya Mathkar, and Chris McNally assisted by independently testing the setup and coding). Mattieu Nannini, Don Berry, Jun Li, Lino Eugene, Simon Bernard, and Scott Hoch contributed with discussions on nanofabrication. Raphael St-Gelais contributed to Sec. 3.2.3 with discussions on the angular spectrum method. Abeer Barasheed and Bogdan Piciu contributed with discussions on the finite-element model (COMSOL) used to simulate eigenfrequencies and mode profiles of fabricated trampoline resonators. My main contributions were: development of the silicon nitride trampoline resonator fabrication protocol, design and fabrication of all investigated trampolines, measurement and data analysis of the results presented in Sec. 3.3.1-3.3.2. The measurement presented in Sec. 3.3.3 was performed by Alexey Shkarin at the Harris Lab, Yale University, on devices that I fabricated. Aashish Clerk, Peter Grütter, Christian Degen, and Gary Steele contributed with discussions.

- Chapter 4: Tina Müller assisted in building the vacuum Fabry-Perot cavity setup, which I designed. Furthermore, she incorporated the trampoline into the cavity and took the data presented in Sec. 4.2.2 which was analyzed by both of us.
- Chapter 5: Tina Müller implemented an initial version of the feedback loop, which she operated together with the “membrane-in-the-middle” cavity setup presented in Chapter 4. For the characterization presented in this chapter and a journal article on this topic, I built a new Fabry-Perot cavity setup, added the heterodyne readout capability and adjustable attenuator to the original feedback circuit, and recorded and analyzed all the data. Erika Janitz, Maximilian Ruf, Alexandre Bourassa, Simon Bernard, Abeer Barasheed, and Vincent Dumont contributed with discussions.

Name	Role	Affiliation
Abeer Barasheed	Graduate Researcher	Sankey Lab, McGill University
Simon Bernard	Graduate Researcher	Sankey Lab, McGill University
Don Berry	Cleanroom Staff	McGill Nanotools - Microfab
Alexandre Bourassa	Undergraduate Researcher	Sankey Lab, McGill University
Aashish Clerk	Professor	McGill University
Christian Degen	Professor	ETH Zurich
Vincent Dumont	Graduate Researcher	Sankey Lab, McGill University
Lino Eugene	Cleanroom Manager	McGill Nanotools - Microfab
Peter Grütter	Professor	McGill University
Scott Hoch	Graduate Researcher	Yale University
Erika Janitz	Graduate Researcher	Childress Group, McGill University
Jun Li	Cleanroom Staff	McGill Nanotools - Microfab
Vikramaditya Mathkar	Undergraduate Researcher	Sankey Lab, McGill University
Chris McNally	Undergraduate Researcher	Sankey Lab, McGill University
Tina Müller	Postdoc	Sankey Lab, McGill University
Mattieu Nannini	Cleanroom Manager	McGill Nanotools - Microfab
Bogdan Piciu	Undergraduate Researcher	Sankey Lab, McGill University
Maximilian Ruf	Graduate Researcher	Sankey Lab, McGill University
Alexey Shkarin	Graduate Researcher	Yale University
Gary Steele	Professor	TU Delft
Raphael St-Gelais	Postdoc	Sankey Lab, McGill University
Yishu Zhou	Undergraduate Researcher	Sankey Lab, McGill University

Contents

1	Introduction & Overview	1
2	Theoretical Concepts	8
2.1	One-Dimensional Harmonic Oscillator	9
2.1.1	Simple Harmonic Oscillator Model and Definitions	10
2.1.2	Thermal Noise	12
2.1.2.1	Power Spectral Density Basics	13
2.1.2.2	Thermal Noise Power Spectral Density	15
2.2	Optical Resonances of Fabry-Perot Cavity	
	with Incorporated Membrane	19
2.2.1	Optical Transfer Matrix Method	20
2.2.2	Optical Resonances of a Fabry-Perot Cavity	25
2.2.3	Optical Resonances of a Fabry-Perot Cavity with Incorporated Membrane	32
2.2.4	Steady State Optical Forces	42
2.2.5	Linear and Quadratic Dispersive Frequency Shift	45
2.2.6	Dynamical Optical Forces and Laser Cooling	48
3	Fabrication & Mechanical Characterization of Si_3N_4 Trampoline Resonators	54
3.1	Si_3N_4 Trampoline Resonator Fabrication	59
3.1.1	Fabricated Trampoline Resonator	61
3.1.2	Fabrication Protocol	63
3.2	Fiber Interferometer for Measuring Nanomechanical Motion	69

3.2.1	Design	69
3.2.2	Displacement Calibration Based on Optical Plane Wave Model	72
3.2.3	Diverging Beam Effects	77
3.3	Characterization of Mechanical Resonances	82
3.3.1	Identifying Mechanical Resonances and Measuring Q_m	82
3.3.2	Thermal Noise Measurement	85
3.3.3	Q_m of Cleaved and Glued Trampoline	88
4	Vacuum Fabry-Perot Cavity with Incorporated Si_3N_4 Trampoline Resonator	91
4.1	Vacuum Cavity Setup with Trampoline Alignment Structure	92
4.1.1	Cavity Support Structure	92
4.1.2	Trampoline Alignment Structure	98
4.1.3	Vacuum Chamber	100
4.2	Optical Characterization	103
4.2.1	Optical Setup & Empty Cavity Finesse Measurement	103
4.2.2	Cavity with Incorporated Trampoline	108
4.3	Simulation of Q_m -Increase Through Optical Trapping	116
5	Simple Delay-Limited Sideband Locking with Heterodyne Readout	122
5.1	A Brief Review of Laser Feedback	125
5.2	Modified Pound-Drever-Hall Readout and Dynamical Response	127
5.3	Apparatus for Sideband Locking with Heterodyne Readout	131
5.4	Performance	133
5.5	Conclusion	137
6	Conclusion & Outlook	138
A	Theoretical Concepts	143
A.1	Reflection and Transmission Coefficient of a One-Dimensional Slab	143
A.2	Reflection and Transmission Coefficient of a DBR	147
A.3	Derivation of Cavity Finesse	148

A.4	Maxwell Stress Tensor	150
B	Fabrication & Mechanical Characterization of Si₃N₄ Trampoline Resonators	153
B.1	Power Spectral Density Measurement with a Lock-In Amplifier	153
B.2	Gas Damping	157
C	Vacuum Fabry-Perot Cavity with Incorporated Si₃N₄ Trampoline Resonator	161
C.1	Transverse Electromagnetic Cavity Modes	161
C.2	Cavity Finesse Tuning by Mirror Etching	163
D	Simple Delay-Limited Sideband Locking with Heterodyne Readout	169
D.1	Reflection from an Asymmetric Cavity	169
D.2	Transfer Function from Laser Noise to Error Signal	170
D.2.1	Shorthand Notation	170
D.2.2	Propagating Laser Noise Through the Readout System	170
D.2.3	Case 1: Frequency Noise only, Ideal EOM, Cavity Resonant with Carrier	174
D.2.4	Case 2: Frequency Noise only, Ideal EOM, Cavity Resonant with Upper Sideband	175
D.2.5	Case 3: Amplitude Noise only, Ideal EOM, Cavity Resonant with Carrier	175
D.2.6	Case 4: Amplitude noise only, ideal EOM, cavity resonant with upper sideband	176
D.3	Error Signal for Wider Range of VCO Outputs	176

Chapter 1

Introduction & Overview

Advances in nanofabrication over the past decades have enabled the growth and patterning of pristine materials, and the creation of mechanical sensors of extraordinary quality [3]. Cantilevers sensitive to attonewton forces¹ at room temperature have been fabricated from silicon (e.g. 50 aN/Hz^{1/2} [4]) and diamond (26 aN/Hz^{1/2} [5]) using “top-down” techniques, while “bottom-up” fabricated devices can in principle achieve below 10 aN/Hz^{1/2} at room temperature (e.g. approaching ~ 5 aN/Hz^{1/2} for silicon nanowires [6] or carbon nanotubes [7]), and 1 zN/Hz^{1/2} at low temperatures (nanotubes [8]). These complementary approaches carry with them an important trade-off: on one hand, bottom-up techniques can assemble fewer atoms into smaller, more sensitive structures, but the technology is comparatively young, and it is more difficult to incorporate additional structures and/or probes. These low-mass objects also tend to have very low spring constants (i.e. below ~ 10 mN/m), making them highly susceptible to van der Waals “sticking” forces at short distances. On the other hand, top-down devices are currently not as sensitive at low temperature (e.g. ~ 500 zN/Hz^{1/2} for diamond at 93 mK [5]), but are reliably fabricated, are compatible with a wide variety of probes, and naturally integrate with other on-chip systems. Some of their remarkable achievements to date include detection of a single electron spin [9], nanoscale clusters of nuclei [10], persistent currents in normal metal rings [11], and the force noise associated

¹The force sensitivity, here specified in units of force per square root of frequency, indicates for how long the trajectory of a mechanical resonator has to be measured, in order to resolve a force of a certain magnitude acting on the resonator. For example, a force sensitivity of 10 aN/Hz^{1/2} indicates, that a measurement time of 1 s is required in order to resolve a force of 10 aN (assuming the force acts on the mechanical resonator at a frequency within the detection bandwidth.)

with the quantized nature of light [12]. Further, integrating with quantum electronics and / or optical cavities has provided (among other things) access to a regime in which quantum effects play a central role in the mechanical element's motion [13, 14, 15, 16, 17, 18, 19, 20].

The control of nano- and micro-mechanical resonators by means of the electromagnetic field of an optical cavity or a superconducting LC circuit is studied in the field of cavity optomechanics [21]. Pioneering work, carried out in the context of interferometric gravitational wave detectors (1960s), showed, that laser light incident on an oscillating mirror applies a frictional force to the mirror and thereby damps its motion [22]. This effect is coined optomechanical cooling, as the incident laser light effectively lowers the mirror's temperature by removing phonons from its oscillatory motion. It was shown that this effect is strongly enhanced for the end mirrors of a Fabry-Perot cavity, interacting with the intra-cavity field, and that it can be reversed, thereby resulting in anti-damping of the mirror's motion [22]. More recently cavity optomechanics has found widespread interest since it provides a means of controlling the motion of nano- and micro-mechanical resonators, down to the quantum level. For example, exploiting optomechanical cooling in conjunction with conventional refrigeration techniques has enabled cooling of a (MHz to GHz) mechanical resonator into its quantum ground state of motion [14, 15] and, more recently, to [23], and beyond [24] the quantum back action limit. At this point, the resonator's base temperature is fundamentally limited by quantum noise in the cooling laser field. Other milestone experiments have shown, that optomechanics can be exploited to generate optomechanically induced transparency [25, 26], to provide a coherent interface for the conversion between photons of vastly different frequencies, e.g. optical to optical [27, 28], optical to microwave [29, 30] or optical to radio-frequency [31], to create squeezed states of light [32, 33] or mechanical motion [34], and to establish non-reciprocal transport of mechanical energy [35] or light [36]. Furthermore, integrating optomechanical systems with quantum systems, such as an atomic ensemble, provides additional quantum-compatible means to manipulate the mechanical resonator. This approach has enabled, e.g., enhanced cooling of a nanomechanical resonator, beyond what is possible with conventional optomechanical sideband cooling alone [37], and back-action-evading measurement of its motion [38].

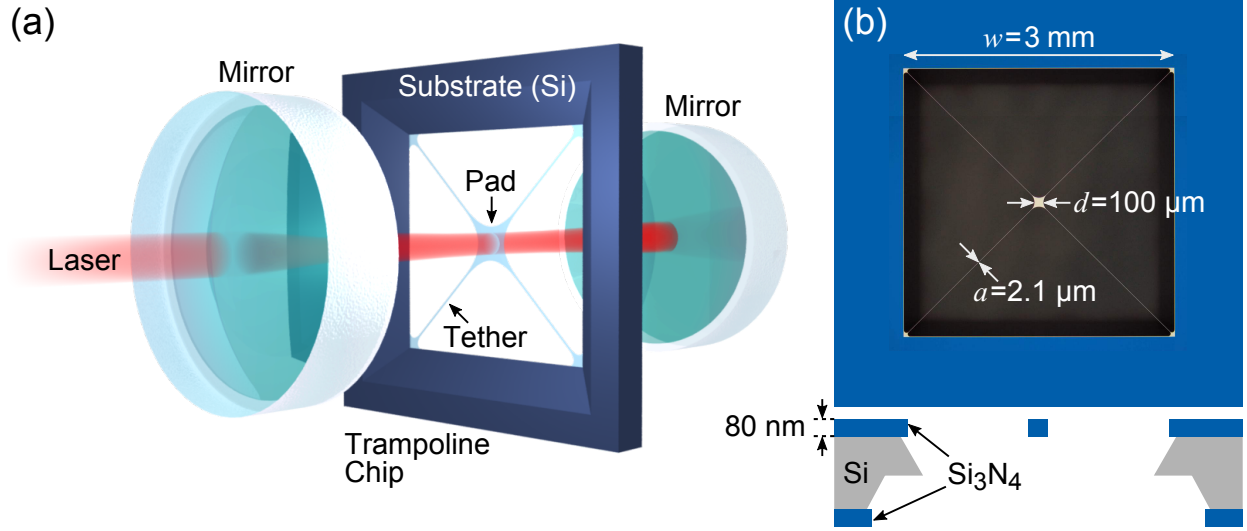


Figure 1.1: Optomechanical “membrane-in-the-middle” (MIM) setup with trampoline resonator. (a) A silicon nitride (Si_3N_4) trampoline resonator is incorporated close to the center of a Fabry-Perot cavity, formed by two mirrors facing each other. The trampoline comprises a central pad which is suspended by four tethers from a silicon (Si) substrate. The setup is probed by a laser. (Image courtesy of Jack Sankey) (b, upper) Photo of fabricated Si_3N_4 trampoline resonator with a window size of $w = 3 \text{ mm}$, a central pad width of $d = 100 \mu\text{m}$, and four tethers, each with width of $a = 2.1 \mu\text{m}$ (released nitride appears pale yellow and nitride on silicon appears blue, due to optical interference). (b, lower) Schematic of trampoline chip’s anisotropically etched cross section with Si_3N_4 device layer thickness of 80 nm.

This dissertation deals with the construction and characterization of an optomechanical setup in which a pristine mechanical force sensor is incorporated close to the center of a Fabry-Perot cavity. A schematic of the setup is shown in Fig. 1.1(a), where the cavity is formed by two mirrors facing each other and a silicon nitride (Si_3N_4) “trampoline resonator” resembles the mechanical sensor. The trampoline can be seen as a square membrane from which four identical triangularly-shaped areas are cut-out, thereby creating a central pad which is suspended by four tethers from a silicon (Si) chip. The filleted shapes in the center and at the outer corners help to reduce mechanical dissipation by eliminating regions of highly concentrated stress, thereby allowing us to achieve extraordinarily low force noise sensitivity. Figure. 1.1(b, upper) shows a photo of a Si_3N_4 trampoline resonator, fabricated and characterized in the course of this dissertation (released nitride appears pale yellow and nitride on silicon appears blue, as a consequence of optical interference). Its dimensions are given by window size $w = 3 \text{ mm}$, central pad width $d = 100 \mu\text{m}$, and tether width $a = 2.1 \mu\text{m}$.

Figure 1.1(b, lower) shows a schematic of the trampoline chip’s cross section. The angled sidewalls of the silicon chip (gray) and the knife edge in the middle of the chip are consequences of an anisotropic, silicon etch (by means of potassium hydroxide) from the bottom and top side of the chip. This device [1], together with Ref. [39] (submitted simultaneously), consistently achieve an intrinsic force noise below $20 \text{ aN/Hz}^{1/2}$ at room temperature (293 K). Our measured value $16.2 \pm 0.8 \text{ aN/Hz}^{1/2}$ is similar to what is in principle possible using a single layer of graphene [40] and represents the highest force sensitivity (to our knowledge) for “top-down” batch-fabricated mechanical sensors. Furthermore, this low noise is accompanied by spring constants $\sim 1 \text{ N/m}$ that are $\sim 2 - 5$ orders of magnitude higher than those of competing devices [3, 4, 5, 6, 7, 40], and the $\sim 100 \times 100 \mu\text{m}^2$ surface area is compatible with the incorporation of additional structures [1, 39].

Our setup (see Fig. 1.1(a)) resembles a variation of the “membrane-in-the-middle” (MIM) geometry, in which, “most commonly”, instead of a trampoline resonator an extended membrane is installed close to the cavity center. After its introduction in 2008 [41], this setup was quickly adopted by other research groups and has since produced a variety of impressive results in the field [12, 30, 33, 35, 37, 38, 42, 43]. The membrane resonator employed in these studies is made out of silicon nitride, most commonly Si_3N_4 , due to the material’s exceptionally-low mechanical and optical dissipation [42, 43]. State of the art MIM experiments rely on further decreasing mechanical dissipation in the membrane, on the one hand by operating the experiments at cryogenic temperatures [44, 45] and on the other hand by fabricating membrane resonator’s with optimized design [46, 47, 48]. Besides of reducing mechanical dissipation, an additional objective for fabricating specifically-tailored devices has been to increase the optomechanical coupling strength, e.g. by increasing the resonator’s reflectivity (the fraction of incident light that is reflected) and/or its mechanical compliance [1, 39, 49, 50, 51, 52, 53, 54, 55, 56]. The former can be achieved by depositing a dielectric mirror coating onto the mechanical element [49, 50, 51]. Since this approach comes at the expense of increased resonator mass (and dissipation, due to the extra layers), an alternative method has been object to recent studies; patterning a photonic crystal in the form of a periodic array of either holes or stripes into the membrane [39, 52, 53, 54, 55, 56] furnishes it with optical resonances that strongly increase its reflectivity. The second objective, of en-

hancing the resonator’s mechanical compliance, requires adjusting its geometry in a way that reduces its weight and/or its mechanical resonance frequency. These considerations resulted in (among others) the trampoline geometry [51] discussed in this dissertation (see Fig. 1.1). Creating increasingly optimized device geometries is an ongoing endeavor in the field and has recently lead to a new class of devices in which the mechanical resonator is formed by a geometrical defect in a periodically patterned Si_3N_4 membrane [57]. The defect is located in the center of the membrane and the surrounding periodic pattern (forming a phononic crystal) isolates it from mechanical dissipation channels. The result is an unprecedented degree of suppressed mechanical dissipation and promising prospects for cooling a mechanical resonator into its ground state of motion without cryogenically pre-cooling it (together with Ref. [39]).

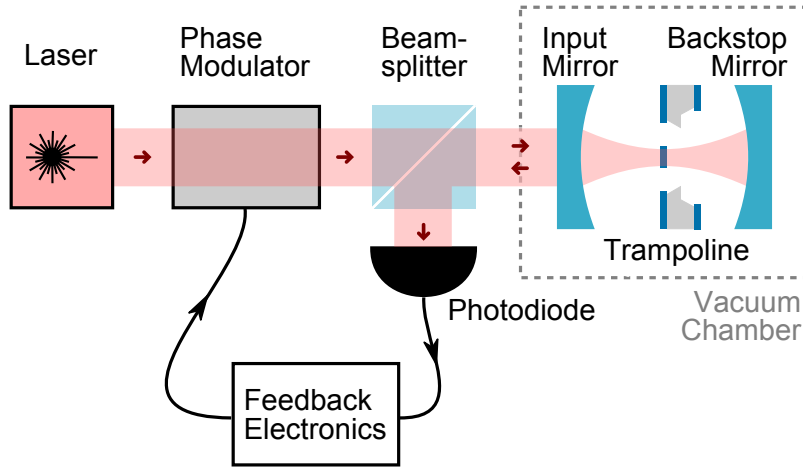


Figure 1.2: Schematic of experimental “membrane-in-the-middle” (MIM) setup. (a) Laser light is phase modulated and coupled to an optical cavity, formed by an input mirror and a backstop mirror, with trampoline resonator incorporated close to its center. The MIM cavity is installed into a vacuum chamber. Upon interaction with the MIM setup, the laser light is routed by a beam splitter towards a photodiode. Processing the detected signal with analog electronics and feeding it back to the phase modulator enables frequency stabilization of the incident laser with respect to the cavity resonance.

Ultimately, we wish to position a trampoline within a high finesse optical cavity and control its motion with laser light. For these sensitive systems, one cannot simply set the laser to the cavity frequency with a knob, however. In practice, ambient mechanical noise of the cavity and classical noise of the laser prevent the laser from remaining at a fixed frequency

relative to the cavity resonance, and so one must stabilize them with respect to one another. Figure 1.2 shows a basic schematic of our desired setup; an incident laser beam (at telecom wavelength 1550 nm) is phase modulated, passes through a beam splitter and is coupled to a MIM cavity, formed by an input mirror, a backstop mirror, and a Si_3N_4 trampoline resonator installed in the cavity center. The MIM cavity is situated in a vacuum chamber to prevent collisions with surrounding air molecules from diminishing the trampoline’s mechanical performance. The light reflected from the cavity, comprising the portions leaving the cavity and the one promptly reflected from the input mirror, is routed by a beamsplitter to a photodiode. The detected signal is processed by analog feedback electronics and applied to the phase modulator. Here the phase modulator is used to dither the light, probing the difference in frequency between the laser and the cavity. In the traditional Pound-Drever-Hall technique [58], this information is sent back to the laser frequency or the cavity length, but for our highly sensitive systems, this type of feedback cannot sufficiently stabilize the laser to prevent mechanical instabilities driven by fluctuations. Hence, we have developed a modified Pound-Drever-Hall setup, where instead of the laser carrier a first-order phase modulation sideband is locked to the cavity resonance [2].

The structure of this dissertation is as follows: In Chapter 2 we introduce the formal framework to describe the experimental results presented in subsequent chapters. Here we introduce the theory to express the thermally-limited force sensitivity of a mechanical sensor and provide a model for the optical resonances of a Fabry-Perot cavity with incorporated trampoline resonator. To illustrate optomechanical coupling between the intra-cavity field and the trampoline’s motion, we give expressions for the radiation force acting on the trampoline resonator and the corresponding optical spring constant. In anticipation of future optomechanics experiments with our setup, we outline the theory of optomechanical sideband cooling and briefly discuss its quantum limits, for a cooling laser beam described by a coherent state of light.

In Chapter 3 we discuss the fabrication and mechanical characterization of high-aspect-ratio, nanogram-scale Si_3N_4 “trampoline” resonators. We give details of the trampoline’s wafer-scale batch fabrication procedure and discuss its geometrical features. To characterize mechanical resonances of the fabricated structures, we measure their motion in a Fabry-Perot

fiber interferometer. We describe this setup and perform an optical analysis to calibrate the trampolines' displacement amplitude. We identify mechanical resonances with frequencies in the range of 40–570 kHz and mechanical ringdown times up to ~ 6 minutes (1 mHz linewidth) at room temperature (corresponding to a mechanical quality factor up to $\sim 5 \times 10^7$). By investigating the trampoline's thermally driven motion we measure a force sensitivity of $S_F = 16.2 \pm 0.8 \text{ aN/Hz}^{1/2}$. Finally, in a first step of integrating our devices in a compact cryogenic fiber cavity setup (performed by our collaborators from the Harris Lab at Yale University), we investigate how gluing a trampoline chip (at three spots) to a metal mount affects Q_m . With the result of a modest decrease by 13 %.

In Chapter 4 we describe the construction of the vacuum MIM setup and its optical characterization. To demonstrate the trampoline's suitability for sensitive interferometric readout and optomechanics applications we position an extended membrane (fabricated by the same means) within the cavity of finesse 20,000, finding no evidence of additional bulk or surface optical losses from the processed nitride at telecom wavelength (1550 nm), consistent with literature [59, 43]. In fact, for certain membrane positions, the cavity finesse is increased to 40,000, as expected for a lossless dielectric slab in a single-port cavity. Finally, to set an approximate upper bound on the size of the cavity field required for high-finesse applications, we position a trampoline in a cavity field wide enough that 0.045% of the light falls outside the structure. Consistent with recent simulations [60], we find that the majority of this “clipped” light is in many cases recovered by the cavity.

In Chapter 5, motivated by challenges encountered in initial attempts of locking our trampoline MIM cavity, we present the development and characterization of a simple, low-power, high-bandwidth, post-emission laser locking technique with built-in heterodyne readout. Our setup is based on the Pound-Drever-Hall technique [58] and employs a voltage controlled oscillator in combination with a phase modulator as frequency actuator, thereby enabling locking of a first order phase modulation sideband to the cavity resonance. After outlining basic feedback theory we briefly describe our technique and the resulting dynamic response of the feedback loop. We then present the experimental apparatus and discuss measurements of its closed-loop transfer function and noise spectrum.

Chapter 2

Theoretical Concepts

Statement of contribution: Vincent Dumont provided Eq. 2.79 and contributed to Sec. 2.2.6 with discussions.

At the heart of this dissertation lies a Fabry-Perot cavity with incorporated mechanical membrane resonator. Our eventual goal is to conduct experiments in which the membrane's motion is strongly controlled by the light in the cavity; hereby, our central concerns are the mechanical resonator's decoupling from the thermal environment (a source of noise and decoherence), and the optomechanical coupling strength. In the following, we outline the theoretical concepts employed throughout the later chapters to characterize the mechanical and optical properties of this setup.

In Sec. 2.1 we introduce the model of a one-dimensional damped harmonic oscillator, which is driven by the thermal excitations in its environment. While in reality we are dealing with an essentially two-dimensional mechanical membrane resonator in our experiment, this one-dimensional model is a useful tool in describing the behavior of a single normal mode. In Sec. 2.2 we focus on the optical characterization of, first, a Fabry-Perot (FP) cavity, and, second, the combined setup of a FP cavity with incorporated mechanical membrane resonator. We apply a transfer matrix model to describe the propagation of an optical field in these systems, which enables to understand their optical resonances. With regard to possible optomechanics experiments with our system, we briefly discuss the steady state optical force, with resulting spring constant acting on the incorporated membrane, and summarize key

aspects of optically damping (laser cooling) the membrane’s motion by means of the intra-cavity light field.

2.1 One-Dimensional Harmonic Oscillator

Here we discuss a harmonic oscillator which is dissipatively coupled to its thermal environment. To maintain thermal equilibrium, this coupling provides a means for the thermal environment to randomly inject energy, which can be modeled as stochastic "thermal force noise" exerted upon the oscillator [61, 62]. This imposes a fundamental limit on the oscillator’s sensitivity to external forces. Of particular interest to this work are two kinds of dissipative coupling; the first one is “gas damping”, which describes energy loss due to the resonator’s interaction with surrounding gas molecules, and the second one is “structural damping”, wherein the oscillator’s motion transfers mechanical energy to internal degrees of freedom. In Sec. 3.3.1, we provide evidence that the dissipation of our resonators is influenced by both. As these two mechanisms are characterized by a different frequency dependency of the oscillator’s response to a force acting on it (see Sec. 2.1.2.2), one could in principle measure this dependency to discern between the two damping mechanisms. Such an investigation was recently presented by another research group [63]. To achieve a measurement sensitivity sufficient to resolve the difference between the aforementioned damping mechanisms, the experiment presented in Ref. [63] relied on interferometrically measuring the mechanical resonator’s position by means of an optical cavity (see Sec. 2.2.2). The sensitivity provided by our comparatively simple measurement setup (see Sec. 3.2) is not sufficient to resolve the difference between structural damping and gas damping.

In Sec. 2.1.1 we briefly review the harmonic oscillator’s equation of motion and its transient solution with characteristic ring-down time and corresponding quality factor. In Sec. 2.1.2 we discuss the stationary solution of the thermally driven harmonic oscillator and derive the magnitude of the thermal force noise and displacement power spectral densities relevant to this work.

2.1.1 Simple Harmonic Oscillator Model and Definitions

The equations of motion for a harmonic oscillator of mass m and frequency Ω_m for the cases of gas damping and structural damping are given by [62]

$$m\ddot{x} + m\Gamma_m\dot{x} + m\Omega_m^2x = F_{th} \quad (\text{gas damping}) \quad (2.1)$$

$$m\ddot{x} + m\Omega_m^2[1 + i\Phi_m]x = F_{th} \quad (\text{structural damping}), \quad (2.2)$$

where $x = x(t)$ is the displacement from equilibrium, Γ_m (Φ_m) is the gas damping rate (structural "loss angle"), and $F_{th} = F_{th}(t)$ is the fluctuating thermal force. The latter is an inevitable consequence of the presence of damping in the equation of motion, as required to maintain the equipartition theorem (with thermal energy of $1/2k_B T$ per degree of freedom) in thermal equilibrium. The gas damping model introduces dissipation by means of a velocity-dependent frictional force. In the case of structural damping, energy loss results from a phase lag, commonly referred to as loss angle [64, 62], between restoring force and oscillator's displacement.

We get the transient solutions ($F_{th} = 0$) to the above given equations of motion (Eqs. 2.1-2.2), by plugging in a test function of the form $x(t) = x_0 \exp(iAt)$. The resulting trajectories are given by the real part of

$$x(t) = \begin{cases} x_0 e^{i\sqrt{\Omega_m^2 - \Gamma_m^2/4}t - \Gamma_m t/2} & \approx x_0 e^{i\Omega_m t} e^{-\Gamma_m t/2} & (\text{gas damping}) \\ x_0 e^{i\Omega_m \sqrt{1+i\Phi_m}t} & \approx x_0 e^{i\Omega_m t} e^{-\Omega_m \Phi_m t/2} & (\text{structural damping}). \end{cases} \quad (2.3)$$

The approximation applies in the case of a significantly underdamped oscillator ($\Gamma_m \ll \Omega_m$, $\Phi_m \ll 1$), which is the case for the mechanical resonators studied throughout this dissertation. By defining the mechanical ring-down time

$$\tau_m = \begin{cases} 2/\Gamma_m & (\text{gas damping}) \\ 2/(\Omega_m \Phi_m) & (\text{structural damping}), \end{cases} \quad (2.4)$$

both of the approximated solutions (Eq. 2.3) can be expressed as

$$x(t) = x_0 e^{-t/\tau_m} \cos(\Omega_m t). \quad (2.5)$$

The transient solution (Eq. 2.3) describes the response of the oscillator when an external driving force is instantaneously switched off. Then the oscillator's performs an exponential decay.

A commonly employed figure of merit for the isolation of a mechanical oscillator from its thermal environment, is the mechanical quality factor, defined as [65]

$$Q_m \equiv 2\pi \frac{U_m}{\Delta U_m}. \quad (2.6)$$

Here U_m is the average energy per cycle of oscillation stored in the oscillator and ΔU_m is the energy lost per cycle of oscillation. The total energy of a harmonic oscillator is given by the sum of kinetic and potential energy

$$E_m = \frac{1}{2} m \dot{x}^2 + \frac{1}{2} m \Omega_m^2 x^2. \quad (2.7)$$

Plugging in the transient solution (Eq. 2.3) in the previous expression and averaging over one cycle of oscillation (for which the amplitude decay is negligible) gives

$$U_m = \frac{1}{2} m \Omega_m^2 x_0^2. \quad (2.8)$$

The dissipated energy per cycle of oscillation is equivalent to the work done by the damping force F_{damp} during one cycle of oscillation:

$$\Delta U_m = \oint dx F_{damp} = \int_0^{2\pi/\Omega_m} dt \dot{x} F_{damp}. \quad (2.9)$$

Substituting the gas damping force (Eq. 2.1, 2nd term) together with the transient solution (Eq. 2.3) yields the energy lost per cycle of oscillation in the case of gas damping¹

$$\Delta U_m^{\text{gas}} = m \Gamma_m \int_0^{2\pi/\Omega_m} dt [\text{Re}(\dot{x})]^2 = m \Gamma_m \Omega_m^2 x_0^2 \int_0^{2\pi/\Omega_m} dt \sin^2(\Omega_m t) = 2\pi \frac{\Gamma_m}{\Omega_m} U_m$$

¹Since we assume low dissipation, e.g. $\Gamma_m \ll \Omega_m$, $\Phi_m \ll 1$, the amplitude decay in Eq. 2.3 is negligible during one cycle of oscillation. Furthermore we make use of $\int_0^{2\pi/\Omega_m} dt \sin^2(\Omega_m t) = \pi/\Omega_m$.

and similarly for the structural damping force (Eq. 2.2, 2nd term) we have

$$\Delta U_m^{\text{structural}} = m\Omega_m^2 \Phi_m \int_0^{2\pi/\Omega_m} dt \text{Re}(\dot{x}) \text{Re}(ix) = m\Omega_m^3 \Phi_m x_0^2 \int_0^{2\pi/\Omega_m} dt \sin^2(\Omega_m t) = 2\pi\Phi_m U_m.$$

Together with Eq. 2.6 and Eq. 2.8) follows

$$Q_m = \begin{cases} \Omega_m/\Gamma_m & (\text{gas damping}) \\ 1/\Phi_m & (\text{structural damping}). \end{cases} \quad (2.10)$$

By substituting Eq. 2.4 we have the common expression

$$Q_m = \Omega_m \tau_m / 2, \quad (2.11)$$

which, regardless of the particular damping mechanism, relates the mechanical quality factor to the oscillator's resonance frequency and ring-down time.

2.1.2 Thermal Noise

In this section we discuss the stationary solution as the oscillator's response to the random thermal driving force from the environment. The environment typically can be modeled as a large reservoir of degrees of freedom, which, due to their coupling to the oscillator, provide energy loss channels [66]. This reservoir is characterized by a broad energy distribution, whereby its density of states depends on the nature of its constituents (we will see that there is a difference, e.g., between internal degrees of freedom and those provided by surrounding gas molecules). The degrees of freedom in the reservoir are themselves in thermal equilibrium (i.e. randomly gyrating), thereby exerting a random “thermal force” on the oscillator, which drives it to thermal equilibrium [62]. This phenomenon is known as thermal noise or Brownian motion, where the latter terminology is motivated by similarities to the random motion of microscopic particles in a fluid [67]. Due to the large number of degrees of freedom in the thermal environment, the time-dependent noise-driven motion of the oscillator is characterized by a time-dependent amplitude.

In Sec. 2.1.2.1 we introduce the power spectral density (PSD) as commonly employed

means to describe the frequency spectrum of a time-dependent noisy signal, and discuss some of its properties. In Sec. 2.1.2.2 we present a description of a thermally driven harmonic oscillator in terms of PSDs. Hereby, we derive the displacement and force noise PSDs for the cases of structural and gas damping (see also Sec. 2.1.1).

2.1.2.1 Power Spectral Density Basics

We closely follow [66] to introduce a few key concepts for the spectral analysis of a classical signal. The signal is assumed to be stationary so that its statistical properties are time-independent, in the sense that sampling the signal “long enough” (clarified below) at different times will reveal the same statistical properties (e.g., mean value). A commonly-used expression for the spectrum or “frequency content” of a continuous signal $x(t)$ is the power spectral density (PSD), which is a measure for the amount of power carried by a certain frequency range of the signal. The PSD $S_{xx}(\omega)$ is defined by means of the windowed Fourier transform

$$x_T(\omega) \equiv \frac{1}{\sqrt{T}} \int_{-T/2}^{T/2} dt e^{-i\omega t} x(t). \quad (2.12)$$

as

$$\begin{aligned} S_{xx}(\omega) &:= \lim_{T \rightarrow \infty} |x_T(\omega)|^2 \\ &= \lim_{T \rightarrow \infty} \frac{1}{T} \int_{-T/2}^{T/2} dt e^{-i\omega t} x(t) \int_{-T/2}^{T/2} dt' e^{i\omega t'} x^*(t'), \end{aligned} \quad (2.13)$$

where T is the time over which the signal is measured (obtaining a reliable estimate of $S_{xx}(\omega)$ experimentally requires an ensemble average over many individual observations). Practically, the limit $T \rightarrow \infty$ can be expressed as $T \gg \tau_c$, with τ_c being a characteristic time scale on which $x(t)$ changes. In the case of a harmonic oscillator coupled to a classical thermal bath, τ_c is represented by the mechanical ring-down time τ_m (Sec. 2.1.1), as this is the time it takes to reach steady state when conditions change.. The normalization factor $1/\sqrt{T}$ of the windowed Fourier transform assures that $x_T(\omega)$ becomes independent of T for $T \gg \tau_c$. This basically says that the power associated with the signal is quadratic in its magnitude, as is the case, e.g., for a harmonic oscillator (Sec. 2.1.1).

In the following we employ the Fourier transform (denoted by operator \mathcal{F}) and its inverse [66]

$$\begin{aligned}\mathcal{F}[x(t)] &= x(\omega) = \int_{-\infty}^{\infty} dt e^{-i\omega t} x(t) \\ \mathcal{F}^{-1}[x(\omega)] &= x(t) = \int_{-\infty}^{\infty} \frac{d\omega}{2\pi} e^{i\omega t} x(\omega)\end{aligned}\tag{2.14}$$

to realize an alternative expression of the PSD; the inverse Fourier transform of Eq. 2.13 gives (where we drop the ensemble average for simplicity)

$$\begin{aligned}\int_{-\infty}^{\infty} \frac{d\omega}{2\pi} S_{xx}(\omega) e^{i\omega\tau} &= \lim_{T \rightarrow \infty} \frac{1}{T} \int_{-T/2}^{T/2} dt \int_{-T/2}^{T/2} dt' x(t) x^*(t') \int_{-\infty}^{\infty} \frac{d\omega}{2\pi} e^{-i\omega(t-t'-\tau)} \\ &= \lim_{T \rightarrow \infty} \frac{1}{T} \int_{-T/2}^{T/2} dt \int_{-T/2}^{T/2} dt' x(t) x^*(t') \delta(t-t'-\tau) \\ &= \lim_{T \rightarrow \infty} \frac{1}{T} \int_{-T/2}^{T/2} dt x(t) x^*(t-\tau) \\ &\equiv \langle x(t) x^*(t-\tau) \rangle,\end{aligned}$$

where we have made use of a definition of the delta function $\delta(t-t'-\tau)$ and the autocorrelation function $\langle x(t) x^*(t-\tau) \rangle$ with time average denoted by $\langle \dots \rangle$ [68]. Fourier transforming both sides of the previous expression results in the Wiener-Khinchin theorem [66]

$$S_{xx}(\omega) = \int_{-\infty}^{\infty} d\tau e^{-i\omega\tau} \langle x(t) x^*(t-\tau) \rangle,\tag{2.15}$$

which says that the PSD of a signal is given by the Fourier transform of its autocorrelation function. The special case $\tau = 0$ yields Parseval's theorem

$$\langle |x(t)|^2 \rangle = \int_{-\infty}^{\infty} \frac{d\omega}{2\pi} S_{xx},\tag{2.16}$$

which relates the mean square of the signal to the area under the PSD.

The PSD $S_{xx}(\omega)$, as defined above, is commonly referred to as “double-sided” PSD which highlights the fact that it distributes the signal content over positive and negative ω . For classical signals (i.e. not complex, such as $\cos(\omega t) = (e^{i\omega t} + e^{-i\omega t})/2$) however, this distribution

is symmetric with respect to $\omega = 0$

$$S_{xx}(-\omega) = S_{xx}(\omega), \quad (2.17)$$

motivating the definition of the single-sided PSD

$$S_x(\omega) \equiv 2S_{xx}(\omega), \quad (2.18)$$

which is defined only for positive frequencies, with a corresponding Parseval relationship

$$\langle |x(t)|^2 \rangle = \int_0^\infty \frac{d\omega}{2\pi} S_x. \quad (2.19)$$

2.1.2.2 Thermal Noise Power Spectral Density

In the following we apply the concepts presented in Sec. 2.1.2.1 to express the stationary solution of a thermally-driven harmonic oscillator in terms of power spectral densities (PSDs). Performing a Fourier transform (Eq. 2.14) on the oscillator's equations of motion (Eqs. 2.1-2.2) gives²

$$\begin{aligned} m [(\Omega_m^2 - \omega^2) + i\Gamma_m\omega] x(\omega) &= F_{th}(\omega) && \text{(gas damping)} \\ m [(\Omega_m^2 - \omega^2) + i\Phi_m\Omega_m^2] x(\omega) &= F_{th}(\omega) && \text{(structural damping)} \end{aligned}$$

The frequency-dependent oscillator response, the mechanical susceptibility $\chi_m(\omega)$, is defined as

$$x(\omega) \equiv \chi_m(\omega) F_{th}(\omega) \quad (2.20)$$

$$\chi_m(\omega) = \begin{cases} m^{-1} [(\Omega_m^2 - \omega^2) + i\Gamma_m\omega]^{-1} & \text{(gas damping)} \\ m^{-1} [(\Omega_m^2 - \omega^2) + i\Phi_m\Omega_m^2]^{-1} & \text{(structural damping)} \end{cases} \quad (2.21)$$

From this, combined with the displacement PSD (Eq. 2.13) and the definition of a single-sided

²Making use of $\mathcal{F} \left[\frac{d^n}{dt^n} x(t) \right] = (i\omega)^n x(\omega)$

spectrum (Eq. 2.18), it follows that

$$S_x(\omega) = |\chi_m(\omega)|^2 S_F(\omega), \quad (2.22)$$

where $S_F(\omega)$ is the single-sided force noise PSD. For the system under consideration, the general expression for the thermal force noise PSD is given by [61]

$$S_F(\omega) = \frac{4k_B T}{\omega} \text{Im} [\chi_m^{-1}(\omega)]. \quad (2.23)$$

Then, applying linear time-dependent perturbation theory gives the previous expression.

With the above given susceptibilities (Eq. 2.21) follows

$$S_F(\omega) = \begin{cases} 4mk_B T \Gamma_m & (\text{gas damping}) \\ 4mk_B T \Phi_m \Omega_m^2 / \omega & (\text{structural damping}) \end{cases} \quad (2.24)$$

and with Eq. 2.22 we find the oscillator's response to the external drive

$$S_x(\omega) = \begin{cases} \frac{4k_B T \Gamma_m}{m [(\Omega_m^2 - \omega^2)^2 + \Gamma_m^2 \omega^2]} & (\text{gas damping}) \\ \frac{4k_B T \Phi_m \Omega_m^2}{m \Omega [(\Omega_m^2 - \omega^2)^2 + \Phi_m^2 \Omega_m^4]} & (\text{structural damping}) \end{cases} \quad (2.25)$$

In the case of low dissipation ($\Gamma_m \ll \Omega_m$, $\Phi_m \ll 1$) and frequencies close to the resonance ($\omega \approx \Omega_m$), both of the previous expressions can be approximated by a ‘‘Lorentzian’’

$$S_x(\Omega) \approx \frac{2\tau_m k_B T}{m \Omega_m^2 [1 + (\omega - \Omega_m)^2 \tau_m^2]}, \quad (2.26)$$

where we have made use of expressions 2.4 to substitute Γ_m and Φ_m by τ_m . In a similar fashion, for ($\omega \approx \Omega_m$), we can approximate both expressions 2.24 by

$$S_F = 8mk_B T / \tau_m. \quad (2.27)$$

Figure 2.1 shows a plot of the three different expressions given for $S_x(\omega)$ (Eqs. 2.25-2.26) (plot parameters $\Omega_m = 41.36$ kHz, $m = 2.3$ ng, $\tau_m = 285$ s, $\Gamma_m = 7$ mHz, $\Phi_m = 2.7 \times 10^{-8}$, corresponding to a typical trampoline device discussed in Chapters 3-4). The blue curve corresponds to gas damping, the red curve describes structural damping and the approximated PSD is plotted in green. In vicinity of a few kHz around $\Omega_m/2\pi$, the curves are indistinguishable on the plotted scale. Outside this range clear deviations are apparent; The structural model, due to a thermal driving force $\propto 1/\omega$ (Eq. 2.24), goes to infinity for $\omega \rightarrow 0$ (may be seen as an indication that the model is not applicable in that range). In contrast, the gas damping model converges to a constant value, as a consequence of the frequency-independent (“white”) force noise (Eq. 2.24). For $\omega \rightarrow \infty$ the parameters within both models go to 0, where, by the same reasoning as for $\omega \rightarrow 0$, the structural model decays faster than the gas damping model. The approximated PSD becomes meaningless further away from resonance.

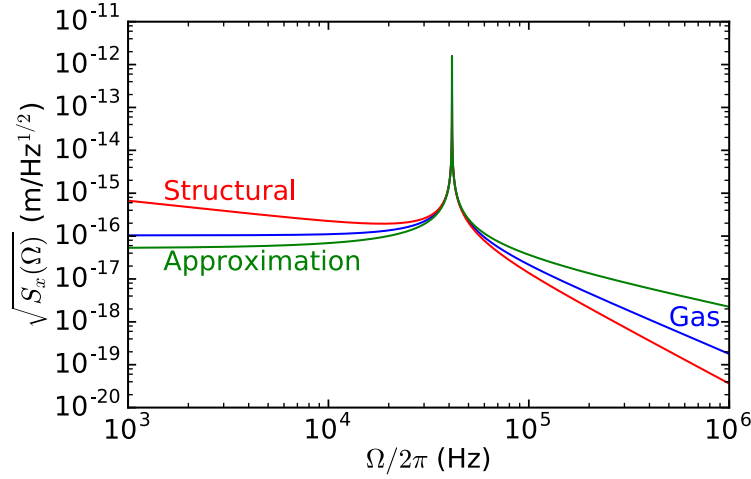


Figure 2.1: Displacement power spectral densities of a thermally driven harmonic oscillator with structural damping (blue) or velocity damping (red) (Eq. 2.25, upper and lower). The green curve represents a Lorentzian approximation (Eq. 2.26) valid for both models in the case of low dissipation ($\Gamma_m \ll \Omega_m$, $\Phi_m \ll 1$) and frequencies close to the resonance ($\omega \approx \Omega_m$). The plot parameters are $\Omega_m = 41.36$ kHz, $m = 2.3$ ng, $\tau_m = 285$ s, $\Gamma_m = 7$ mHz, and $\Phi_m = 2.7 \times 10^{-8}$.

For the approximate case, we can provide a sanity-check for this solution by applying Parseval’s theorem (Eq. 2.19) to expression 2.26 to obtain the mean square amplitude of the

thermally excited oscillator. By substituting

$$y = (\omega - \Omega_m)\tau_m \quad d\omega = \frac{dy}{\tau_m} \quad (2.28)$$

we have

$$\begin{aligned} \langle x^2(t) \rangle &= \int_0^\infty \frac{d\omega}{2\pi} S_x = \frac{2k_B T}{m\Omega_m^2} \frac{1}{2\pi} \int_{-\Omega_m\tau_m}^\infty dy \frac{1}{y^2 + 1} \\ &= \frac{k_B T}{m\Omega_m^2} \frac{1}{\pi} \arctan(y) \Big|_{-\Omega_m\tau_m}^\infty \\ &= \frac{k_b T}{m\Omega_m^2}. \end{aligned}$$

This result is in agreement with the equipartition theorem [69]

$$\left\langle x \frac{\partial H}{\partial x} \right\rangle = \langle m\Omega_m^2 x^2(t) \rangle = k_b T, \quad (2.29)$$

where we have substituted the system's Hamiltonian H by the oscillator's total energy (2.7).

The root mean square (rms) displacement is then

$$x_{\text{rms}} = \sqrt{\frac{k_b T}{m\Omega_m^2}}, \quad (2.30)$$

which represents the average amplitude of oscillation for a thermally driven harmonic oscillator with either gas damping or structural damping (in the latter case a small enough bandwidth of observation is required so that the peak around Ω_m (see Fig. 2.1) provides the main power of the signal). This result equally applies when considering the oscillation of a three-dimensional object along one spatial direction, i.e. when considering a single degree of freedom, as is the case in the experimental studies of our fabricated mechanical resonators (see Sec. 3.3.1).

2.2 Optical Resonances of Fabry-Perot Cavity with Incorporated Membrane

Throughout this thesis we employ different kinds of optical interferometers such as free-space Fabry-Perot cavities, with or without incorporated membrane, and a fiber interferometer. These setups are probed by a monochromatic laser beam with Gaussian intensity profile at near infrared wavelength $\lambda = 1550$ nm. Here we provide a one-dimensional plane wave description of this interaction in which the electromagnetic field only depends on the location along its direction of propagation and is uniform in the lateral directions. This simplified treatment enables fundamental insight in the underlying interference phenomena, and provides quantitative models for observables, such as the system's optical resonance frequencies, reflected, transmitted, and internal optical fields, and the storage time of the light inside the system. Mathematically, the combined system (comprising an input mirror, free space, a membrane / trampoline, free space, and a second mirror) can be described by a transfer matrix [70] (or similarly a characteristic matrix [71]), and the optical field propagating through the system can be expressed in terms of the transfer matrix elements and the incident field(s). In Sec. 2.2.1 we pedagogically review basic properties of electromagnetic waves (following Ref. [72]) and introduce elementary transfer matrices describing propagation through a homogenous medium (i.e., free space or a dielectric), an interface between two dielectrics, a freestanding dielectric membrane (e.g., a trampoline), and a distributed Bragg reflector (DBR). In Sec. 2.2.2 we apply the transfer matrix method to a Fabry-Perot cavity, consisting of two DBRs and an intermediate air/vacuum layer, to derive expressions for the resonance frequency spectrum, reflected, transmitted, and circulating optical fields, and the cavity finesse (unitless quantity proportional to storage time of light inside cavity). We discuss how the intra-cavity field gives rise to a mechanical force acting on the mirrors. Thereby, we introduce the concept of linear optomechanical coupling. Sec. 2.2.3 is similar to Sec. 2.2.2 but for a Fabry-Perot cavity with incorporated membrane. In Sec. 2.2.4 we examine the steady state optical force acting on the membrane inside the cavity and the optical spring effect resulting from positioning the membrane at a field antinode (in a latter chapter (Sec. 4.3) we investigate the prospects for exploiting this effect to increase the

mechanical quality factor of our trampoline resonator's (see Sec. 3.1.1)). In Sec. 2.2.5 we briefly discuss how the optical resonance's dependence on the membrane displacement along the cavity axis gives rise to linear and quadratic optomechanical coupling. With regard to studying the quantum motion of one of our trampolines in a future experiment, in Sec. 2.2.6 we outline the method of cavity-assisted laser cooling and its quantum limits. Hereby we identify the single photon cooperativity as a figure of merit for controlling the membrane's trajectory with small amounts of light (which is ~ 10 in our system, as presented in a later chapter (Sec. 4.2.2)).

2.2.1 Optical Transfer Matrix Method

An optical transfer matrix (TM) represents a component of a stratified optical medium, such as an interface or an individual layer, and relates the optical fields on the left and right side of the component to each other. The field at any location x_i in the stratified medium constitutes a right traveling wave and a left traveling wave³ with field amplitudes A_i and B_i and wavenumber k , such that the total (complex) field is given by

$$E(x_i) = A_i e^{ikx_i} + B_i e^{-ikx_i}. \quad (2.31)$$

The propagation is taken to be along the direction of stratification, which is set as the x -direction. In the above given expression we omitted the time dependency; the real electric field at location x and time t is given by $\text{Re}[E(x) e^{-i\omega t}]$. The wavenumber k is related to the optical angular frequency ω by the dispersion relation $\omega = ck$, where c is the speed of light. Both c and k depend on the refractive index n of the medium in which the light propagates; if c_0 and k_0 are the values in vacuum, then inside the medium they are given by $c = c_0/n$ and $k = nk_0$ (in general n is complex valued, where the imaginary part describes optical loss). The corresponding dispersion relation $\omega = ck = c_0 k_0$ highlights that it is the frequency that remains constant for the waves propagating in different media (as long as n is independent

³For a monochromatic plane wave given by $\text{Re}[E_0 e^{\pm ikx - i\omega t}]$ its direction of propagation becomes evident from tracking a wave front, which is a plane of constant phase. For propagation by distance Δx in time interval Δt , the constant phase requires $\pm kx - kct = \pm kx \pm k\Delta x - kct - kc\Delta t$ and therefore $\Delta x = \pm c\Delta t$, where the plus (minus) sign corresponds to a right (left) traveling wave.

of E). The wavenumber is related to the wavelength by $k = n2\pi/\lambda$.

Let us consider the propagation of light described by Eq. 2.31 in a uniform medium. A schematic of this situation is shown in Table 2.1(a), where the field at location x_1 is given by

$$E_1 = A_1 e^{ikx_1} + B_1 e^{-ikx_1}. \quad (2.32)$$

and the field at location $x_2 = x_1 + \Delta x$ is given by

$$\begin{aligned} E_2 &= A_1 e^{ikx_2} + B_1 e^{-ikx_2} \\ &= A_1 e^{ik(x_1 + \Delta x)} + B_1 e^{-ik(x_1 + \Delta x)} \\ &=: A_2 e^{ikx_1} + B_2 e^{-ikx_1}. \end{aligned}$$

The relation between the field amplitudes at x_1 and x_2 is given by

$$\begin{aligned} A_2 &= A_1 e^{ik\Delta x} \\ B_2 &= B_1 e^{-ik\Delta x}, \end{aligned}$$

and written in a TM representation

$$\begin{pmatrix} A_2 \\ B_2 \end{pmatrix} = \begin{pmatrix} e^{ik\Delta x} & 0 \\ 0 & e^{-ik\Delta x} \end{pmatrix} \begin{pmatrix} A_1 \\ B_1 \end{pmatrix}. \quad (2.33)$$

We now consider a more general case, where the outgoing fields (B_1, A_2) are a linear superposition of the incoming fields (A_1, B_2) :

$$B_1 = r_{12}A_1 + t_{21}B_2 \quad (2.34)$$

$$A_2 = t_{12}A_1 + r_{21}B_2, \quad (2.35)$$

with directional reflection and transmission coefficients r_{12} , r_{21} and t_{12} , t_{21} . In the case of lossless propagation, energy conservation requires (see Appendix A.4) $|A_1|^2 + |B_2|^2 =$

$|B_1|^2 + |A_2|^2$, which, together with Eqs. 2.34-2.35, results in the conditions

$$|r_{12}|^2 + |t_{12}|^2 = |r_{21}|^2 + |t_{21}|^2 = 1 \quad (2.36)$$

$$r_{12}t_{21}^* = -t_{12}r_{21}^*. \quad (2.37)$$

The first expression represents conservation of optical energy. The second relation constraints the phase relation between the reflection and transmission coefficients. We convert Eqs. 2.34-2.35 into a TM representation by solving the first equation for B_2 and replacing B_2 in the second equation by this expression, resulting in

$$\begin{pmatrix} A_2 \\ B_2 \end{pmatrix} = t_{21}^{-1} \begin{pmatrix} t_{21}t_{12} - r_{21}r_{12} & r_{21} \\ -r_{12} & 1 \end{pmatrix} \begin{pmatrix} A_1 \\ B_1 \end{pmatrix}. \quad (2.38)$$

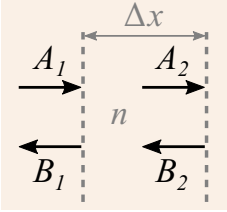
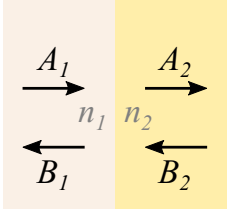
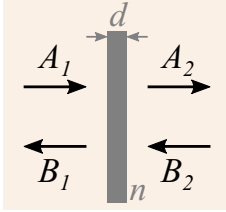
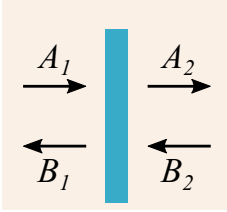
(a) Propagation	(b) Interface	(c) Slab	(d) DBR
			
$\begin{pmatrix} e^{ik_0n\Delta x} & 0 \\ 0 & e^{-ik_0n\Delta x} \end{pmatrix}$	$t_{21}^{-1} \begin{pmatrix} 1 & -r_{12} \\ -r_{12} & 1 \end{pmatrix}$	$t_d^{-1} \begin{pmatrix} -e^{i2\phi_r} & r_d \\ - r_d & 1 \end{pmatrix}$	$-it^{-1} \begin{pmatrix} -1 & -r \\ r & 1 \end{pmatrix}$

Table 2.1: Transfer matrices for optical plane wave propagation in a stratified medium. (a) Propagation of length Δx in a homogeneous medium with refractive index n . (b) Propagation through the interface between two dielectric media with Fresnel coefficients r_{12}, t_{21} (Eqs. 2.39-2.40) depending on refractive indices n_1 and n_2 . (c) Propagation through a dielectric slab (thickness d , refractive index n) with reflection (transmission) coefficient r_d (t_d) (Eqs. 2.41-2.42), which is surrounded by air/vacuum (refractive index 1). Reflection coefficient is written in terms of amplitude and phase $r_d = |r_d| e^{i\phi_r}$. (d) Propagation through a distributed Bragg reflector (DBR) with transmission (t) and reflection (r) coefficients (both assumed real and positive for convenience; see Appendix A.2 for details).

In the following, we discuss a few special cases of the general TM (Eq. 2.38), which will be applied in later chapters. We start with the basic example of an interface formed by two dielectric media with refractive indices n_1, n_2 . A schematic of this situation is shown in

Table 2.1(b). Here, reflection and transmission coefficients are given by Fresnel coefficients [71]

$$r_{ab} = \frac{n_a - n_b}{n_a + n_b} \quad (2.39)$$

$$t_{ab} = \frac{2n_a}{n_a + n_b}, \quad (2.40)$$

with $(a, b) \in \{(1, 2), (2, 1)\}$. For these coefficients $t_{21}t_{12} - r_{21}r_{12} = 1$, so that only the off-diagonal matrix elements in Eq. 2.38 are different from 1, resulting in the interface TM given in Table 2.1(3rd row, 2nd column).

Another special case of Eq. 2.38 describes the situation of a freestanding dielectric slab surrounded by air/vacuum. A corresponding schematic is shown in Table 2.1(c) where a dielectric slab with thickness d and refractive index n is surrounded by air/vacuum with refractive index 1. The symmetry of this configuration requires $r_{12} = r_{21} = r_d$ and $t_{12} = t_{21} = t_d$ with complex-value reflection and transmission coefficients r_d, t_d given by

$$r_d = \frac{(1 - n^2) \sin(knd)}{(n^2 + 1) \sin(knd) + i2n \cos(knd)} \quad (2.41)$$

$$t_d = \frac{2in}{(n^2 + 1) \sin(knd) + i2n \cos(knd)}, \quad (2.42)$$

(see Appendix A.1 for derivation). Then the upper left TM element (Eq. 2.38) can be written

$$t_d^2 - r_d^2 = |t_d|^2 e^{i2\phi_t} - |r_d|^2 e^{i2\phi_r} = e^{i2\phi_r} (|t_d|^2 e^{i2(\phi_t - \phi_r)} - |r_d|^2) = -e^{i2\phi_r}, \quad (2.43)$$

where we have expressed the reflection and transmission coefficients in terms of their magnitude $|r_d|, |t_d|$ and phase ϕ_r, ϕ_t . In the last step we applied Eqs. 2.36-2.37, which yield the phase relation $\phi_t - \phi_r = \pm(2q + 1)\pi/2$ with $q \in \mathbb{N}$ (see Fig. A.1) and consequently $e^{i2(\phi_t - \phi_r)} = -1$. The resulting TM is given in Table 2.1 (3rd row, 3rd column).

Finally, we introduce the TM of a lossless distributed Bragg reflector (DBR). The DBR reflection and transmission coefficients are given by $r_{12} = r_{21} = -r$ and $t_{12} = t_{21} = it$ with $r, t \in [0, 1]$ (see Appendix A.2 for details and derivation of reflection and transmission coefficients). The resulting TM is shown in Table 2.1 (3rd row, 4th column).

Up to now we introduced TMs that describe individual optical elements (see Table 2.1). In the following two sections - and in later chapters - we employ the introduced TMs to model systems that comprise several of the individual elements discussed here. The entire system is described by the matrix resulting from multiplying the individual TMs of each component together: Let us consider a stratified medium formed by N individual components, where component i is represented by transfer matrix \mathbf{M}_i with $i \in \{1, 2, \dots, N\}$. Then the transfer matrix of the entire system is given by

$$\mathbf{M} = \mathbf{M}_N \dots \mathbf{M}_i \dots \mathbf{M}_2 \mathbf{M}_1 \equiv \begin{pmatrix} \mu_{11} & \mu_{12} \\ \mu_{21} & \mu_{22} \end{pmatrix}$$

and the optical fields on the left and right side of the system are related by

$$\begin{pmatrix} A_N \\ B_N \end{pmatrix} = \begin{pmatrix} \mu_{11} & \mu_{12} \\ \mu_{21} & \mu_{22} \end{pmatrix} \begin{pmatrix} A_1 \\ B_1 \end{pmatrix}, \quad (2.44)$$

where we have written \mathbf{M} in terms of its elements μ_{ab} with $a, b \in \{1, 2\}$. At this point, we've reduced a system of $2N+2$ fields to a system of two equations. If one specifies the input fields (A_1 and B_N), for example, one can now quickly calculate the transmission and reflection of the entire system by solving this system for A_N and B_1 , respectively⁴.

Similarly, we can relate the fields to the left of component j to the fields on the left of the entire system

$$\begin{pmatrix} A_j \\ B_j \end{pmatrix} = \begin{pmatrix} \tilde{\mu}_{11} & \tilde{\mu}_{12} \\ \tilde{\mu}_{21} & \tilde{\mu}_{22} \end{pmatrix} \begin{pmatrix} A_1 \\ B_1 \end{pmatrix} \quad (2.45)$$

where $\tilde{\mu}_{ab}$ are the elements of matrix $\mathbf{M}_{j-1} \dots \mathbf{M}_2 \mathbf{M}_1$. By means of Eq. 2.44 we can replace the outgoing field B_1 by the incoming fields A_1 , B_N

$$B_1 = \frac{B_N - \mu_{21}A_1}{\mu_{22}} \quad (2.46)$$

which yields the following relation of the “internal fields” A_j and B_j to the input fields A_1

⁴Additionally, n copies of this system would be described by a matrix \mathbf{M}^n , a trick that can dramatically increase computation speed for DBR's. See Appendix A.2.

and B_N

$$A_j = \left(\tilde{\mu}_{11} - \tilde{\mu}_{12} \frac{\mu_{21}}{\mu_{22}} \right) A_1 + \frac{\tilde{\mu}_{12}}{\mu_{22}} B_N \quad (2.47)$$

$$B_j = \left(\tilde{\mu}_{21} - \tilde{\mu}_{22} \frac{\mu_{21}}{\mu_{22}} \right) A_1 + \frac{\tilde{\mu}_{22}}{\mu_{22}} B_N. \quad (2.48)$$

Reflection from and transmission through the complete stack is obtained for $\tilde{\mu}_{ab} \rightarrow \mu_{ab}$.

2.2.2 Optical Resonances of a Fabry-Perot Cavity

Here we employ the transfer matrix (TM) method introduced in the previous section to characterize the optical resonances of a Fabry-Perot cavity. A schematic of the setup is shown in Fig. 2.2, where two mirrors face each other at a distance L_c . Each mirror is characterized by a reflection coefficient (r_1, r_2 respectively) and a transmission coefficient (t_1, t_2 respectively). Note that both r_i, t_i ($i \in \{1, 2\}$) are real valued for convenience (see also previous section). Incoming light with amplitude E_{in} and wavenumber k is partially reflected at the input mirror and partially coupled to the right and left traveling intra-cavity fields E_{cl} and E_{cr} . Light reflected from and transmitted through the cavity is denoted by E_r and E_t respectively. Note that we have adopted a different nomenclature here with respect to the previous section; since there are only five field components of interest, we have chosen more intuitive symbols, e.g., E_t for the transmitted field instead of A_3 . Furthermore, with regard to an analytical calculation of the circulating optical power inside the cavity we only consider intra-cavity field components E_{cr} (right-moving) and E_{cl} (left-moving), located at the interface between left mirror and cavity. The field components at other locations within the cavity are characterized by the same amplitude but different phase.

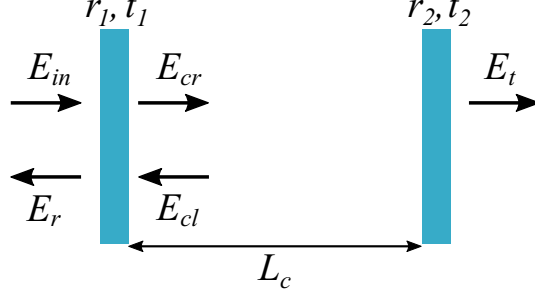


Figure 2.2: Schematic of a one-dimensional Fabry-Perot cavity. The cavity is formed by two mirrors facing each other at a distance set by the cavity length L_c . Right (Left) mirror is characterized by its reflection coefficient r_1 (r_2) and transmission coefficient t_1 (t_2). Incident light with amplitude E_{in} is partially reflected at the input mirror and partially coupled to the intra-cavity fields E_{cl} and E_{cr} . Light reflected from and transmitted through the cavity is denoted by E_r and E_t respectively.

The fields on the right and left side of the cavity are related by

$$\begin{pmatrix} E_t \\ 0 \end{pmatrix} = \mathbf{M}_{\text{cav}} \begin{pmatrix} E_{in} \\ E_r \end{pmatrix} = \begin{pmatrix} \mu_{11} & \mu_{12} \\ \mu_{21} & \mu_{22} \end{pmatrix} \begin{pmatrix} E_{in} \\ E_r \end{pmatrix}, \quad (2.49)$$

with the cavity's TM \mathbf{M}_{cav} , given by a product of a left mirror TM, a propagation TM, and a right mirror TM (see Table 2.1)

$$\begin{aligned} \mathbf{M}_{\text{cav}} &= \frac{1}{it_2} \begin{pmatrix} -1 & -r_2 \\ r_2 & 1 \end{pmatrix} \begin{pmatrix} e^{ikL_c} & 0 \\ 0 & e^{-ikL_c} \end{pmatrix} \frac{1}{it_1} \begin{pmatrix} -1 & -r_1 \\ r_1 & 1 \end{pmatrix} \\ &= \frac{1}{t_1 t_2} \begin{pmatrix} e^{-ikL_c} r_1 r_2 - e^{ikL_c} & e^{-ikL_c} r_2 - e^{ikL_c} r_1 \\ e^{ikL_c} r_2 - e^{-ikL_c} r_1 & e^{ikL_c} r_1 r_2 - e^{-ikL_c} \end{pmatrix}. \end{aligned} \quad (2.50)$$

The reflected field follows from Eq. 2.48 (with $B_N = 0$)

$$\frac{E_r}{E_{in}} = -\frac{\mu_{21}}{\mu_{22}} = \frac{r_1 - r_2 e^{2ikL_c}}{-1 + r_1 r_2 e^{2ikL_c}} \quad (2.51)$$

and the corresponding fractional reflected power is given by

$$\left| \frac{E_r}{E_{in}} \right|^2 = \frac{r_1^2 + r_2^2 - 2r_1 r_2 \cos(2kL_c)}{1 + r_1^2 r_2^2 - 2r_1 r_2 \cos(2kL_c)}. \quad (2.52)$$

The optical power with unit Watt is given by multiplying the previous expression by $c\varepsilon_0 n\mathcal{J}/2$, with speed of light c , dielectric permittivity ε_0 , refractive index n , and cross-sectional area of optical field \mathcal{J} . In the following, by “power” we refer just to the absolute square of the complex field amplitude.

Transmitted field and power follow from Eq. 2.47 (with $B_N = 0$)

$$\frac{E_t}{E_{in}} = \mu_{11} - \frac{\mu_{12}\mu_{21}}{\mu_{22}} = \frac{t_1 t_2 e^{ikL_c}}{-1 + r_1 r_2 e^{2ikL_c}} \quad (2.53)$$

$$\left| \frac{E_t}{E_{in}} \right|^2 = \frac{t_1^2 t_2^2}{1 + r_1^2 r_2^2 - 2r_1 r_2 \cos(2kL_c)}. \quad (2.54)$$

With Eq. 2.47 also follows the right traveling intra-cavity field and power ($B_N = 0$)

$$\frac{E_{cr}}{E_{in}} = \tilde{\mu}_{11} - \tilde{\mu}_{12} \frac{\mu_{21}}{\mu_{22}} = \frac{-it_1}{-1 + r_1 r_2 e^{2ikL_c}} \quad (2.55)$$

$$\left| \frac{E_{cr}}{E_{in}} \right|^2 = \frac{t_1^2}{1 + r_1^2 r_2^2 - 2r_1 r_2 \cos(2kL_c)}, \quad (2.56)$$

where $\tilde{\mu}_{ab}$ ($a, b \in \{1, 2\}$) correspond to matrix elements of left mirror TM. The left traveling cavity field is given by $E_{cl} = r_2 E_{cr}$. In the case of a highly reflective end mirror, left and right traveling cavity fields are roughly identical, e.g. $r_2 > 0.99$ results in a deviation $< 1\%$, so that one refers to either of them as the circulating field $E_c \equiv E_{cr} \approx E_{cl}$. With this choice of end mirror coefficients, the circulating power $P_c \propto |E_c|^2$ (Eq. 2.56) is maximal when the resonance condition

$$k_N = N \frac{\pi}{L_c} \quad (N \in \mathbb{N}) \quad (2.57)$$

is fulfilled, or, in terms of the wavelength

$$L_N = N \frac{\lambda}{2}. \quad (2.58)$$

This expression coincides with the resonance condition for clamped boundary conditions. The integer N represents the longitudinal mode order. Multiplying the previous expression by c yields the resonance frequencies

$$\omega_N = N \frac{\pi c}{L_c} =: N \omega_{\text{FSR}}, \quad (2.59)$$

where in the last step we have defined the free spectral range ω_{FSR} as increment between subsequent longitudinal modes. The previous expression tells us which frequency or wavelength $\lambda_N = 2\pi c/\omega_N$ is required for light incident on the cavity in order to meet the resonance condition. Alternatively, the resonance condition for incident light of fixed λ can be met by adjusting L_c ; from $k_N = 2\pi/\lambda$ together with Eq. 2.57 follows the expression for the resonance cavity length.

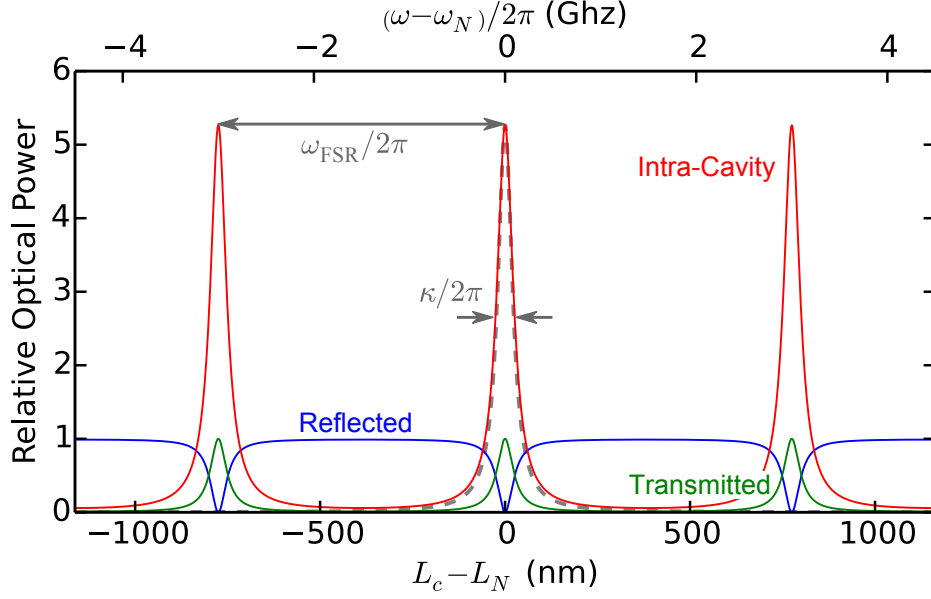


Figure 2.3: Resonance spectrum of a Fabry-Perot cavity with mirror reflectivities $r_1 = r_2 = 0.9$ and cavity length $L_c \approx 5$ cm, which is probed by laser light with frequency $\omega \approx 2\pi \times 1.94 \times 10^{14}$ Hz corresponding to wavelength $\lambda \approx 1550$ nm. Blue, green, and red curves correspond to reflected, transmitted, and intra-cavity power (all three relative to input power, given by Eqs. 2.52, 2.54, 2.56 respectively) versus cavity length L_c and optical frequency ω . Lower axis describes the situation in which cavity length is changed around a resonance length L_N (Eq. 2.58, longitudinal mode number $N = 64516$) for incident light with wavelength $\lambda = 1550$ nm. Neighboring peaks are separated by $\lambda/2$. Upper axis describes frequency detuning of light incident on a cavity with fixed $L_c = 5$ cm, with respect to cavity resonance frequency ω_N (Eq. 2.59, $N = 64516$). The spacing between consecutive modes is given by free spectral range $\omega_{\text{FSR}} = 2\pi \times 3$ GHz. Resonance linewidth $\kappa = 2\pi \times 0.2$ GHz corresponds to full width at half maximum of peaks. Gray dashed curve shows Lorentzian approximation of central resonance (Eq. 2.60).

Figure 2.3 shows the resonance spectrum of a Fabry-Perot cavity with $r_1 = r_2 = 0.9$ and $L_c \approx 5$ cm, which is probed by light with frequency $\omega \approx 2\pi \times 1.94 \times 10^{14}$ Hz ($\lambda \approx 1550$ nm). Blue, green, and red curves correspond to reflected, transmitted, and intra-cavity power

(all three normalized with respect to input power), given respectively by Eqs. 2.52, 2.54, 2.56. The lower horizontal axis represents the situation in which the incident laser has a fixed frequency and the cavity length is changed within few $\lambda/2$ around a resonance length $L_N \approx 5$ cm (Eq. 2.58, $N = 64516$). The upper horizontal axis applies to the case of fixed cavity length $L_c = 5$ cm and incident light is tuned to within a few free spectral ranges $\omega_{FSR} = 2\pi \times 3$ GHz around a cavity resonance $\omega_N \approx 2\pi \times 1.94 \times 10^{14}$ Hz (Eq. 2.59, $N = 64516$). When the resonance condition (Eqs. 2.58, 2.59) is satisfied, the intra-cavity field builds up. As a consequence the transmitted power approaches one and the reflected power goes to zero. The latter results from destructive interference between the promptly reflected light from the input mirror and the intra-cavity light that is transmitted through the input mirror. The resonance linewidth of the resulting peaks/dips is defined as the full width at half maximum (FWHM) $\kappa = 2\pi \times 0.2$ GHz.

A single cavity resonance, for $r_1, r_2 \approx 1$, can be approximated by a Lorentzian; for small detuning $\Delta = \omega_l - \omega_N$ between an incident laser with frequency ω_l and a cavity resonance ω_N , we can expand the cosine in Eq. 2.56. This yields ⁵

$$\left| \frac{E_{cr}}{E_{in}} \right|^2 = \frac{(t_1 c / 2L_c)^2}{\Delta^2 + \kappa^2 / 4}, \quad (2.60)$$

which represents a Lorentzian with FWHM κ (gray dashed curve in Fig. 2.3). Similarly to a harmonic oscillator, - which has a frequency spectrum characterized by a Lorentzian resonance (see Sec. 2.1) - is the inverse of the FWHM associated with a decay time $\tau_c = \kappa^{-1}$, representing the time scale on which the intra-cavity field responds to a change in its operating conditions, e.g., τ_c is the characteristic time scale for the exponential decay of the intra-cavity power when an incident laser is switched off.

A measure for the enhancement of the intra-cavity power with respect to the incident power is provided by the cavity finesse, defined as

$$\mathcal{F} := \frac{\omega_{FSR}}{\kappa} = \frac{\pi}{2 \arcsin \left(\frac{1-r_1 r_2}{2\sqrt{r_1 r_2}} \right)} \quad (2.61)$$

⁵By Δ small we consider $\Delta \ll \omega_{FSR}$: $\cos(2kL_c) = \cos(2\omega_l L_c / c) = \cos[2(\omega_N + \Delta)L_c / c] = \cos(2\Delta L_c / c) = \cos(2\pi\Delta / \omega_{FSR})$.

(see Appendix A.3 for derivation of κ). In the case of highly-reflective mirrors ($r_1, r_2 \approx 1$) the previous expression can be approximated as

$$\mathcal{F} \approx \frac{\pi}{1 - r_1 r_2} \approx \frac{2\pi}{2 - r_1^2 - r_2^2}. \quad (2.62)$$

Comparing this expression to the circulating power (Eq. 2.56) in a symmetric cavity ($r_1 = r_2$) yields $P_c/P_0 = \mathcal{F}/\pi$ (Eq. 2.56, 2.62). Alternatively, we can express \mathcal{F} in terms of the cavity ring-down time $\tau_c = \kappa^{-1}$

$$\mathcal{F} = \frac{\pi c \tau_c}{L_c}. \quad (2.63)$$

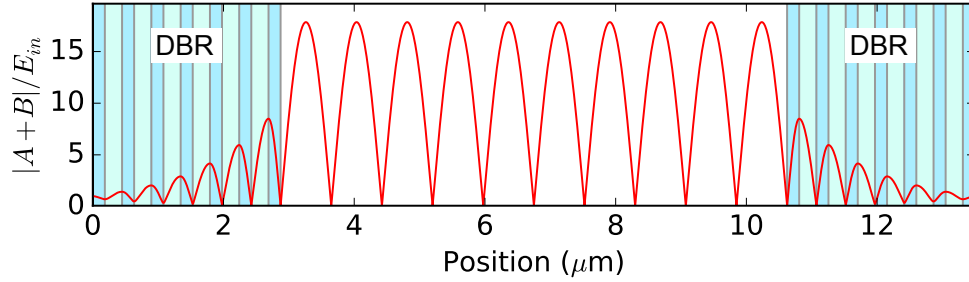


Figure 2.4: Electric field amplitude distribution $|A + B|$ (relative to input E_{in}), with amplitude of right and left traveling field respectively given by A and B , inside a Fabry-Perot cavity (see text for details). Cavity is formed by two distributed Bragg reflectors (DBRs, see Appendix A.2 for details) each comprising six and a half layer pairs of material a (light blue, refractive index 2.10, e.g. Ta_2O_5) and material b (light green, refractive index 1.47, e.g. SiO_2) corresponding to $r_1 = r_2 = 0.991$ (Eq. A.9, with refractive index of substrate $n_s = 1.47$) and $\mathcal{F} = 175$ (Eq. 2.62). Optical length (physical length times refractive index) of each layer is $\lambda/4$ with wavelength $\lambda = 1550$ nm. The mirrors are separated by 5λ corresponding to mode order $N = 10$ (Eq. 2.58).

Figure 2.4 shows the electric field amplitude distribution $|A + B|/E_{in}$ inside a Fabry-Perot cavity, designed for light with wavelength $\lambda = 1550$ nm, where A and B are the position-dependent right and left traveling field amplitudes. The cavity is formed by two identical distributed Bragg reflectors (DBRs). Each DBR is composed of six and a half layer pairs of material a (light blue, refractive index 2.10, e.g. Ta_2O_5) and material b (light green, refractive index 1.47, e.g. SiO_2). The optical length (physical length times refractive index) of each layer is $\lambda/4$ with $\lambda = 1550$ nm. These parameters correspond to $r_1 = r_2 = 0.991$ (Eq. A.9) and $\mathcal{F} = 175$ (Eq. 2.61). The mirrors are separated by 5λ corresponding to longitudinal

mode order $N = 10$ (Eq. 2.58). Field amplitudes A and B are calculated numerically; TM of depicted cavity is a product of TMs describing individual layers and interfaces (given in Table 2.1). The electric field at each position x within the cavity and DBRs is of the form $E(x) = Ae^{ikx} + Be^{-ikx}$ (see Sec. 2.2.1), where right (left) traveling field amplitude A (B) is given by Eq. 2.47 (Eq. 2.48). The intra-cavity field decays exponentially towards the outer sides of the DBR, where it is one.

The intra-cavity field causes a mechanical force (see Appendix A.2 for a classical derivation)

$$F_c = \pm 2 \frac{P_c}{c} \quad (2.64)$$

to act on the cavity mirrors (a photon of energy $E = \hbar ck$, with reduced Planck constant \hbar , transfers a momentum of $p = 2\hbar k$ to an object upon reflection from it, it follows $p/E = F/P = 2/c$, with force F and power P of the photon). The positive (negative) sign holds for the right (left) mirror, which means that the intra-cavity field tends to push the mirrors apart. Generally, the radiation force depends on the detuning from resonance; e.g. when detuned by $\kappa/2$, P_c (and therefore the force F_c) depends approximately linearly on L_c (see Fig. 2.4).

If we consider this point as equilibrium position (e.g. radiation force balanced by structural forces), and if one changes the cavity length slowly enough to allow the cavity field to remain in steady state, then the cavity mirrors experience a force $\pm \mathcal{K}x$ (positive/negative sign holds for left/right side of resonance) for small elongations x from the equilibrium position, with optical spring constant \mathcal{K} . The case with a negative sign resembles Hook's law (Sec. 2.1.1), consequently it is referred to as optical spring effect. In the case of a positive sign, one speaks of the optical anti-spring effect [21]. For an oscillating cavity mirror the radiation force gives rise to dynamical effects, which occur as a consequence of the delayed response (by τ_c) of P_c to a change in the cavity configuration (L_c). In Sec. 2.2.6 we briefly discuss how this effect can be used to damp or amplify mechanical vibrations of the mirror (e.g. Brownian motion, see Sec. 2.1.2.2), which is of central interest in the field of cavity optomechanics [21]. A key parameter for optomechanics applications is the dispersive frequency shift $G := \partial\omega_c/\partial x$ with small elongation from resonance x and x -dependent cavity resonance frequency $\omega_c(x)$. In the

present case of a Fabry-Perot cavity, we have for the cavity resonance frequency (Eq. 2.59) $\omega_c = N \frac{\pi c}{L_c + x} \approx \omega_N (1 - x/L_c)$ and the dispersive coupling $G = -\omega_N/L_c$.

Depending on which property of the intra-cavity field is altered by the mirror displacement x , one distinguishes between different kinds of optomechanical coupling. The case discussed in the previous paragraph, where the cavity resonance frequency is a function of the mirror displacement, is referred to as “dispersive” optomechanical coupling [21]. Other examples are dissipative optomechanical coupling [73, 74, 75, 76, 77] and optomechanical mode field coupling [78]. The former is characterized by a x -dependent cavity decay rate $\kappa(x)$. The latter concerns the mode field distribution; displacement x of the cavity boundaries causes the optical field to appear/disappear in certain areas of the cavity.

2.2.3 Optical Resonances of a Fabry-Perot Cavity with Incorporated Membrane

In this section we characterize the optical resonances of a membrane in the middle (MIM) setup by means of the transfer matrix (TM) method (Sec. 2.2.1). The here presented analysis expands upon the treatment presented in Ref. [79] (which is based on a scattering matrix formalism). Figure 2.5 shows a sketch of a one-dimensional MIM setup which comprises a Fabry-Perot cavity (see Sec. 2.2.2) with dielectric membrane incorporated close to its center. Mirrors and membrane are characterized by reflection (transmission) coefficients r_1, r_d, r_2 (t_1, t_d, t_2) respectively (left to right). The mirrors are separated by the cavity length L_c and the membrane displacement from the cavity center x is small, so that $x \ll L_c/2$. Incident light E_{in} is partially reflected at the input mirror and partially coupled to the intra-cavity fields E_{lr}, E_{ll}, E_{rr} , and E_{rl} . Light reflected from and transmitted through the cavity is denoted by E_r and E_t respectively. Note, that similarly to the previous section, we here adopt a different nomenclature with respect to the one employed in the general introduction of the transfer matrix formalism (Sec. 2.2.1); e.g., the transmitted field is denoted by E_t instead of A_4 . Furthermore, with regard to an analytical calculation of the circulating optical power inside the cavity, either on the left or right side of the membrane, we only consider intra-cavity field components E_{lr} (right-moving), E_{ll} (left-moving), located at the interface between left

mirror and left cavity side, and E_{rr} (right-moving), E_{rl} (left-moving), located at the interface between membrane and right cavity side. The field components at other locations within the same cavity side are characterized by the same amplitude but different phase.

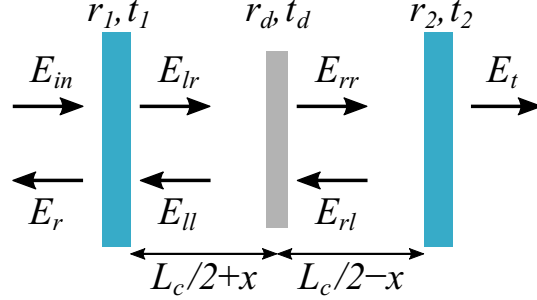


Figure 2.5: Schematic of a one-dimensional Fabry-Perot cavity with membrane incorporated close to its center. The cavity is formed by two mirrors facing each other at a distance set by the cavity length L_c . Each mirror is characterized by its reflection coefficient r_1 , r_2 respectively and transmission coefficient t_1 , t_2 respectively. The membrane, with reflection (transmission) coefficient r_d (t_d), is located close to the cavity center, with displacement from the center $x \ll L_c/2$. Incident light E_{in} is partially reflected at the input mirror and partially coupled to the intra-cavity fields E_{lr} , E_{ll} , E_{rr} , and E_{rl} . Light reflected from and transmitted through the cavity is denoted by E_r and E_t respectively.

The transfer matrix of the MIM setup is given by a product of five individual matrices (see Sec. 2.2.1)

$$\mathbf{M}_{\text{mim}} = \frac{1}{it_2} \begin{pmatrix} -1 & -r_2 \\ r_2 & 1 \end{pmatrix} \begin{pmatrix} e^{i\delta_-} & 0 \\ 0 & e^{-i\delta_-} \end{pmatrix} \frac{1}{t_d} \begin{pmatrix} -e^{i2\phi_r} & |r_d| \\ -|r_d| & 1 \end{pmatrix} \begin{pmatrix} e^{i\delta_+} & 0 \\ 0 & e^{-i\delta_+} \end{pmatrix} \frac{1}{it_1} \begin{pmatrix} -1 & -r_1 \\ r_1 & 1 \end{pmatrix}, \quad (2.65)$$

which represent (right to left): left cavity mirror, propagation from left mirror to membrane, membrane, propagation from membrane to right mirror, and right cavity mirror. The phase accumulated upon propagation from a mirror to the membrane, or vice versa, is given by $\delta_{\pm} = k(x \pm L_c/2)$, where the positive (negative) sign holds for the left (right) mirror. The membrane's reflection coefficient is expressed in terms of amplitude and phase $r_d = |r_d| e^{i\phi_r}$. The reflected, transmitted, and intra-cavity optical powers follow from the above given TM

and Eqs. 2.47-2.48 for a single input E_{in} from the left

$$\left| \frac{E_r}{E_{in}} \right|^2 = \left| -\frac{r_1 [e^{i(kL_c+2\phi_r)} + r_d r_2 e^{2ikx}] + r_2 e^{-ikL_c} + r_d e^{-2ikx}}{r_1 [r_2 e^{i(kL_c+2\phi_r)} + r_d e^{2ikx}] + e^{-ikL_c} + r_d r_2 e^{-2ikx}} \right|^2 \quad (2.66)$$

$$\left| \frac{E_t}{E_{in}} \right|^2 = \left| \frac{t_1 t_2 (-r_d^2 + e^{2i\phi_r}) e^{ik(L_c+2x)}}{t_d \{r_d e^{ikL_c} (r_2 + r_1 e^{4ikx}) + r_1 r_2 e^{2i[k(L_c+x)+\phi_r]} + e^{2ikx}\}} \right|^2 \quad (2.67)$$

$$\left| \frac{E_{lr}}{E_{in}} \right|^2 = \left| \frac{it_1 (r_2 r_d e^{ikL_c} + e^{2ikx})}{r_d e^{ikL_c} (r_2 + r_1 e^{4ikx}) + r_1 r_2 e^{2i[k(L_c+x)+\phi_r]} + e^{2ikx}} \right|^2 \quad (2.68)$$

$$\left| \frac{E_{ll}}{E_{in}} \right|^2 = \left| \frac{it_1 e^{ik(L_c+2x)} [r_2 e^{i(kL_c+2\phi_r)} + e^{2ikx} r_d]}{r_d e^{ikL_c} (r_2 + r_1 e^{4ikx}) + r_1 r_2 e^{2i[k(L_c+x)+\phi_r]} + e^{2ikx}} \right|^2 \quad (2.69)$$

$$\left| \frac{E_{rr}}{E_{in}} \right|^2 = \left| -\frac{it_1 (-r_d^2 + e^{2i\phi_r}) e^{ik(L_c+2x)}}{t_d \{r_d e^{ikL_c} (r_2 + r_1 e^{4ikx}) + r_1 r_2 e^{2i[k(L_c+x)+\phi_r]} + e^{2ikx}\}} \right|^2 \quad (2.70)$$

$$\left| \frac{E_{rl}}{E_{in}} \right|^2 = \left| \frac{it_1 r_2 (-r_d^2 + e^{2i\phi_r}) e^{ik(L_c+2x)}}{t_d \{r_d e^{ikL_c} (r_2 + r_1 e^{4ikx}) + r_1 r_2 e^{2i[k(L_c+x)+\phi_r]} + e^{2ikx}\}} \right|^2 \quad (2.71)$$

In principle, one could determine the values $k(x)$ (L_c fixed) or $L_c(x)$ (k fixed) for which incident light is on resonance with the cavity, by finding the extrema of one of the previous expressions. Instead, we take an approximate route by considering a closed cavity with mirror reflection coefficients $r_1 = r_2 = 1$. The transfer matrix in this case reduces to

$$\widetilde{\mathbf{M}}_{\text{mim}} = \begin{pmatrix} e^{i\delta_-} & 0 \\ 0 & e^{-i\delta_-} \end{pmatrix} \frac{1}{t_d} \begin{pmatrix} -e^{i2\phi_r} & r_d \\ -r_d & 1 \end{pmatrix} \begin{pmatrix} e^{i\delta_+} & 0 \\ 0 & e^{-i\delta_+} \end{pmatrix} = \frac{1}{t_m} \begin{pmatrix} -e^{i(kL_c+2\phi_r)} & r_d e^{-i2kx} \\ -r_d e^{i2kx} & e^{-ikL_c} \end{pmatrix} \quad (2.72)$$

with

$$\begin{pmatrix} E_{rr} \\ E_{rl} \end{pmatrix} = \widetilde{\mathbf{M}}_{\text{mim}} \begin{pmatrix} E_{lr} \\ E_{ll} \end{pmatrix}. \quad (2.73)$$

For perfectly reflective mirrors $E_{ll} = -E_{lr}$, $E_{rl} = -E_{rr}$ and together with Eqs. 2.72-2.73 we have

$$\begin{aligned}\frac{E_{rr}}{E_{lr}} &= \frac{1}{t_d} [-e^{i(kL_c+2\phi_r)} - r_d e^{-i2kx}] \\ \frac{E_{rr}}{E_{lr}} &= \frac{1}{t_d} [r_d e^{i2kx} + e^{-ikL_c}],\end{aligned}\tag{2.74}$$

from which follows the resonance condition

$$\begin{aligned}-e^{i(kL_c+\phi_r)} - |r_d| e^{-i2kx} &= |r_d| e^{i2kx} + e^{-i(kL_c+\phi_r)} \\ -\cos(kL_c + \phi_r) &= |r_d| \cos(2kx).\end{aligned}\tag{2.75}$$

We assume the membrane causes a small perturbation Δk_N of the empty cavity resonance $k_N = N\pi/L_c$ ($N \in \mathbb{N}$) (Eq. 2.57), and write the resonance wavenumber as

$$k_{\text{MIM},N} = k_N + \Delta k_N.\tag{2.76}$$

Plugging this into Eq. 2.75 and making use of the identity $\cos(a+b) = \cos(a)\cos(b) - \sin(a)\sin(b)$ gives

$$\begin{aligned}-\cos(k_N L_c) \cos(\Delta k_N L_c + \phi_r) + \sin(k_N L_c) \sin(\Delta k_N L_c + \phi_r) &= |r_d| \cos[2k_N (1 + \Delta k_N/k_N) x] \\ (-1)^{(N+1)} \cos(\Delta k_N L_c + \phi_r) &\approx |r_d| \cos(2k_N x),\end{aligned}$$

where in the last step we have approximated $1 + \Delta k_N/k_c \approx 1$. The resonance wavenumber detuning with respect to k_N is given by

$$\Delta k_N = \frac{-\phi_r + \arccos[(-1)^{(N+1)} |r_d| \cos(2k_N x)]}{L_c} \quad (N \in \mathbb{N}).\tag{2.77}$$

Instead of tuning the incident light on resonance, e.g. by detuning its wavelength ($\Delta k_N = 2\pi/\Delta\lambda_N$), one can change the cavity length; following the same procedure as for the wavenumber detuning, we find for the length detuning

$$\Delta L_N = \frac{-\phi_r + \arccos[(-1)^{(N+1)} |r_d| \cos(2k_N x)]}{k} \quad (N \in \mathbb{N}).\tag{2.78}$$

The resonance MIM cavity lengths are given by $L_{\text{MIM},N} = L_N + \Delta L_N$, with resonance lengths of empty cavity L_N (Eq. 2.58). Note that the expression for ΔL_N , opposed to the expression for Δk_N , does not require an approximation and therefore applies to any membrane position x within the cavity.

In order to determine the cavity finesse $\mathcal{F}_{\text{MIM}} = \omega_{\text{FSR}}/\kappa_{\text{MIM}}$, we calculate the rate κ_{MIM} at which optical energy \mathcal{E}_{MIM} leaves the cavity

$$\frac{d\mathcal{E}_{\text{MIM}}}{dt} = -\kappa_{\text{MIM}}\mathcal{E}_{\text{MIM}} = -(t_1^2 P_l + t_2^2 P_r), \quad (2.79)$$

with optical power P_l (P_r) in the left (right) half of the cavity given by Eq. 2.68 (Eq. 2.70). For the total energy inside the cavity we have

$$\mathcal{E}_{\text{MIM}} = \frac{(L_c + 2x) P_l + (L_c - 2x) P_r}{c}. \quad (2.80)$$

Combining the previous two expression yields the cavity decay rate

$$\kappa_{\text{MIM}} = c \left[\frac{t_1^2 P_l + t_2^2 P_r}{(L_c + 2x) P_l + (L_c - 2x) P_r} \right]. \quad (2.81)$$

Dividing $\omega_{\text{FSR}} = \pi c/L_c$ by κ_{MIM} yields the finesse

$$\mathcal{F}_{\text{MIM}} = \pi \left[\frac{(1 + 2x/L_c) P_l + (1 - 2x/L_c) P_r}{t_1^2 P_l + t_2^2 P_r} \right], \quad (2.82)$$

where P_r and P_l are given by Eqs. 2.68, 2.70. In the case of highly reflective mirrors we can simplify this expression by dividing both numerator and denominator by P_l , thereby expressing \mathcal{F}_{MIM} in terms of the power ratio P_r/P_l , for with an approximation is given by the absolute square of Eq. 2.74

$$\frac{P_r}{P_l} = \frac{1 + |r_d|^2 + 2|r_d| \cos[k_{\text{MIM}}(L_c + 2x) + \phi_r]}{|t_d|^2}. \quad (2.83)$$

For mirror reflectivities $r_1, r_2 = 0.99$, this expression deviates by less than 2 % from the exact expression, given by Eqs. 2.68, 2.70.

In the case of a bare Fabry-Perot cavity (previous section), we have discussed that the

cavity finesse divided by π corresponds to the enhancement factor of the circulating power inside the cavity with respect to the incident power. In the present case of a MIM cavity, the average circulating power is given by

$$P_{c,\text{MIM}} = \frac{(L_c/2 + x) P_l + (L_c/2 - x) P_r}{L_c}. \quad (2.84)$$

In the next paragraph we discuss (among other things) the relation between \mathcal{F}_{MIM} and $P_{c,\text{MIM}}$.

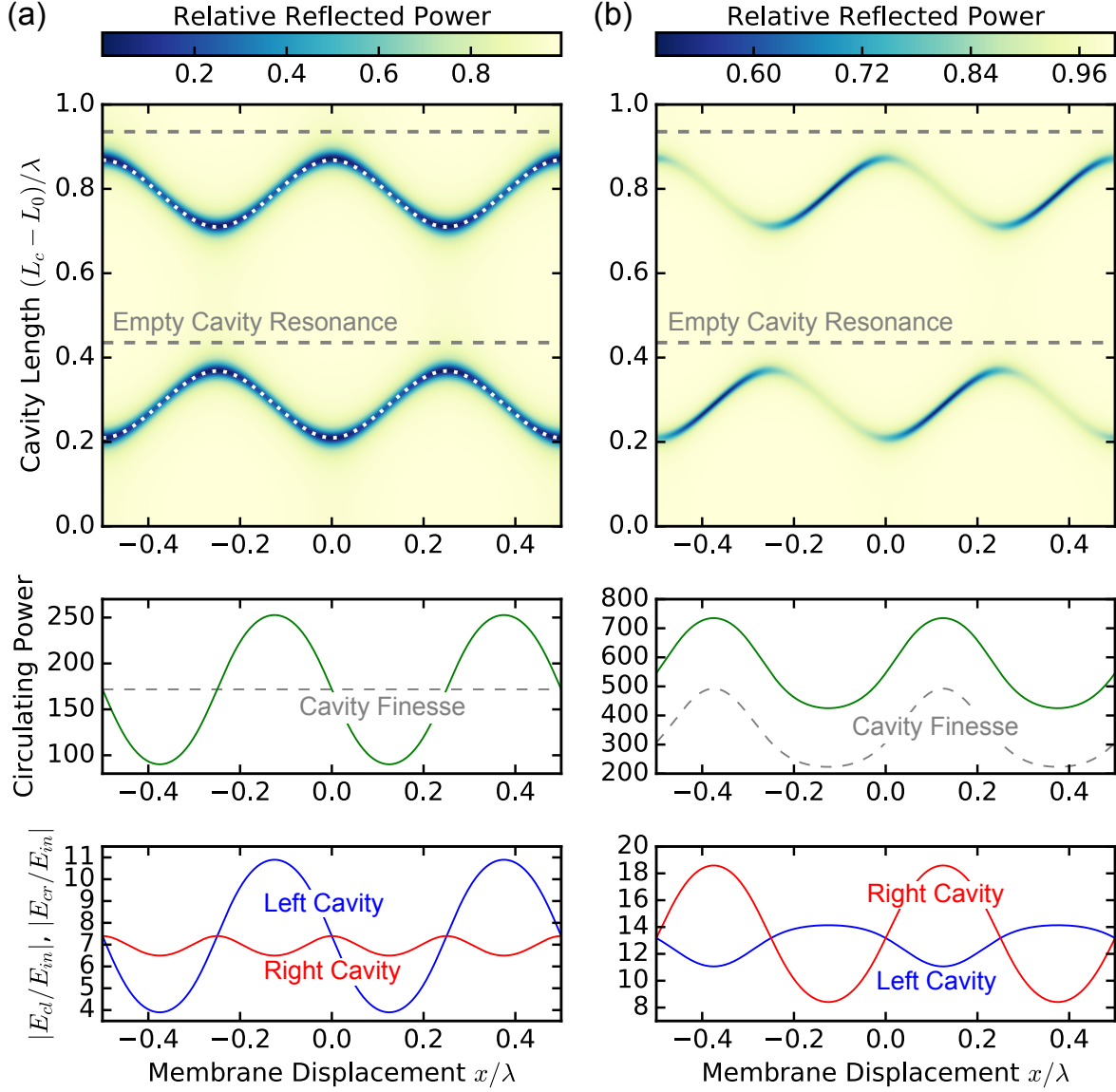


Figure 2.6: Optical resonances of a cavity with membrane (thickness $d = 100$ nm, refractive index $n_d = 2.0$, reflection coefficient $r_d = 0.48 \exp(i 2.49 \text{ rad})$ (Eq. A.3)) incorporated close to its center. Wavelength of incident light $\lambda = 1550$ nm. (a, upper) Reflected power (relative to input power, Eq. 2.66) for a symmetric cavity (mirror reflectivities $r_1 = r_2 = 0.9$) versus membrane displacement x (from cavity center) and cavity length L_c ($L_0 = 5$ cm). Gray dashed lines indicate empty cavity resonances of order $N = 64517$ and $N = 64518$ (bottom to top, Eq. 2.58). White dotted curves show resonance length detuning (Eq. 2.78). (a, center) Green solid curve shows scaled circulating power $\pi P_{c,\text{MIM}}$ (Eq. 2.84) for mode of order $N = 64517$ for a symmetric cavity (mirror reflectivities $r_1 = r_2 = 0.991$). Gray dashed line shows corresponding cavity finesse (Eq. 2.82). (a, lower) Normalized right traveling electric field amplitudes on left (blue) and right (red) side of membrane (Eqs. 2.68-2.70, N , r_1 , r_2 same as in (a, center)). (b, upper) Same as (a, upper) but for an asymmetric cavity with mirror reflectivities $r_1 = 0.85$, $r_2 = 0.99$. (b, center & lower) Same as (a, center & lower) but for an asymmetric cavity with mirror reflectivities $r_1 = 0.991$, $r_2 = 0.999$.

Figure 2.6(a, upper) shows the reflected optical power (Eq. 2.66) from a MIM cavity versus membrane displacement x and cavity length change ΔL_c with respect to $L_c = 5$ cm. Note that we consider symmetric lengthening of the cavity, whereby both cavity mirrors move apart from each other by the same amount. This leaves the relative positioning between optical field nodes and membrane unchanged as the cavity length is altered. We implement this approach experimentally with the measurement presented in Sec. 4.2.2. The mirror reflection coefficients considered in Fig. 2.6(a, upper) are $r_1 = r_2 = 0.9$, corresponding to a symmetric cavity. The membrane thickness $d = 100$ nm and refractive index 2.0 result in a reflection coefficient $r_d = 0.48 \exp(i 2.49 \text{ rad})$ (Eq. A.3). The plot shows two resonances (blue areas), which are periodic in x with period $\lambda/2$. The periodicity is a consequence of the field distribution inside the cavity (see also Fig. 2.7); if the membrane is located at a field antinode, the optical resonance is maximally altered from the empty cavity resonance (gray dashed line, Eq. 2.58). This is because a significant part of the field is located inside a medium with a refractive index different from the one of the surrounding cavity (in our case they are different by a factor of 2). In the opposite case, when the membrane is located at a field node, the interaction between light and membrane is minimized and so is the effect on the optical resonance. The described behavior is consistent with the mode orders $N = 64517$ and $N = 64518$ (bottom to top, Eq. 2.58) of the shown resonances, where N odd (even) corresponds to a field antinode (node) at the cavity center ($x = 0$). As a result, consecutive resonances are horizontally shifted by $\lambda/4$. The white dotted curves represent the cavity resonance lengths $N\lambda/2 + \Delta L_N$ (Eq. 2.78). Figure 2.6(a, center) shows the scaled circulating power $\pi P_{c,\text{MIM}}$ (green curve, Eq. 2.84) together with the finesse \mathcal{F}_{MIM} (dashed gray line, Eq. 2.82) for a MIM cavity with $r_1 = r_2 = 0.991$ and r_d as given above. Here $\mathcal{F}_{\text{MIM}}/\pi$ represents the mean value of $P_{c,\text{MIM}}(x)$, whereas in the case of a bare symmetric cavity ($r_1, r_2 \approx 1$) $\mathcal{F}/\pi \approx P_c$, see Sec. 2.2.2). Blue and red curves in Fig. 2.6(a, lower) show respectively left and right cavity field amplitudes (for the same cavity as in Fig. 2.6(a, center)). The amplitude of the field variation on the left is eight times bigger than the one on the right, because the presence of the membrane decreases the efficiency of pumping the field on the right. The left field amplitude is periodic in x with period $\lambda/2$ and the right field amplitude has periodicity $\lambda/4$.

Figure 2.6(b) shows the same plots as Figure 2.6(a) but for an asymmetric cavity. In Fig 2.6(b, upper) the mirror reflectivities are $r_1 = 0.85$ and $r_2 = 0.99$. As a consequence of the asymmetry, the reflected power depends on whether the slope of the resonance is positive or negative. This can be understood by regarding the back mirror together with the membrane as a compound mirror, with an “effective reflectivity” depending on the relative distance between membrane and mirror. If the effective reflectivity is lower (higher) a smaller (bigger) fraction of the intra-cavity light exits the cavity through the front mirror, resulting in a higher (lower) relative reflected power from the cavity (formed by interference of light promptly reflected from input mirror and light leaving the cavity) for the given cavity configuration.

The mirror reflectivities for Fig. 2.6(a, center & lower) are $r_1 = 0.991$ and $r_2 = 0.999$. Opposed to the symmetric case (Fig. 2.6(a, center)), \mathcal{F}_{MIM} depends on the membrane position and modulates together with $P_{\text{c,MIM}}(x)$ with a period of $\lambda/2$ (see Fig. 2.6(a, center)). The dependency of \mathcal{F}_{MIM} on x is referred to as dissipative optomechanical coupling [73, 74, 75, 76, 77]. Figure 2.6(b, lower) shows the circulating field amplitudes inside the left and right half of the cavity. In contrast to the symmetric case (Fig. 2.6(a, lower)), the right cavity power varies more strongly than the left cavity power with variation amplitudes three times higher. Both components are periodic in x with period $\lambda/2$. This is also contrary to the symmetric case where only the left field is periodic with $\lambda/2$ and the right field is periodic with $\lambda/4$. Consistent with $r_2 > r_1$, the finesse is maximized when most of the light is located between membrane and right cavity mirror which has higher reflectivity r_2 .

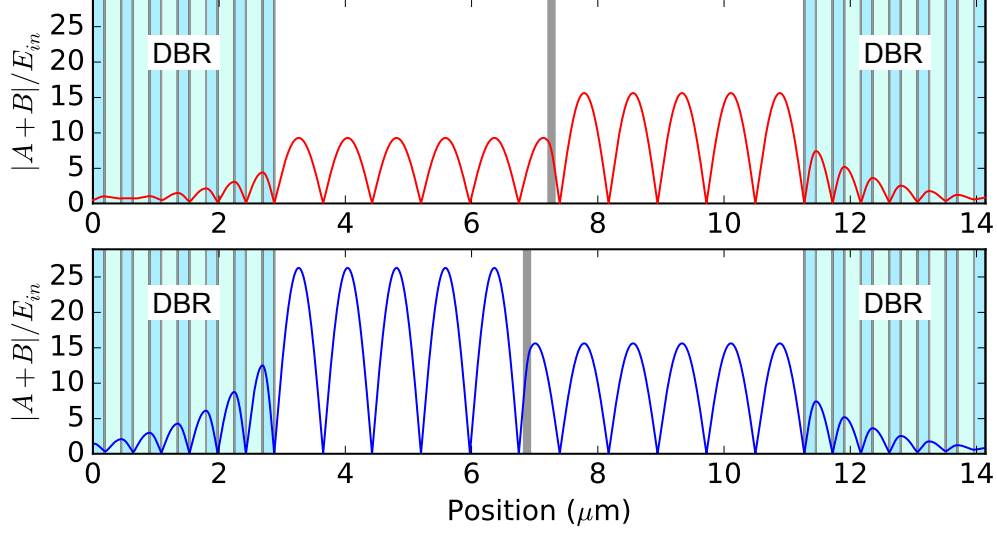


Figure 2.7: Electric field amplitude distribution $|A + B|$ (relative to input E_{in}), with amplitude of left and right traveling field respectively given by A and B , inside a Fabry-Perot cavity with membrane (gray, thickness $d = 100$ nm, refractive index $n_d = 2.0$, reflection coefficient $r_d = 0.48 \exp(i 2.49 \text{ rad})$ (Eq. A.3)) incorporated $\pm\lambda/8$ away from cavity center; positive (negative) sign holds for upper (lower) plot. Cavity is formed by two distributed Bragg reflectors (DBRs, see Sec. A.2 for details) each comprising six and a half layer pairs of material a (light blue, refractive index 2.10, e.g. Ta_2O_5) and material b (light green, refractive index 1.47, e.g. SiO_2) corresponding to $r_1 = r_2 = 0.991$ (Eq. A.9, with refractive index of substrate (not shown) $n_s = 1.47$). Optical length (physical length times refractive index) of each layer is $\lambda/4$ with wavelength $\lambda = 1550$ nm. The mirrors are separated by $\approx 5.5\lambda$, corresponding to mode order $N = 11$ (Eq. 2.58).

Figure 2.7 shows the electric field amplitude distribution $|A + B|/E_{in}$ inside a MIM setup designed for light with wavelength $\lambda = 1550$ nm. The cavity is formed by two identical distributed Bragg reflectors (DBRs, see Sec. A.2 for details). Each DBR comprises six and a half layer pairs of material a (light blue, refractive index 2.10, e.g. Ta_2O_5) and material b (light green, refractive index 1.47, e.g. SiO_2) corresponding to $r_1 = r_2 = 0.991$ (Eq. A.9, with refractive index of substrate (not shown) $n_s = 1.47$). Optical length (physical length times refractive index) of each layer is $\lambda/4$. The mirrors are separated by $\approx 5.5\lambda$, corresponding to longitudinal mode order $N = 11$ (Eq. 2.58). The membrane (gray) with thickness $d = 100$ nm, refractive index $n_d = 2.0$, and resulting reflection coefficient $r_d = 0.48 \exp(i 2.49 \text{ rad})$ (Eq. A.3) is located $+\lambda/8$ (Fig. 2.7(upper)) or $-\lambda/8$ (Fig. 2.7(lower)) away from the cavity center. Field amplitudes A and B are calculated numerically; TM of depicted cavity is a

product of TMs describing individual layers and interfaces (given in Table 2.1). The electric field at each position x within the cavity, DBRs, and membrane is of the form $E(x) = Ae^{ikx} + Be^{-ikx}$ (see Sec. 2.2.1), where right (left) traveling field amplitude A (B) is given by Eq. 2.47 (Eq. 2.48). The field amplitude on the right side of the cavity is identical for both membrane positions, whereas the left cavity field amplitude reaches its minimal (maximal) value for membrane displacement $+\lambda/8$ ($-\lambda/8$) (see also Fig. 2.6(c)). This illustrates that, for the same amount of incident light, the amount of intra-cavity light depends on the membrane position. The intra-cavity light decays exponentially towards the outside of the DBRs. Both reflected and transmitted powers for the field distributions shown in Fig. 2.7(upper & lower) are identical. Identical transmission for $x = +\lambda/8$ and $x = -\lambda/8$ follows from identical field amplitudes on the right cavity side for both of these configurations. The fact that the reflected cavity power is equal for both configurations can be understood by considering the destructive interference of the field leaving the cavity to the left E_{leave} with the field promptly reflected from the input mirror $r_1 E_{in}$; the reflected cavity power is given by $|E_l - r_1 E_{in}|^2$, with $r_1 E_{in} \approx 1$, for the given cavity configuration. This implies that for values of E_{leave} which are either smaller or bigger than 1 by the same amount, the resulting reflected power is the same. This is the case for the two configurations presented in Fig. 2.7, where for $x = +\lambda/8$ we have $E_{leave} = 0.52$ and for $x = -\lambda/8$ we have $E_{leave} = 1.48$.

2.2.4 Steady State Optical Forces

In the previous section we have examined how optical resonance frequency, field distribution, and finesse of a cavity with incorporated membrane depend on the membrane position. Here we show, that the optical field inside the cavity causes a force to act on the membrane and that positioning the membrane at a field antinode results in a steady state “optical spring”. This effect is of interest to this work, as it shows promise for increasing the mechanical quality factor of our trampoline resonators (see Sec. 3.1.1) beyond the limits posed by their intrinsic dissipation mechanisms. Inspired by previous studies of similar systems [80, 60, 81], in Sec. 4.3 we present a finite-element simulation of an optical spring acting on a trampoline resonator, with the result of an increase in its mechanical quality factor.

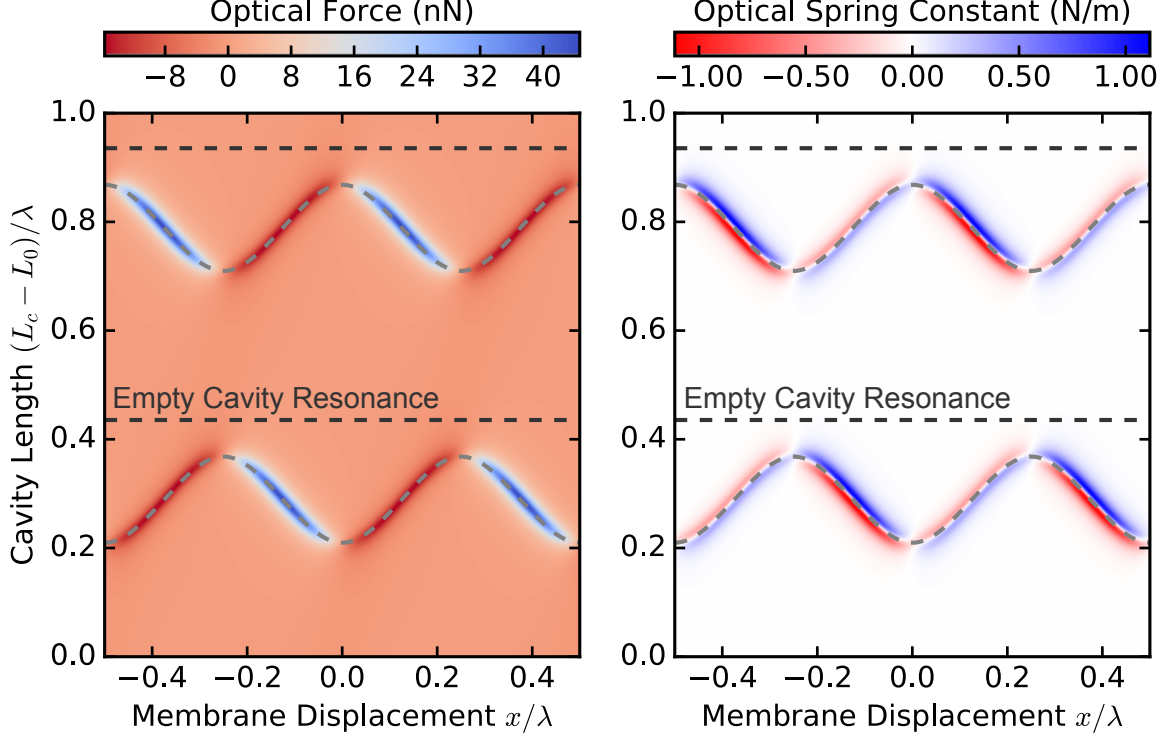


Figure 2.8: Optical force and optical spring constant for a membrane (thickness 100 nm, refractive index 2.0) situated close to the center of a Fabry-Perot cavity (both mirrors with reflection coefficient 0.9). Wavelength of intra-cavity light $\lambda = 1550$ nm. (left) Optical force (Eq. 2.85) versus membrane displacement x and cavity length L_c ($L_0 = 5$ cm). Dashed black lines represent empty cavity resonances of order $N = 64517$ and $N = 64518$ (Eq. 2.58). Dashed gray curves show resonance lengths for cavity with incorporated membrane (Eq. 2.78). (right) Similar to left but for derivative of optical force with respect to x , which corresponds to optical spring constant.

Figure 2.8(left) shows the optical force acting on the membrane in a MIM setup (parameters are identical to that of Fig. 2.6(a)) versus membrane displacement x (from cavity center) and cavity length (with respect to $L_0 = 5$ cm). The optical force can be calculated from momentum conservation (see Appendix A.4) and is given by

$$F_{\text{RP, MIM}} = \frac{P_{\text{in}}}{c} \left(\left| \frac{E_{lr}}{E_{in}} \right|^2 + \left| \frac{E_{ll}}{E_{in}} \right|^2 - \left| \frac{E_{rr}}{E_{in}} \right|^2 - \left| \frac{E_{rl}}{E_{in}} \right|^2 \right), \quad (2.85)$$

with incident power P_{in} and normalized intra-cavity powers (Eqs. 2.68-2.71). Dashed black lines show the empty cavity resonance lengths for modes of order $N = 64517$ and $N = 64518$ (Eq. 2.58). Dashed gray curves show the corresponding MIM resonance lengths (Eq. 2.78).

For values of x and L_c in vicinity of a resonance, there is a force acting on the membrane. If the membrane is located at a field node or antinode, corresponding to maximum or minimum of cavity resonance curve, the force vanishes as a consequence of the optical powers on each cavity side being equal. In the case of an antinode this results in a stable equilibrium, since the force acts to push the membrane back toward the antinode.. Conversely, in vicinity of a field node, the forces tend to push the membrane away, resulting in an unstable equilibrium. Figure 2.8(right) shows the optical spring constant $-d/dx F_{\text{RP,MIM}}$ (Eq. 2.85). Similar to the case of an empty Fabry-Perot cavity (Sec. 2.2.2), slight x -detuning to the right (left) from resonance results in an optical spring (anti-spring). Similar to the optical force, the spring effect is more pronounced for cavity configurations which maximize the field on the left cavity side (see Fig. 2.6(a)). The force and spring constant discussed here, describe the situation in which x or L_c are changed on a time scale much longer than the cavity ringdown time $\tau_{\text{MIM}} = 1/\kappa_{\text{MIM}}$. On the contrary, if, e.g., the membrane oscillates at a frequency which is comparable to τ_{MIM} , the optical force will have an additional dynamic component. This is a consequence of the delayed response (by τ_{MIM}) of the intra-cavity field with respect to a change in x (or L_c). In Sec. 2.2.6 we briefly discuss how this dynamic effect can be used to damp (or antidamp) the membrane's motion (e.g. Brownian motion, see Sec. 2.1.2.2), which is of central interest in the field of cavity optomechanics [21].

In the following, we analytically calculate the optical spring constant at a field antinode, which represents a stable equilibrium position (see previous paragraph). In the case of highly reflective cavity mirrors ($r_1, r_2 = 1$), we can express the optical force (Eq. 2.85) as

$$F_{\text{RP,MIM}} = \frac{P_l}{c} (1 - P_r/P_l), \quad (2.86)$$

with P_l (P_r) optical power on the left (right) cavity side. Substituting Eq. 2.83 for P_r/P_l and taking the derivative with respect to x yields the spring constant

$$\mathcal{K}_{\text{MIM}} = -\frac{dF_{\text{RP,MIM}}}{dx} = \frac{4kP_l}{c} \frac{|r_d| \sin[k(L_c + 2x) + \phi_r]}{|t_d|^2}. \quad (2.87)$$

At equilibrium we have $F_{\text{RP,MIM}} = 0$ so that from Eq. 2.86 together with Eq. 2.83 follows

$$\begin{aligned}\cos [k (L_c + 2x) + \phi_r] &= -|r_d| \\ \sin [k (L_c + 2x) + \phi_r] &= \sqrt{1 - \cos^2 [k (L_c + 2x) + \phi_r]} = |t_d|\end{aligned}$$

and for the spring constant

$$\mathcal{K}_{\text{MIM}} = \frac{4kP_l}{c} \frac{|r_d|}{|t_d|} \quad (2.88)$$

(equivalently, expressing \mathcal{K}_{MIM} in terms of circulating power instead of P_l requires additional factor of 2 [81]).

2.2.5 Linear and Quadratic Dispersive Frequency Shift

In the previous section we have shown that positioning a dielectric membrane at an antinode of the optical field inside a Fabry-Perot cavity causes a steady state optical spring to act on it. The designation “steady state” highlights the fact, that the cavity is not required to realize this effect, and that it equally can be achieved by positioning the membrane at the antinode of an optical standing wave resulting from, e.g., reflecting a laser beam of a mirror [81]. In the following section we give a brief outlook on dynamical optical forces, which result specifically from the interaction of an intra-cavity field with a mechanical resonator. In preparation for this treatment, we here briefly discuss the “dispersive” shift of the optical resonance frequency as a consequence of the mechanical resonator’s displacement, which is involved in the mathematical description of the dynamical optical forces (following section).

The linear dispersive frequency shift is defined as $G \equiv \partial\omega_c/\partial x$, with mechanical resonator elongation x and x -dependent cavity resonance frequency $\omega_c(x)$. For our “membrane-in-the-middle” (MIM) setup (see Sec. 2.2.3), the cavity resonance frequencies are given by $\omega_{\text{MIM}} = \omega_N + c\Delta k_N$, with empty cavity resonance frequency ω_N (Eq. 2.59) and (membrane-induced) resonance frequency detuning $\Delta\omega_N = c\Delta k_N$ (Eq. 2.77). The linear dispersive

frequency shift follows as

$$\frac{\partial \Delta \omega_N}{\partial x} = \omega_{\text{FSR}} \frac{2k_c}{\pi} \frac{(-1)^{(N+1)} |r_d| \sin(2k_N x)}{\sqrt{1 - |r_d|^2 \cos^2(2k_N x)}}. \quad (2.89)$$

An additional feature of the MIM setup compared to the empty Fabry-Perot cavity (see end of Sec. 2.2.2), is a pronounced quadratic dispersive frequency shift

$$\frac{\partial^2 \Delta \omega_N}{\partial x^2} = -\omega_{\text{FSR}} \frac{4k_c^2}{\pi} \frac{(-1)^{(N+1)} |r_d| (|r_d|^2 - 1) \cos(2k_N x)}{[1 - |r_d|^2 \cos^2(2k_N x)]^{3/2}}. \quad (2.90)$$

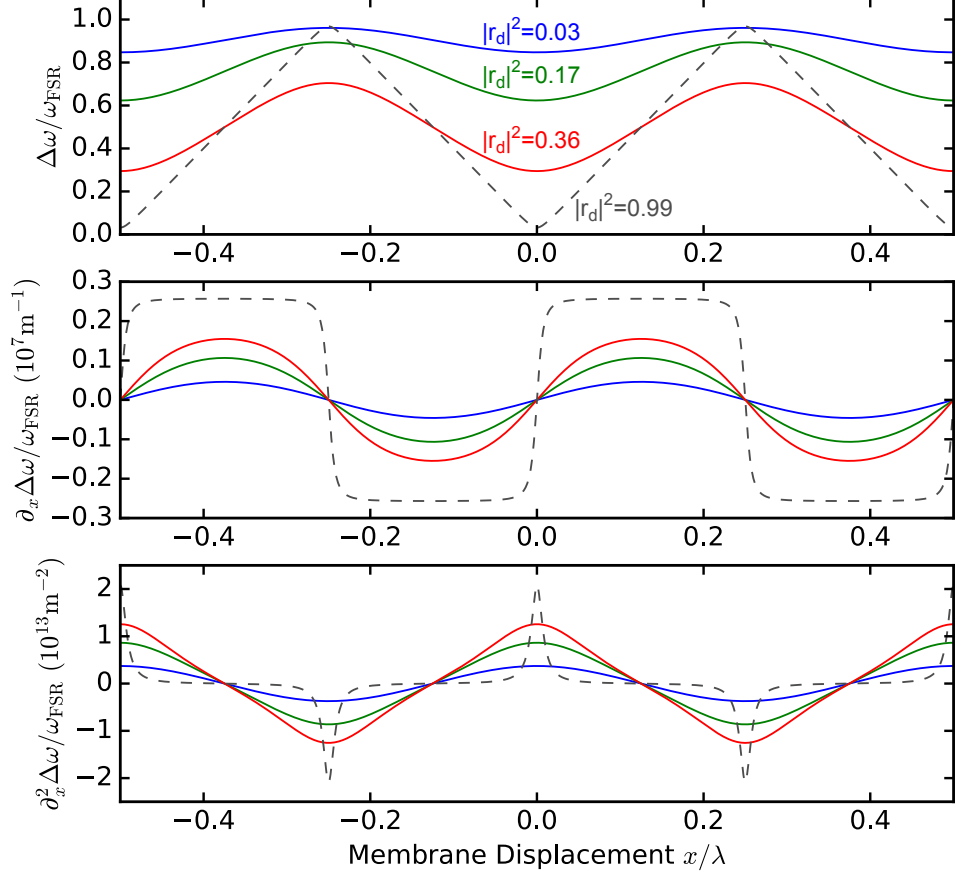


Figure 2.9: Resonance frequency detuning, linear, and quadratic dispersive frequency shifts for a cavity with membrane incorporated close to its center, all three relative to free spectral range ω_{FSR} (Eq. 2.59). Blue, red, and green curves correspond to membranes with thickness $d = \{30, 80, 194\}$ nm and refractive index $n_d = 2.0$ (e.g. Si_3N_4 at $\lambda = 1550$ nm), resulting in reflection coefficients $r_d = \{0.18 \exp(i 1.87 \text{ rad}), 0.41 \exp(i 2.32 \text{ rad}), 0.60 \exp(i 3.14 \text{ rad})\}$. Gray dashed curves correspond to an infinitely thin membrane with $r_d = 0.995$. (top) Resonance frequency detuning $\Delta\omega_N = c\Delta k_N$ with speed of light c and resonance wavenumber detuning Δk_N (Eq. 2.77, $N = 2q + 1$ with $q \in \mathbb{N}$). (center) Linear dispersive frequency shift $\partial_x \Delta\omega$ (shorthand for $\partial/\partial x \Delta\omega_N$, Eq. 2.89). (lower) Quadratic dispersive frequency shift $\partial_x^2 \Delta\omega_N$ (shorthand for $\partial^2/\partial x^2 \Delta\omega_N$, Eq. 2.90) (subscript N is omitted in all y -axis labels).

Figure 2.9 shows a plot of $\Delta\omega_N$, $\partial\Delta\omega_N/\partial x$, and $\partial^2\Delta\omega_N/\partial x^2$ (mode order N odd) relative to ω_{FSR} . Blue, red, and green curves correspond to membranes with thickness $d = \{30, 80, 194\}$ nm and refractive index $n_d = 2.0$ (e.g. Si_3N_4 at $\lambda = 1550$ nm), resulting in reflection coefficients $r_d = \{0.18 \exp(i 1.87 \text{ rad}), 0.41 \exp(i 2.32 \text{ rad}), 0.60 \exp(i 3.14 \text{ rad})\}$. Gray dashed curves show behavior of an infinitely thin membrane with $r_d = 0.995$. Membranes with $d = \{30, 80, 194\}$ nm achieve $\{18, 41, 60\}$ % of the maximal linear dispersive

frequency shift. For the present case of a membrane with $n = 2.0$, r_d reaches its maximal value at $d = 194$ nm (see Fig. A.1). A common strategy to enhance linear and quadratic dispersive shifts is to increase the membrane's reflectivity by fabricating a photonic crystal reflector (PCR) into it [82, 39, 56, 55, 52]. A PCR is a periodic structure (e.g., an array of cut-out stripes or holes) with periodicity $\sim \lambda$. Matching λ of incident light to certain optical resonances of the PCR results in an interference which suppresses transmission of light through the PCR while enhancing reflection of incident light. Depending on the design parameters, this enables membrane reflectivities $> 99\%$. A second strategy to enhance dispersive optomechanical coupling aims at reducing the cavity length L_c (see Eqs. 2.89-2.90 with $\omega_{\text{FSR}} \propto 1/L_c$, Eq. 2.59); Fabry-Perot cavities with L_c of a few 10 μm to 100 μm and incorporated mechanical resonator, e.g. a carbon-based nanorod [83] or a Si_3N_4 membrane[84, 85], have been implemented based on fiber cavities.

2.2.6 Dynamical Optical Forces and Laser Cooling

One of the long term goals with our optomechanical (OM) system (see Chapter. 1) is to control the trampoline's trajectory with a precision down to the quantum level, e.g., to measure the quantized nature of its motional energy. In a proposal of such a measurement [86], for a system similar to ours, the mechanical resonator needs to be cooled to a degree where thermal noise is precluded from dominating over the quantum nature of its motion. In the case of our trampoline resonators, with mechanical resonance frequencies up to ~ 0.5 MHz (see Chapter 3), this can not be achieved with conventional refrigeration techniques alone and requires additional means of cooling⁶. Therefore, in this section we discuss cavity-assisted laser cooling as a possible route of cooling a mechanical resonator (with resonance frequencies significantly smaller than ~ 1 GHz) into a regime where less than one thermally-excited quantum of energy occupies the resonator [14, 15].

In the previous sections we have seen how the optical field amplitude (Sec. 2.2.3) and the optical resonance frequency (Sec. 2.2.5) of a cavity with incorporated membrane depend on

⁶State-of-the-art dilution refrigerators achieve temperatures $T \sim 10$ mK. From the equipartition theorem (see end of Sec. 2.1.2.2) follows that this temperature corresponds to a thermal energy equal to one quantum of energy of a harmonic oscillator with a resonance frequency $k_B T / \hbar = 1.3$ GHz, with Boltzmann constant k_B and reduced Planck constant \hbar .

the membrane position along the cavity axis. In the following, we discuss how the interplay between membrane motion and intra-cavity field results in a dynamical back action [87, 88, 21], where a displacement of membrane (or cavity mirror(s)) causes a change in the optical resonance which acts back on the moving object by a change in the radiation force. In general, this interaction is governed by a set of coupled non-linear differential equations [21] (as a consequence of non-linear dependency of, e.g., optical resonance frequency on displacement (see Fig. 2.9)). In the following, we briefly summarize the realm of linearized optomechanics, in which the intra-cavity field is described by a superposition of a coherent steady state component and a fluctuating part, where the latter is much smaller than the former [21].

A mechanical resonator with mass m linearly coupled to an optical mode will experience a shift in frequency Ω_m and damping rate Γ_m , such that the susceptibility (Eq. 2.21) becomes [21]

$$\chi_{\text{om}}^{-1}(\omega) = m \left[\Omega_m^2 + 2\omega\delta\Omega_{\text{opt}} - \omega^2 + i\omega(\Gamma_m + \Gamma_{\text{opt}}) \right], \quad (2.91)$$

where the optomechanical frequency shift $\delta\Omega_{\text{opt}}$ and damping rate Γ_{opt} are given by

$$\delta\Omega_{\text{opt}} = g_0^2 n_{\text{cav}} \left[\frac{\Delta + \Omega_m}{(\Delta + \Omega_m)^2 + \kappa^2/4} + \frac{\Delta - \Omega_m}{(\Delta - \Omega_m)^2 + \kappa^2/4} \right] \quad (2.92)$$

$$\Gamma_{\text{opt}} = g_0^2 n_{\text{cav}} \left[\frac{\kappa}{(\Delta + \Omega_m)^2 + \kappa^2/4} - \frac{\kappa}{(\Delta - \Omega_m)^2 + \kappa^2/4} \right], \quad (2.93)$$

with optomechanical single-photon coupling strength $g_0 = Gx_{\text{ZPF}}$, dispersive frequency shift $G = \partial\omega_c/\partial x$ (see Fig. 2.9), quantum zero point fluctuation $x_{\text{ZPF}} = \sqrt{\hbar/2m\Omega_m}$ (quantum mechanical uncertainty of oscillator position in ground state), n_{cav} average number of intra-cavity photons, $\Delta = \omega_l - \omega_c$ is the detuning between incident laser frequency ω_l and cavity resonance frequency ω_c (Eq. 2.59), and cavity decay rate κ (rate at which intra-cavity photons leave cavity). Note that Eqs. 2.91-2.93 rely on $\kappa \gg \Gamma_m + \Gamma_{\text{opt}}$ and high mechanical quality factor ($Q_m \gg 1$).

The frequency shift is referred to as optomechanical spring effect and the change in the mechanical damping rate is known as optomechanical damping/anti-damping rate [21]. The latter is of particular interest in quantum optomechanics, since it provides a means of extracting thermal energy from the resonator, to a degree that quantum mechanical effects

dominate the resonator's trajectory [14, 15]. That the presence of Γ_{opt} enables cooling (heating) of the resonator can be seen by executing an analysis similar to the one presented at the end of Sec. 2.1.2.2, to calculate the mean square oscillation amplitude of the thermally driven oscillator: in vicinity of the mechanical resonance ($\Omega \approx \Omega_m$) and for small frequency shifts ($\delta\Omega_{\text{opt}} \ll \Omega_m$), the displacement power spectral density (see Sec. 2.1.2.2) is given by

$$S_x(\omega) = |\chi_{\text{om}}(\omega)|^2 4k_B T \Gamma_m = \frac{4k_B T \Gamma_m}{m\Omega_m^2 (\Gamma_m + \Gamma_{\text{opt}})^2 [4(\Omega_m + \delta\Omega_{\text{opt}} - \omega)^2 / (\Gamma_m + \Gamma_{\text{opt}})^2 + 1]}, \quad (2.94)$$

with Boltzmann constant $k_B = 1.38 \times 10^{-23} \text{ m}^2 \text{ kg s}^{-2} \text{ K}^{-1}$, and temperature of environment T . By applying Parseval's theorem (Eq. 2.19) and substituting $y = 2(\Omega_m + \delta\Omega_{\text{opt}} - \omega) / (\Gamma_m + \Gamma_{\text{opt}})$ and $d\omega = dy (\Gamma_m + \Gamma_{\text{opt}}) / 2$ we have

$$\langle x^2(t) \rangle = \int_0^\infty \frac{d\omega}{2\pi} S_x = \frac{2k_B T}{m\Omega_m^2 (\Gamma_m + \Gamma_{\text{opt}})} \frac{1}{2\pi} \int_{y_0}^\infty dy \frac{1}{y^2 + 1} = \frac{k_B T}{m\Omega_m^2 (\Gamma_m + \Gamma_{\text{opt}})}. \quad (2.95)$$

A comparison with the equipartition theorem (Eq. 2.29) shows, that this expression corresponds to a harmonic oscillator connected to a thermal environment with effective temperature

$$T_{\text{eff}} = T \frac{\Gamma_m}{(\Gamma_m + \Gamma_{\text{opt}})}. \quad (2.96)$$

For $\Gamma_{\text{opt}} > 0$ (< 0) the OM interaction causes cooling (heating) of the resonator by reducing (increasing) T_{eff} . From Eq. 2.93 follows that OM cooling (heating) requires red (blue) detuning of the incident laser beam with respect to the cavity resonance, with $\Delta < 0$ (> 0). For reasons that will be elucidated further below, this type of OM cooling is sometimes referred to as sideband cooling. Other types of OM cooling require the use of active feedback [49, 89] or the existence of dissipative OM coupling, wherein motion adjusts the power in the cavity through its loss rate $\kappa(x)$ (see Fig. 2.6(b) for an example of dissipative coupling $\mathcal{F}(x)$ ($\propto \kappa^{-1}(x)$)) [73, 74, 75, 76, 77].

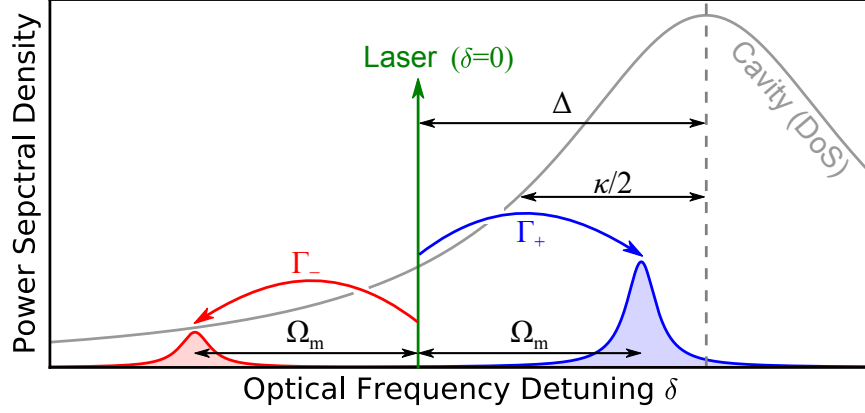


Figure 2.10: Schematic of optomechanical sideband cooling showing the optical power spectral density as a function of detuning δ between an incident laser and an optical cavity resonance (similar to Fig. 1(a) in Ref. [24]). Green arrow represents a laser with frequency ω_l which is red-detuned from an optical cavity resonance (gray curve, representing the cavity's density of states (DoS)) with frequency ω_c , so that $\Delta = \omega_l - \omega_c < 0$. The cavity comprises a mechanical resonator (e.g. moving end mirror or flexible membrane in between end mirrors) which oscillates at its resonance frequency Ω_m and thereby scatters laser light into a red (blue) sideband, located at $-\Omega_m$ ($+\Omega_m$) with respect to incident laser. Scattering light into red (blue) sideband transfers energy from light (mechanical resonator) to mechanical resonator (light) and happens at a rate proportional to the optomechanical anti-damping (damping) rate Γ_- (Γ_+) given by second (first) term of Eq. 2.93. Depending on detuning Δ and cavity linewidth κ (full width at half maximum) the cavity response suppresses one sideband more than the other, which for $\Delta < 0$ (> 0) results in effective cooling (heating) of the mechanical element.

Figure 2.10 shows a schematic of optical sideband cooling. An incident laser with frequency ω_l is scattered by the mechanical resonator into a red (blue) sideband (with lineshape corresponding to a mechanical resonator (see Fig. 2.1) of linewidth $\Gamma_m + \Gamma_{\text{opt}}$), located at $-\Omega_m$ ($+\Omega_m$) with respect to ω_l ⁷. Scattering light into red (blue) sideband transfers energy from light (mechanical resonator) to mechanical resonator (light). Depending on detuning Δ and cavity linewidth κ (full width at half maximum) the cavity response (density of states) suppresses one sideband more than the other, which for $\Delta < 0$ (> 0) results in effective cooling (heating) of the mechanical element. This process is most efficient in the resolved-sideband

⁷In a classical picture, the mechanical resonator phase modulates the intra-cavity field, given by real part of $E_c e^{i\omega_l t + ia \sin(\Omega_m t)}$ with field amplitude E_c and small modulation amplitude $a \ll 1$. Taylor expanding gives $E_c e^{i\omega_l t + ia \sin(\Omega_m t)} \approx E_c e^{i\omega_l t} [1 + ia \sin(\Omega_m t)] = E_c [e^{i\omega_l t} + \frac{a}{2} e^{i(\omega_l + \Omega_m)t} - \frac{a}{2} e^{i(\omega_l - \Omega_m)t}]$, where second and third term correspond to red and blue sideband. In a quantum picture, intra-cavity photons can be scattered by resonator phonons. Hereby, a photon (ω_l) can create or absorb a phonon (Ω_m) while being scattered to $\omega_l + \Omega_m$ or $\omega_l - \Omega_m$.

regime ($\Omega_m \sim \kappa$) where the red sideband is strongly suppressed while blue is strongly enhanced. Equation 2.96 suggests, that cooling to arbitrarily low temperatures is feasible by continuously increasing Γ_{opt} . In the case of sideband cooling with a coherent state of light, an achievable minimum value for T_{eff} arises as a consequence of the quantum mechanical properties of the OM interaction. The cooling and heating rates can be calculated from linear time-dependent perturbation theory (Fermi's golden rule) and are respectively given by $\Gamma_+ n_m$ and $\Gamma_- (n_m + 1)$ [21], where Γ_+ (Γ_-) corresponds to the first (second) term of Eq. 2.93, and n_m is the (current) average number of phonons in the mechanical resonator mode. Now, as one cools the resonator, thereby reducing n_m , an equilibrium between heating and cooling $\Gamma_+ n_{m,0} = \Gamma_- (n_{m,0} + 1)$ will be reached eventually, which sets the lower bound

$$n_{m,0} = \frac{\Gamma_-}{\Gamma_+ - \Gamma_-} = -\frac{\kappa^2 + 4(\Delta_0 + \Omega_m)^2}{16\Delta_0\Omega_m}. \quad (2.97)$$

The second expression, with $\Delta_0 = -\sqrt{\kappa^2 + 4\Omega_m^2}/2$, follows from Eqs. 2.92-2.93 and minimizing with respect to Δ . The fact that a minimum value for the resonator's occupation $n_{m,0}$ exists is a consequence of the inherent asymmetry in cooling rate ($\propto n_m$) and heating rate ($\propto n_m + 1$). To establish this limit we assumed the resonator to be not connected to a (mechanical) thermal environment and that OM cooling and heating were the only processes to change the resonator's occupation.

We now move on to include the resonator's connection to a thermal environment (modeled as an infinite set of mechanical oscillators [66]). The net cooling and heating rates are modified by a purely mechanical component ($\propto \Gamma_m$), which describes the connection to the thermal environment with phonon occupation at resonance frequency $n_{m,\text{th}} = k_B T / \hbar \Omega_m$ (consequence of equipartition theorem, see end of Sec. 2.1.2.2). In equilibrium we have $(\Gamma_+ + A_+) n_{m,\text{min}} = (\Gamma_- + A_-) (n_{m,\text{min}} + 1)$, with mechanical cooling and heating rates respectively given by $A_+ = \Gamma_m (n_{m,\text{th}} + 1)$ and $A_- = \Gamma_m n_{m,\text{th}}$. In the case of optimal detuning Δ_0 and with Eq. 2.97, the minimum value for the resonator's phonon occupation follows as

$$n_{m,\text{min}} = \frac{\Gamma_m n_{m,\text{th}} + \Gamma_{\text{opt}}(\Delta_0) n_{m,0}}{\Gamma_m + \Gamma_{\text{opt}}(\Delta_0)}. \quad (2.98)$$

Even in the case of strong OM cooling ($\Gamma_{\text{opt}}(\Delta_0) \gg \Gamma_m n_{m,\text{th}}$) the minimum value $n_{m,\text{min}}$ is

ultimately bounded by $n_{\text{m},0}$.

In the (deep) resolved sideband regime ($\Omega_{\text{m}} \gg \kappa$) the optimal cooling rate is given by

$$\Gamma_-(-\Omega_{\text{m}}) \approx 4n_{\text{c}}g_0^2/\kappa. \quad (2.99)$$

This motivates the definition of the single photon cooperativity

$$C_0 \equiv 4g_0^2/(\Gamma_{\text{m}}\kappa) \quad (2.100)$$

which represents the ratio of cooling/damping rate for an average cavity occupancy of a single photon (at the optimal detuning) to intrinsic damping of the mechanical element. For $C_0 = 1$ a single intra-cavity photon (on average) provides a cooling rate equal to the intrinsic thermal damping rate (Eqs. 2.99-2.100). For the setup studied in this dissertation, formed by a Fabry-Perot cavity with incorporated trampoline resonator (see Sec. 2.2.3), we can express C_0 by substituting $\Gamma_{\text{m}} = 2/\tau_{\text{m}}$ (Eq. 2.4), $\kappa = \pi c/(\mathcal{F}L_{\text{c}})$ (see Sec. 2.2.2) and $g_0 = \sqrt{\hbar/2m\Omega_{\text{m}}}\partial\omega_{\text{c}}/\partial x$ with $\partial\omega_{\text{c}}/\partial x$ given by Eq. 2.89, into Eq. 2.100, resulting in

$$C_0 = \frac{4\pi\hbar c|r_d|^2\tau_{\text{m}}\mathcal{F}}{\lambda^2L_{\text{c}}m\Omega_{\text{m}}}, \quad (2.101)$$

with phonon lifetime τ_{m} , speed of light c , cavity finesse \mathcal{F} , cavity length L_{c} , optical wavelength λ , and reflection coefficient of trampoline r_d .

Chapter 3

Fabrication & Mechanical

Characterization of Si_3N_4 Trampoline

Resonators

Statement of contribution: Alexandre Bourassa built the vacuum chamber and a previous version of the fiber interferometer that is employed in this chapter. For the presented measurements, I upgraded the fiber interferometer (replaced a homebuilt two-axis stage with a commercial one (closed-loop), assisted in interfacing it (python ctypes), designed and built a new support structure for the stage, replaced a fiber optical circulator with a four port fiber coupler, and added a preamplifier before the lock-in amplifier. Yishu Zhou, Vikramaditya Mathkar, and Chris McNally assisted by independently testing the setup and coding). Matthieu Nannini, Don Berry, Jun Li, Lino Eugene, Simon Bernard, and Scott Hoch contributed with discussions on nanofabrication. Raphael St-Gelais contributed to Sec. 3.2.3 with discussions on the angular spectrum method. Abeer Barasheed and Bogdan Piciu contributed with discussions on the finite-element model (COMSOL) used to simulate eigenfrequencies and mode profiles of fabricated trampoline resonators. My main contributions were: development of the silicon nitride trampoline resonator fabrication protocol, design and fabrication of all investigated trampolines, measurement and data analysis of the results presented in Sec. 3.3.1 - 3.3.2. The measurement presented in Sec. 3.3.3 was performed by Alexey Shkarin at the Harris Lab, Yale University, on devices that I fabricated. Aashish Clerk, Peter Grütter,

Christian Degen, and Gary Steele contributed with discussions.

Mechanical resonators fabricated from silicon nitride, particularly the stoichiometric form Si_3N_4 , have attracted widespread interest over the past decade. This has led to rapid improvements in their performance and increased understanding of the mechanisms limiting its optical and mechanical performance. By now, these combined efforts have resulted in fabricated devices with unprecedented mechanical figures of merit, namely mechanical quality factors Q_m (for resonator masses $m_{\text{eff}} \sim \text{fg} - \text{ng}$ and frequencies $f_m \sim 10 \text{ kHz} - 100 \text{ MHz}$), products $Q_m f_m$, and (among “top-down” batch-fabricated mechanical sensors) force sensitivities¹ (see Sec. 2.1.2.2)

$$S_F = 8m_{\text{eff}}k_B T / \tau_m, \quad (3.1)$$

with effective mass² m_{eff} , Boltzmann constant k_B , temperature T , and mechanical ringdown time τ_m . Due to the way in which they are grown, most high-performance Si_3N_4 resonators have a quasi one- or two-dimensional design with a Si_3N_4 layer thickness in the range of $10 \text{ nm} - 400 \text{ nm}$ and lateral extents in the range of $1 \mu\text{m} - 5 \text{ cm}$, as well as a high tensile (in-plane) stress on the order of 1 GPa . To give an everyday example, this amount of tensile stress would be created in a letter size paper (thickness $100 \mu\text{m}$), oriented upright, if a weight of two metric tons was hung from its bottom edge (given the material strength would permit it).

The dependency of mechanical performance parameters on material properties and device geometry of Si_3N_4 resonators has been systematically investigated by various groups. These independently executed studies were primarily carried out on doubly-clamped string/beam resonators and extended two-dimensional membranes. The common finding was, that Q_m , $Q_m f_m$, and S_F benefit from higher film stress [91, 92], larger lateral resonator dimensions (e.g. beam/string length and membrane area) [91, 93, 94, 59, 92, 95], and smaller film thickness

¹The force sensitivity S_F in units of force per square root of frequency, indicates for how long the trajectory of a mechanical resonator has to be measured, in order to resolve a force of a certain magnitude acting on the resonator. For example, a force sensitivity of $10 \text{ aN/Hz}^{1/2}$ indicates, that a measurement time of 1 s is required in order to resolve a force of 10 aN (assuming the force acts on the mechanical resonator at a frequency within the detection bandwidth.)

²The effective mass is given by $m_{\text{eff}} = \rho_m \int dV \zeta^2(x, y) / \zeta_0^2$ [90] with material density ρ_m , trampoline volume V , trampoline displacement amplitude $\zeta(x, y)$ from its equilibrium configuration (in xy -plane), and maximum displacement ζ_0 .

[94, 59, 92, 39, 57]. Furthermore, maximal $Q_m f_m$ is typically obtained for higher order modes for both, strings/beams and membranes, with highest measured $Q_m f_m$ values of $\sim 10^{13}$ for the former [39, 96] and $\sim 10^{14}$ for the latter [92, 57]. A characteristic of string/beam resonators is that their mechanical performance degrades for beam widths exceeding few μm [94]. Whereas higher $Q_m f_m$ values have been achieved for membranes compared to strings/beams (partially owing to the bigger lateral extent of the former in the referenced studies), string/beam-based structures been shown to provide higher force sensitivity [97, 1, 39]. This is because they offer a mechanical performance comparable to that of membranes at orders-of-magnitude-lower mass (Eq. 3.1).

The exact scaling of performance parameters with respect to in-plane stress and device geometry, roughly outlined above, depends on the particular mechanism that limits the mechanical performance. A recent review [98] summarizes the current state of knowledge about the underpinnings of mechanical energy dissipation in Si_3N_4 resonators. By now it is understood that the mechanical performance is fundamentally limited by “clamping” and “bending” losses. The former describes energy dissipation by radiation of phonons into the substrate (can be reduced by using thicker chip substrates [59, 39], as this increases the mechanical impedance mismatch at the clamps). The latter assumes coupling of bending induced strain fields to internal defects in the material. This loss is a sum of contributions from bending in the clamp areas and bending at modal antinodes. The exact details are still subject of an ongoing discussion but accumulating evidence points at two-level defect states as the prime suspect of dissipating bending energy [99, 98].

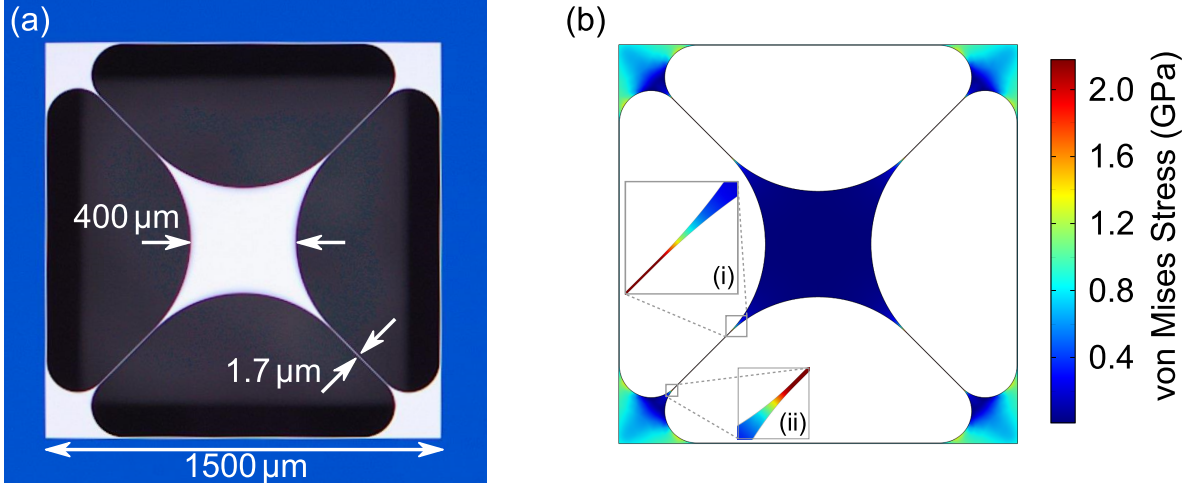


Figure 3.1: Fabricated Si_3N_4 trampoline resonator with redistributed in-plane stress upon release. (a) Optical image of fabricated device with a window size of $w = 1.5 \text{ mm}$, central pad diameter $d = 400 \mu\text{m}$, and tether width $a = 1.7 \mu\text{m}$ (released Si_3N_4 appears white, Si_3N_4 on Si substrate appears blue). (b) Finite element simulation (COMSOL) of in-plane stress for device of (a), with material parameters: density 2700 kg/m^3 , Young's modulus 250 GPa , Poisson ratio 0.23 , and internal stress 0.95 GPa .

In recent years, based on the insights gained with Si_3N_4 resonators of the fundamental string/beam and membrane geometries (see above), a variety of specifically-engineered devices has emerged. Hereby, the objectives have been to circumvent certain limitations encountered in strings/beams or membranes and to improve specific features. For example, it had repeatedly been reported [42, 98, 92] that mounting conditions of resonator chips can have a severe impact on the device performance. In these studies, particularly lower-order membrane modes benefited strongly from minimal contact with the structure supporting the chip, where gluing the chip at several spots to its support decreased Q_m by a factor up to $\sim 10^2$ [42]. This finding motivated patterning the Si substrate surrounding the membrane into a periodic structure, with the intent to suppress propagation of phonons at certain membrane resonance frequencies in the substrate, thereby increasing the membrane's isolation from its environment [46, 47]. A trampoline resonator is another type of device which is specifically tailored, here with regards to its application in optomechanics [51]. Figure 3.1(a) shows a fabricated trampoline comprising a central pad, to interact with an incident laser beam, that is weakly suspended by four tethers. This geometry increases the mechanical compliance with respect to an unpatterned membrane and thereby enhances the resonator's

susceptibility to the force of incident light. Trampoline resonators have been demonstrated to provide low force noise $\sqrt{S_F} \sim 15 \text{ aN}/\sqrt{\text{Hz}}$ [1, 39] and high $Q_m f_m \gtrsim 10^{13}$ [39]. Achieving this high performance is partially attributed to a stress redistribution in the fabricated devices. Figure 3.1(b) shows a finite element simulation of the stress distribution for the trampoline of Fig. 3.1(a). The tethers provide only a small force compared to the large area pad, causing the pad to contract while the tethers are stretched. As a result, the central pad is completely stress-relieved, with a tensile stress level of 10 MPa while, while the stress level in the tethers is 2.2 GPa, which represents an increase by more than two times with respect to the residual film stress of the Si_3N_4 device layer. A similar approach of “stress engineering” was reported for beam resonators [100]; instead of directly clamping a beam of uniform thickness at the substrate, it is connected to the substrate via a wider nitride area, which upon release contracts and thereby increases the beam stress. A recent benchmark for Si_3N_4 resonators was obtained with periodically-patterned membranes featuring a central defect [57]; the defect modes provide both highly reduced clamping and bending losses compared to any other geometry realized so far. This is by virtue of the confinement of the defect mode to the central area of the membrane, which results in greatly reduced oscillation amplitudes at the clamp, thereby reducing clamping loss. Furthermore, by replacing strong bending at the clamps with soft clamping in areas where the geometrical defect transitions into the periodically patterned part of the membrane, bending-induced dissipation is strongly reduced. These features have enabled resonators with $Q_m > 10^8$ at $f_m = 1 \text{ MHz}$ and resulting $Q_m f_m \gtrsim 10^{14}$ [57].

In this chapter we present the fabrication and mechanical characterization of Si_3N_4 trampoline resonators. In Sec. 3.1 we discuss the geometrical features of a fabricated trampoline and detail its fabrication procedure. In Sec. 3.2 we present the vacuum fiber interferometer setup, used to measure the trampoline’s mechanical resonances, and discuss the calibration procedure to express the trampoline’s oscillation amplitude in terms of length units. This calibration relies on a one-dimensional optical model, which agrees with a more involved two-dimensional model within 10 % (see Sec. 3.2.3). Since the latter is more complicated to apply to the experimental data we employ the former, justified by the modest deviation. In Sec. 3.3 we identify mechanical resonances of a trampolines resonator, which agree with

a finite element simulation (COMSOL) within 1 %. By measuring the mechanical ringdown time, after switching off a resonant piezo drive, we extract Q_m of the identified modes, which all have values $> 10^7$. The highest value was measured for the fundamental resonance with $Q_m = 4.5 \times 10^7$. We measure the thermal displacement spectrum (at room temperature) of this resonance and extract a thermal force noise of $16.2 \text{ aN/Hz}^{1/2}$. With regard to future integration of the trampolines, e.g. in an optical cavity, we cleave them (post release) into individual device chips and glue them at three spots to metal support, resulting in a moderate $\sim 10\%$ reduction of Q_m for the fundamental resonance (note this result is for smaller, 570 kHz devices having bare Q_m 's of 5×10^6).

3.1 Si_3N_4 Trampoline Resonator Fabrication

High aspect ratio Si_3N_4 mechanical resonators find widespread use, e.g. in cavity optomechanics experiments [21] or as cantilever in atomic force microscopy [101], as they combine exceptional mechanical performance (see introduction to this chapter) with low optical loss. Devices made out of Si_3N_4 are typically fabricated on an Si substrate, oriented such that a (100) crystal plane is parallel to the resonator. This geometry enables one to define sharp terminating edges in the substrate at the resonator's clamping areas by wet releasing in potassium hydroxide solution (due to high etch selectivity with respect to crystal planes; etch rate along [100] crystal direction about a factor $\sim 10^2$ bigger than along [111]). Improving the mechanical performance by virtue of this wet-release comes at the expense of dealing with additional technical challenges, as it exposes the highly-fragile (once released) Si_3N_4 structures to forces exerted by the liquid (all the more, as it requires additional cleaning steps in which the released resonator has to be transferred between different chemical baths). Therefore, in the course of developing our trampoline fabrication protocol we soon identified chip handling as a factor with crucial impact on device breaking and cleanliness. To circumvent the encountered limitations, we designed a sample carrier which protects the chips against flow in the chemical baths and minimizes tweezer-based chip handling. By virtue of this carrier, we achieved an overall fabrication yield of $\sim 50\%$ (up to 100 % on individual chips) for the trampoline resonators mechanically-characterized in later sections of this chapter.

In Sec. 3.1.1 we present optical and scanning electron microscope pictures of a fabricated trampoline resonator and discuss its geometric features and design considerations. In Sec. 3.1.2 we discuss the Si_3N_4 trampoline resonator fabrication protocol and give details on the employed machines, tools, and recipes.

3.1.1 Fabricated Trampoline Resonator

Drawing inspiration from similar structures [102], those having embedded Bragg mirrors [50, 51], and high- Q_m nitride strings [91], we pattern single-layer resonators suitable for a “membrane-in-the-middle” [41] optomechanical geometry.

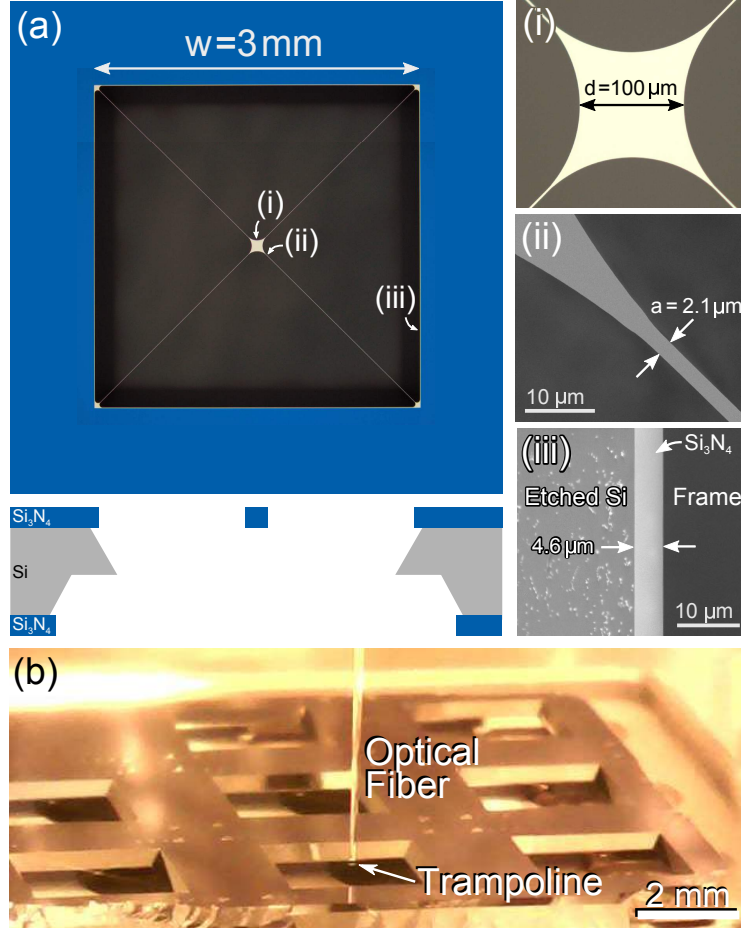


Figure 3.2: Fabricated Si_3N_4 “trampoline” resonators. (a) Optical image of the released structure with a window size of $w = 3\text{ mm}$ (upper) and a schematic of its KOH-etched cross-section (lower). Right-hand images show (i) an optical image of the $d = 100\text{ }\mu\text{m}$ -wide central pad, (ii) a scanning electron microscope (SEM) image of the $a = 2.1\text{ }\mu\text{m}$ -wide tether (near the pad), and (iii) an SEM image of the $4.6\text{-}\mu\text{m}$ -wide overhanging Si_3N_4 . Left from the overhang is the angled, KOH-etched silicon substrate showing typical roughness and residues. (b) Optical image of chip with eight trampoline resonators and optical fiber aligned on one of the trampolines for characterization of mechanical motion (see Sec. 3.2.1).

We fabricated and tested Si_3N_4 trampoline resonator ranging from $250\text{ }\mu\text{m}$ to $3000\text{ }\mu\text{m}$ window size, $40\text{ }\mu\text{m}$ to $400\text{ }\mu\text{m}$ pad diameter, and $1.4\text{ }\mu\text{m}$ to $3.5\text{ }\mu\text{m}$ tether width. The

most successful device (in terms of force noise sensitivity) is shown in Fig. 3.2(a), comprising (i) an 80-nm-thick, 100- μm -wide central pad suspended by (ii) 2.1- μm -wide tethers. These devices are suspended from a 675- μm -thick, (single-side-polished) silicon wafer, upon which 100 nm of stoichiometric Si_3N_4 was commercially deposited via low-pressure chemical vapor deposition.³ Nitride on silicon appears blue, and suspended nitride appears yellow. The filleted shapes [91] of the central nitride pad and corner clamping points ensure that all suspended structures are held flat by the nitride’s internal stress (nominally ~ 1 GPa), and that regions of concentrated strain in the structure’s normal modes are minimized. The fillets are nominally circular; on the central pad their radius defines the pad diameter d and the corner fillets are defined to have a quarter of this radius, to reduce their relative mass. The tethers are long (2.1 mm) to simultaneously increase the mechanical quality factor Q_m [94] and decrease the mechanical frequency Ω_m ⁴, thereby maximizing the mechanical ringdown time $\tau_m = 2Q_m/\Omega_m$ (see Sec. 2.4) without contributing too much mass. This in turn benefits the thermal force noise (Eq. 3.1). The cross section of the wafer (lower image of Fig. 3.2(a), also faintly visible from above) results from the minimum anisotropic KOH etch required to cut a clear-shot window through the silicon. This choice minimizes the region of overhanging Si_3N_4 (iii), a known source of mechanical dissipation [81, 94]. The size of the square window on the back side of the chip is chosen (on photolithography mask (see following section)) so that etching the Si substrate just from the back would yield sidewalls flush (up to overhang) with the outer boundaries of trampoline. In the present case of double side etching, this causes the top and back etch profile to be offset with respect to each other, resulting in a sharp edge half way along the substrate thickness. The angle of the etched silicon associated with the anisotropic etch also serves to further increase the rigidity of the supporting frame at the clamping points.

³Note Si_3N_4 -coated wafers purchased from University Wafer and Addison Engineering produce similar results.

⁴Resonance frequencies of a highly-stressed doubly-clamped beam are given by $q \sqrt{\sigma/\rho}/(2l_t)$ [103, 91], with mode index $q \in \mathbb{N}$, tensile stress σ , material density ρ , and beam length l_t . For a trampoline with $a, d \ll l_t$ this expression provides an estimate for the trend of its (lower order) resonance frequencies, whereby the increased mass, with respect to the beam, due to the central pad, can be described by an increased ρ .

3.1.2 Fabrication Protocol

Here we discuss details of our fabrication protocol for Si_3N_4 trampoline resonators (see previous section). Fig. 3.3 shows an illustration of the process flow, based on vertical cross sections and names of employed chemicals for each process step. In Tables 3.1-3.2 we list details of the employed tools, machines, and fabrication recipe parameters. In the following we briefly describe the essential steps carried out during fabrication and refer the reader to the aforementioned figure and tables for specifics.

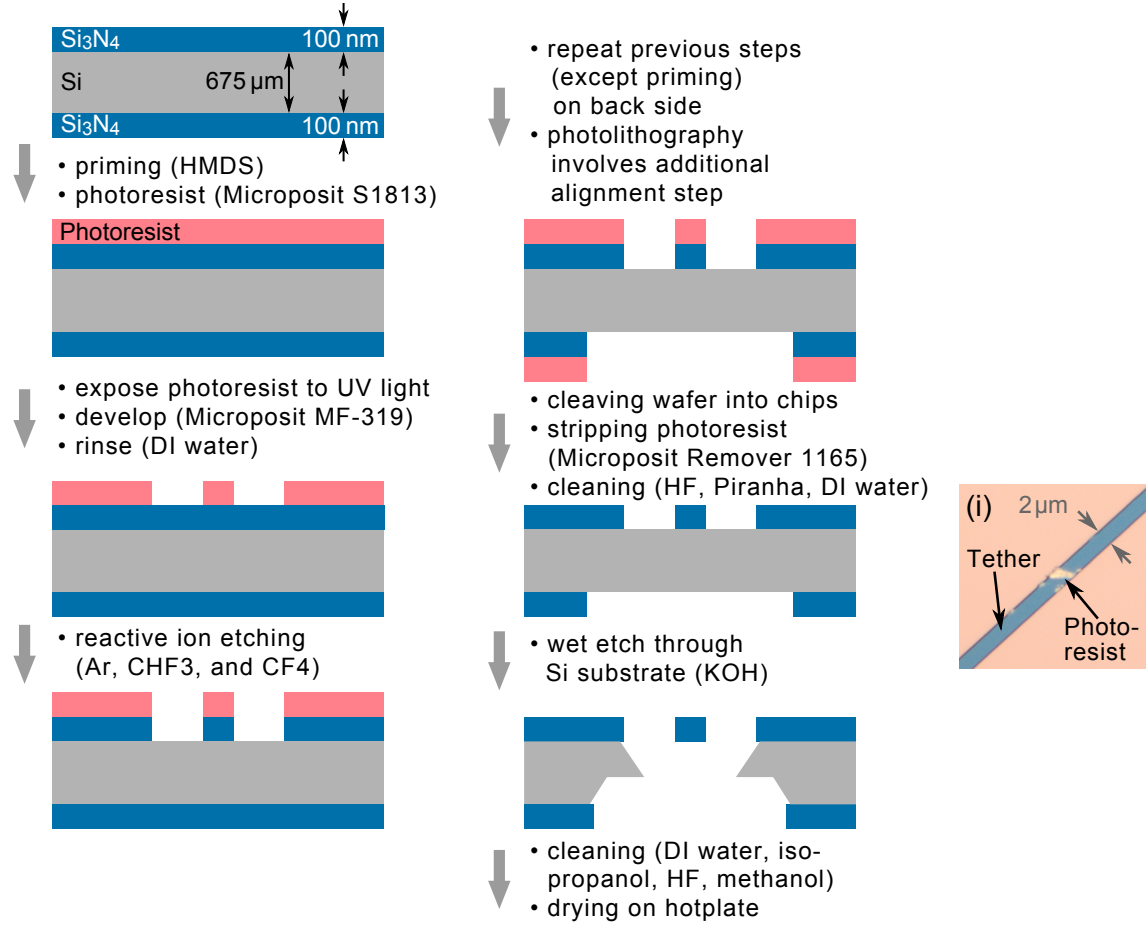


Figure 3.3: Schematic of trampoline cross section at different stages in fabrication process (see Tables 3.1-3.2 for recipe details). From top to bottom and left to right: silicon (Si) wafer ($\varnothing = 6\ \text{inch}$), coated on top and back side with $100\ \text{nm}$ thick layer of Si_3N_4 , is vapor primed with hexamethyldisilazane (HMDS) and spin coated with $1.5\ \mu\text{m}$ thick layer of photoresist (Microposit S1813). Trampoline geometry is transferred into photoresist by means of photolithography and resist development (Microposit MF-319). Residues are washed off with deionized (DI) water. Trampoline is written into top Si_3N_4 layer by magnetically-enhanced reactive ion etch, with plasma comprising Argon (Ar), Fluoroform (CHF_3), and Tetrafluoromethane (CF_4). Previous steps (except priming) are repeated on backside to write a square window into Si_3N_4 layer. Additional backside alignment is required to overlay square window and trampoline. Wafer is manually cleaved (using diamond scribe and wafer pliers) into chips of $15\ \text{mm} \times 15\ \text{mm}$. Photoresist is stripped (Microposit Remover 1165). Individual cases require additional cleaning in piranha solution (mixture of sulfuric acid and hydrogen peroxide) to remove excess photoresist. Chips are dipped in hydrofluoric acid (HF), rinsed in DI water and transferred to potassium hydroxide solution (SI etch). Chips are rinsed first in DI water then isopropanol followed by HF surface treatment, DI water rinse, and methanol rinse. Trampoline chips are dried on hotplate. (i) Optical image of tether (blue) on silicon (peach) showing “hard-to-remove” excess photoresist after stripping.

Fabrication begins by lithographically defining a $1.5\text{-}\mu\text{m}$ -thick photoresist mask in the shape of a trampoline on the top surface and transferring it to the nitride with a CF_4/CHF_3 reactive ion etch. The remaining resist is left as a protective layer while an array of square openings is patterned into the backside nitride using the same technique. The wafer is then diced into chips of $15\text{ mm} \times 15\text{ mm}$ for handling, each hosting 8 identical devices and one unpatterned “reference” membrane (see Fig. 3.2(b); reference membrane can be fully etched if desired), and mounted in a chemically-resistant Polytetrafluoroethylene (PTFE) carrier. Figure 3.4(a) shows a photo of this carrier with chips rigidly held in a vertical orientation, while allowing liquid to slowly enter and drain via slits in the bottom; we find it plays a crucial role in device survival during wet chemical processing. The photoresist is stripped in Microposit Remover 1156 at 80°C (initially we used acetone, but switched to Remover 1156 since it can be heated up to significantly higher temperatures). This process takes typically 1-2 hours, until there are no more photoresist residues visible with a microscope (Olympus MX 40). Hereby, it takes longest to strip resist of the tethers, with increasing stripping time for decreasing tether width.⁵ Inset (i) shows an optical microscope image of a tether (blue, width $2\text{ }\mu\text{m}$) on Si (peach), displaying a typical example of “hard-to-remove” photoresist. If we encounter these residues after ~ 2 hours of stripping, we perform a Piranha clean (see Table 3.2, 1st Clean) on the chips, which removes all the remaining residues. During this process the device chips are rigidly clamped to the PTFE carrier to avoid them floating out of their slots. A CAD drawing of the chips clamped to the carrier is shown in Fig. 3.4(b), where additional crossbars (polypropylene) are installed onto the carrier with screws (not shown, fixed through holes indicated by red dashed lines). Each chip is clamped to the carrier with a screw through a hole in the crossbar. We move on to remove the newly-exposed silicon’s native oxide with a 1-minute 10:1 Hydrofluoric (HF) acid dip at room temperature. To release the trampolines, the chips are briefly rinsed in DI water and then transferred to a 45 % potassium hydroxide (KOH) solution at 60°C , where the silicon is etched at a rate of $18\text{ }\mu\text{m/hr}$ for 19 hours. This removes the requisite $340\text{ }\mu\text{m}$ from both sides of the wafer,

⁵A possible reason for the “hard-to-remove” photoresist residues on the tethers might be, that the resist in these areas was baked harder compared to, e.g., the central pad. We suspect that this might be related to a geometry-dependent heat transfer during RIE. To examine this we reduced the etch power from 500 W to 200 W with no measurable effect on the duration of the resist stripping process. Note that the 200 W RIE recipe requires a 5 times longer etch time compared to the 500 W recipe (see Table 3.2).

resulting in the profile shown on the bottom right of Fig. 3.3. Faster etches could be achieved at higher temperatures (e.g. $\sim 30 \mu\text{m/hr}$ at 75°C , but we find this significantly reduces device yield, likely due to increased H_2 bubble formation [104]. We suspect the rising bubbles break the tethers by either directly exposing them to surface tension forces and pressure variations, or by violently shaking the chip (if loosely mounted), thereby dragging the pad (a.k.a. “the giant sail”) through the solution. While keeping the released devices submerged, the KOH solution is then diluted to 0.1 % of its original strength by iteratively removing existing solution, without exposing the devices to air, and refilling with DI water. This dilution process is repeated with isopropanol to further clean and reduce surface tension. The chips are then transferred to a 10:1 HF solution for 10 min, which gently etches $\sim 10 \text{ nm}$ of nitride (from all exposed surfaces) along with any lingering residues [105]. Finally the chips are transferred to DI water and then methanol for a final rinse before removing and drying on a hotplate at 85°C . With this protocol, 6 of the 8 devices in Fig. 3.2(b) survived, consistent with a survival rate of $\sim 50\%$ for all device types discussed in this dissertation.

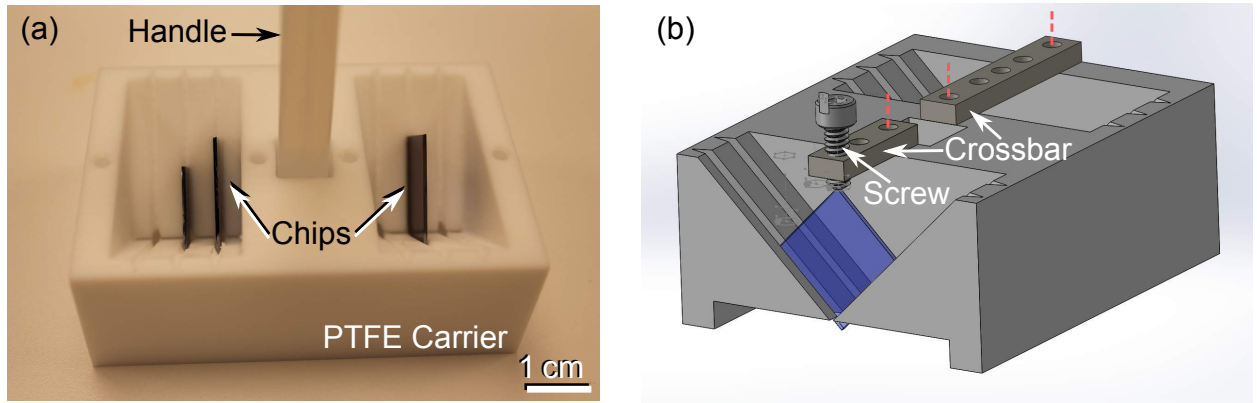


Figure 3.4: Chip carrier made out of Polytetrafluoroethylene (PTFE) for wet chemistry steps in Si_3N_4 trampoline fabrication. (a) Photo of carrier with device chips mounted vertically in v-grooves. Handle is made out of polypropylene. (b) CAD drawing of carrier with crossbars (polypropylene, fixed to carrier by means of screws (polypropylene or stainless steel, not shown) thorough holes indicated by red dashed lines). Chip is clamped by means of screw (polypropylene or stainless steel) through crossbar.

Process Step	Process Information			
Priming	T: Yield Engineering Systems (YES) 310			
	R: thumbwheel set to “2”			
	C: hexamethyldisilazane (HMDS)			
	D: 22 min (25 min)			
	N: temperature in oven is set to 150°C			
Spin Coating	T: Laurell WS-400-6NPP-LITE			
	R: program “C”			
	C: Microposit S1813			
	D: (10 min)			
	N: spreading at 500 rpm for 5 s, spinning at 4000 rpm for 30 s			
Soft Bake	T: hotplate (Electronic Micro Systems Ltd 1000-1)			
	D: 1 min			
	N: bake wafer at 115°C for 1 min			
UV Exposure	T: EVG620			
	R: “TopSide-7inMask-6in-1.4um”, “BackSide-7inMask-6in-1.4um”			
	D: (20 min (top side), 30 min (back side))			
		Top Side		Back Side
	Process:	Manual Top Side	Manual Bottom Side	
	N: Process Mode:	Transparent	Overlay	
	Exposure Mode:	Constant Dose	Constant Dose	
	Contact Mode:	Hard Contact	Soft Contact	
	mask, substrate size: 7 in, 6 in, separation: 50 μm, Dose: 65 mJ/cm²			
	thickness mask, substrate, resist: 3.06 mm, 0.68 mm, 1.4 μm			
Developing	C: Microposit MF-319			
	D: 45 s (10 min)			
	N: After developing rinse in deionized water			
O₂ Clean	T: Applied Materials Precision 5000			
	R: “O2 CLEAN”			
	C: O₂ (45 scc)			
	(during rampdown only Ar (70 scc))			
	D: (10 min)			
		Stabilization	Etch	Rampdown
	Step Time:	15 s	180 s	10 s
	N: Pressure:	150 mTorr	150 mTorr	fully open
	RF Power:	0 W	500 W	50 W
	Magnet Field:	0 Gauss	70 Gauss	0 Gauss

Table 3.1: Trampoline fabrication tools and recipes (part 1). Process parameter abbreviations stand for T: tool/equipment name, R: recipe name or settings, C: name of used chemicals, D: duration of recipe (time given in paranthesis is optimistic estimate for total duration of fabrication step, including preparation and cleaning of tool, equipment and/or workspace), N: additional notes and details.

Process Step	Process Information			
Si ₃ N ₄ Etching	T: Applied Materials Precision 5000			
	R: “Si ₃ N ₄ ETCH SH”, “ Si₃N₄ CHRISTOPH ”			
	C: Ar (70 scc), CHF ₃ (30 scc), CF ₄ (7 scc)			
	D: (10 min)			
		Stabilization	Etch	Rampdown
N:	Step Time:	15 s	45 s (240 s)	15 s
	Pressure:	30 mTorr	30 mTorr	fully open
	RF Power:	0 W	500 W (200 W)	20 W
	Magnet Field:	0 Gauss	70 Gauss (60 Gauss)	0 Gauss
Cleaving	T: diamond scribe & Fletcher wafer pliers N: make scratch (1-2 mm) on both ends of cleave line, center pliers on a scratch, and apply very little pressure only			
Stripping	T: Crest Ultrasonics (solvent bench) R: time: 1-2 hr, temperature: 85°C, sonication power level 5 (out of 10) C: Microposit Remover 1165, IPA and DI water rinse D: 1-2 hours N: hardest to strip resist from tethers → inspect carefully (microscope)			
1 st Clean	T: acid wet bench, HF wet bench C: HF 10:1, H ₂ SO ₄ : H ₂ O ₂ 2:1 mixture (piranha), DI water rinse N: HF dip (1 min), if excess photoresist → piranha (20 min), then HF optional piranha procedure: preheat H ₂ SO ₄ (35°C) then add H ₂ O ₂			
Si Etching	T: Si etch bench, hotplate, syringe with tubing C: KOH 45 % solution N: Fill 500 ml of KOH (45 %) in 800 ml Pyrex beaker, D: (20M100-150hr) cover beaker with PTFE lid, etch at 60°C for 19 hr optional: place beaker in water bath (glass bowl) on hotplate when etch done pump out KOH (chips barely submerged), refill beaker with DI water (repeat two times), pump out DI water and refill 200 ml of IPA			
2 nd Clean	T: HF wet bench, solvent bench C: HF 10:1, DI water, methanol N: Transfer chips from IPA to HF (PP beaker, for 10 min) transfer to beaker with DI water (200 ml) transfer to beaker with methanol (200 ml)			
Drying	T: hotplate (Fisher Scientific Isotemp) N: cover hotplate at 85°C with wipe take chips out of methanol and place on hotplate			

Table 3.2: Trampoline fabrication tools and recipes (part 2). Process parameter abbreviations stand for T: tool/equipment name, R: recipe name or settings, C: name of used chemicals, D: duration of recipe (time given in paranthesis is optimistic estimate for total duration of fabrication step, including preparation and cleaning of tool, equipment and/or workspace), N: additional notes and details. Other abbreviations stand for IPA: isopropanol, DI: deionized, PP: polypropylene.

3.2 Fiber Interferometer for Measuring Nanomechanical Motion

Optical interferometry is a widely-employed high-precision method for measuring the distance between two objects. The measurement principle relies on interference of two portions of light, which have a relative phase difference dependent on the displacement of interest. This phase difference is translated into a corresponding level of optical power and read out with a photodetector. This method resembles an omnipresent tool in different branches of physics, such as gravitational wave detection with few-km-long free-space optical interferometers [106] or nanomechanical motion measurements in a $\sim \mu\text{m}$ -long fiber interferometer [101].

Here we describe the interferometric measurement that we carry out to characterize the mechanical resonances of our trampoline resonators. In Sec. 3.2.1 we present the employed Fabry-Perot fiber interferometer, describe its optical, electronic, and vacuum components and give a brief overview over its measurement principle. In Sec. 3.2.2 we present our calibration procedure, which is based on an optical plane wave model, to convert the measured voltage into a displacement amplitude. As this model neglects divergence of the light beam propagating in the interferometer, in Sec. 3.2.3 we test its applicability by comparing it to a two-dimensional model which includes beam divergence. We find a mutual deviation of up to 10 % between plane-wave model and diverging-beam model and therefore employ the former in our calibration procedure, due to its ease.

3.2.1 Design

To assure that the mechanical performance of our Si_3N_4 trampoline resonators (see Sec. 3.1.1) is not limited by air damping (see Appendix B.2) we characterize their mechanical resonances in a vacuum chamber at a pressure below 10^{-6} Torr.⁶ Figure 3.5(a) shows a view inside the chamber where the central pad of a trampoline is aligned with respect to an optical fiber at

⁶After pumping down from ambient conditions to pressures $\sim 10^{-7}$ Torr with a turbo pumping station (Pfeiffer HiCube ECO), we cross over to an ion pump (Duniway DSD-05005125-M), to prevent vibrations from the turbo pump to corrupt our nanomechanical motion measurements. A gauge inside the ion pump measures a pressure of $\sim 10^{-7}$ Torr. The trampoline is installed in the middle of a six-inch vacuum cube which is connected to the pump via a vacuum tee with connection length of 15 inch and diameter of 2–5 inch.

a distance of 50 - 100 μm . To measure the trampoline's motion, laser light is directed along the fiber towards a cleaved tip, and the interference between reflections from the cleave and trampoline records the instantaneous displacement.

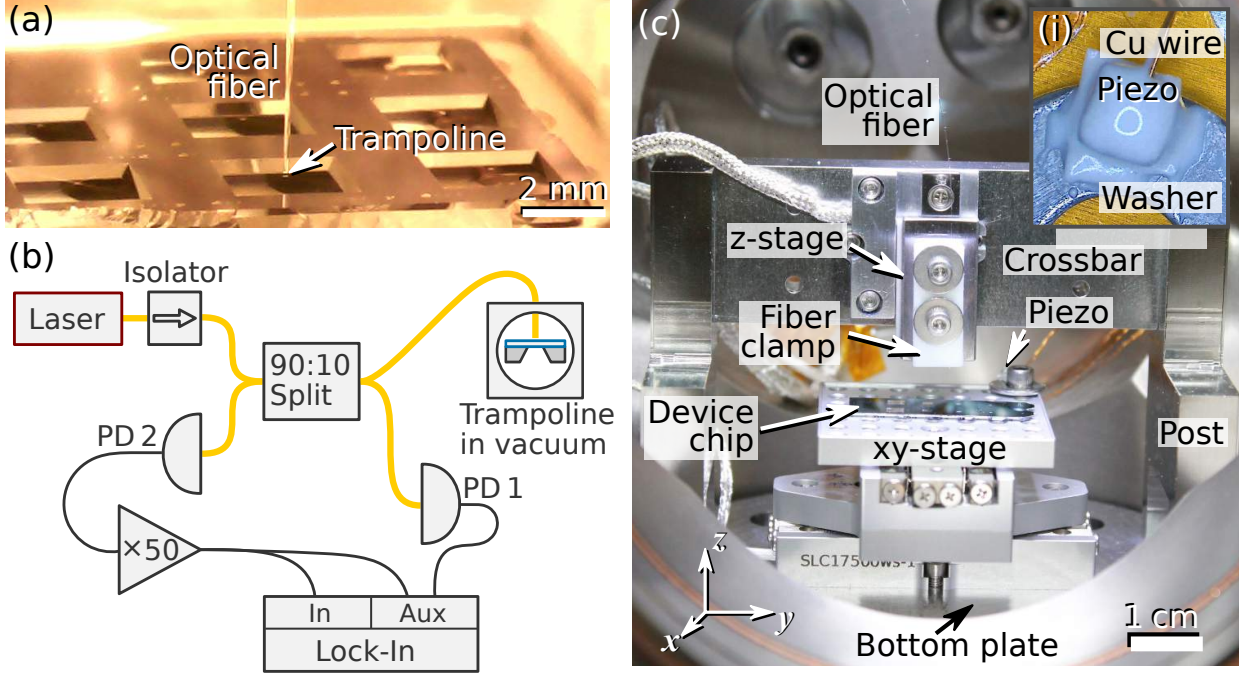


Figure 3.5: Vacuum fiber interferometer setup (pressure below 10^{-6} Torr). (a) Optical image of a chip with eight trampoline resonators inside a vacuum chamber. An optical fiber is aligned within a distance of 50 - 100 μm from a central pad of a trampoline resonator. (b) Schematic of the complete measurement setup. Yellow (black) curves represent optical fibers (electronic cables). A fiber coupled laser (wavelength $\lambda = 1550$ nm) passes through an isolator and a splitter. Ten percent of the incident light is routed to the fiber interferometer towards cleaved tip of fiber and 90 % are directed to photodiode 1 (PD 1). Reflected light from fiber interferometer, made up by partial reflections at fiber cleave and trampoline resonator, is split so that 90% land on photodiode 2 (PD 2) and 10 % are blocked by the isolator. Voltage from PD 1 is measured on auxiliary input (Aux, acts as voltmeter) of a lock-in amplifier. Voltage from PD 2 is amplified $\times 50$ by a low-noise preamplifier and subsequently split. Oscillatory component is measured by means of lock-in detection and DC component is measured on auxiliary input. (c) Optical image of fiber interferometer with device chip and nanopositioning stages in vacuum chamber. A support structure, comprising a bottom plate, two posts, and a crossbar is employed for mounting a xy-stage and z-stage. Fiber is fixed to z-stage by means of a fiber clamp. A piezo actuator is installed on xy-stage. Inset (i) shows piezo, electrically contacted by means of a copper (Cu) wire, glued to a washer.

Figure 3.5(b) shows a schematic of the combined optical and electronic measurement setup. All optical components are fiber coupled, with optical fibers represented by yellow

curves. Electronic cables are drawn as black curves. A fiber coupled laser diode (Thorlabs SFL1550P⁷), with wavelength 1550 nm and output power 40 mW, is connected to an isolator (Thorlabs IO-H-1550APC), two attenuators (Thorlabs FA05T-APC and FA10T-APC, not shown) with combined attenuation of 15 dB, and a 90:10 splitter (Thorlabs 10202A-90-APC), which routes 90 % of the incident optical power to a photodiode (PD 1, Thorlabs PDA10CF) and 10 % towards the fiber cleave inside the vacuum chamber. The optical power measured right at the fiber cleave is 50 μ W (in agreement with laser diode output power and nominal attenuation from optical components). The back-reflected light from the fiber interferometer is routed by the splitter so that 90 % land on a photodiode (PD 2, Thorlabs PDA10CF) and 10 % are blocked by the isolator. The voltage from PD 1 is measured on the auxiliary input (Aux) of our lock-in amplifier (Zurich Instruments HF2), which acts as a voltmeter. By monitoring this signal up to several hours we have confirmed that the laser diode's output power is stable over this time span. The voltage from PD 2 is amplified by a low-noise preamplifier (Stanford Research Systems SR560 with additional 50 Ω resistor installed parallel to 100 M Ω input resistance) by a factor of 50 and subsequently split. The AC component, oscillating at the trampoline's mechanical resonance frequency (see next section for details), is demodulated⁸ on the lock-in amplifiers input (In). The DC component of the signal (used to calibrate trampoline's oscillation signal in length units, see following section) is measured on Aux.

Figure 3.5(c) shows a photo of the fiber interferometer installed inside a vacuum chamber. We use a single mode fiber (SM980-5.8-125), which is stripped down to the cladding ($\varnothing = 125 \mu\text{m}$) and cleaved to provide an optically smooth surface. The refractive index of the fiber core is 1.45 at our operating wavelength of 1550 nm [personal communication with Thorlabs employee, June 9, 2017]. Vacuum-compatible pass through of the fiber inside the vacuum chamber is achieved by using a polytetrafluoroethylene (PTFE) fiber ferrule installed in a

⁷we now recommend using a Redfern Integrated Optics Orion system instead, as that laser/controller combination has significantly lower amplitude noise over these frequencies.

⁸The following description of lock-in detection is taken from Ref. [107]. Measured signal voltage $u_s(t) = A_s \cos(\omega_s t + \varphi)$, with amplitude A_s , frequency $\omega_s/2\pi$, and phase φ , is multiplied (with electronic mixer) by reference signal $u_r(t) = \sqrt{2} \exp(i\omega_r t)$, with frequency $\omega_r/2\pi$. This results in $u_s(t)u_r(t) = A_s/\sqrt{2} \{\exp[i(\omega_s - \omega_r)t + \varphi] + \exp[i(\omega_s + \omega_r)t + \varphi]\}$. Subsequent low-pass filtering (filter transfer function $F(\omega)$) yields $F(\omega_s - \omega_r) A_s/\sqrt{2} \exp[i(\omega_s - \omega_r)t + \varphi]$. Choosing ω_r as close as possible to ω_s and the low pass as selective as possible to the resulting signal, realizes a measurement which highly suppresses signals oscillating at frequencies different from $\omega_s/2\pi$, resulting in a highly increased signal to noise ratio.

$\varnothing 1/8$ inch tube Swagelok compression fitting [108]. The fiber is fixed to a linear stage “z-stage” (Micronix PP-20, 12 mm travel range, 1 nm resolution) by means of a PTFE clamp. We use the z-stage to set the distance between fiber and trampoline. Typically, we aim for a separation in the range of 50 – 100 μm (estimated based on fiber thickness) as a trade-off between readout sensitivity (see Sec. 3.2.3) and practical considerations, such as the ability to optically resolve the fiber-trampoline separation. Here we employ two Califone CM1-USB cameras, with resolution $\sim 10 \mu\text{m}$, to observe fiber and membrane chip during alignment. These cameras are pointed at vacuum viewports (roughly oriented along x - and y -axis) from outside the chamber to verify alignment along all three spatial directions. For respective alignment of fiber and trampoline in the xy -plane we rest the trampoline chip on a 2-axis stage (Smaract SLC-17, 31 mm travel range, 1 nm resolution). In order to resonantly excite the trampoline’s motion, we have installed a piezo actuator (Noliac CSAP01) onto this stage. Inset (i) of Fig. 3.5(c) shows the piezo glued to a washer, which is screwed onto the top plate of the xy -stage (see. Fig. 3.5(c)). By connecting this piezo to the lock-in amplifier’s output, we can drive mechanical resonances up to 2 MHz (examined by Simon Bernard, [personal communication, July 3, 2017]).

3.2.2 Displacement Calibration Based on Optical Plane Wave Model

The fiber interferometer discussed in the previous section converts the trampoline’s (see Sec. 3.1) oscillation amplitude into a voltage signal, which is read out with a lock-in amplifier. In this section we describe our calibration procedure to extract the displacement amplitude from the measured voltage. Our method relies on an optical plane wave model, in which the electromagnetic field depends only on the location along its axis of propagation. In the following section we present a two-dimensional model, in which the light is treated as a diverging Gaussian beam. Comparison of the two models shows a deviation of at most 10% for all the trampolines studied in this dissertation. This justifies using the “simpler-to-apply” 1D model in our calibration procedure.

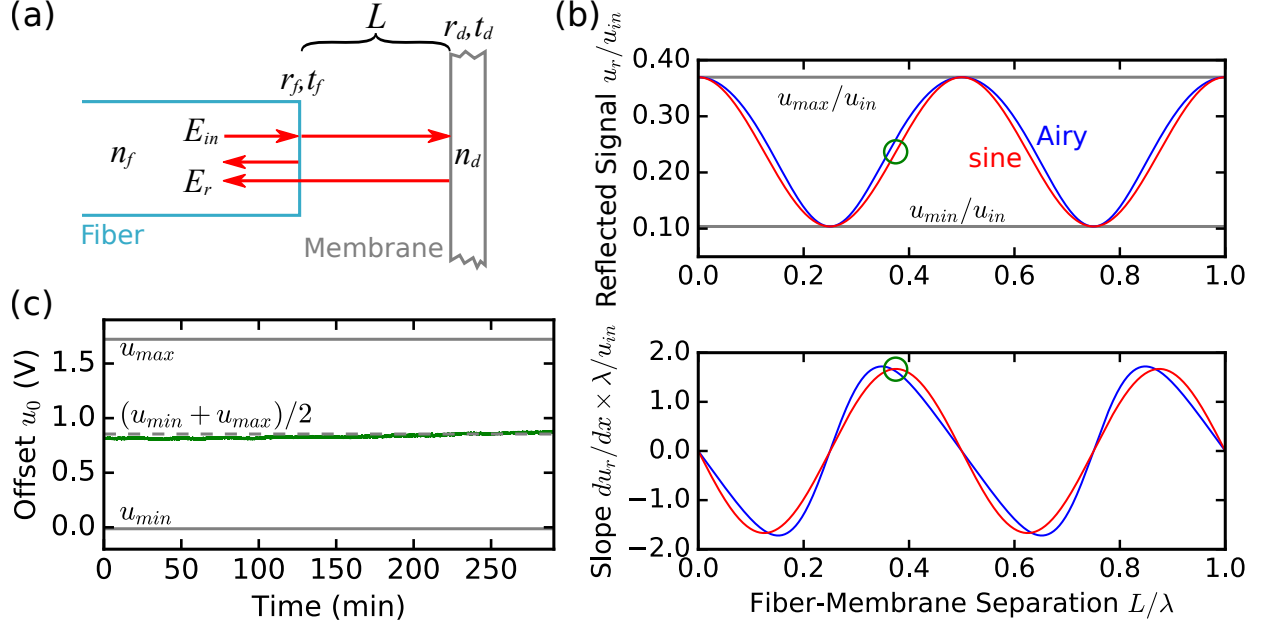


Figure 3.6: Optical plane wave propagation in fiber interferometer, resulting interference fringe, and experimentally observed fringe drift. (a) Schematic of fiber interferometer with optical fiber (blue, refractive index n_f) separated by distance L from trampoline resonator (gray, refractive index n_d). Reflected light E_r results from interference of partial reflections of incident light E_{in} (wavelength $\lambda = 1550$ nm) at fiber-vacuum interface (reflection and transmission coefficients r_f and t_f) and trampoline (reflection and transmission coefficients r_d and t_d). (b, upper) Blue curve shows Airy function describing normalized reflected signal u_r/u_{in} (Eq. 3.3 with $u_r \propto E_r^2$, $u_{in} \propto E_{in}^2$) versus fiber-membrane separation L/λ . Red curve shows sinusoidal fringe (Eq. 3.4). Gray line indicates minimum (maximum) fringe values u_{min}/u_{in} (u_{max}/u_{in}). Green circle indicates fringe center $(u_{min} + u_{max})/2u_{in}$. (b, lower) same as (b, upper) but for slope of fringe $du_r/dL \times \lambda/u_{in}$. Green circle is at same L/λ value as in (b, upper) and indicates maximum value for slope of sinusoidal fringe. (c) Green curve shows offset voltage u_0 versus time. Solid gray line shows minimum (maximum) fringe voltages u_{min} (u_{max}). Dashed gray line shows fringe center $(u_{min} + u_{max})/2$.

Figure 3.6(a) shows a schematic for optical plane wave propagation in the fiber interferometer. An optical fiber (blue) is separated by distance $50 \mu\text{m} < L < 100 \mu\text{m}$ from a trampoline resonator (gray). Light E_{in} is incident from the left, with wavelength $\lambda = 1550$ nm and wavenumber $k = 2\pi/\lambda$. Reflected light E_r results from interference of partial reflections from cleaved fiber tip and trampoline. Reflection and transmission at the cleave are governed by Fresnel coefficients $r_f = (n_f - 1)/(n_f + 1)$ and $t_f = 2n_f/(n_f + 1)$ (Eqs. 2.39-2.40), with refractive index of fiber $n_f = 1.45$ (see Sec. 3.2.1 for details). Trampoline reflection and transmission coefficients $r_d = |r_d|e^{i\phi_r}$ (written in terms of magnitude $|r_d|$ and phase ϕ_r) and

t_d are given by Eqs. A.3-A.4, with membrane thickness $d = 100$ nm and refractive index $n_d = 2.0$ (Si_3N_4 at 1550 nm). The optical transfer matrix (TM, see Sec 2.2 for details), describing propagation of light through this setup, is a product of a TM governing (from left to right) reflection at the trampoline (modeled as a dielectric slab, see Appendix A.1), propagation in between fiber and trampoline, and reflection at the fiber-vacuum interface (see Table 2.1)

$$\mathbf{M}_{\text{fi}} = \frac{1}{t_d} \begin{pmatrix} -e^{2i\phi_r} & |r_d| \\ -|r_d| & 1 \end{pmatrix} \begin{pmatrix} e^{ikL} & 0 \\ 0 & e^{-ikL} \end{pmatrix} \frac{1}{t_f} \begin{pmatrix} 1 & -r_f \\ -r_f & 1 \end{pmatrix}. \quad (3.2)$$

The reflected optical power is given by (Eq. 2.48)

$$P_r(L) = P_{in} \left| \frac{\mu_{21}}{\mu_{22}} \right|^2 = P_{in} \left[1 + \frac{r_d^2 + r_f^2 - r_d^2 r_f^2 - 1}{1 + r_d^2 r_f^2 + 2r_d r_f \cos(2kL)} \right] \quad (3.3)$$

with incident power $P_{in} \propto |E_{in}|^2$ (see Appendix A.4) and lower left (lower right) matrix element μ_{21} (μ_{22}) of \mathbf{M}_{fi} . Equation 3.3 resembles an Airy function, similar to the one obtained for the reflected optical power of a Fabry-Perot cavity (Eq. 2.52). This is consistent with the picture that the fiber interferometer sketched in Fig. 3.6(a) resembles a Fabry-Perot cavity for which the fiber-vacuum interface represents the input mirror and the trampoline acts as back mirror. In the present parameter regime ($|r_d|^2 = 0.228$, $|r_f|^2 = 0.034$, both small compared to high-finesse cavity mirror reflectivities > 0.99), the L -dependent reflected optical power from the fiber interferometer features a smooth modulation (see following paragraph) in contrast to sharp resonances, as for the Fabry-Perot cavities studied in theory in Sec. 2.2.2 and investigated experimentally in Sec. 4.2.1.

With our experimental setup (see Sec. 3.2.1) we measure a voltage proportional to the reflected optical power $u_r \propto P_r$ (Eq. 3.3). The blue curve in Fig. 3.6(b, upper) represents the normalized reflected signal $u_r/u_{in} = P_r/P_{in}$ (Eq. 3.3), with $u_{in} \propto P_{in}$, versus normalized fiber-trampoline separation L/λ . This so-called interference fringe varies periodically with L and period $\lambda/2$. The blue curve in Fig. 3.6(b, lower) represents the displacement sensitivity du_r/dL , normalized with respect to input signal and wavelength.

Equation 3.3 establishes a relation between the trampoline's displacement and reflected

signal. This suggests, that based on the knowledge of n_f , n_d , and λ one can convert the measured voltage into a displacement amplitude. In the following section we present an optical model in which the light exiting the fiber is more precisely described as a diverging Gaussian beam (see Sec. C.1) instead of a plane wave. The main consequence of beam divergence is that the fringe extent decreases for increasing L , resulting in convergence of minimum and maximum fringe value, denoted respectively by u_{min} and u_{max} (indicated by solid gray lines in Fig. 3.6(b, upper)). For our typical fiber-trampoline separation in the range of $50 - 100 \mu\text{m}$ (see Sec. 3.2.1), the fringe extent, taking into account beam divergence, is significantly smaller than the one predicted by Eq. 3.3 (see Fig. 3.7). We therefore perform the following calibration procedure: First, we coarsely align the fiber on top of the trampoline's central pad, with $L = 50 - 100 \mu\text{m}$ (see Sec. 3.2.1). Subsequently, we change L in steps of $\sim 10 \text{ nm}$ with the goal of recording u_{min} and u_{max} . Based on these parameters and k we define the sinusoidal calibration function

$$\tilde{u}_r(L) = u_{amp} \sin(2kL) + u_{mid}, \quad (3.4)$$

with fringe amplitude u_{amp} and center u_{mid} given respectively by

$$\begin{aligned} u_{amp} &= (u_{max} - u_{min}) / 2 \\ u_{mid} &= (u_{max} + u_{min}) / 2. \end{aligned}$$

The red curves in Fig. 3.6(b) represent \tilde{u}_r/u_{in} (Fig. 3.6(b, upper)) and $d\tilde{u}_r/dL \times \lambda/u_{in}$ (Fig. 3.6(b, lower)). The displacement sensitivity of $\tilde{u}_r(L)$ is maximized at locations L_{mid} where $\tilde{u}_r(L_{mid}) = u_{mid}$ (indicated by green circles in Fig. 3.6). Therefore, after scanning the fringe for u_{min} and u_{max} , we move the fiber to an offset value L_0 within $\approx 50 \text{ nm}$ to L_{mid} , indicated by an offset voltage $u_0 \approx u_{mid}$. This is the initial situation for performing measurements of the trampoline's motion. Note that the relative difference between slope of sine and Airy function at L_{mid} is $\approx 3\%$.

For a trampoline resonator oscillating around its equilibrium position $L_0(t)$, the displace-

ment between fiber and membrane at time t is given by

$$L(t) = L_0(t) + x(t). \quad (3.5)$$

The second term describes the trampoline's oscillatory motion $x(t) \propto \sin(\Omega_m t)$, with mechanical resonance frequency $\Omega_m/2\pi$. The time dependency of $L_0(t)$ is due to intrinsic changes in the fiber-membrane separation through, e.g., thermal drift. The green curve in Fig. 3.6(c) shows a typical $u_0(t)$ trace. Over a time span of 290 minutes, $u_0(t)$ drifts within 0.08 V around $u_{mid} = 0.85$ V, corresponding to a drift in $L_0(t)$ of 74 nm.

Assuming that $x(t) \ll \lambda$, the reflected signal can be approximated as

$$u(t) \approx u_0(t) + \left. \frac{d\tilde{u}_r}{dL} \right|_{L_0(t)} x(t) \equiv u_0(t) + \tilde{u}(t). \quad (3.6)$$

With the measurement setup described in Sec. 3.2.1, we read out $u_0(t)$ and $\tilde{u}(t)$ separately. As a first step, we extract $L_0(t)$ from $u_0(t)$; with Eq. 3.4 we have

$$u_0(t) = u_{amp} \sin[2kL_0(t)] + u_{mid}. \quad (3.7)$$

Solving for $L_0(t)$ yields

$$L_0(t) = \frac{1}{2k} \arcsin \left[\frac{u_0(t) - u_{mid}}{u_{amp}} \right]. \quad (3.8)$$

Substituting this expression in the derivative in Eq. 3.6 gives

$$\begin{aligned} \left. \frac{d\tilde{u}_r}{dL} \right|_{L_0(t)} &= 2ku_{amp} \cos \left\{ \arcsin \left[\frac{u_0(t) - u_{mid}}{u_{amp}} \right] \right\} \\ &= 2ku_{amp} \sqrt{1 - \left[\frac{u_0(t) - u_{mid}}{u_{amp}} \right]^2} \end{aligned}$$

From this expression finally follows the calibrated oscillation amplitude

$$x(t) = \frac{\tilde{u}(t)}{2ku_{amp} \sqrt{1 - \left[\frac{u_0(t) - u_{mid}}{u_{amp}} \right]^2}}. \quad (3.9)$$

3.2.3 Diverging Beam Effects

In Section 3.2.2 we treated the optical field propagating in between fiber and membrane by a one-dimensional transfer matrix model, thereby assuming the wavefronts to be planes. More precisely, the light exiting the single-mode fiber is approximately described by a Gaussian beam [109], which is laterally confined and diverging after the exit of the cleaved fiber end (i.e. the location of the waist). As a consequence, the amount of light coupled back into the fiber, after multiple reflections between fiber and trampoline, is reduced for increasing beam propagation length. In the following, we estimate the effect of beam divergence on the fiber interferometer's displacement sensitivity.

Figure 3.7(a, inset(i)) shows a schematic of the low-finesse cavity formed by fiber tip and trampoline (thickness d), separated by distance L . The lateral mode profile (in xy -plane) of the incident optical field inside the single-mode fiber (Sec. 3.2.1) is approximately described by a Gaussian function [109] (mode field diameter $2w_0 = 10.4 \mu\text{m}$ at 1550 nm, see Appendix C.1)

$$E_{in}(x, y) = \sqrt{\frac{2}{\pi w_0^2}} \exp\left[-\frac{x^2 + y^2}{w_0^2}\right], \quad (3.10)$$

which is normalized so that $P_{in} = \int_{-\infty}^{\infty} dx dy E_{in}^2(x, y) = 1$. The field exiting the fiber is described by a Gaussian beam $E_{00}(x, y, z)$, which is reflected multiple times between fiber and membrane and slightly distorted upon each reflection at either trampoline or fiber-vacuum interface, as discussed in detail in the following.

Propagation of the Gaussian beam in the fiber interferometer can be described with a transfer matrix method, as carried out for optical plane waves in the previous section. As a first step, this requires us to represent the incident field (Eq. 3.10) by its plane wave spectrum, also referred to as angular spectrum [110, 111]. This is done by means of the two-dimensional spatial Fourier transform [112]

$$\tilde{E}_{in}(k_x, k_y) = \frac{1}{2\pi} \int_{-\infty}^{\infty} \int_{-\infty}^{\infty} dx dy E_{in}(x, y) \exp[-i(k_x x + k_y y)],$$

which yields the incident Gaussian Fourier spectrum⁹

$$\tilde{E}_{in}(k_x, k_y; z = 0) = \sqrt{\frac{w_0^2}{2\pi}} \exp \left[-w_0^2 \frac{k_x^2 + k_y^2}{4} \right]. \quad (3.11)$$

This function represents the distribution of plane waves with lateral wave numbers k_x and k_y , forming the Gaussian beam. Therefore, similarly to the case of a single plane wave (Sec. 3.2.2), we can describe propagation, reflection or transmission of this spectrum by multiplying an “optical transfer function”, which generally depends on k_x , k_y (equivalently, angle of propagation with respect to z -axis): Propagation along the z -axis is described by multiplying a phase factor

$$\tilde{E}(k_x, k_y; z) = \tilde{E}(k_x, k_y; z = 0) \exp(ik_z z), \quad (3.12)$$

where the wave vector along the direction of propagation is given by

$$k_z = \sqrt{k^2 - k_x^2 - k_y^2} \approx k - \frac{k_x^2 + k_y^2}{2k}. \quad (3.13)$$

with absolute wave number $k = 2\pi/\lambda$. The approximation is applicable in the paraxial limit which requires $k_x, k_y \ll k$, as is the case for a Gaussian beam [109]. Reflection from or transmission through the interface between fiber (refractive index $n_1 = 1.45$ (see Sec. 3.2.1)) and vacuum/air (refractive index $n_0 = 1.0$) (see Fig. 3.7) is described by multiplication with Fresnel coefficients (see Appendix A.1)

$$\begin{aligned} r_{10}^s &= -r_{01}^s = \frac{k_{1z} - k_{0z}}{k_{1z} + k_{2z}} \\ t_{10}^s &= \frac{k_{0z}}{k_{1z}} t_{10}^s = \frac{2k_{1z}}{k_{1z} + k_{0z}}, \end{aligned}$$

with $k_{1/0z} = kn_{1/0} - (k_x^2 + k_y^2) / (2kn_{1/0})$. The superscript s denotes perpendicular polarization, describing the electric field component that points in the direction perpendicular to the plane of incidence. The opposite case is parallel or p polarization, describing the electric

⁹Making use of the relation $\int_{-\infty}^{\infty} dx \exp(-ax^2 + bx) = \sqrt{\frac{\pi}{a}} \exp(b^2/4a)$. Note that the Fourier transform is unitary (by choice of its prefactor), therefore preserving the normalization $P_{in} = \int_{-\infty}^{\infty} dk_x dk_y E_{in}^2(k_x, k_y) = 1$.

field component that is parallel to the plane of incidence. We found that the results of the following analysis differ only by $\sim 1\%$ between s - and p -polarization, and therefore present only the former case.

The reflection coefficient of the trampoline (modeled as dielectric slab with refractive index $n_2 = 2.0$ (see Sec. 3.2.2), thickness $d = 50$ nm, 100 nm) is given by [113] (see Appendix A.1 for derivation)

$$r_d^s = \frac{(k_{0z}^2 - k_{2z}^2) [1 - \exp(i2kn_2d)]}{(k_{0z} + k_{2z})^2 - (k_{0z} - k_{2z})^2 \exp(i2kn_2d)}.$$

The intra-cavity field \tilde{E}_{cav} in between fiber and trampoline can be calculated by multiplying the incident field with the sum over all possible paths inside the cavity. We multiply t_{10} for initial transmission from fiber into cavity, r_d (r_{10}) for each reflection at membrane (fiber tip), and $\exp(ik_z 2L)$ for each round-trip

$$\begin{aligned} \tilde{E}_{cav} &= t_{10} r_d \exp(ik_z 2L) \sum_{j=1}^{\infty} [r_d r_{10} \exp(ik_z 2L)]^j \tilde{E}_{in} \\ &= \frac{t_{10} r_d \exp(ik_z 2L)}{1 - r_d r_{10} \exp(ik_z 2L)} \tilde{E}_{in} \end{aligned}$$

(note that \tilde{E} -fields and Fresnel coefficients depend on k_x, k_y). The field which is generated inside the fiber by the intra-cavity field can be calculated by projecting \tilde{E}_{cav} on \tilde{E}_{in} [114]

$$\begin{aligned} \tilde{E}_{cav,f}(L) &= t_{01} \int_{-\infty}^{\infty} \int_{-\infty}^{\infty} dk'_x dk'_y \tilde{E}_{cav}(k'_x, k'_y; L) \tilde{E}_{in}^*(k'_x, k'_y) \tilde{E}_{in}(k_x, k_y) \\ &= t_{01} 2\pi \int_0^{\infty} dk'_\rho k'^2_\rho \tilde{E}_{cav}(k'_\rho; L) \tilde{E}_{in}^*(k'_\rho) \tilde{E}_{in}(k_\rho), \end{aligned}$$

where in the last step we have exploited circular symmetry of the fields around the z -axis¹⁰.

The overall reflected field is a superposition of the promptly reflected light at the fiber-vacuum

¹⁰We set $k_\rho^2 = k_x^2 + k_y^2$ and carry out the integration in polar coordinates, thereby treating k_ρ as radial wave number component.

interface and the portion of the intra-cavity field which is coupled back into the fiber

$$\tilde{E}_r(k_\rho; L) = r_{10}\tilde{E}_{in}(k_\rho) + \tilde{E}_{cav,f}(k_\rho; L). \quad (3.14)$$

The reflected intensity is given by

$$P_r(L) = 2\pi \int_0^\infty dk_\rho k_\rho^2 \left| \tilde{E}_r(k_\rho; L) \right|^2. \quad (3.15)$$

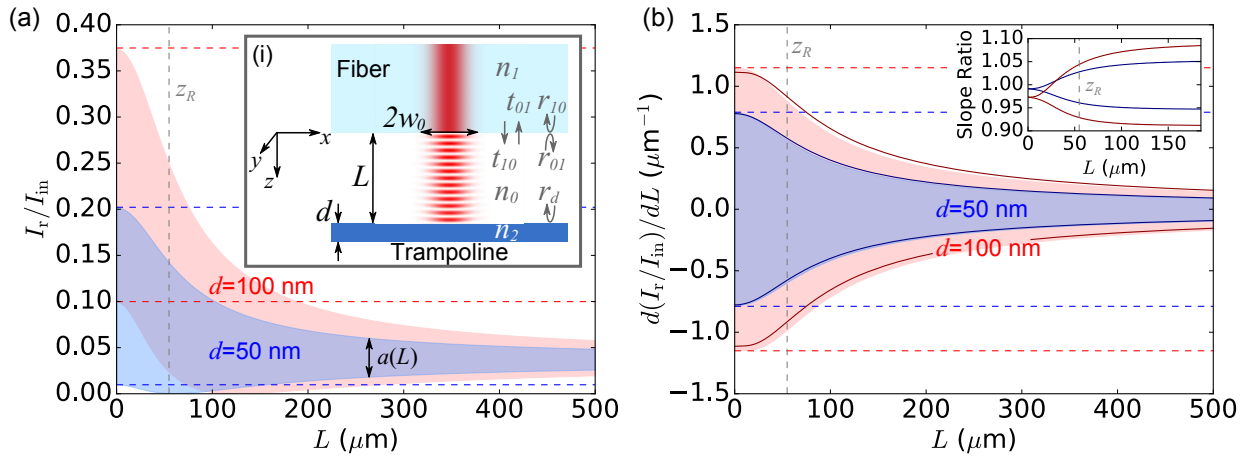


Figure 3.7: Interference fringe and displacement sensitivity for diverging Gaussian beam. (a, inset(i)) Schematic of low-finesse cavity formed by fiber (refractive index $n_1 = 1.45$) tip and trampoline (thickness d , refractive index $n_2 = 2.00$), separated by distance L . Lateral field envelope (xy -plane) inside fiber (red) is described by a Gaussian function (mode field diameter $2w_0 = 10.4 \mu\text{m}$ at wavelength $\lambda = 1550 \text{ nm}$). Field propagating in between fiber and trampoline (red) resembles diverging Gaussian beam. Transmission through (reflection from) fiber-vacuum interface is governed by Fresnel coefficients t_{01} , t_{10} (r_{01} , r_{10}). Reflection coefficient of trampoline is given by r_d . (a) Theoretical prediction for extent of interference fringe $P_r(L)/P_{in}$ for $d = 50 \text{ nm}$ (blue area) and $d = 100 \text{ nm}$ (red area). The distance between upper and lower bound of the fringe is given by $a(L)$. Dashed blue (red) lines mark extent of interference fringe, predicted by plane wave model (Fig. 3.6), for $d = 50 \text{ nm}$ ($d = 100 \text{ nm}$). Gray dashed line indicates Rayleigh range $z_R = 54.8 \mu\text{m}$. (b) Similar to (a), but for displacement sensitivity $d[P_r(L)/P_{in}]/dL$. The solid blue (red) curves show the sinusoidal slope $2\pi a(L)/\lambda$ for $d = 50 \text{ nm}$ ($d = 100 \text{ nm}$). (inset ii) Red (blue) curves represent ratio of predicted sensitivity (outer bounds of colored areas) and sinusoidal slope (solid curves) for $d = 50 \text{ nm}$ ($d = 100 \text{ nm}$).

Figure 3.7(a) shows the extent of the interference fringe $P_r(L)/P_{in}$ (colored areas) for a

fiber interferometer with a 50 nm (blue area) or 100 nm (red area) thick trampoline¹¹. Figure 3.7(b) similarly shows the extent of the fringe's derivative $d[P_r(L)/P_{in}]/dL$, where the outer edges mark the maximum displacement sensitivity for a given fiber trampoline separation. Dashed horizontal lines indicate the extent of $P_r(L)/P_{in}$ (Fig. 3.7(a)) and $d[P_r(L)/P_{in}]/dL$ (Fig. 3.7(b)) predicted by the plane wave model (see Sec. 3.2.2) for $d = 50$ nm (blue) and $d = 100$ nm (red) thick trampoline. For L exceeding a few μm , plane wave and Gaussian beam model clearly deviate from each other; while for sufficiently small L , the fiber-coupled intra-cavity light outweighs the promptly reflected light, causes beam divergence the two portions to be matched eventually. At this point ($L \approx 60 \mu\text{m}$ ($L \approx 120 \mu\text{m}$) for $d = 50$ nm ($d = 100$ nm) thick trampoline), the lower boundary of the fringe reaches zero. When further increasing L , the promptly reflected light becomes the predominant contribution to $P_r(L)/P_{in}$. The dashed vertical line indicates the Rayleigh range of $E_{00}(x, y, z)$. In a similar fashion to the fringe extent, the displacement sensitivity (Fig. 3.7(b)) is clearly reduced with respect to the 1D model, already within z_R .

In the following we discuss the implications of the 2D model on our calibration procedure (Sec. 3.2.3). In our calibration procedure, we measure the difference between minimum and maximum value of the fringe $a(L)$ and employ $a(L) \sin(4\pi L/\lambda)/2$ (up to an offset) as calibration function. The solid blue (red) curves in Fig. 3.7(b) represent the maximum/minimum slope $\pm 2\pi a(L)/\lambda$ of this calibration function in the case of a $d = 50$ nm ($d = 100$ nm) trampoline. Due to the sinusoidal nature of the calibration function, these lines mark a symmetric area with respect to the x-axis, thereby highlighting the asymmetry in the displacement sensitivity arising in the Gaussian beam model. Inset (ii) shows the relative deviation between sinusoidal slope and 2D model for $d = 50$ nm (blue curves) and $d = 100$ nm (red curves). In the former case, the relative deviation converges to within $\pm 6\%$. In the latter case, to within $\pm 9\%$. For $L \approx 0$ the interference fringe is given by an Airy function (see Sec. 3.2.2)

In this section and the previous section we have applied two different optical models to describe the propagation of light in our Fabry-Perot fiber interferometer. The goal of this investigation was, to establish a calibration procedure which enables quantifying the

¹¹The device thicknesses $d = 50$ nm, 100 nm are chosen based on the specs of our fabricated devices; $d = 100$ nm resembles the maximally achievable thickness with our fabrication protocol. The thinnest device characterized in the following section has $d = 44$ nm.

trampoline’s displacement amplitude. Our analysis showed that the reflected signal from the fiber interferometer, in dependence on the fiber-trampoline separation, can be approximately described by a sine with period $\lambda/2$ and an amplitude that is readily measured. The precision provided by this calibration function, with respect to the exact solutions of the employed optical plane wave model (Sec. 3.2.2) and Gaussian beam model (this section), is within 10 % for all devices experimentally characterized in the following section.

3.3 Characterization of Mechanical Resonances

In the following we characterize the mechanical resonances of our Si_3N_4 trampoline resonators (see Sec. 3.1.1). This characterization is based on measuring the trampoline’s nanomechanical oscillations by means of interferometric readout and lock-in demodulation (see Sec. 3.2.1). In Sec. 3.3.1 we identify resonances by applying an oscillatory mechanical drive of swept frequency to the trampoline. The measured resonance frequencies (in the range of 40 – 280 kHz) agree to those predicted by a finite-element simulation (COMSOL) within 1 %. We measure the mechanical ringdown times τ_m of the mode amplitudes corresponding to these resonances and obtain values up to $\tau_m \approx 6$ min for the fundamental out-of-plane mode, corresponding to a mechanical quality factor $Q_m \approx 5 \times 10^7$. In Sec. 3.3.2 we study the trampoline’s thermally driven motion at room temperature and measure a thermal force noise of $16.2 \pm 0.8 \text{ aN}/\sqrt{\text{Hz}}$. The measurements presented in Secs. 3.3.1-3.3.2 are carried out on chips containing 8 trampolines (practical chip size for fabrication, see Sec. 3.1.2). With regard to future integration of the trampolines in a compact cryogenic setup, in Sec. 3.3.3 we cleave chips hosting eight released trampolines into individual devices and subsequently glue the “single-device-chip” at three spots onto a metal mount. We find that Q_m of the glued devices is reduced up to 13 % compared to the values measured before cleaving.

3.3.1 Identifying Mechanical Resonances and Measuring Q_m

In an initial step of characterization, we apply an external drive to the trampoline resonator to excite its mechanical resonances. Hereby, the trampoline chip rests on a metal plate, to which a piezo actuator is installed (see Fig. 3.5). Applying a voltage of swept frequency to

the piezo permits measuring the trampoline's mechanical resonance spectrum.

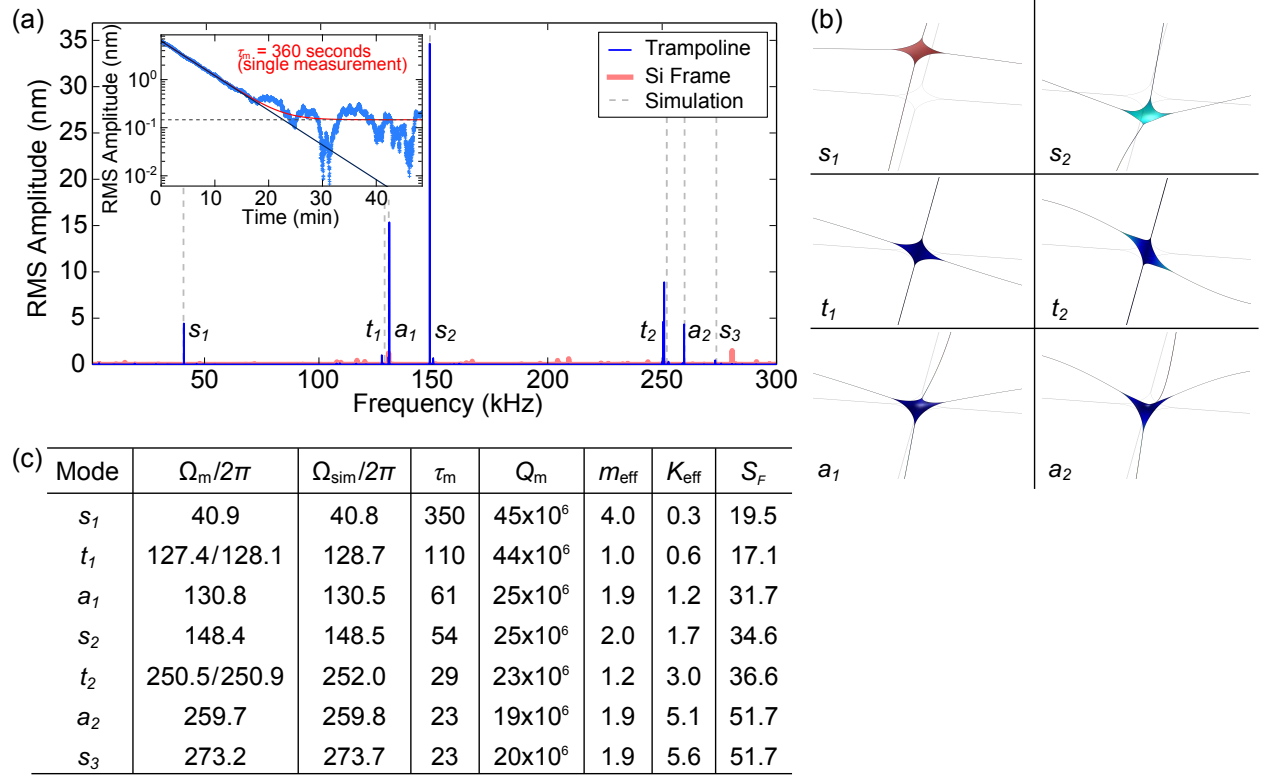


Figure 3.8: Mechanical modes of a trampoline (window size of $w = 3$ mm, central pad width of $d = 100 \mu\text{m}$, tether width of $a = 2.1 \mu\text{m}$, and thickness of 80 nm , see Fig. 3.2) measured with a fiber interferometer operating at wavelength 1550 nm and power $220 \mu\text{W}$. (a) Approximate response to piezo drive, showing first nine resonances (thin blue line). Pink line shows the response of the Si frame. Simulated resonance frequencies (dashed gray lines) agree to within 1 % of measured values with Si_3N_4 parameters density 2700 kg/m^3 , Young's modulus 250 GPa , Poisson ratio 0.23 , and internal stress 0.95 GPa . Inset shows a “typical” ringdown for the fundamental (“symmetric” s_1) mode with fit (red curve) having functional form $\sqrt{(x_0 e^{-t/\tau_m})^2 + x_1^2}$, where x_0 , τ_m , and x_1 are allowed to float. Black line shows the ringdown extrapolated from the early data, and gray dashed line shows x_1 (run-to-run variation by a factor of ~ 2). The ringdown time $\tau_m = 350 \pm 15 \text{ s}$ (error represents statistical fluctuations of multiple measurements) corresponds to a room temperature force noise $\sqrt{S_F} = 19.5 \pm 0.5 \text{ aN/Hz}^{1/2}$. (b) Simulated displacement profiles for the “symmetric” (s_i), “torsional” (t_i) and “antisymmetric” (a_i) modes labeled in (a). (c) Measured frequency $\Omega_m/2\pi$ (kHz), simulated frequency $\Omega_{sim}/2\pi$ (kHz), ringdown time τ_m (s), quality factor Q_m , mass m_{eff} (ng), spring constant K_{eff} (N/m) and force noise $\sqrt{S_F}$ ($\text{aN/Hz}^{1/2}$) for the first 9 modes. The mass has a $\sim 10 \%$ systematic error due to uncertainty in the thickness and density of the nitride.

Figure 3.8(a) shows the amplitude of driven oscillations as a function of frequency for

the fiber positioned over the nitride pad (blue) and silicon frame (pink). Both curves contain many peaks, and several very strong resonances (labeled) emerge whenever the tip is positioned over the pad. There are a few ways to convincingly identify these as trampoline modes, aside from noting their large response. First, they uniformly exhibit significantly larger quality factors $Q_m > 10^7$ (measured by ringdown; see below), whereas supporting frame resonances exhibit low-amplitude peaks of $Q_m < 10^5$. Second, we compare the observed frequencies with those predicted by a finite-element simulation (COMSOL) of our geometry. We simulate the volume of the released nitride in the membrane limit¹², and apply perfectly-clamped boundary conditions along the outer edges of the overhanging nitride. The nitride itself is modeled using the material parameters listed in the caption, and we set its internal stress to 0.95 GPa. The resulting normal mode frequencies are indicated with dashed lines in Fig. 3.8(a), and the corresponding mode shapes are illustrated in Fig. 3.8(b). These parameters reproduce all 9 frequencies of the high- Q_m resonances (i.e. the 7 labeled in Fig. 3.8(a), with twofold degeneracies for the “torsional” modes t_1 and t_2) to within 1 % of the observed values. It is worth noting that some peaks in Fig. 3.8(a) appear artificially small because we did not let the drive dwell on resonance long enough for the mode to ring up; this requires > 10 minutes per point, and small temperature drifts shift the resonance by more than the (sub-mHz) linewidth during this time.

To determine Q_m , we instead perform a mechanical ringdown by suddenly switching off a near-resonant drive and monitoring the amplitude decay. A “typical” ringdown is shown in Fig. 3.8(a, inset), along with an exponential fit (red) for the 40.9-kHz fundamental (“symmetric” s_1) mode. Due to the thermally-driven noise of the mode (visible at the end of the ringdown and discussed in the following section) repeated fit values span $\tau_m = 350 \pm 15$ seconds, corresponding to $Q_m = 45 \pm 2 \times 10^6$. We apply Eq. 3.1 to infer the thermal force noise $\sqrt{S_F} = 19.5 \pm 0.5 \text{ aN/Hz}^{1/2}$.

¹²In the membrane model, the mechanical resonator is treated as two-dimensional sheet in which the elastic restoring force is a sole consequence of in-plane tensile stress σ ; the structure doesn’t have any bending stiffness. The governing equation of motion is the two-dimensional wave equation $\sigma \left(\frac{\partial^2 \zeta}{\partial x^2} + \frac{\partial^2 \zeta}{\partial y^2} \right) = \rho d \frac{\partial^2 \zeta}{\partial t^2}$, with out-of-plane displacement ζ , mass density ρ , and membrane thickness d [103, 115].

w	d	a	$\Omega_m/2\pi$	τ_m	Q_m	m_{eff}	K_{eff}	S_F
375	100	1.4	196.3	8	5×10^6	2.5	3.8	101.8
750	100	1.6	101.9	25	8×10^6	3.0	1.2	62.3
2400	90	2.0	51.5	238	39×10^6	3.7	0.4	22.4
3000	100	2.1	40.9	350	45×10^6	4.0	0.3	19.5

Table 3.3: Frequency $\Omega_m/2\pi$ (kHz), ringdown time τ_m (s), quality factor Q_m effective mass m_{eff} (ng), spring constant K_{eff} (N/m), and force noise S_F (aN/Hz^{1/2}) for the fundamental (s_1) mechanical resonance of trampolines having varied window size w (μm), pad diameter d (μm), and tether width a (μm).

The fit values for the higher-order mechanical modes are listed in Fig. 3.8(c). Of note, the first “torsional” mode t_1 achieves a marginally lower force noise, and may in fact be more useful for some of the classical sensing geometries suggested in Chapter 6. The second “torsional” mode t_2 achieves the highest value of $Q_m f_m \equiv Q_m \Omega_m/2\pi = 5.8 \times 10^{12}$. This is in agreement with the finding that $Q_m f_m$ of a beam resonator typically is maximal for a higher-order mode [116, 96]. For reference, Table 3.3 also lists the properties of the fundamental modes of other trampolines having similar pad diameters d and tether widths a but different window sizes w (see Ref. [39] for additional parameter variations). In agreement with independent studies of beam resonators [94, 91] and trampolines [39], we find larger Q_m for longer tethers.

It is interesting to note that an estimation, presented in Appendix B.2 suggests, that the Q_m s presented here might be partially limited by air damping. A direct measurement of the pressure dependency of Q_m is planned to be carried on future devices.

3.3.2 Thermal Noise Measurement

In the previous section we have measured the trampoline’s oscillation in response to an external drive. From the measured mechanical resonance frequency $\Omega_m/2\pi$ and ringdown time τ_m we inferred the thermal force noise $\sqrt{S_F}$. Here, we directly measure the thermal force noise, by analyzing the trampoline’s thermally-driven motion. This measurement is performed on a device similar to the one of the previous section, having the same lateral dimensions as that of Fig. 3.2 and Fig. 3.8, but with a reduced thickness of 44 nm, owing to a more aggressive HF etch (see Sec. 3.1.2). The fundamental mode frequency $\Omega_m = 2\pi \times 41.4$ kHz, mass $m_{eff} = 2.3$ ng, and ringdown time $\tau_m = 285$ seconds (measurement described in

Sec. 3.3.1) of this device correspond to a thermal force noise of $\sqrt{S_F} = 16.2 \text{ aN/Hz}^{1/2}$ (Eq. 3.1) and root-mean-squared displacement $x_{\text{RMS}} = \sqrt{2k_B T / (m_{\text{eff}} \Omega_m^2)} = 161 \text{ pm}$ (see Sec. B.1), with Boltzmann constant $k_B = 1.38 \times 10^{-23} \text{ m}^2 \text{ kg s}^{-2} \text{ K}^{-1}$ and temperature $T = 293 \text{ K}$.

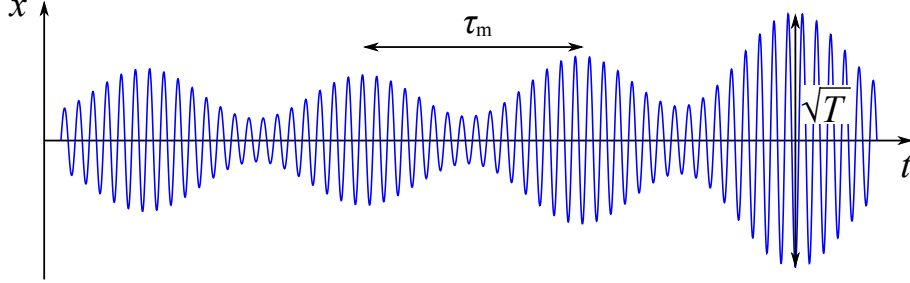


Figure 3.9: Schematic of a mechanical resonator's thermally excited motion (similar to [21]). The resonator oscillates at its resonance frequency $\Omega_m/2\pi$ while its amplitude and phase fluctuate on a time scale set by the mechanical ring-down time τ_m (typically $\tau_m \gg \Omega_m$), with mean amplitude $\propto \sqrt{T}$ at temperature T .

Figure 3.9 qualitatively shows the thermally excited oscillation of a mechanical resonator. The trajectory is given by [117]

$$x(t) = x_0(t) \cos [\Omega_m t + \phi(t)], \quad (3.16)$$

which represents harmonic oscillation at resonance frequency $\Omega_m/2\pi$ with fluctuating amplitude $x_0(t)$ and phase $\phi(t)$. These fluctuations happen on a time scale set by the mechanical ringdown time τ_m and resemble the random nature of the resonator's interaction with its thermal environment (see also Sec. 2.1.2.2). For a resonator at temperature T , the mean value of $x_0(t)$ is given by x_{rms} (Eq. B.5). For pristine nanomechanical resonators, the harmonic oscillation happens at vastly shorter time scales than the fluctuations, e.g. $\Omega_m \tau_m \sim 10^7$ for the trampoline resonator studied here. The thermally driven motion in this case resembles a harmonic oscillation with slowly varying amplitude.

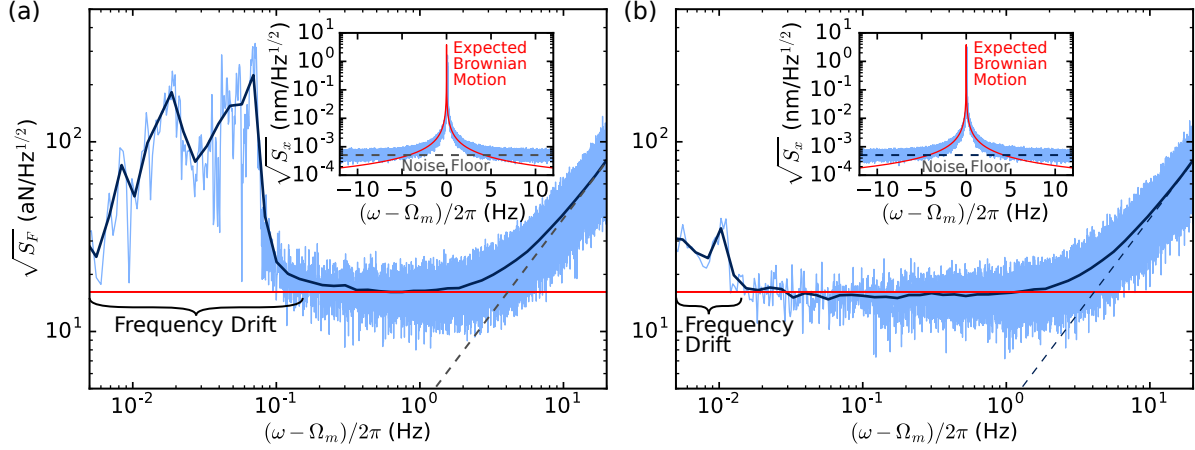


Figure 3.10: Force noise measurement for the s_1 mode of a 44 nm-thick trampoline. (a) Inset shows the displacement noise spectrum $S_{x,\text{obs}}^{1/2}$ (blue) observed for a laser power of 50 μW , along with the spectrum expected for the measured device parameters $S_x^{1/2}$ (red) and the displacement noise floor of the interferometer (dashed, $509 \pm 44 \text{ fm/Hz}^{1/2}$). Main panel shows the force noise spectrum $S_{F,\text{obs}}^{1/2} = (S_{x,\text{obs}} S_F / S_x)^{1/2}$ (blue), consistent (within a $\sim 5\%$ systematic calibration error) with the expected $16.2 \pm 0.8 \text{ aN/Hz}^{1/2}$ (red) over many thousands of linewidths. Dark blue line is the same data “coarsened” by averaging together points within 10% of each other. Dashed line again indicates the displacement noise floor. (b) Same as (a) but with compensation of frequency drift (see text).

Experimentally we characterize the trampoline’s thermally driven motion by means of interferometric readout and lock-in demodulation (see Sec. 3.2.1). As a result we obtain the in-phase and quadrature components, respectively given by (see Sec. B.1 for details)

$$X_1(t)/\sqrt{2} \equiv x_0(t) \cos[\phi(t)]/\sqrt{2}, \quad (3.17)$$

$$X_2(t)/\sqrt{2} \equiv x_0(t) \sin[\phi(t)]/\sqrt{2}. \quad (3.18)$$

Letting the system evolve without drive for 38 hours (56 Hz sampling rate, 25 Hz measurement bandwidth) we observe $x_{\text{rms,obs}} = \sqrt{\langle X_1^2(t) + X_2^2(t) \rangle / 2} = 165 \pm 5 \text{ pm}$ (from Eqs. B.7-B.8), which agrees with the expected value $x_{\text{rms}} = 161 \text{ pm}$ (from Eq. B.5). Figure 3.10(a, inset) shows the displacement noise spectrum $S_{x,\text{obs}}^{1/2} = S_{YY}^{1/2}$ (Eq. B.3), with $Y \equiv [X_1(t) + iX_2(t)]/\sqrt{2}$, for this data (blue data), which follows the expected form [62] (see Sec. 2.1.2.2),

$$S_x = \frac{2\tau_m k_B T}{m_{\text{eff}} \omega_m^2 [1 + (\omega - \omega_m)^2 \tau_m^2]} \quad (3.19)$$

(red curve, not a fit), before the displacement noise floor dominates above ~ 4 Hz from resonance. Since the displacement noise spectrum S_x is just the (white) force noise spectrum S_F (see beginning of this section) “filtered” by the harmonic oscillator susceptibility, we can extract the force noise spectrum $S_{F,\text{obs}}$ by multiplying $S_{x,\text{obs}}$ by the ratio S_F/S_x , the result of which is plotted in the main panel. Note in this plot, we are demodulating just below the mean frequency to show the majority of the power spectrum. Near resonance (within 300 mHz), the noise is limited by drift in the mechanical frequency, and above 300 mHz, we observe a noise floor consistent with S_F over more than thousand mechanical linewidths. This illustrates that these trampolines should present no surprising technical challenges in achieving the inferred sensitivities.¹³ Figure 3.10(b) shows the same as Figure 3.10(a) but with manually compensated frequency drift: We obtain $S_{x,\text{obs}}$ from $X_1(t)$ and $X_2(t)$ by means of a windowed Fourier transform in which we split up the time traces $X_1(t)$ and $X_2(t)$ into N “windows” with 131072 data points (corresponding to 40 min sampling duration) each. For these windows we calculate $S_{x,q}$, with window index $q \in \{1, 2, \dots, N\}$, (see Sec. B.1) and obtain $S_{x,\text{obs}}$ by averaging over all windows $S_{x,\text{obs}} = \sum_{q=1}^N S_{x,q}/N$. Over the duration (~ 40 min) of a window, we typically observe a monotonically increasing or decreasing phase drift. In the case of frequency compensation (Fig. 3.10(b)), we adjust the demodulation frequency post-acquisition by centering the spectrum on the frequency with the largest power at the beginning of each window. This results in reduced frequency drift compared to Fig. 3.10(a) and an increase of 17 % in the frequency range over which $S_{F,\text{obs}}$ is consistent with S_F .

3.3.3 Q_m of Cleaved and Glued Trampoline

With our fabrication protocol presented in Sec. 3.1, we obtain chips of $15\text{ mm} \times 15\text{ mm}$, each hosting eight identical trampoline resonators and an unpatterned area of equal size (see Fig. 3.2). This “9-chip” represents a 3×3 grid of 9 individual “1-chips” of $5\text{ mm} \times 5\text{ mm}$, hosting and individual trampoline or membrane. Whereas the dimensions of the 9-chip are practical for handling during fabrication, is it often desirable to have a 1-chip for installation in an experimental setup. For example, when installing a trampoline chip inside a compact

¹³Note that our fiber interferometer was constructed without any consideration to thermal stability or vibration isolation: devices rest on a piezo stage fixed to a stainless plate; this rests directly on a vacuum flange, and the whole chamber is supported by metal blocks on a work bench (see Sec. 3.2.1).

fiber cavity operated at cryogenic temperatures in a dilution refrigerator. On a first attempt, we manually cleaved a 9-chip, by making scratches (few mm long) with a diamond scribe at both ends of the 9-chip and subsequently applying a torque to the chip to break of a column of three 1-chips from the 9-chip. Both of these steps generated flakes from the chip which contaminated the trampolines, as was observed with an optical microscope. Despite the contamination, none of the devices broke during the cleave, even trampolines with a window size $w = 3\text{ mm}$ (see Fig. 3.2(a)), comparable to the chip size of 5 mm. In order to avoid contamination, we now cover the trampolines with Kapton tape before cleaving. Figure 3.11(a) shows a schematic of this procedure for a chip formed by two 1-chips (left). As a first step, we attach strips of Kapton tape along the 4 outer edges of each trampoline (center). Secondly, we lay a square of Kapton tape across the trampoline, which is attached to the elevated strips, and therefore does not touch the trampoline. After cleaving along the line indicated by “cleave line” (Fig. 3.11), the tape is (readily) peeled off with tweezers.

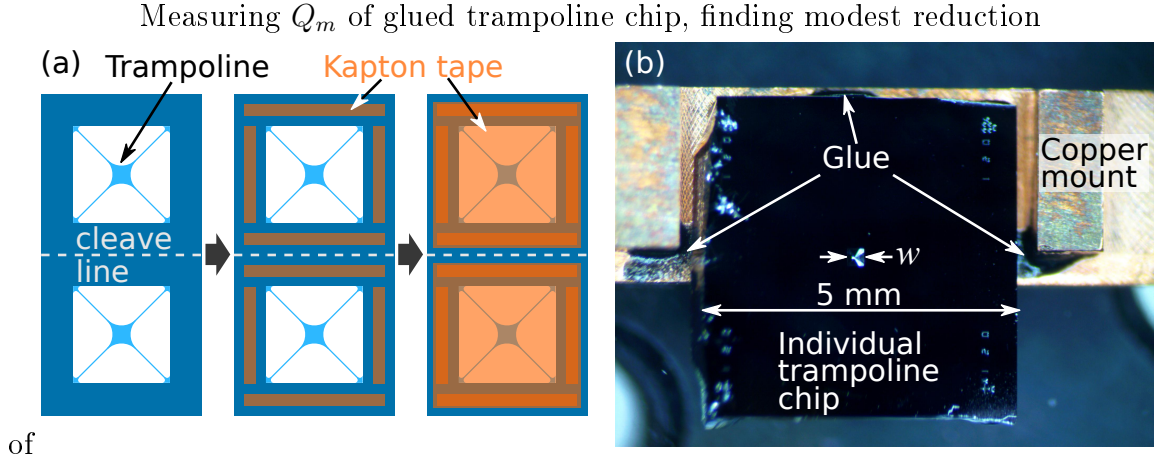


Figure 3.11: Cleaving and gluing of trampoline chips. (a) Left to right: Schematic of chip with two trampolines. Four Kapton tape strips are attached parallel to outer edges of each trampoline. Kapton squares are attached to strips to cover trampolines. (b) Individual trampoline chip (window size $w = 250\text{ }\mu\text{m}$) glued at three spots to a copper mount (image courtesy of Alexey Shkarin, Harris Lab, Yale University).

Figure 3.11(b) shows a 1-chip ($w = 250\text{ }\mu\text{m}$) glued at three spots (black areas, glue: Stycast 2850) to a copper mount.

Dimensions			9-chip		1-chip		1-chip glued	
w	d	a	$\Omega_m/2\pi$	$Q_m (10^6)$	$\Omega_m/2\pi$	$Q_m (10^6)$	$\Omega_m/2\pi$	$Q_m (10^6)$
250	40	1.5	565.4	4.6	564.2	4.6	/	/
			566.1	4.8	565.4	4.5	564.5	3.9
			/	/	564.3	5.3	564.1	4.8
500	40	3.5	343.5	5.6	343.4	5.6	/	/
			343.8	5.0	343.8	5.3	/	/

Table 3.4: Frequency $\Omega_m/2\pi$ (kHz) and quality factor Q_m for the fundamental out of plane (s_1 , see Fig. 3.8) mechanical resonance of trampolines of varied window size w (μm), pad diameter d (μm), and tether width a (μm). (data courtesy of Alexey Shkarin, Harris Lab, Yale University)

In previous studies [42, 94, 59, 92] of the mechanical performance of Si_3N_4 membrane and string resonators, it was found that Q_m , particularly of the fundamental and consecutive low-order modes, significantly degrades (up to $\sim 10^2$ times [42]) when the resonator chip is glued at multiple spots to a support structure. It has been suggested that this might be related to strain introduced in the glued chip [59] or the fact that rigidly connecting the chip to a supporting structure changes the mechanical density of states in such a way, that coupling of the resonator’s high- Q_m resonance to lower- Q_m resonance in its environment is enhanced [94]. Motivated by these findings, we investigate the change in Q_m of the fundamental out-of-plane (s_1 , see Fig. 3.8) trampoline resonance as a consequence of cleaving a 9-chip into a 1-chip and subsequent gluing of the 1-chip at three points to a metal mount. Table 3.4 shows measured $\Omega_m/2\pi$ and Q_m values (see Sec. for measurement details) for uncleaved (“9-chip”), cleaved (“1-chip”), and glued individual chip (“1-chip glued”) devices with varied dimensions of window w , pad d , and tether a (see Fig. 3.2). The Q_m values for 1-chip and 9-chip stay the same in two cases (line1, line4) and change by -6% (line 2) or $+6\%$ (line 5) respectively in one case. The measured Q_m values for the glued trampolines show a decrease of 10% (line 3) and 13% (line 2) with respect to the unglued value.

In conclusion, the 9-chips can readily be split up into 1-chips of $5\text{ mm} \times 5\text{ mm}$ without a significant change in Q_m . Gluing of the chips at three spots to a metal mount, results in a decrease of the Q_m by up to 13% , a moderate loss compared to the 100-times decrease reported for the fundamental mode of a Si_3N_4 membrane [59].

Chapter 4

Vacuum Fabry-Perot Cavity with Incorporated Si_3N_4 Trampoline Resonator

Statement of contribution: Tina Müller, assisted in building the vacuum Fabry-Perot cavity setup, which I designed. Furthermore, she incorporated the trampoline into the cavity and took the data presented in Sec. 4.2.2 which was analyzed by both of us.

After its introduction in 2008 [41], the configuration of a Fabry-Perot cavity with a membrane ($\sim 10\text{--}100$ nm thickness) incorporated close to its center quickly became a generic optomechanical setup [42, 43, 12, 33, 30]. The membrane material of choice, typically, is high-stress Si_3N_4 due to its exceptionally-low mechanical and optical dissipation [42, 43]. While commercially available square membranes (available at, e.g., Norcada, Inc.) have been employed “most commonly”, are more recent efforts aimed toward highly engineered devices with the goal of improving the mechanical performance and increasing the optomechanical coupling strength [49, 50, 51, 52, 53, 54, 1, 39, 55, 56]. In that regard, trampoline resonators (see Sec. 3.1.1) are promising since they offer a mass m which is reduced by orders of magnitudes compared to a square membrane with the same oscillation frequency, thereby enabling increased optomechanical coupling strength ($g_0 \propto 1/\sqrt{m}$, see Sec. 2.2.6).

In this chapter we examine the feasibility of employing a Si_3N_4 trampoline resonator in-

stead of a square membrane in a “membrane-in-the-middle” (MIM) optomechanical setup. In order to suppress a decrease in the trampoline’s mechanical quality factor resulting from its interaction with surrounding gas molecules, our cavity is installed in a vacuum chamber. In Sec. 4.1 we discuss the construction of our vacuum Fabry-Perot cavity with incorporated trampoline and provide details on the trampoline alignment structure. In Sec. 4.2 we characterize the optical resonances of the empty cavity and measure a bare cavity finesse of 20,000. To confirm that our fabrication protocol doesn’t introduce additional optical losses, we incorporate one of our fabricated square membranes in the cavity. We find that, depending on its position, the presence of the membrane increases the measured finesse up to 40,000, as expected for a lossless dielectric slab in a single-port cavity. Finally, we incorporate a trampoline into our cavity for which 0.045% of the light extends over the trampoline’s sidewalls. Consistent with recent simulations [60], we find that the majority of this “clipped” light is, for many trampoline positions along the cavity axis, recovered by the cavity.

4.1 Vacuum Cavity Setup with Trampoline Alignment Structure

Implementations of the “membrane in the middle” (MIM) configuration range from using fiber optical cavities with length $L_c \sim 10 \mu\text{m}$ [84][118] to free-space optical cavities with L_c of a few cm [43, 119]. Here we present the construction (Sec. 4.1.1) of a 5-cm-long vacuum-compatible Fabry-Pérot cavity comprising two piezo-actuator-controlled mirror mounts, which enables in-situ alignment and length change of the cavity while under vacuum. In Sec. 4.1.2 we discuss how to align the Si_3N_4 trampoline with respect to the optical intra-cavity field by means of a manual 5-axis stage and subsequent gluing of the chip into the cavity. In Sec. 4.1.3 we describe the vacuum chamber setup into which the cavity is incorporated.

4.1.1 Cavity Support Structure

Here we present the construction of a vacuum-compatible “membrane in the middle” (MIM) cavity support structure. As this structure is the first of its kind in our lab, we are aiming

for flexibility with regard to achievable cavity lengths, Si_3N_4 structure positions, and deployable mirror substrate diameters. A particular requirement is that, among the possible configurations, should be a cavity with length $L_c \approx 5$ cm. This request has two reasons: First, a few-cm-long cavity together with the trampolines' mechanical resonance frequency $f_m \sim 10$ kHz...100 kHz (see Sec. 3.3.1) and an anticipated cavity finesse of a few 10,000 (see Sec. C.2) enables operation in the resolved-sideband limit (see Sec. 2.2.6). Second, we aim for a small optical mode field diameter (MFD) (see Appendix C.1) to avoid scattering losses of the optical field from the trampoline sidewalls (see Sec. 4.2.2). To achieve small cavity waists (few 10s of μm) with cm-long cavities requires working near the spherical limit $R_c \approx L_c/2$, with mirror radius of curvature R_c . At the time (2012) we bought our mirrors (see Sec. C.2 for details), the smallest available (to our knowledge) radius of curvature was $R_c = 2.5$ cm, hence demanding $L_c \approx 5$ cm for the spherical limit.

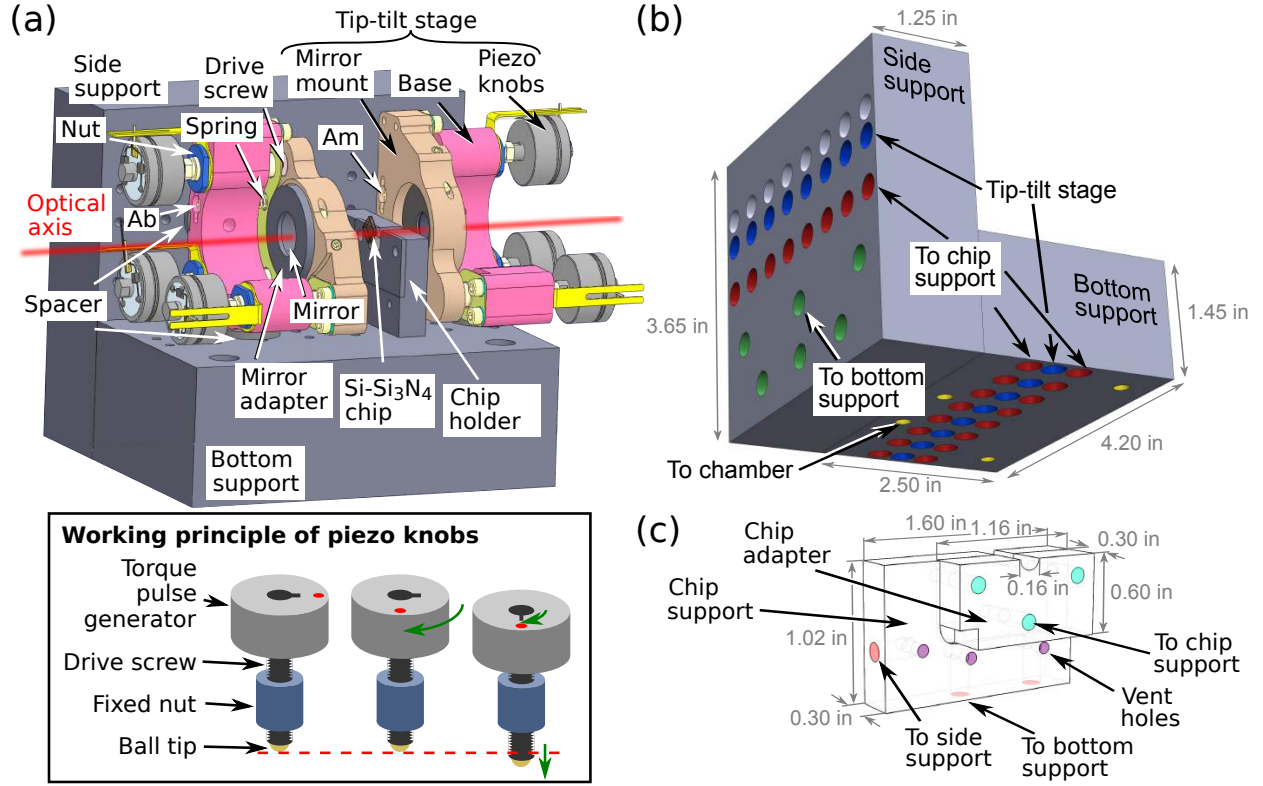


Figure 4.1: Design of vacuum compatible “membrane in the middle” cavity. (a, upper) CAD drawing of the cavity formed by two mirrors, each mounted to a tip-tilt stage (stainless steel and titanium, [Janssen Precision Engineering B.V. \(JPE\) PFOM1](#)) by means of an adapter (stainless steel, outer $\varnothing = 1$ in). Three “piezo knobs” control the tip-tilt of the mirror mount by pushing a drive screw against the spring-loaded mount (spring anchored in mount (Am) and base (Ab)). The base of each tip-tilt stage is fixed to the bottom and side support plates (invar, see (b) for details). This requires the use of spacers (stainless steel) since the piezo knobs extend over the base. In the center of the cavity is a Si-Si₃N₄ mechanical resonator chip aligned with respect to the optical axis (see Sec. 4.1.2) and glued to a holding fixture (see (c) for details). (a, lower) Piezo knobs (JPE CLA2601) comprise a torque pulse generator which performs stick-slip based rotation of a drive screw. (b) Back view of the invar support plates showing colored arrays of through holes (yellow) and counterbores of through holes (blue, red, green, gray); invar side support (4.20 in \times 3.65 in \times 1.25 in) and bottom support (4.20 in \times 1.45 in \times 2.50 in) are screwed together through green, chip holder is fixed through red and tip-tilt stages are mounted through blue. The bottom support is screwed from the top (yellow) to the vacuum chamber (see Sec. 4.1.3). (c) Two-parts chip holder comprising a chip support (0.30 in \times 1.02 in \times 1.60 in) and a chip adapter (0.30 in \times 0.60 in \times 1.16 in) which are connected through turquoise holes. The chip support is mounted through red holes (vented by violet holes) to the invar support plates (see (b)). Semicircular clearance ($\varnothing = 0.16$ in) is centered around intra-cavity optical axis.

Figure 4.1(a, upper) shows a CAD drawing of our cavity design, which at its heart has two

piezo-controlled tip-tilt stages (stainless steel and titanium, [Janssen Precision Engineering B.V.](#) (JPE) PFOM1). Each of the stages comprises a mirror mount a base and three piezo knobs (JPE CLA2601). The mirror mount is spring-loaded with respect to the base by two springs that are anchored in the mirror mount (Am) and in the base (Ab). The tip-tilt is adjusted by three piezo knobs, each pushing a drive screw against the mirror mount. The smallest step size at room temperature is specified by JPE to be 5–25 nm and the maximum travel range as 1.2 cm. This gives us the possibility to both align the cavity and change its length (within ≈ 2.4 cm) by means of an electronic controller (JPE CPSC with CADM, MCM). We make use of this functionality mainly when the cavity is under vacuum (see Sec. [4.1.3](#)), while under ambient conditions we typically rotate the piezo knobs by hand.

The mirror mounts are designed for $\varnothing = 1$ inch mirror substrates which enabled us to build cavities from mirrors with substrate sizes ranging from $\varnothing = 1$ inch (Newport 10CV00SR.70F, Layertec 109501¹) to $\varnothing = 0.3$ inch, 0.5 inch (Advanced Thin Films, see Sec. [C.2](#)). To install $\varnothing < 1$ inch mirrors we use adapters (stainless steel, machined in the McGill physics department machine shop based on Thorlabs AD1²).

Each of the two tip-tilt stages is mounted by its base to a bottom and a side support plate (invar). This requires the use of spacers (stainless steel, 0.1 in thickness) in between base and bottom support, since the piezo knobs laterally (perpendicular to optical axis) extend over the base³. Halfway in between the tip-tilt stages is a holding fixture installed to the support plates to which the Si-Si₃N₄ resonator chip is glued. Figure [4.1.1\(b\)](#) shows a back view of the support structure with color coded mounting through-holes; they are used for (according to sequence of assembly): Connecting side to bottom support plate (green), mounting tip-tilt stages (blue), mounting chip holder (red), and installing assembled cavity to vacuum chamber (yellow, see Sec. [4.1.3](#)). Here green, blue, and red are counterbores (screw is inserted from depicted side) whereas yellow is just the through-hole (screw is inserted from the cavity side, see Fig. [4.2](#)). When connecting the support plates we tighten the six screws iteratively, since

¹not recommended due to optical losses

²To increase stability, we recommend using a "clamp" style adapter and / or epoxy to more rigidly fix the mirror in place.

³Note this is a prototyping cavity. For a real adjustable cavity (once the desired length is known), we recommend machining extra space into the invar support to accommodate the knobs, removing the need for these spacers.

they over-constrain the connection. Equally we tighten the screws iteratively when installing the tip-tilt stages and the chip holder. The eight slots in the support structure for both the tip-tilt stages and the chip holder enable a variety of cavity lengths ranging from ≈ 10 cm (requires reversing tip-tilt stages so that piezo knobs point toward chip) to submillimeter (requires specifically designed mirror adapters).

The bottom plate (dimensions 4.2 in \times 2.5 in \times 1.45 in) and the side plate (dimensions 4.2 in \times 1.25 in \times 3.65 in) (machined in the machine shop of the McGill Physics department) are made out of invar, which features a ~ 10 times lower thermal expansion coefficient than common stainless steels, such as type 304 or 316, thereby reducing cavity length changes due to temperature drift.

Figure 4.1(c) shows the chip holding fixture comprising a chip support (dimensions 0.30 in \times 1.02 in \times 1.60 in) and a chip adapter (dimensions 0.30 in \times 0.60 in \times 1.16 in) (both stainless steel) which are screwed together (turquoise holes). The chip support is mounted to the invar support (red holes, vented by violet holes). The structure is designed so that the optical axis goes through the center of the semicircular clearance ($\varnothing = 0.16$ in) on top of both components. After alignment with the optical intra-cavity field (see Sec. 4.1.2) the chip is glued to the chip adapter. The two-parts construction provides flexibility with regard to exchanging the chip or changing the chip position within the cavity, both of which can be readily conducted by exchanging the chip adapter without the need to take out the cavity of the vacuum chamber to exchange the chip support.

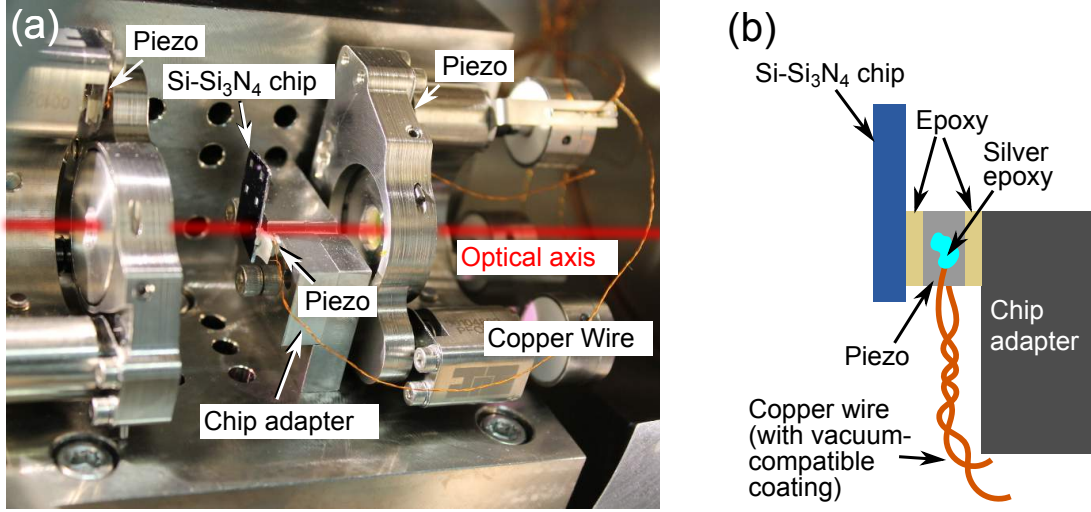


Figure 4.2: Vacuum “membrane in the middle” cavity as built in our lab. (a) In addition to the components described in Fig. 4.1, there is a piezo actuator (Noliac NAC2002) positioned between one drive screw and contact point of each mirror mount. This enables us to measure the cavity photon lifetime based on rapidly sweeping the cavity length [120] (see Sec. 4.2). The Si-Si₃N₄ mechanical resonator chip is glued to a piezo actuator (Noliac NAC2002) which in turn is glued to the chip adapter (see (b) for details). The piezo moves the chip along the optical axis to characterize the Si₃N₄ structure dependent optical cavity resonances (see Sec. 4.2.2). The three piezo actuators and the 6 piezo knobs are contacted by copper wires. (b) Sketch of the interconnection between chip adapter and Si-Si₃N₄ chip (not to scale). The connections between chip, alumina sheet, piezo and chip adapter are made with vacuum compatible, electrically non-conducting epoxy (Lesker Torr Seal). We electrically contact the piezo by means of two copper wires and silver epoxy (Epo-Tek H20E).

Figure 4.2(a) shows the assembled cavity (based on design presented in Fig. 4.1). In addition to the components shown in Fig. 4.1 we have installed a piezo actuator (Noliac NAC2002) between one drive screw and contact point of each mirror mount. The maximum free stroke of these piezos is specified by Noliac to be 3 μm and their unloaded resonance frequency as $> 486 \text{ kHz}$. We use these piezos to measure the cavity lifetime by rapidly sweeping the cavity length [120] (see Sec. 4.2.1). The piezo knobs’ specified (by JPE) maximum velocity of 15 $\mu\text{m/s}$ is not sufficient since we require a sweep velocity of 44 $\mu\text{m/s}$ in our photon lifetime measurements (see Sec. 4.2.1). We glue the mechanical resonator chip to the same kind of piezo (Noliac NAC2002), which is attached to the chip adapter; moving the chip along the optical axis enables us to characterize the dependency of the optical cavity resonances on the Si₃N₄ structure position within the cavity (see Sec. 4.2.2). The three piezo actuators

and six piezo knobs are each electrically contacted by a pair of twisted copper wires which are connected by means of electrically conducting, vacuum-compatible silver epoxy (Epo-Tek H20E). A schematic of the interconnection between mechanical resonator chip, piezo and chip adapter is shown in Fig. 4.2(b); all components are glued together by means of electrically non-conducting, vacuum-compatible epoxy (Lesker Torr Seal). The twisted copper wires are glued (Epo-Tek H20E) to the electrical contacts of the piezo, which are located on the sides parallel to the stroke direction.

4.1.2 Trampoline Alignment Structure

A crucial step in assembling a membrane in the middle (MIM) setup is the alignment of the membrane with respect to the intra-cavity optical field. Two main goals, hereby, are to avoid optical mode mixing, caused, e.g., by a tilt of the membrane with respect to the wavefronts [43, 80], and to optimize optomechanical coupling by maximizing the overlap of optical intensity profile (TEM00 with Gaussian mode profile, see Appendix C.1) and mechanical displacement mode profile. In the present case, where a trampoline resonator is aligned inside the cavity, we wish to achieve maximal overlap of the optical mode with the fundamental out-of-plane mechanical mode (see Fig. 3.8). This requires laterally (normal to cavity axis) centering the intra-cavity mode profile on the trampoline’s central pad (see Fig. 3.2). Aligning the trampoline parallel to the wavefronts inside the cavity relies on control over its position along the cavity axis, to place it within a few wavelengths (1550 nm) of the cavity waist, where the wavefronts are planar. Furthermore, this requires the ability to directly adjust the trampoline, tilt with respect to the wavefronts.

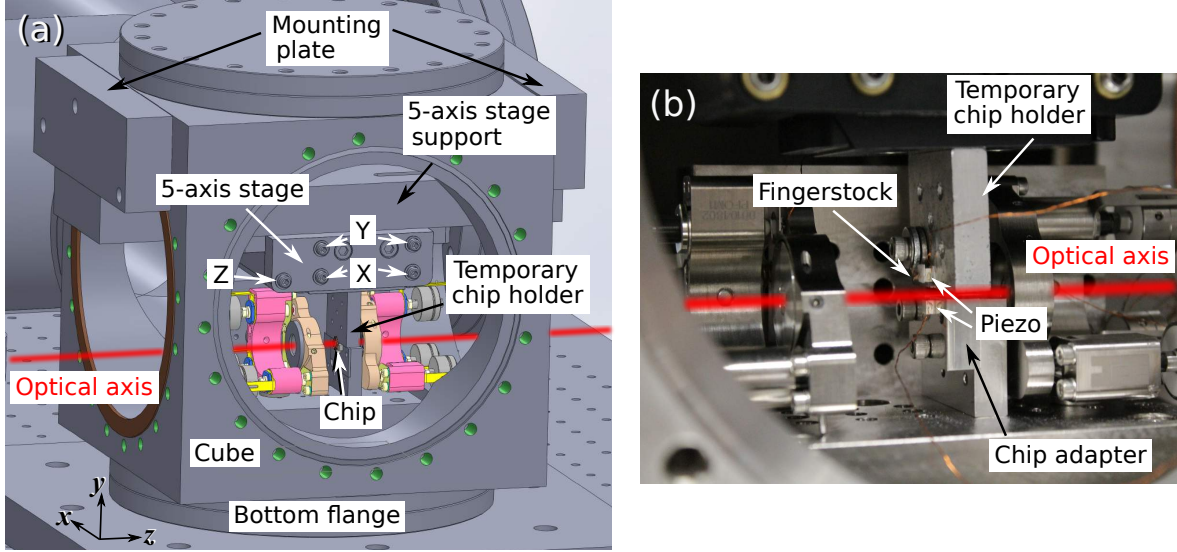


Figure 4.3: Cavity inside vacuum chamber with chip alignment structure. (a) CAD drawing showing the cavity setup (see Fig. 4.1) installed on the bottom flange of a vacuum cube (stainless steel, edge length 8 in, LDS Vacuum Products, Inc. Conflat Cube). We mount and align a mechanical resonator chip into the cavity by means of a manual five axis stage (Newport 9081) in combination with a temporary chip holder (aluminum). The five axis stage is connected to the cube by a horizontal support plate and two vertical mounting plates (both aluminum). Turning both X (Y) screws equal amounts in the same direction results in translation along the x -axis (y -axis). Turning the X (Y) screws in opposite directions tilts the stage around the y -axis (x -axis). Turning the Z screw causes translation along the optical axis. (b) Close-up of cavity and alignment structure inside the cube. During alignment, a beryllium copper fingerstock clamps down the mechanical resonator chip to a piezo (Noliac NAC2002) which is a part of the temporary chip holder. With this piezo we move the Si_3N_4 structure along the optical axis to verify its alignment with respect to the optical intra-cavity field (see Sec. 4.2.2). Once aligned the chip is glued (Lesker Torr Seal) to the piezo (Noliac NAC2002) of the cavity chip support (see Fig. 4.2(b)).

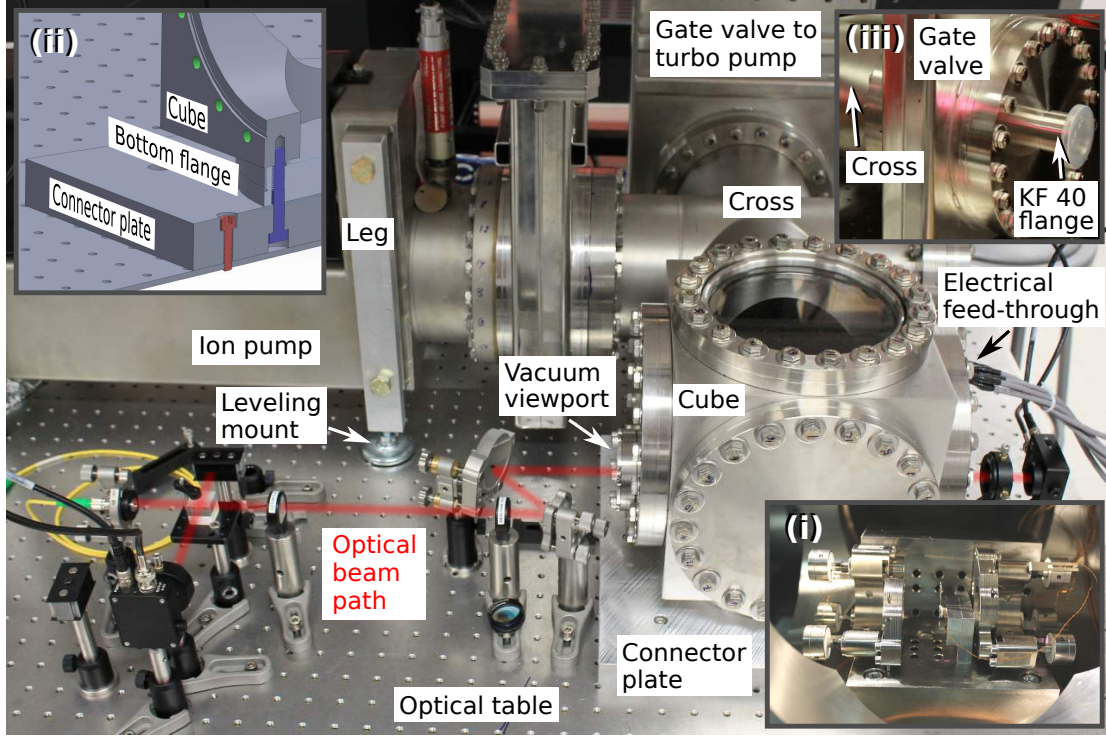
Figure 4.3(a) shows a CAD drawing of the cavity (see Sec. 4.1.1) inside a vacuum cube (stainless steel, edge length 8 in, LDS Vacuum Products, Inc. Conflat Cube) together with the chip alignment structure. In order to align the trampoline chip we use a manual five-axis stage (Newport 9081) with a temporary chip holder (similar to chip support, see Fig. 4.1.1). The stage allows translation along x , y , and z with a travel range of 3 mm and rotation around x and y with an angular range of 8° . The stage is adjusted by manually turning its five set screws: Turning both X (Y) screws equal amounts in the same direction results in translation along x (y). Turning the X (Y) screws in opposite directions tilts the stage around y (x). Turning the Z screw causes translation along the optical axis (z). To incorporate the

stage into the cube we first install a horizontal support plate by means of two mounting plates to the left and the right side of the cube. Then we hang the stage upside-down from the horizontal support plate.

Figure 4.3(b) shows a close-up of the five-axis stage installed above the cavity. During alignment the mechanical resonator chip is clamped by fingerstock down to a piezo (Noliac NAC2002) which is attached to the temporary chip holder (similar to Fig. 4.2(b)). The piezo perpetually moves the trampoline back and forth along the optical axis while we monitor the optical cavity resonance spectrum in real time (see Sec. 4.2.2). Comparing the observed spectrum with the theoretically predicted one allows for the identification and compensation of tilt between trampoline and optical axis. Similarly we analyze and adjust the centering of the trampoline's central pad with the optical field. Once the trampoline is aligned, we glue (Lesker Torr Seal) the chip to the chip adapter's piezo. Subsequently, we let the glue cure under ambient conditions for a few days. When the curing is completed we dismantle the chip alignment structure in the following way: As a first step we remove the fingerstock and retract the five-axis stage with temporary chip support. As a second step we take out the five axis stage of the cube. Finally, we remove the five-axis stage support and the mounting plates from the cube. At this point, the trampoline is aligned and mounted inside the cavity and the vacuum chamber can be closed (see following section). Fine adjustments to the tip and tilt of the cavity mode (relative to the trampoline) can then be made in situ with the mirror mounts.

4.1.3 Vacuum Chamber

In Sec. 2.2.6 we have introduced the single-photon cooperativity C_0 as a figure of merit for controlling the trajectory of, e.g., one of our Si_3N_4 trampoline resonators, with extremely small amounts of light, on the order of a single cavity photon (on average). In order to enable high C_0 (figure of merit for optomechanical interaction, see Sec. 2.2.6) we need to install our cavity with incorporated trampoline into a vacuum chamber. This is because the interaction of the trampoline with surrounding gas molecules damps its mechanical motion (see Appendix B.2) and causes a decrease of its mechanical quality factor Q_m , where $C_0 \propto Q_m$ (from Eqs. 2.101, 2.11).



Cavity vacuum chamber installed on optical table. At the heart of the vacuum chamber is a conflat cube (stainless steel, edge length 8 in) in which the cavity (inset (i)) is attached to the bottom conflat flange (inset (ii)). The cavity is optically addressed through two anti-reflection-coated (designed for $\lambda = 1550$ nm) vacuum viewports by means of an optical probing setup (beam path shown, see Sec. 4.2.1 for details). The cavity mirror mounts and piezo actuators (see Sec. 4.1) are electrically contacted through a D-subminiature feedthrough (25 gold-plated pins). Inset (ii) shows the cube fixed to the optical table by means of a connector plate (aluminum): First, we fix the connector plate through the bottom flange to the cube (violet screw). Second, we install the connector plate to the optical table (red screw). We evacuate the chamber by means of a turbo pump with integrated roughing pump (Pfeiffer HiCube ECO) and an ion pump (Varian RVA-140-DD-M). Both pumps are linked to the cube via a cross and each can be connected or disconnected by opening or closing a gate valve. The ion pump stands on the optical table, supported by legs (aluminum) and leveling mounts (steel, rubber). The turbo pump stands on the floor and is connected to the gate valve (see inset (iii)) through a KF 40 flange and a vacuum bellows.

In view of future optomechanics experiments, we constructed the vacuum chamber presented in Fig. 4.1.3, where the cavity is installed into a conflat cube (inset (i), Sec. 4.1.1). The cube is fixed to an optical table (inset (ii)) by means of a connector plate (aluminum) in two steps: first, the connector plate is attached to the cube through the bottom flange (violet screw); second, the connector plate with cube is mounted to the optical table (red screw). Furthermore, the vacuum system comprises an ion pump (Varian RVA-140-DD-M)

which is connected to the cube through a conflat cross (8 inch) and a gate valve (8 inch). The ion pump stands on the optical table, supported by legs (aluminum) and leveling mounts (McMaster-Carr 6167K19). The leveling mounts are screwed into the legs and permit fine adjustment of the ion pump’s height before installing it to the cross. We connect a turbo pump with integrated roughing pump (Pfeiffer HiCube ECO) to the second gate valve installed to the cross through a KF 40 flange (see inset (iii)) and a stainless vacuum bellows (length 1 m); the turbo pump typically stands on the lab floor. In order to establish vacuum in the chamber we first pump down with the turbo pump until a pressure $< 10^{-6}$ Torr (measured at the input of the turbo pump) is reached, which takes about 12 hours. At this point we turn on the ion pump (or open its gate valve if it is already running and under vacuum) and subsequently disconnect the turbo pump from the chamber by closing its gate valve and switching it off. This is the “vacuum operation mode” which after a few days of operation reaches a base pressure of typically $\approx 10^{-8}$ Torr (measured at the ion pump with the Ultek 60-154 ion pump controller). This base pressure is achieved without baking the chamber or any of the cavity constituents. Our main precautions with respect to achieving a low base pressure are the use of vacuum compatible materials, mainly stainless steel (type 304, type 316) and invar (see Sec. 4.1.1), and thorough cleaning of the components prior to their installation in the vacuum chamber. Components bought from vacuum product retailers/manufacturers (LDS Vacuum Products, Kurt J. Lesker Company) are wiped down with acetone and isopropanol. Custom parts that were specifically machined (McGill physics department machine shop, Proto Labs) are cleaned according to the following sequence: washing with water and soap, wiping down with acetone and isopropanol; sonication in acetone bath, rinsing with acetone and isopropanol, cleaning threaded holes with cleanroom compatible swabs soaked in acetone/isopropanol, final wipe-down with acetone then isopropanol.

Installed on the left and the right side of the cube are two custom-made conflat flanges (8 inch, Accu-Glass Products), both featuring an anti-reflection-coated vacuum viewport which provides optical access to the cavity (beam path of optical probing setup shown, see Sec. 4.2.1 for details). Additionally, installed to the right flange is an electrical feedthrough (D-subminiature, 25 gold-plated pins) through which we connect the electronic cavity components (see Sec. 4.1.1).

4.2 Optical Characterization

Here we characterize the optical resonances of a Fabry-Perot cavity with incorporated trampoline resonator. With regard to realizing a high single-photon cooperativity C_0 (a figure of merit for how strongly light on single-photon level affects the mechanical resonator’s trajectory, see Sec. 2.2.6), we investigate how the presence of the trampoline affects the cavity finesse \mathcal{F} ($C_0 \propto \mathcal{F}$, Eq. 2.101).

In Sec. 4.2.2 we discuss the optical components of our Fabry-Perot cavity setup and the measurement of the empty cavity’s finesse, with a resulting value of $\mathcal{F} = 20,000$. To verify whether our fabrication protocol introduces additional optical loss, in Sec. 4.2.2 we incorporate one of our fabricated extended membranes into the cavity. Depending on the membrane’s position we measure a finesse up to 40,000, which agrees with the predictions of a lossless optical model. Finally, to set an approximate upper bound on the size of the cavity field required for high-finesse applications, we position a trampoline in a cavity field wide enough that 0.045 % of the light falls outside the structure. Consistent with recent simulations [60], we find that the majority of this “clipped” light is, in many cases, recovered by the cavity.

4.2.1 Optical Setup & Empty Cavity Finesse Measurement

The most sensitive way to estimate small optical losses associated with our fabricated structures is to position them inside a cavity and measure their effect on the finesse. Figure 4.4 shows a schematic of the cavity setup: two high-reflectivity mirrors (2.5 cm radius of curvature) form a Fabry-Pérot cavity of length $L_c = 4.7$ cm, which, at our operating wavelength $\lambda = 1550$ nm, yields a fundamental transverse electromagnetic mode (TEM_{00} , see Appendix C.1 for details on cavity eigenmodes) diameter $2w_0 = 110 \mu\text{m}$ and a free spectral range $\text{FSR} = 3.2$ GHz. The input mirror (left-hand) is designed (see Appendix C.2 for a description of how we tune a mirror’s reflectivity by etching away layers from its dielectric coating) to have a “modest” reflectivity of ≈ 0.9997 while the “backstop” (right-hand) mirror reflectivity exceeds 0.999993, forcing the majority of cavity light to exit through the input mirror. We probe the cavity by shining laser light on the input mirror and measuring the op-

tical signals reflected and transmitted by the cavity. Efficient coupling of the incoming laser beam to the TEM₀₀ cavity mode is realized by means of a collecting lens, a diffusing lens, and two adjustable silver mirrors (see caption of Fig. 4.4 for details). We sweep the cavity length L_c to scan for optical resonances by applying a 45 ms linear voltage ramp $V_c(t)$ from 0 to 60 V to a piezo actuator positioned between one drive screw and contact point of each mirror mount. This compresses the cavity symmetrically about the waist by $\Delta L_c \sim 2 \mu\text{m}$ corresponding to roughly ~ 2.5 free spectral ranges. Note this actuation method tilts the end mirrors by ~ 0.01 degrees over the full sweep range, corresponding to a $\sim 4 \mu\text{m}$ shift in the location of the cavity waist for this radius of curvature. The piezo voltage V_c is supplied by a data acquisition (DAQ) module (National Instruments PXI-6115) in combination with a homemade inverting voltage amplifier ($\times -20$).

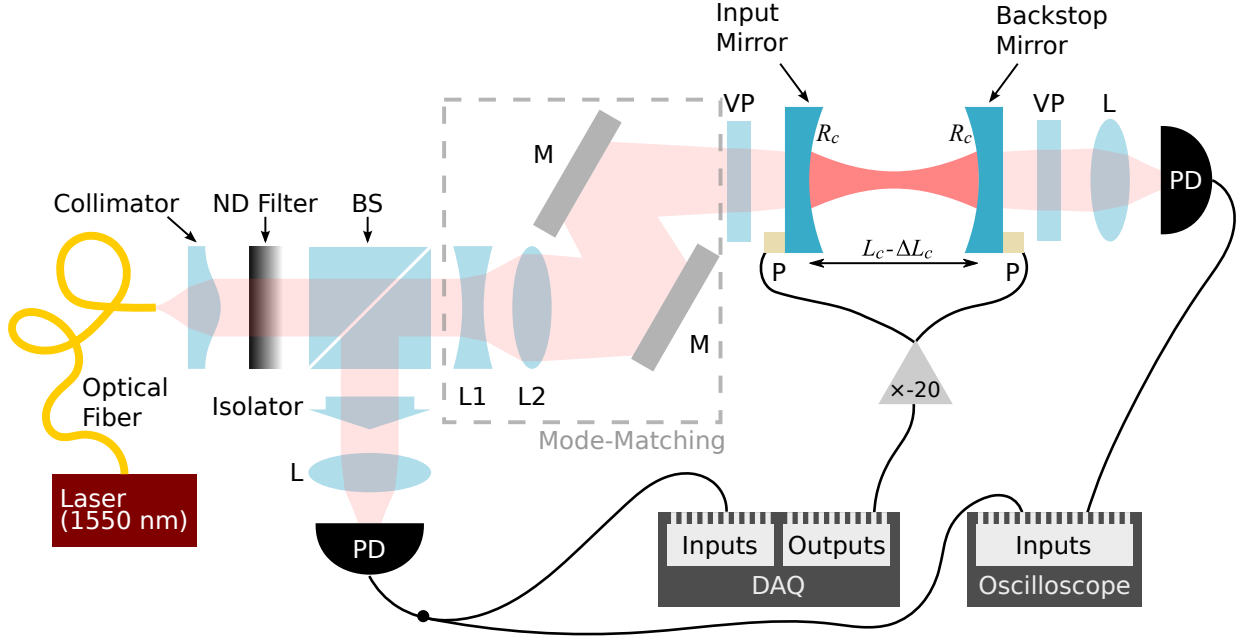


Figure 4.4: Light from a fiber coupled laser (wavelength 1550 nm, power 40 mW, linewidth ~ 200 Hz) is collimated ($1/e^2$ intensity beam diameter 3 mm) and passes through an adjustable neutral density (ND) filter, a 50:50 beam splitter (BS), mode-matching lenses L1, L2 (-10 cm and 15 cm focal length, separated by 19 cm) mirrors M, and an anti-reflection-coated vacuum viewport (VP) before landing on a cavity formed by an input mirror (32 cm from L2) of reflectivity $|r_i|^2 \approx 0.9997$ and a “backstop” mirror of reflectivity $|r_b|^2 > 0.999993$. The radius of curvature of both mirrors is $R_c = 2.5$ cm. Light reflected from the cavity passes through an optical isolator and is focused on a photodiode (PD, 150 MHz bandwidth) by a 3 cm focal length lens. The transmitted light passes through an anti-reflection-coated vacuum viewport and is focused on a photodiode (150 MHz bandwidth) by a 3 cm focal length lens. The PD voltages are monitored on an oscilloscope and the reflected light is recorded on a data acquisition (DAQ) module. The cavity length L_c is swept symmetrically about the waist by applying a voltage to the mirror piezo actuators (P) which compresses the cavity by ΔL_c . The voltages are generated by the DAQ module and amplified by a low-noise, high-voltage amplifier (designs available upon request) of voltage gain ≈ -20 .

Figure 4.5(a) shows the reflected optical power from the cavity, recorded by the DAQ module and normalized with respect to the off-resonance value (corresponding to all light being promptly reflected by the input mirror), for a typical cavity length sweep of a reasonably well-aligned empty cavity. The data (solid blue line) shows a pattern of dips repeated three times, once for each free spectral range. When well-aligned, the largest dip is the TEM_{00} mode, as verified by an image of its spatial profile viewed on the transmission side by an infrared camera (not shown). We can also corroborate these observations by predicting the

locations of the TEM resonances $\Delta V_{lmn} = a\Delta L_{lmn} + b$, where

$$\Delta L_{lmn} = \frac{\lambda}{2\pi} \left[l\pi + 2(m+n+1) \arctan \left(\frac{1}{\sqrt{2R_c/L_c - 1}} \right) \right] \quad (4.1)$$

are the expected resonance lengths of our cavity⁴ (see Appendix C.1 for derivation) which are transformed to voltages by coefficients a and b . The dashed lines in Fig. 4.5(a) represent the expected peak positions ΔV_{lmn} for cavity parameters $R_c = 2.5$ cm, $L_c = 4.87$ cm, mode orders $l = 0...5$ (relative to $l_0 \sim 63,000$), $m+n = 0...4$, and coefficients $a = -27.1$ V/ μ m, $b = 127.0$ V.

The slight mismatch between observed and expected resonance positions is most likely a consequence of piezo nonlinearities, which result in a nonlinear relation between cavity length change and piezo voltage $\Delta L_c(V_c)$. We determine $\Delta L_c(V_c)$ (see Fig. 4.5(b)) by fitting a fourth order polynomial to the measured resonance voltages under the condition that TEM modes of consecutive transverse order $m+n$ are separated by a constant value and consecutive longitudinal modes are separated by $\lambda/2 = 775$ nm (see Eq. 4.1). The dashed gray line is plotted to illustrate the deviation of the measured piezo expansion from ideal linear behavior. The fit residuals are randomly distributed between -4 nm and 4 nm which is ~ 10 times higher than the RMS L_c noise observed in a similar cavity of fixed length⁵ [2].

⁴For perfectly circular (and non-birefringent) cavity mirrors, the resonance spectrum is degenerate in m, n . In practice this degeneracy is usually lifted due to slightly elliptic cavity mirrors and / or birefringence in the mirror or cavity materials, resulting in a small splitting between the TEM_{mn} and TEM_{nm} modes (typically a fraction of the splitting between neighboring TEM modes for a cavity of our dimension [43]). Therefore, another way to discern the TEM₀₀ modes from higher order TEM_{mn} modes is to zoom in on the peaks in Fig. 4.5 and check for a splitting.

⁵The sawtooth voltage ramp applied to sweep the cavity length is composed of a spectrum of sinusoidal tones that act as mechanical drive on the mirror mounts; the increased L_c noise is consistent with resulting mirror oscillations. For sensitive sweeps, we now recommend driving with a continuous sine, so that there is exactly one frequency applied to the mounts and a steady state can be achieved. For the cavity characterization presented in the following sections the demonstrated L_c stability of 5 nm is sufficient.

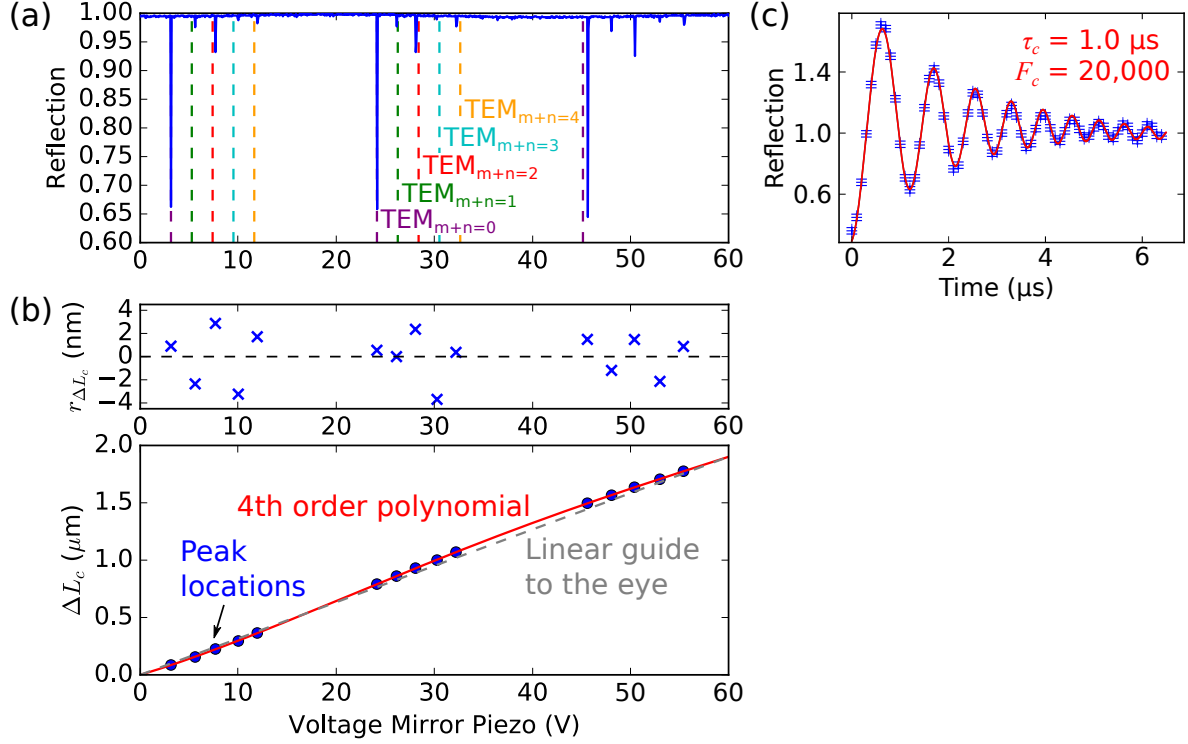


Figure 4.5: Characterization of empty cavity resonances. (a) Reflected optical power from the cavity (normalized by the off-resonance signal) as a function of the voltage (45 ms linear voltage ramp $V_c(t)$ from 0 to 60 V) applied to the mirror piezo actuators. Dashed lines represent expected resonance positions of TEM modes of longitudinal mode order $l = 0 \dots 5$ (relative to $l_0 \sim 63,000$) and transverse mode order $m+n = 0 \dots 4$ for mirror radius of curvature $R_c = 2.5$ cm and cavity length $L_c = 4.87$ cm. (b, lower) Cavity length change ΔL_c as a function of the voltage applied to the mirror piezos. The red curve is obtained by requiring that all transverse modes within a subset are equally spaced and that adjacent transverse modes of the same order are separated by $\lambda/2 = 775$ nm. (b, upper) Fit residuals representing the difference between measured positions and the fitted curve show no obvious signs of systematics. (c) Ringdown of the cavity's reflected power (normalized by the off-resonance value): After passing through resonance, light exiting the cavity beats with the prompt reflection, resulting in power fluctuations [120] $ae^{-t/2\tau_c} \cos[(\omega_0 + bt)t + c]$ for fit (red curve) parameters a , ω_0 , b , c , and power ringdown time $\tau_c = 1.00 \pm 0.05 \mu\text{s}$ (finesse $\mathcal{F} = 20,100 \pm 1,000$; error represents statistical fluctuations of multiple measurements).

In view of future optomechanics experiments we are interested in the time the photons spend inside the cavity, the so called “photon lifetime” τ_c , which is proportional to the cavity finesse $\mathcal{F} = \pi c \tau_c / L_c$ (see Sec. 2.2.2). We measure τ_c by sweeping through the resonance faster than its lifetime [120] resulting in the sinusoidal ringdown signal presented in Fig. 4.5(b) for the TEM_{00} mode.

The signal beats at the frequency difference between the promptly reflected light from the cavity input mirror and the light exiting the cavity which was Doppler shifted in frequency as a consequence of multiple reflections from the moving cavity mirrors. The extracted bare cavity photon lifetime is $\tau_c = 1.00 \pm 0.05 \mu\text{s}$ corresponding to $\mathcal{F} = 20,000 \pm 1,000$. Note that the mirrors, as purchased, nominally achieve finesse $\sim 1,000,000$ (see Sec. C.2 for details on tuning the mirror reflectivity).

4.2.2 Cavity with Incorporated Trampoline

While the high mechanical performance of the trampolines presented in Chapter 3 makes them excellent candidates for mechanical sensing and dissipation studies, we also wish to use them for precision interferometry and optomechanics experiments. To this end we characterize their optical performance by measuring their effect on the cavity characterized in Sec. 4.2.1.

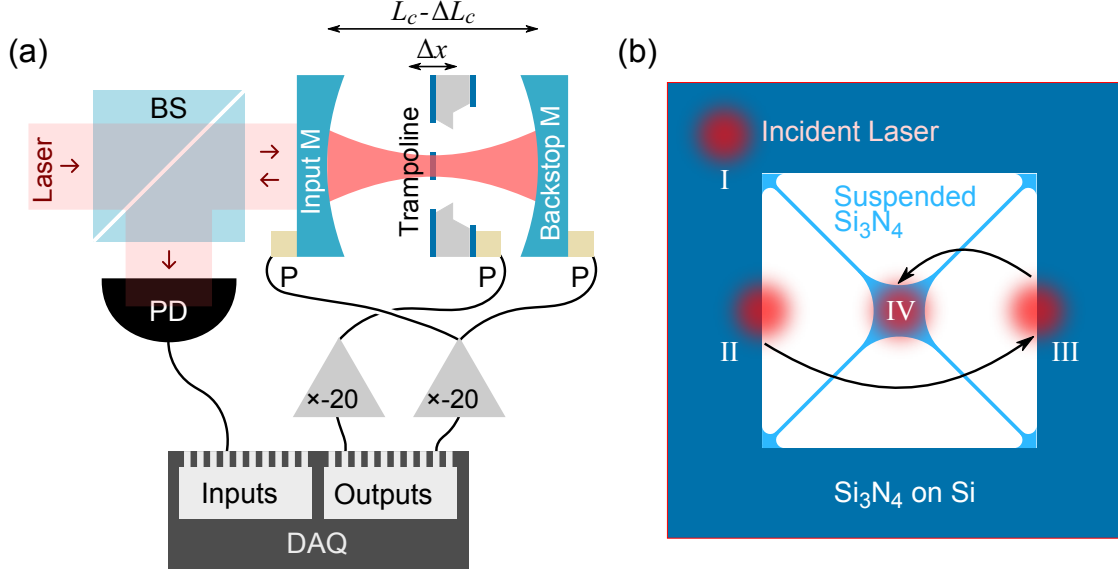


Figure 4.6: Simplified Fabry-Pérot cavity setup with incorporated Si_3N_4 structure and trampoline positioning with respect to the incident laser beam during alignment. (a) Incident laser light (wavelength 1550 nm, power ~ 10 mW, linewidth ~ 200 Hz) lands on a cavity formed by an input mirror (M) and a “backstop” mirror (see Fig. 4.4 for details) with trampoline resonator (or extended membrane) positioned near the waist. Light reflected from the cavity passes through a 50:50 beam splitter (BS) and is detected by a photodiode (PD, 150 MHz bandwidth). The PD voltage is recorded on a data acquisition (DAQ) module. The cavity length L_c is swept symmetrically about the Si_3N_4 structure (ΔL_c) by applying a voltage to the mirror piezo actuators (P) and the Si_3N_4 structure can be moved along the optical axis by applying a voltage to its piezo actuator, resulting in a displacement Δx . The voltages are generated by the DAQ module and amplified by low-noise, high-voltage amplifiers (designs available upon request) of voltage gain ≈ -20 . (b) Typical sequence of trampoline (membrane) positioning with respect to the incident laser beam during alignment. First, the beam is retroreflected from area I, where unpatterned Si_3N_4 (thickness 90-100 nm) sits on top of a Si substrate (thickness ≈ 675 μm). Second, the chip is moved to position II where the laser partially overlaps with area I and the region of suspended Si_3N_4 where the Si substrate is completely removed. Third, we move the chip along a line until we reach III which is the same as II but on the opposite site of the “window area”. Fourth, we go to position IV by covering half the distance back toward II.

Figure 4.6(a) shows the simplified cavity setup formed by an incident laser beam, an input mirror (M), a backstop mirror, a trampoline (or membrane) aligned close to the waist, all three mounted to piezo actuators (P), a beam splitter (BS), a photodiode (PD) and a data acquisition module that records the photodiode voltage and supplies voltages to the mirror and membrane/trampoline piezos, in combination with low-noise, high-voltage amplifiers of voltage gain ≈ -20 (see Fig. 4.4 for details) .

To test whether our fabrication protocol introduces additional bulk absorption or surface losses, we first align an extended membrane, fabricated similarly to the trampolines, near the cavity waist. Unpatterned Si_3N_4 membranes fabricated elsewhere have been shown to exhibit very little optical loss [43, 42], and, in particular, the bound placed on the imaginary index $\text{Im}[n] < 1.5 \times 10^{-6}$ [43] would in principle make these structures compatible with a cavity finesse $\mathcal{F} \sim 10^6$, even when positioned at an antinode of the intracavity field. Furthermore, we incorporate a trampoline in the cavity to investigate scattering and diffraction losses due to overlap of the TEM_{00} cavity mode with the trampoline sidewalls.

The alignment of either a square membrane or a trampoline inside our cavity starts with a partially disassembled cavity comprising only the “backstop” mirror and a pinhole replacing the input mirror. In a first step, we make sure the incident laser is properly retroreflected from the “backstop” mirror, guided back through the pinhole and landing on the photodiode. We then clamp the membrane or trampoline chip by means of fingerstock onto a piezo actuator that is glued to the temporary chip support of a manual five axis stage (see Fig. 4.3). Figure 4.6(b) shows how the Si_3N_4 structure is consecutively positioned with respect to the incident laser beam during the alignment procedure. We start by aiming the laser at a region away from the released structure where unpatterned Si_3N_4 (refractive index 2 for $\lambda = 1550$ nm) sits on top of the Si (refractive index 3.7 for $\lambda = 1550$ nm) substrate (position I). The chip’s tilt is aligned so that the beam is again retroreflected through the pinhole. We then center the laser on the released Si_3N_4 structure by moving the stage lateral to the optical axis. We roughly hit the center of the structure (position IV) by counting the screw turns from leaving the chip area on, e.g., the left side (position II) to reaching the chip area on the right side (position III) of the membrane or trampoline and consecutively going back by half the amount of turns. Hereby, leaving (or reaching) the chip area is usually obvious from a change in reflected intensity landing on the photodiode. At this point the Si_3N_4 structure is roughly centered and perpendicular with respect to the cavity axis and we move on to install and align the input mirror so that the incident light is retroreflected, which typically results in a coarsely aligned cavity. If successful, higher-order TEM modes are now visible in the reflection spectrum. Fine alignment can then be achieved by adjusting the trampoline’s position and tilt, with the goal of increasing the size of the reflection dips

while reducing their number⁶.

The resonance lengths for a cavity with one of our Si₃N₄ structures aligned close to its waist are given by

$$\Delta\tilde{L}_{lmn} = \frac{\lambda}{2\pi} \left\{ l\pi + 2(m+n+1) \tan^{-1} \left(\frac{1}{\sqrt{\frac{2R_c}{L_c} - 1}} \right) - \phi_r + \cos^{-1} \left[-|r| \cos \left(\frac{4\pi}{\lambda} \Delta x + l\pi \right) \right] \right\}. \quad (4.2)$$

The first two terms describe TEM resonances of the empty cavity (see Sec. 4.2.1) with length L_c , and mirror radius of curvature R_c . The third and fourth terms represent the modification in the resonance length caused by the presence of the Si₃N₄ structure (see Sec. 2.2.3) with membrane reflection coefficient $r = |r| \exp(i\phi_r)$ and relative position Δx along the optical axis. Figure 4.7(a, left) shows a plot of the power reflected from the cavity as a function of cavity length and membrane position. This data was taken by ramping the cavity mirror piezos (as in Sec. 4.2.1) and stepping the membrane piezo's voltage from 0 to 60 V (0.3 V steps) in between each ramp. For each pair of cavity and chip piezo voltages we normalize by the off-resonance value (corresponding to all incident light being promptly reflected by the cavity). The dark regions occur when the laser is resonant with the cavity.

⁶Note this is not always the best "goal" for a low-loss, single-port (over-coupled) cavity, since the reflected power should ideally remain constant, even though a lot of light builds up inside the cavity.

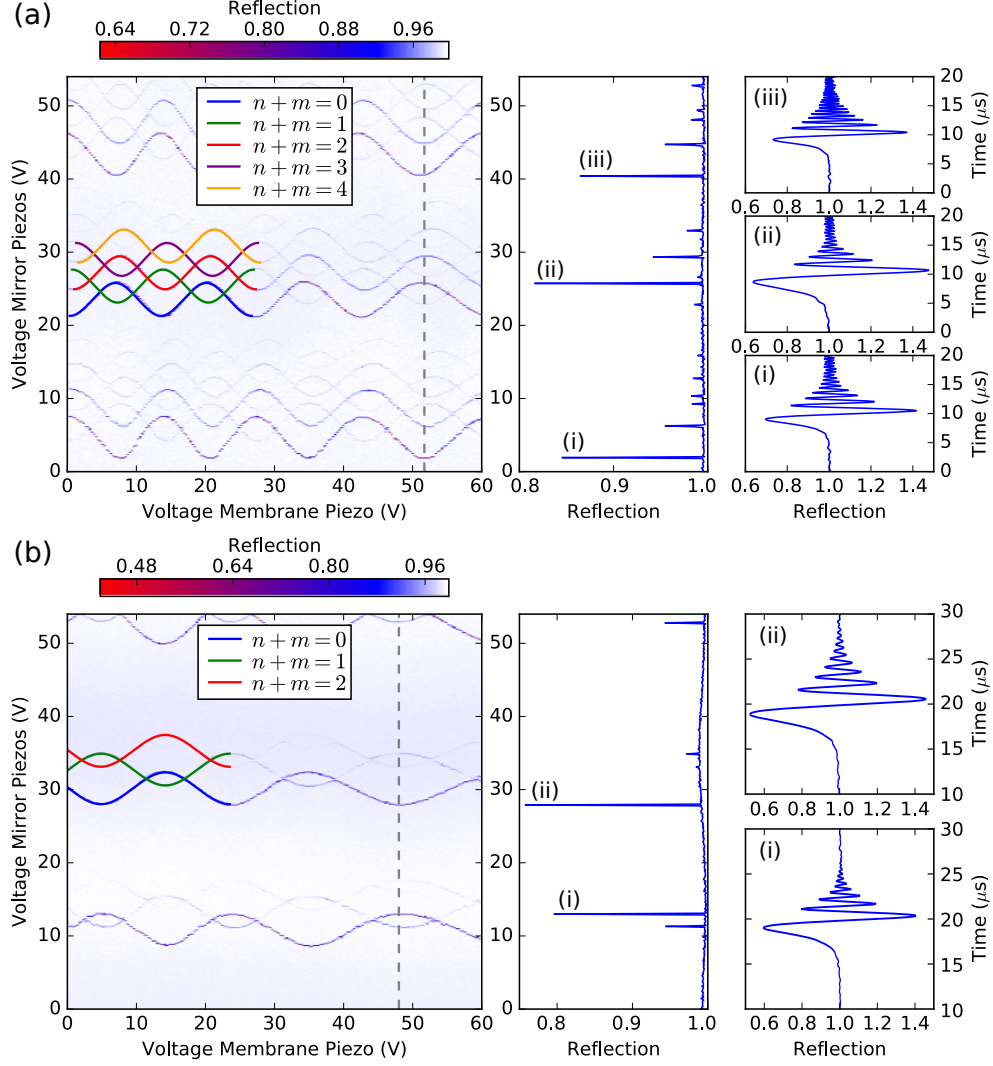


Figure 4.7: Reflection signal (normalized by off-resonance value) of a cavity having either a membrane or trampoline aligned close to its waist. (a, left) Reflected intensity from a cavity with an extended membrane as a function of the voltage applied to the mirror piezos and the membrane piezo. The cavity length L_c is rapidly swept (45 ms linear voltage ramp $V_c(t)$ from 0 to 60 V) and the membrane position is stepped (voltage increase by $\Delta V_m = 0.3$ V up to 60 V) after the L_c sweep. Colored curves show expected cavity resonances for $\lambda = 1550$ nm, $L_c = 4.80$ cm, cavity mirror radius of curvature $R_c = 2.5$ cm, absolute $|r| = 0.48$ and phase $\phi_r = -0.65$ of membrane reflection coefficient, longitudinal mode order $l = 0 \dots 4$ (relative to $l_0 \sim 62,000$), and transverse mode order $m+n = 0 \dots 4$ transformed to voltages by coefficients $a = -18.3 \text{ V}/\mu\text{m}$ and $b = 102.8 \text{ V}$. The dashed line indicates a single L_c sweep ($V_m = 51.7$ V) which is shown in (a, middle). Consecutive fundamental transverse electric resonances (TEM_{00}) are labeled by (i)-(iii) for which respective power ringdown data are shown in (a, right). (b) Same as (a) but for a patterned trampoline of width $d = 200 \mu\text{m}$. Colored curves show expected cavity resonances for $\lambda = 1550$ nm, $R_c = 2.5$ cm, $L_c = 4.75$ cm, $|r| = 0.37$, $\phi_r = -0.89$, $l = 1 \dots 3$ (relative to $l_0 \sim 61,000$), and $m+n = 0 \dots 2$, $a = -23.0 \text{ V}/\mu\text{m}$, and $b = 112.9 \text{ V}$.

The periodicity $\sim \lambda/2$ (up to Gouy phase shift, see Appendix C.1) of the resonances in Δx is a consequence of the intra-cavity optical intensity profile. Along the vertical axis is a pattern (spanning ≈ 15 V) of dips repeated three times (once for each free spectral range) present, where the lowest resonance corresponds to the TEM₀₀ mode (see. Sec. 4.2.1) and the weaker resonances (separated by $\Delta V_c \approx 3$ V) originate from higher order TEM _{$m+n \geq 1$} modes. Due to piezo nonlinearities and hysteresis, the resonances are distorted along the horizontal and the vertical axis (see Sec. 4.2.1). We identify the transverse mode orders by plotting the expected resonances $\Delta \tilde{V}_{lmn} = a\Delta \tilde{L}_{lmn} + b$ (colored curves) with $\Delta \tilde{L}_{lmn}$ (Eq. 4.2) for $\lambda = 1550$ nm, $R_c = 2.5$ cm, $L_c = 4.80$ cm, $|r| = 0.48$, $\phi_r = -0.65$, $l = 0 \dots 4$ (relative to $l_0 \sim 62,000$), and $m + n = 0 \dots 4$ transformed to voltages by $a = -18.3$ V/ μ m and $b = 102.8$ V. Resonances of consecutive transverse order are shifted horizontally by 0.3 V due to a membrane displacement Δx slightly away from the cavity waist, where modes of different transverse order have slightly different Gouy phases (see Appendix C.1). The vertical dashed line indicates a single L_c sweep, taken for $V_m = 51.7$ V, which is plotted in Fig. 4.7(a, middle) where the three TEM₀₀ resonances are indicated by (i)-(iii). Their swept ringdown signal (see Sec. 4.2.1) is plotted in Fig. 4.7(a, right) from which we extract \mathcal{F} (see Sec. 4.2.1 for details). Figure 4.7(b) is similar to Fig. 4.7(a) but the data is taken with the trampoline instead of the membrane, and the expected resonances $\Delta \tilde{V}_{lmn}$ (colored curves) are plotted for $\lambda = 1550$ nm, $R_c = 2.5$ cm, $L_c = 4.75$ cm, $|r| = 0.37$, $\phi_r = -0.89$, $l = 1 \dots 3$ (relative to $l_0 \sim 61,000$), and $m + n = 0 \dots 2$, $a = -23.0$ V/ μ m, and $b = 112.9$ V.

The resonance scans presented in Fig. 4.7(a, left) and Fig. 4.7 (b, left) are smoothly distorted and slightly sheered due to piezo nonlinearity and creep, combined with temperature drift. Figure 4.8(a, top) and Fig. 4.8(b, top) show two consecutive TEM₀₀ resonances (white cuves) where these nonidealities are eliminated by simultaneously fitting the resonant values to their known functional dependence (Eq. 4.2) incorporating fourth-order polynomial distortion (see Sec. 4.2.1) and linear sheer correction terms. Doing so allows us to extract the cavity detunings induced by the membrane, along with the membrane's reflectivity $|r_m| = 0.38 \pm 0.01$. Using a lower-order polynomial does not significantly change our result, but minor systematics do eventually become visible. Note this value of $|r_m|$ corresponds to that expected for a Si₃N₄ (refractive index 2.0) slab of thickness 72 ± 2 nm, which

is smaller than the nominal value of 80 nm. However, this scheme is known for its systematic underestimate of $|r_m|$ [43], which is attributed to slight misalignment of the membrane and / or level repulsion between the TEM_{00} and higher-order transverse modes of the cavity, both of which tend to flatten the sinusoidal perturbation.

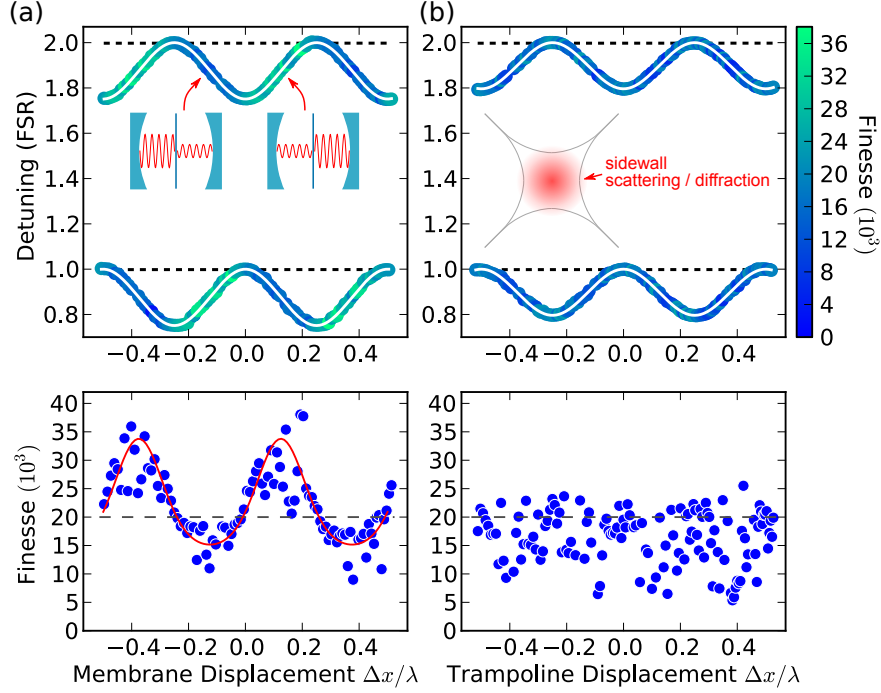


Figure 4.8: Finesse characterization of a cavity containing either a membrane or trampoline aligned close to its waist. (a, upper) Finesse and cavity mode detuning versus the displacement of an extended membrane. White curves show fit (see text), and solid dashed lines show the approximate empty cavity resonance frequencies. Inset shows qualitative sketch of left and right cavity modes (a, lower) Comparison of finesse (from the topmost resonance) with prediction for a lossless membrane (red). Dashed line indicates empty cavity finesse $\mathcal{F} \approx 20,000$. (b) Same as (a) but for a patterned trampoline of width $d = 200 \mu\text{m}$, in this case, the trampoline’s effective reflectivity is $|r_t| = 0.31 \pm 0.01$. Inset shows a qualitative sketch of the cavity cross-section at the trampoline.

The finesse (color scale and lower plot of Fig. 4.8(a)) is found to oscillate with position, in fact exceeding the bare cavity finesse $\mathcal{F} \approx 20,000$ (dashed line in lower plot of Fig. 4.8(a)) measured in Sec. 4.2.1. This can be readily understood by viewing the membrane as “one more dielectric layer” of the input mirror that, with the proper air-gap, enhances its reflectivity. A transfer matrix theory [79] assuming zero optical loss in the membrane (red curve, zero free parameters) reproduces the oscillations. This implies that, so long as the optical mode waist

$2w_0$ is sufficiently small compared to the diameter d of the pad, it should readily achieve a cavity finesse of 40,000 or higher. Note, as observed previously [43], the error bar on individual finesse measurements is significantly smaller than the fluctuations in Fig. 4.8; the larger, non-statistical variations are known to arise from membrane-mediated hybridization between the TEM₀₀ mode and higher-order modes of the cavity (each having its own value of finesse) whenever they approach degeneracy.

Finally, in an effort to place an approximate upper bound on the cavity mode diameter required to achieve this finesse with a patterned device, we replace the membrane with a trampoline having a pad diameter $d = 200\ \mu\text{m}$, such that $\sim 0.045\%$ of the cavity light (mode diameter $2w_0 = 110\ \mu\text{m}$) does not land on the structure. If we naively assume this light is lost from the cavity, the finesse would be limited to 7,000. However, simulations of a similar geometry [60] suggest higher value, since the end mirrors can collect and recycle some of the scattered light. As shown in Fig. 4.8(b), despite these “clipping” losses, a finesse equal to the empty-cavity value of 20,000 is achievable within a short distance of any trampoline position, even near the antinodes of the intracavity field. Clipping effects are still evident, however: the regions of boosted finesse have vanished, and the rapid finesse variations dip to much lower values. This is consistent with an intuition that sidewall scattering further breaks the symmetry of the cavity, increasing the TEM₀₀ mode’s coupling to even higher-order, lossier transverse modes.

In the context of optomechanical sideband cooling (see Sec. 2.2.6), we have introduced the single photon cooperativity C_0 as a figure of merit, which is proportional to the optomechanical cooling rate and can be written

$$C_0 = \frac{4\pi\hbar c |r_d|^2 \tau_m \mathcal{F}}{\lambda^2 L_c m \Omega_m}, \quad (4.3)$$

for our geometry. The demonstrated optical parameters ($L_c = 4.7\ \text{cm}$, $\mathcal{F} = 40,000$, $\lambda = 1550\ \text{nm}$, $r_m = 0.4$) together with the trampoline’s mechanical characteristics (effective mass $m_{\text{eff}} = 4.0\ \text{ng}$, ringdown time $\tau_m = 6.0\ \text{min}$, and resonance frequency $\Omega_m = 2\pi \times 40.9\ \text{kHz}$, see Sec. 3.3.1) correspond to a single-photon cooperativity $C_0 \sim 8$ in the resolved-sideband limit (“resolved” in the sense that the back-action-limited cooling would result in an average

phonon occupancy $n_{\text{m,min}} = 0.2 < 1$ (Eq. 2.98)). In Sec. 2.2.6 we have discussed, that for $C_0 = 1$ a cooling laser (in the resolved-sideband limit) having an average intensity of a single photon doubles the dissipation rate of the bare mechanical element. So with our value $C_0 \sim 8$, we are in the regime wherein the mechanical trajectory will be significantly altered when the apparatus contains a single photon on average. Indeed, our initial attempts to frequency stabilize an external laser to the cavity with incorporated trampoline failed, because the trampoline's oscillation was strongly anti-damped by the fluctuations of the incident laser (as soon as the trampoline is antidamped, it rings up and the system is unusable for minutes). This motivated the development and characterization of our sideband locking technique, presented in Chapter 5.

4.3 Simulation of Q_m -Increase Through Optical Trapping

Optically levitated mechanical sensors can be isolated from classical noise sources so that the momentum imparted by single photons becomes the dominant noise source [121]. This approach typically involves subwavelength-scale dielectric nanoparticles which are optically trapped inside a Fabry-Perot cavity ([121], and references cited therein). Patterned dielectric membranes can be designed to benefit from partial optical levitation, where an optical trapping potential provides a restoring force acting in conjunction with the elastic restoring force of the membrane material [60]. In an experimental implementation of this scheme [81], the mechanical quality (Q_m) factor of a Si pendulum was increased 50-fold when aligned in an optical standing wave (few Watts incident power). Theoretical treatments [60, 122] have proposed that partial levitation can yield a Q_m -increase of more than three orders of magnitude.

In the following, we adopt the approach presented in [60, 122, 123] to simulate the effect of a strong optical trap on the 80-nm-thick trampoline of Fig. 3.2. Hereby, we are particularly interested in the achievable enhancement of the mechanical quality (Q_m) factor. The finite-element simulation is carried out in COMSOL Multiphysics.

Inset (i) in Fig. 4.9 shows the fundamental (s_1) trampoline mode (see also Fig. 3.8) with

an optical trapping beam applied to the central pad. We model the optical trap as external force

$$F_{\text{trap}} = m_{\text{eff}} \omega_{\text{trap}}^2 f(x, y) \zeta(x, y), \quad (4.4)$$

acting along the direction of the trampoline's out-of-plane displacement $\zeta(x, y)$ (see Fig. 4.9, inset (i)). Here $m_{\text{eff}} = \rho_{\text{m}} \int dV \zeta^2(x, y) / \zeta_0^2$ is the effective mass [90] of the mechanical mode, with material density ρ_{m} , maximum trampoline displacement at the center ζ_0 , and volume of the resting trampoline V . The optical trap strength $\omega_{\text{trap}}^2 f(x, y)$ is parametrized by means of trap frequency $\omega_{\text{trap}} = \sqrt{\mathcal{K}_{\text{MIM}}/m_{\text{eff}}}$, with optical spring constant \mathcal{K}_{MIM} given by Eq. 2.88, and a function $f(x, y)$ describing the optical intensity profile. According to the parameters of our experimental cavity setup (Sec. 4.2.2) we set $f(x, y) = \exp[-2(x^2 + y^2)/w_0]$ with $2w_0 = 110 \mu\text{m}$, which represents the Gaussian beam profile of the TEM₀₀ cavity mode. We assume that the optical force, together with the tensile stress (see Sec. 3.1.1), act in a linear fashion on the trampoline, so that its mechanical response can be described by linearly superimposing the effects of the two forces [124]. In this case, the total mechanical energy of the trapped trampoline is given by the sum of the intrinsic mechanical (tensile) energy and the additional optical trapping potential $U_{\text{tot}} = U_{\text{m}} + U_{\text{trap}}$. By assuming that the optical potential contributes no mechanical dissipation channel [60, 122], the definition of the mechanical quality factor (Eq. 2.6) yields

$$Q_{\text{tot}} = 2\pi \frac{U_{\text{m}} + U_{\text{trap}}}{\Delta U_{\text{m}}} = Q_{\text{m}} \left(1 + \frac{U_{\text{trap}}}{U_{\text{m}}} \right) \quad (4.5)$$

for the total quality factor of the trapped trampoline, where ΔU_{m} is the dissipated mechanical energy per cycle of oscillation, and $Q_{\text{m}} = 2\pi U_{\text{m}}/\Delta U_{\text{m}}$ is the intrinsic mechanical quality factor. Alternatively, we can express Q_{tot} in terms of U_{tot} as

$$Q_{\text{tot}} = \frac{Q_{\text{m}}}{1 - U_{\text{trap}}/U_{\text{tot}}}, \quad (4.6)$$

with energies (see Sec. 2.1.1)

$$U_{\text{tot}} = \frac{1}{2} \rho_{\text{m}} d \omega_{\text{tot}}^2 \iint dx dy \zeta^2(x, y) \quad (4.7)$$

$$U_{\text{trap}} = \frac{1}{2} \rho_{\text{m}} d \omega_{\text{trap}}^2 \iint dxdy \zeta^2(x, y) f(x, y), \quad (4.8)$$

and their ratio

$$\frac{U_{\text{trap}}}{U_{\text{tot}}} = \frac{\omega_{\text{trap}}^2}{\omega_{\text{tot}}^2} \frac{\iint dxdy \zeta^2(x, y) f(x, y)}{\iint dxdy \zeta^2(x, y)}. \quad (4.9)$$

Here, the second term represents the normalized overlap of the mechanical displacement squared with the optical intensity profile, which in the present case is biggest for the trampolines symmetric out-of-plane modes (indicated by s_i , with mode index i , in Fig. 3.8), making them primary candidates for Q_m -increase through optical trapping.

In the case of uniform trap strength across the trampoline ($f(x, y) = 1$), the ratio of the integrals in Eq. 4.9 is one and the maximally achievable energy ratio would mainly be limited by the amount of optical power the system can handle. The trapped mechanical frequency in this case is $\omega_{\text{tot}}^2 = \Omega_{\text{m}}^2 + \omega_{\text{trap}}^2$, with mechanical resonance frequency Ω_{m} , which, together with Eq. 4.9, permits to rewrite Eq. 4.6 as

$$Q_{\text{tot}} = Q_{\text{m}} \left(1 + \frac{\omega_{\text{trap}}^2}{\Omega_{\text{m}}^2} \right). \quad (4.10)$$

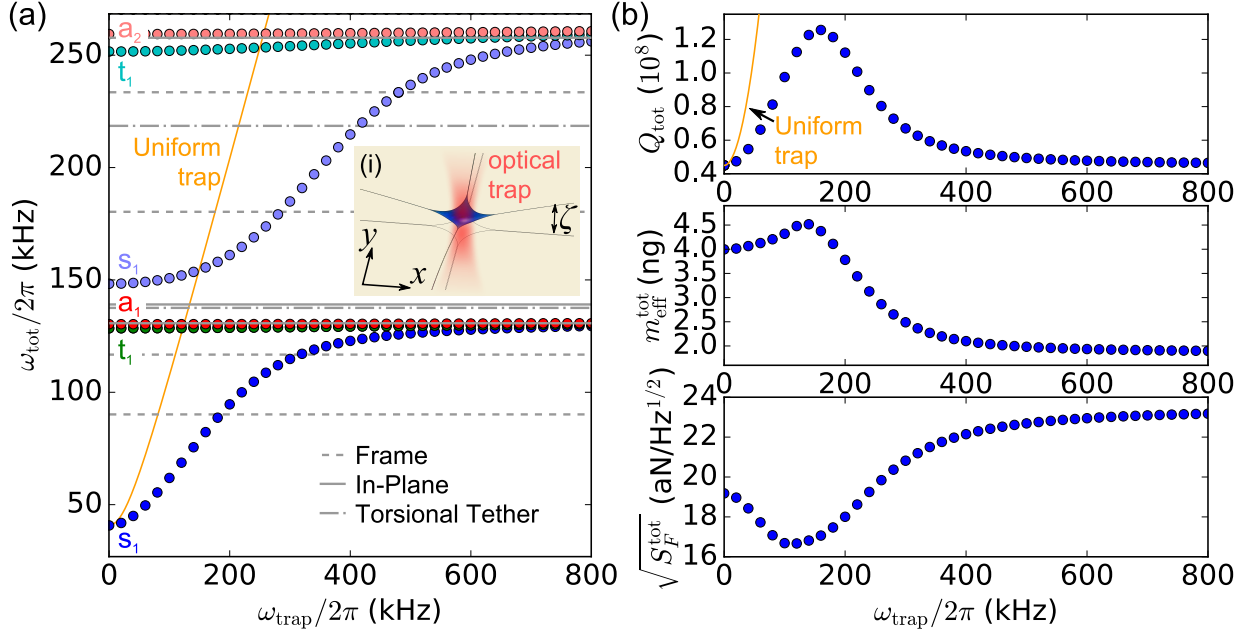


Figure 4.9: Response of a Si_3N_4 trampoline resonator (see Fig. 3.2 for device dimensions) to an optical trap with Gaussian intensity profile (mode field diameter $2w_0 = 110\ \mu\text{m}$). Inset (i) shows the trapped s_1 mode profile (for $\omega_{\text{trap}} = 400\ \text{kHz}$) with applied trapping beam. When at rest, the trampoline lies in the xy -plane, from which it is perpendicularly displaced by ξ for out of plane modes. (a) Colored circles show mechanical resonance frequencies of optically-trapped “symmetric” (s_i), “torsional” (t_i) and “antisymmetric” (a_i) modes ω_{tot} (mode index i , see Fig. 3.8 for plotted mode profiles) versus trap frequency ω_{trap} . The gray lines correspond to modes of the overhanging Si_3N_4 frame (dashed lines, see Fig. 3.2), in-plane modes (solid lines), and torsional tether modes (dot-dashed lines) for which the tethers twist around their longitudinal axis. The orange line shows the case of constant trapping force across the whole mode profile $\omega_{\text{tot}} = (\Omega_m^2 + \omega_{\text{trap}}^2)^{1/2}$. (b) Response of the total mechanical quality factor Q_{tot} (upper), effective mass $m_{\text{eff}}^{\text{tot}}$ (center), and force noise $\sqrt{S_F^{\text{tot}}}$ (lower) to the optical trap for the fundamental (s_1) trampoline mode. The orange line (upper) represents the case of a constant trapping force across the whole mode profile $Q_{\text{tot}} = Q_m (1 + \omega_{\text{trap}}^2/\Omega_m^2)$.

Figure 4.9(a) shows the response of the trampoline’s six lowest mechanical out-of-plane resonances (colored circles), to an optical trap with Gaussian beam profile and trap frequency ω_{trap} . Most strongly affected are the symmetric modes (s_1, s_2), in agreement with the discussion of Eq. 4.9. Their frequency is increased until they hybridize with the above-lying antisymmetric (a_1, a_2) and torsional modes (t_1, t_2), which also hybridize with each other. This hybridization is a consequence of the trap’s confinement to the central pad, which, for increasing strength, progressively clamps it down until merely the tethers are free to oscil-

late. This behavior contrasts the effect of a uniform trap (shown for s_1 , Fig. 4.9(a) orange curve), for which the mode symmetry remains unchanged, theoretically enabling an arbitrary resonance frequency increase⁷. The gray lines in Fig. 4.9(a) represent resonances which are unaffected by the optical trap, due to a vanishing overlap integral in Eq. 4.9. We distinguish between modes of the overhanging Si_3N_4 frame (dashed lines, see Fig. 3.2), in-plane modes (solid lines), and torsional tether modes (dot-dashed lines) for which the tethers twist around their longitudinal axis. Potentially counterproductive are crossings of these resonances with the trapped mode since they provide additional dissipation channels due to mode hybridization.

Figure 4.9(b) shows the response of the total mechanical quality factor Q_{tot} , effective mass $m_{\text{eff}}^{\text{tot}}$ (center), and force noise $\sqrt{S_F^{\text{tot}}}$ (lower) to the optical trap for s_1 . The initial values $\left\{Q_{\text{tot}}, m_{\text{eff}}^{\text{tot}}, \sqrt{S_F^{\text{tot}}}\right\}_{\omega_{\text{trap}}=0} = \left\{4.5 \times 10^7, 4.5 \text{ ng}, 19.5 \text{ aN}/\sqrt{\text{Hz}}\right\}$ are chosen according to the experimental parameters of Sec. 3.3.1. The orange line (upper) represents the case of a constant trapping force across the whole mode profile (Eq. 4.10). The maximum value of Q_{tot} is realized at the point of inflection of ω_{tot} , where the mode hybridization comes into play. From this point Q_{tot} decays back to the untrapped value, due to the increasing hybridization to tether modes (assumed to have the same initial quality factor for simplicity), which are unaffected by the optical trap. The effective mass (Fig. 4.9(b, center)) slightly increases until the “hybridization point”, which agrees with the intuition, that the onsetting trap mainly reduces the maximum displacement ξ_0 , while for stronger traps, the mass of the central pad is more and more excluded from contributing to $m_{\text{eff}}^{\text{tot}}$ due to hybridization, causing it to approach the tether mass. The effect on the force noise combines the previously discussed aspects according to $\sqrt{S_F^{\text{tot}}} = \sqrt{4m_{\text{eff}}^{\text{tot}}\omega_{\text{tot}}k_{\text{B}}T/Q_{\text{tot}}}$ (see Sec. 2.1.2.2). Initially the force noise is improved $\sim 15\%$. Ultimately, the increase in ω_{tot} outweighs the reduction in $m_{\text{eff}}^{\text{tot}}$, causing the force noise to increase up to 18% .

Although our trampoline resonator is not particularly designed to benefit from optical trapping, our simulation (based on experimental parameters) predicts that its Q_{m} can be

⁷Ultimately, the achievable increase is limited by residual optical absorption which will cause the resonator structure to fracture when the incident optical power reaches the damage threshold. In an experimental trapping attempt of a similar device as the one discussed here, a damage threshold of $\sim 10 \text{ W}$ was found [102].

increased by a factor of 2.8 resulting in $Q_{\text{tot}} = 1.3 \times 10^8$ at resonance frequency $\omega_{\text{tot}}/2\pi = 82 \text{ kHz}$. This corresponds to $Q_{\text{tot}} \times \omega_{\text{tot}}/2\pi = 10^{13}$, which meets the requirements for laser cooling to the quantum mechanical ground state [87, 88]. The maximum value of Q_{tot} is realized for $\omega_{\text{trap}} = 160 \text{ kHz}$. For the optical single-mode spring discussed in Sec. 2.2.3, this would require an optical trapping power $\sim 100 \text{ W}$. This value would be reduced to $\sim 1 \text{ W}$ when employing an optimized configuration [122], which exploits the increased trapping efficiency provided by the avoided crossing of the TEM_{00} and TEM_{10} or TEM_{01} cavity mode.

Similar to previous studies [81, 122], we find that mode-hybridization in consequence of a non-uniform trapping potential is the limiting factor for Q_{tot} . In principle, one could enhance the trap uniformity, by increasing the cavities MFD (e.g. shortening the cavity length), to further increase Q_{tot} . In that regard, the results presented in Sec. 4.2.2 show promise that an overlap of the optical intra-cavity field with the trampoline sidewalls is not detrimental to the cavity finesse. Eventually, the maximum obtainable Q_{m} increase might involve a trade-off between the trap uniformity and the reduction in cavity finesse associated with diffraction from the trampoline sidewalls (Sec. 4.2.2).

Chapter 5

Simple Delay-Limited Sideband Locking with Heterodyne Readout

Statement of contribution: Tina Müller implemented an initial version of the feedback loop, which she operated together with the “membrane-in-the-middle” cavity setup presented in Chapter 4. For the characterization presented in this chapter and a journal article on this topic, I built a new Fabry-Perot cavity setup, added the heterodyne readout capability and adjustable attenuator to the original feedback circuit, and recorded and analyzed all the data. Erika Janitz, Maximilian Ruf, Alexandre Bourassa, Simon Bernard, Abeer Barasheed, and Vincent Dumont contributed with discussions.

A common goal in precision optics is to employ feedback [125] to stabilize (lock) the frequency of a continuous-wave (CW) laser to that of an external system, such as a Fabry-Perot optical cavity [58] or atomic transition [126, 127]. This can be used to stabilize the laser itself, or to continuously monitor the dynamics of the external system. For example, by locking a laser to a sufficiently stable cavity, it is possible to produce extraordinarily coherent light [128], which can then be applied to the precision control and spectroscopy of trapped atoms [129], high-accuracy optical clocks [130, 131], or interferometric detection of passing gravitational waves [106]. Alternatively, a locked laser can be used to probe atomic or molecular absorption within the cavity [132], or to resolve the quantum zero-point motion of an embedded mechanical element [17, 18] (see also [16]). Within the latter context (optomechanics [21]), a stable, low-

power lock is particularly important for systems combining a lightweight, highly compliant, ultrahigh- Q_m mechanical system [1, 39, 57] (see also Sec. 3.1.1) with a high-finesse cavity, wherein the radiation pressure from an average cavity occupancy of one photon should in principle profoundly alter the mechanical trajectory [1]. Indeed, our failed attempts to lock the combined system of cavity with incorporated trampoline investigated in Sec. 4.2.2 and Ref. [1] (using traditional methods) is precisely what motivated the present work.

As reviewed in Sec. 5.1 below, all feedback schemes aim to simultaneously achieve the largest possible closed-loop gain (the degree to which noise can be suppressed) and sufficient dynamic range (headroom) to compensate all fluctuations. The closed-loop gain is ultimately limited by the speed with which corrections can be applied (the bandwidth), which itself is fundamentally limited by the delay of the signal propagating through the loop [125]. In many situations, however, the achievable gain is practically limited by other system nonidealities. For example, one means of tuning a laser’s emission frequency is to mechanically stretch an internal optical path, and the bandwidth is then practically limited by the structure’s mechanical resonances. For this reason, low-noise, mechanically tuned lasers (e.g. commercial Nd:YAG lasers) are typically limited to control bandwidths of ~ 100 kHz. Faster feedback can be achieved by controlling the laser’s pump, and commercial diode lasers (e.g.) routinely achieve sufficient pump modulation bandwidth that feedback is limited by other loop non-idealities; as such, using the pump to stabilize against an external cavity is often employed as a first stage to reduce their comparatively large noise [133]. The control bandwidth of the combined system, however, is then limited by the external cavity’s mechanical resonances. Cavity mirror actuation has improved in recent years, achieving 180 kHz with short-travel piezo actuation [134] and now up to ~ 700 kHz with the incorporation of photothermal tuning [135].

An alternative, laser-independent technique is to shift the light’s frequency after emission. For visible wavelengths, this is usually accomplished with an acousto-optical modulator (AOM), achieving ~ 200 kHz closed-loop bandwidth [128] with \sim MHz-scale headroom on its own, and up to 2 MHz bandwidth when combined with an electro-optical modulator (EOM) to correct the high-frequency noise in parallel [136]. At near-infrared (telecom) wavelengths, low-cost fiber modulators are more commonly employed: using serrodyne techniques, wherein

a voltage-controlled oscillator (VCO), nonlinear transmission line (NLTL), and EOM generate a saw-tooth phase that effectively shifts the carrier frequency [137, 138], or single-sideband modulation (SSM), wherein a VCO and Mach-Zehnder interferometer shift a small portion of the carrier [139], it is routine to achieve several-MHz feedback bandwidth and well over 100 MHz headroom.

A second common goal in precision optics is to perform heterodyne readout [140], wherein a weak “signal” beam is overlapped with a strong local oscillator (LO) beam detuned by an electronically measurable frequency. Landing on a photodiode, the beating between these two beams produces an amplified electronic signal with a spectrum shifted to the LO detuning, thereby providing simultaneous access to the signal’s amplitude and phase quadratures (or, equivalently, to its double-sided spectrum). In addition to spectroscopy, polarimetry, laser radar (and lidar), microscopy, and other applications [140], heterodyne readout enables a continuous, self-calibrating measurement of mechanical temperatures in the quantum regime of motion [17, 18].

Here we present and characterize a simple, low-power, high-bandwidth, post-emission laser locking technique with built-in heterodyne readout. This approach employs a high-speed VCO and a single EOM to control the signal beam frequency, and can be implemented with any laser. In contrast to serrodyne systems, it does not require a precise NLTL-generated saw-tooth waveform (or the extra EOM bandwidth to handle it), and, similar to SSM, shifts only a fraction of the laser light. In contrast to both, the carrier is exploited as an optical LO for heterodyne readout, and no alignment or relative path stabilization is required. Using the test ports of our chosen electronics, we directly measure the frequency-dependence of the closed-loop gain, demonstrating a delay-limited feedback bandwidth of 3.5 MHz (one integrator) and excellent agreement with a simple model based on ideal components. From this we propose a modified setup that should realistically achieve a gain of 4×10^7 at 1 kHz (6.6 MHz bandwidth, two integrators). The headroom allowed by these components exceeds 500 MHz, limited only by a 10 V ceiling on the VCO programming voltage imposed by our amplifier (~ 1 GHz should be possible with this VCO/EOM combination, at the expense of added amplitude noise). Section 5.1 briefly reviews requisite concepts in laser feedback. Section 5.2 then introduces the “Pound-Drever-Hall” method for generating an error signal

[141, 58, 142] (including a derivation of its dynamical response) and a simple electronics modification enabling heterodyne readout. We then present the technical details of our “proof-of-concept” system in Sec. 5.3, characterize its performance in Sec. 5.4, and conclude in Sec. 5.5.

5.1 A Brief Review of Laser Feedback

All laser frequency stabilization schemes rely on (i) generation of an “error” signal proportional to the frequency difference (detuning) δ between the laser and an external system, and (ii) processing and routing of this signal to a port that adjusts δ to compensate [125]. 5.1(a) shows a conceptual diagram of a feedback loop for locking a laser to a cavity resonance. Cavity vibrations and laser frequency noise together introduce a nominal detuning δ_n (note these noise sources appear on equal footing, and only the difference δ will be stabilized) that is converted to an electronic signal by a photodiode “ D ”, amplified and filtered by assorted electronics “ $-A$ ”, and sent to a “feedback” port “ F ” to adjust δ . This correction is *added* to the original noise (e.g., by tuning the laser frequency, cavity length, or both), resulting in a relationship for the *net* detuning $\delta = \delta_n - CDAF\delta$, where C , D , $-A$, and F are complex, frequency-dependent gains (transfer functions) for the cavity, diode, electronics, and feedback port. Solving for δ yields

$$\delta = \frac{\delta_n}{1 + CDAF}. \quad (5.1)$$

This immediately highlights the central concerns for stabilization. First, it is desirable to make the “closed-loop gain” $G \equiv CDAF$ as large as possible, to maximally cancel the noise. For $|G| \gg 1$, the overall phase ϕ_G does not matter, but if G approaches -1 at a some “bad” frequency, then the noise at that frequency is *amplified*. This places unavoidable limits on G for the following reasons: (i) any delay t_d in the signal path introduces a phase factor $e^{-i\omega t_d}$, forcing $\phi_G = -\pi$ at finite frequencies, regardless of what electronics are chosen for A , (ii) stability concerns impose that the magnitude of the gain at the lowest of these frequencies $\omega_{-\pi}$ should be less than 1, and (iii) causality places an upper bound $|G| < \omega_{-\pi}^2/\omega^2$ on how much the gain can increase below this frequency [125]. Since most noise occurs at low frequencies, it is therefore desirable to make $\omega_{-\pi}$ large, and to engineer a feedback circuit

such that G increases as rapidly as possible with decreasing frequency.

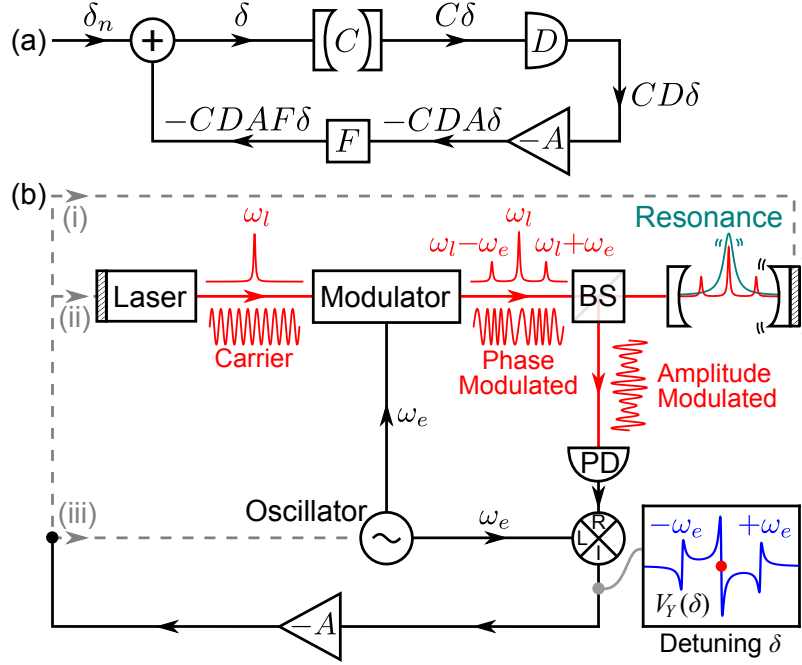


Figure 5.1: Feedback stabilization. (a) Generic control loop for stabilizing a laser’s detuning δ from the resonance of an optical cavity. Noise δ_n enters, is converted to an optical signal by the cavity (transfer function C), collected by a diode (D), manipulated by electronics ($-A$) and sent to a “feedback” port (F). (b) Practical implementation using Pound-Drever-Hall readout. Straight red lines represent optical paths, straight black lines represent electrical paths, and dashed gray lines show potential feedback paths. The laser is phase-modulated, lands on a beam splitter (BS) and interacts with the cavity, which converts phase to amplitude modulation. This is recorded with a photodiode and mixed (demodulated) with a local oscillator. Inset shows the resulting steady-state voltage $V_Y(\delta)$, with a red dot indicating a stable lock point. The manipulated signal can be fed back to (i) the cavity length or (ii) the laser frequency. Feeding back to (iii) the oscillator frequency only adjusts the sidebands.

A readout of δ (the error signal) can be obtained by several methods. A high-finesse optical cavity of length L , input mirror field transmission coefficient t_1 and power ringdown time τ has an overall field reflection coefficient (see Appendix A)

$$r(\delta) \approx \frac{t_1^2 \tau c / L}{1 + i2\tau\delta} - 1. \quad (5.2)$$

The reflected power ($\propto |r|^2$) therefore follows a Lorentzian line shape. On resonance ($\delta = 0$), the reflected power cannot on its own be used for feedback since it does not provide information about the sign of δ . One can generate a bipolar error signal by tuning the laser

away from resonance [143], but this technique couples laser power fluctuations to detuning errors. However, the phase of $r(\delta)$ *does* vary linearly on resonance, and can be extracted via phase modulation [58], heterodyne [140, 144], and homodyne [145] schemes, wherein the mode of interest interferes with one or more reference beams having different frequency or phase. Other techniques employ a second cavity mode as a reference, for example a mode of different polarization [146] or a higher order spatial mode [147, 148]. The powerful “Pound-Drever-Hall” technique [58] is discussed in the following section.

5.2 Modified Pound-Drever-Hall Readout and Dynamical Response

A ubiquitous method for on-resonance laser stabilization is the “Pound-Drever-Hall” (PDH) technique [141, 58], a diagram of which is drawn in Fig. 5.1(b). Stated briefly, this technique effectively amounts to dithering the laser frequency with an electro-optical modulator (EOM) and measuring the induced modulation in the reflected power to infer the *slope* of $|r(\delta)|^2$ (or $\text{Im}[r]$) [142]. The resulting error signal (inset blue curve, near red dot) can then be manipulated with electronics ($-A$) and fed back to either (i) the cavity length or (ii) the laser frequency, as described above. Feeding back to a voltage-controlled oscillator (VCO, iii) will not adjust the *carrier* frequency (or δ) in this configuration, but can be used to lock a sideband as discussed in Sec. 5.3. An elegant, pedagogical derivation of the steady-state error signal (V_Y in Fig. 5.1(b)) for this system can be found in [142]. This accurately captures the system’s ability to convert low-frequency detuning noise into an error signal, but breaks down when the detuning $\delta(t)$ contains frequencies comparable to the cavity’s linewidth $1/\tau$. A straightforward means of deriving the *dynamic* response [149] is to propagate a small laser “noise” component through an EOM, cavity, diode, and demodulation (mixer) circuit in Fig. 5.1(b) to extract a combined transfer function, as follows (see Appendix B for more details). Suppose there exists a laser frequency noise component at frequency ω that is the real part of $\tilde{\Omega}(t) = \Omega_n e^{i\omega t}$, where Ω_n is a constant amplitude. This corresponds to phase modulation $\phi(t) = \phi_n \sin(\omega t)$, where $\phi_n = \Omega_n/\omega$. If this light is fed through a phase

modulator (EOM) driven by voltage $V_{\text{osc}} = V_e \sin(\omega_e t)$, the field landing on the cavity is

$$E = E_l \cos(\omega_l t + \phi_e \sin \omega_e t + \phi_n \sin \omega t) \quad (5.3)$$

where E_l is a constant amplitude and $\phi_e \propto V_e$ according to the efficiency of the EOM. Assuming all modulations are small ($\phi_e, \phi_n \ll 1$), Eq. (5.3) can be written as the sum of a “carrier” at frequency ω_l , four first-order sidebands ($\omega_l \pm \omega_e$ and $\omega_l \pm \omega$) and eight second-order sidebands ($\omega_l \pm 2\omega_e$, $\omega_l \pm 2\omega$, $\omega_l \pm \omega_e \pm \omega$, and $\omega_l \pm \omega_e \mp \omega$). If we also assume the modulator frequency is large compared to the cavity linewidth and noise frequency ($\omega_e \gg 1/\tau, \omega$), and the *carrier* is on resonance, only five beams (ω_l , $\omega_l \pm \omega$, and $\omega_l \pm 2\omega$) acquire a significant change in magnitude and phase upon reflection, as per Eq. (5.2). When the 13 reflected beams land on a photodiode, they produce a time-averaged photocurrent $\propto \langle E^2 \rangle$ containing all frequencies within the photodiode’s bandwidth ($\ll \omega_l$). If this signal is then mixed with the original oscillator voltage V_{osc} , the output is proportional to $\langle E^2 \rangle \sin(\omega_e t)$, and an appropriately chosen low-pass filter can eliminate all terms except those having frequency near ω . After some bookkeeping (Appendix B), the complete transfer function for converting a frequency noise $\tilde{\Omega}$ to a (complex) error signal \tilde{V}_Y is found to be

$$\frac{\tilde{V}_Y}{\tilde{\Omega}} \approx -\frac{2\phi_e E_l^2 \beta \tau^2}{1 + 2i\tau\omega} \quad (5.4)$$

where the constant prefactor β includes a combination of cavity parameters and the conversion efficiencies of the diode and mixer (note our chosen diode and mixers have large bandwidths, and are assumed here to have frequency-independent efficiencies for simplicity; this assumption is validated by the agreement with the measurement in Sec. 5.4). The interpretation of this result is straightforward. Assuming $\phi_n \ll 1$ restricts $V_Y(\delta)$ to the region of linear response (i.e. near the red dot in Fig. 5.1(b)). The resulting transfer function sensibly scales with the laser power and dither amplitude [58, 142], and the cavity’s amplitude ringdown time 2τ imposes a low-pass filter on the readout [149]. Interestingly (as alluded to before [58, 142]), despite the round-trip time of light circulating within the cavity, this transfer function does *not* contain a delay-like factor; the phase tends to a constant value at high frequency.

This motivates the use of a “proportional-integral” (PI) amplifier for the conditioning electronics (A in Fig. 5.1). A PI amplifier has a transfer function

$$A_{PI} = G_0 \frac{1 + i\omega/\omega_{PI}}{1/g + i\omega/\omega_{PI}} \quad (5.5)$$

where G_0 is an overall scaling factor, ω_{PI} is a “PI corner” frequency, above which the response changes from integrator-like to proportional, and g is a gain limit at low frequencies. Often (especially while locked) the gain limit is removed ($1/g \rightarrow 0$), in which case $A_{PI} \rightarrow G_0 (1 - i\frac{\omega_{PI}}{\omega})$; when combined with the readout transfer function (Eq. (5.4)), the choice $\omega_{PI} = 1/2\tau$ then results in a partial-loop transfer function

$$\frac{\tilde{V}_Y}{\tilde{\Omega}} A_{PI} = \frac{\phi_e E_l^2 \beta \tau^2 G_0}{i\tau\omega} \quad (5.6)$$

The total system behaves like an integrator over all frequencies, with increasing gain at low frequencies. The overall phase is far from $-\pi$, preventing the system’s overall delay factor $e^{-i\omega t_d}$ from forcing the closed-loop gain below 1 at a low frequency. This phase margin furthermore provides “wiggle room” for loop nonidealities such as indirectly driven resonances that can cause a temporary excursion in phase (see, e.g., [134]). However, even if the bandwidth of the feedback port F is effectively infinite and / or we have precisely compensated for all of its artifacts, the ultimate gain is limited by the signal delay t_d – in this case from the output of the EOM to the cavity, back to the diode, through the electronics, and through the feedback port – which forces the closed-loop gain to be less than 1 at frequency $\omega_{-\pi} < \pi/4t_d$ for this choice of electronics.

It is also possible to lock the first-order sidebands ($\omega \pm \omega_e$) to the cavity. Following the same analysis for the case of either sideband resonant with the cavity produces a transfer function

$$\frac{\tilde{V}_{Y,\pm}}{\tilde{\Omega}} \approx \frac{\phi_e E_l^2 \beta \tau^2}{1 + 2i\tau\omega} \quad (5.7)$$

which is inverted and half as large as the carrier-resonant case (Eq. (5.4)), consistent with the slope of the steady state solution (V_Y in 5.1(b)) at $\delta = \pm\omega_e$ [58, 142].

Finally, similarly propagating an *amplitude* noise component through this system (i.e.,

setting $E_l \rightarrow (1 + \text{Re}[\tilde{\epsilon}]) E_l$, where $\tilde{\epsilon}(t) = \epsilon_n e^{i\omega t}$ with constant $\epsilon_n \ll 1$) has no impact on \tilde{V}_Y or $\tilde{V}_{Y,\pm}$. However, introducing a relative $\pi/2$ phase shift between the mixer's LO and signal ports provides access to a similar readout of the laser's amplitude noise \tilde{V}_X with an overall transfer function

$$\frac{\tilde{V}_{X,\pm}}{\tilde{\epsilon}} \approx \mp \phi_e E_l^2 \beta \tau \frac{1 + i\tau\omega}{1 + 2i\tau\omega} \quad (5.8)$$

for the upper or lower sidebands on resonance, respectively. We note that, in contrast to the “phase quadrature” $V_{Y,\pm}$, the “amplitude quadrature” $V_{X,\pm}$ is influenced by the off-resonance sideband. Equation 5.8 illustrates that the addition of a second, phase-shifted mixer (or using an IQ mixer) enables heterodyne readout with no additional lasers, optical modulators, or alignment. Conveniently, the steady-state form of this quadrature, discussed below and shown in Fig. 5.2, also provides a simple means of verifying which sideband is locked to the cavity (along with an independent estimate of how well it is locked).

Figure 5.2(a) shows our test setup for locking a first order sideband (at $\omega_l \pm \omega_e$) to a Fabry-Perot cavity resonance. Sidebands are created with a fiber EOM driven at ω_e by a VCO with 90 MHz modulation bandwidth and 0.65-1.75 GHz tuning range. Light from the EOM passes through a beam splitter (BS) and mode-matching optics (shown in (b)), reflects from the cavity, and is collected by a high-bandwidth photodiode. The resulting signal is filtered and amplified before passing through a power splitter that produces a phase shift of 0 and $\pi/2$ at its outputs. These two signals are separately mixed with that of the VCO to produce V_X and V_Y . The VCO output is split prior to the EOM, delayed, and used as the electronic LO for both mixers. In order to maintain a fixed phase between the mixers' LO and signal ports over the full range of VCO frequencies ω_e , the delay between the two signal paths must match. Any difference Δt_d produces a relative phase $\omega_e \Delta t_d$ that must remain small compared to $\pi/2$ at the highest VCO frequency. Here this imposes that $\Delta t_d \ll \pi/2\omega_e \sim 1$ ns, corresponding to a free-space path difference $\ll 30$ cm, which is mostly compensated for with a combination of cables and extension adapters (Fig. 5.2(a)), with mm-scale fine-tuning of the photodiode's position. The higher precision required for larger- ω_e systems can be easily implemented with the diode optics mounted on a translation stage.

Fig. 5.2(b) shows a photograph of the optical path; the electronics are mounted on a nearby platform. The detuning δ between the laser and cavity can be widely adjusted with long-travel piezos in the second mirror mount ("Piezo M"). Fig. 5.2(c) shows a diagnostic measurement of $V_Y(\delta)$ and $V_X(\delta)$ recorded during cavity length sweeps for a few values of ω_e . Each sweep was performed "quickly" (16 ms over the full range) to reduce run-to-run variations from the ambient vibrations of the test cavity. The insensitivity of the quadrature readout to ω_e indicates the delay is matched (see Appendix C for a larger range). The cavity has a power ringdown time $\tau = 1.2 \pm 0.1 \mu\text{s}$ (finesse 4700 ± 400), and so these fast sweeps produce a transient response [150] resulting in a measured V_Y (top plot of (c)) that is consistently not symmetric about $V_Y = 0$, and a measured V_X (bottom plot of (c)) that deviates from a simple peak. This artifact can be highly misleading when tuning the relative delay, and so rather than trying to symmetrize V_Y , we recommend slowly modulating ω_e while quickly sweeping the cavity, and adjusting Δt_d to produce a signal shape that does not vary with ω_e .

The error signal V_Y is then fed through a tunable PI amplifier having the transfer function of Eq. (5.5), with $\omega_{PI} = 110$ kHz and $g = 105 = 40$ dB (measured) before finally being fed back to the VCO. Due to the sidebands' opposed frequency response, one sideband is always stabilized by this feedback and the other is always destabilized; here we (arbitrarily) lock the upper sideband (verified by the negative value of V_X). Despite the open-air design and flagrant disregard for vibration isolation, this system readily locks and remains so indefinitely (it is impervious to chair scoots, door slams, claps, and shrieks, but fails if the table surface is tapped with a wrench).

5.4 Performance

Once locked, we increase the feedback gain G_0 until the system rings (at ~ 3 MHz for this implementation), indicating that the gain at $\omega_{-\pi} \sim 3$ MHz has exceeded unity. We then reduce G_0 until the remaining noise in V_Y is minimized. The most sensitive estimate of V_Y is achieved by referring the PI amplifier's output back to its input using its known (measured) transfer function; together with an independent measurement of the error signal slope on resonance $2\pi \times \partial_\delta V_Y = 388 \pm 40$ mV/MHz, we estimate that the stabilized RMS detuning noise $\delta_{\text{RMS}}/2\pi$ is below 70 Hz (0.0005 cavity resonance full-widths). This is a factor of 3000 lower than the pre-stabilized value of 240 kHz (1.6 fullwidths, corresponding to 0.3 nm RMS cavity length noise), as estimated directly from the PI output and the VCO specifications (52 MHz/V). Figure 5.3(a) shows the power spectral densities of these two inferred detuning signals. The square root of their ratio provides a basic estimate of the closed-loop gain magnitude $|G(\omega)| \sim 1000$ at $\omega/2\pi = 1$ kHz. We note that this estimate of the pre-stabilized noise is made while the system is locked – the cavity's inherent mechanical noise and narrow linewidth together preclude an open-loop estimate – and so this data mainly serves as a consistency check for the closed-loop gain measurement below and our assumptions about the other system components.

To *directly* measure $G(\omega)$, we inject a small amount of “noise” into the locked system and observe how it is suppressed. The PI amplifier provides a second (inverted) input, and an isolated monitor of the in-loop error signal. Using a lock-in amplifier, we apply an oscillatory

signal V_n of frequency ω to this input and record both quadratures of the error signal V_Y at ω (correcting for the transfer functions between the input and error monitor, as well as the lock-in and its measurement cables). Using the same analysis of Fig. 5.1(a) with $CDAF \rightarrow G$, $\delta_n \rightarrow V_n$, and $\delta \rightarrow V_Y$, we solve for the closed-loop gain $G = V_n/V_Y - 1$, which is plotted in Fig. 5.3(b) (blue). Importantly, the observed gain smoothly decreases with ω (approximately as $1/\omega$), and the phase crosses $-\pi$ at $\omega/2\pi = 3.5$ MHz, where $|G| < 1$, consistent with the observed ringing frequency. The measurement noise increases at low frequencies due to the reduced signal at high gain. It is worth pointing out that, despite the addition of sidebands to the VCO output (at $\omega_e \pm \omega$), the measured transfer function through the EOM, cavity, diode, and mixer is identical to that of laser frequency noise (this can be seen by tracking these extra sidebands through a calculation similar to that of Appendix B).

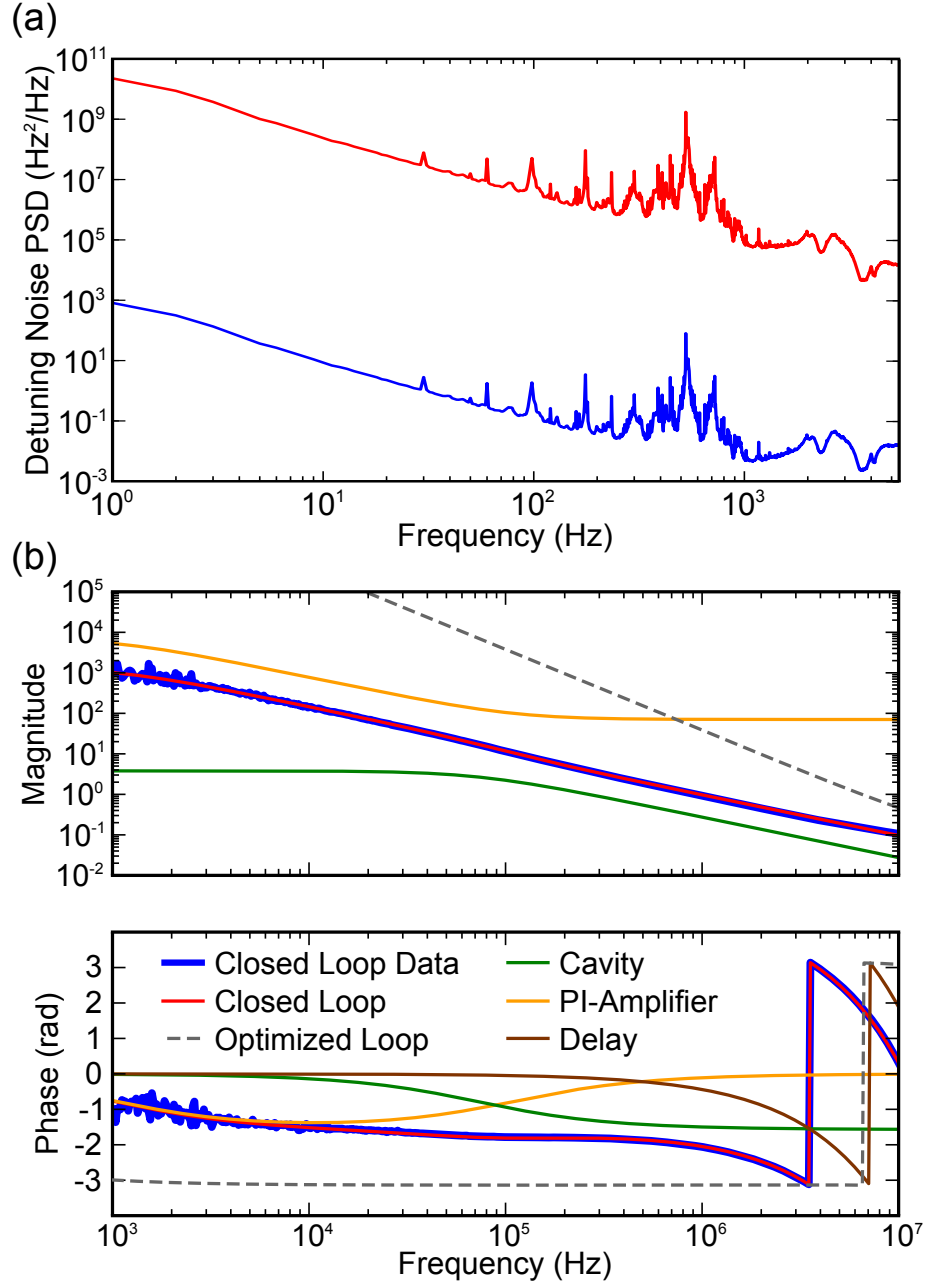


Figure 5.3: (a) Detuning noise power spectral density (PSD) before and after lock, recorded while locked. The pre-feedback noise (red) is inferred from the proportional-integral (PI) amplifier output and the VCO conversion factor 52 MHz/V, while the post-feedback noise (blue) is inferred from the PI output referred back to its input and the independently measured slope of the error function (388 ± 40 mV/MHz) at the lock point. (b) Measured (blue) and modeled (red) closed-loop transfer function. The model includes the cavity (green, ring-down time $\tau = 1.1$ μs), PI amplifier (yellow, $\omega_{PI} = 110$ kHz, and $g = 105$), and a delay (brown, 70 ns, 52 ns from the PI amplifier). Transfer functions of other components are assumed to be “flat” on this scale. The gray dashed line shows a closed-loop gain that could be achieved with optimizations: replacement of the PI amplifier and further delay reductions to 10 ns and two PI filters, one with $\omega_{PI}/2\pi = 70$ kHz, $1/g = 0$, and the other with $\omega_{PI}/2\pi = 15$ MHz and $g = 10^5$.

The red line in Figs. 5.3(b)–5.3(c) represents a simple model for $G(\omega)$ comprising the product of (i) the PI transfer function (Eq. (5.5)) with measured $\omega_{PI}=110$ kHz and $g=105$, (ii) the cavity transfer function (Eq. (5.7)) with $\tau = 1.1 \mu\text{s}$ (i.e. one standard deviation below the measured value), (iii) a closed-loop delay $t_d = 70$ ns, and (iv) an overall scaling factor chosen to match the measured $G(\omega)$. The yellow and green curves show the modeled PI and cavity transfer functions alone for reference, and the brown curve shows the phase contribution from the delay. The employed value of t_d is consistent with the signal travel time of the loop, independently estimated to be approximately 68 ns from the signal path of the lower VCO loop in Fig. 5.2(a): a combined cable and component length of 127" traversed at 2/3 the speed of light (16 ns) plus the measured internal delay of the PI amplifier (52 ns). The agreement between the model and measurement suggests that the chosen components exhibit no important nonidealities up to ~ 10 MHz, and that the other components (the EOM, optics, diode, filters, mixers, amplifiers, attenuators, splitters, and connectors) can be assumed to have a flat response, adding a combined delay on the order of nanoseconds at most.

The phase plot of Fig. 5.3(b) highlights that the achieved bandwidth is limited primarily by the delay. Without it, the phase would remain above $-\pi/2$ to a significantly higher frequency, allowing for larger G_0 . The PI amplifier accounts for 75% of the delay, implying the greatest gains can be made by replacing it with a faster (albeit less flexible) integrated circuit. Modern amplifiers routinely achieve sub-nanosecond delays, and the requisite PI filters can be realized with passives (capacitors and resistors). It is also straightforward to reduce the optical and electronic lengths: using compact mode-matching optics and shorter cables alone can reduce the delay to ~ 10 ns. Furthermore, replacing the existing PI filter with two – one having $\omega_{PI}/2\pi = 70$ kHz and $1/g \rightarrow 0$ and the other having $\omega_{PI}/2\pi = 15$ MHz and $g = 10^5$ – for example, would produce a bandwidth of 6.6 MHz and (more importantly) a near-causality limited gain $|G(2\pi \times 1 \text{ kHz})| \sim 4 \times 10^7$ (Fig. 5.3(b), dashed line). This optimization will be the subject of future work.

To estimate the headroom, we change the cavity length L while locked and monitor the output voltage of the PI amplifier; the system remains locked over the full ~ 100 MHz tuning range presented in Fig. 5.2(b), in this case limited by the cavity's small free spectral range:

the lower sideband of an adjacent mode eventually becomes degenerate with the locked sideband, spoiling the error signal. Performing the same test on a 5-cm cavity, we find a headroom of 550 MHz, limited instead by the maximum output voltage of the PI amplifier (10 V), which covers only half the tuning range of the VCO. A headroom exceeding 1 GHz is in principle possible with these components; however, while more headroom is certainly useful for tracking large fluctuations, the frequency-dependencies of the VCO output, EOM, and other electronics will eventually couple these fluctuations to the amplitude of the optical signal and LO beams (see Appendix C). Further engineering effort is therefore best spent reducing the system's inherent noise.

5.5 Conclusion

We have demonstrated a simple technique for locking a first order laser sideband to an optical cavity with a delay-limited feedback bandwidth of 3.5 MHz with a single integrator, and a headroom exceeding 500 MHz. We directly measured the closed-loop gain, finding excellent agreement with a model based on ideal components, and suggest simple modifications for realizing a gain exceeding 10^7 at 1 kHz. Finally, we note that, by implementing an appropriately weighted sum of V_X and V_Y (or otherwise shifting the relative phase of the mixers' electronic LO and signal ports), it should be possible to create an amplitude-insensitive locking point – a zero crossing in the resulting error signal – at arbitrary detuning.

Chapter 6

Conclusion & Outlook

In this dissertation we have presented the wafer-scale batch fabrication and characterization of high-aspect-ratio, nanogram-scale Si_3N_4 trampoline resonators. Our fabricated devices have resonance frequencies in the range of 40 – 570 kHz and mechanical ringdown times up to ~ 6 minutes (~ 1 mHz linewidth) with corresponding mechanical quality factors up to $\sim 5 \times 10^7$ at room temperature. We have measured the trampolines’ thermally limited force sensitivity and the resulting value of $16.2 \pm 0.8 \text{ aN/Hz}^{1/2}$ (at room temperature), paired with high spring constants ($\sim 1 \text{ N/m}$), and compatibility with low-loss optics, renders them well suited for classical sensing applications. With regard to future integration, e.g., in a compact cryogenic setup, we have investigated how gluing a trampoline chip to a metal mount affects the quality factor (measurements performed by our collaborators from the Harris Lab at Yale University), finding a modest reduction up to 13%. With the goal of employing our devices in a “membrane-in-the middle” optomechanical geometry [41], we have built a high-vacuum Fabry-Perot cavity setup, and incorporated a trampoline close to the cavity center. To set an approximate upper bound on the size of the cavity field required for high-finesse applications, we have chosen the trampoline size so that 0.045% of the light falls outside the structure. Consistent with recent simulations [60], we find that the majority of this “clipped” light is retained by the cavity and that the empty cavity finesse of 20,000 is, in many cases, recovered. The measured mechanical and optical parameters of our optomechanical setup, correspond to a single photon cooperativity $C_0 \sim 8$ in the resolved-sideband limit (“resolved” in the sense that the back-action-limited cooling would

result in an average phonon occupancy $n_{\text{m,min}} = 0.2 < 1$ (Eq. 2.98)). Motivated by failed attempts of frequency stabilizing an external laser to the cavity with incorporated trampoline, with standard methods, we have developed and characterized a robust sideband laser locking technique ideally suited for applications requiring low probe power and heterodyne readout. We have measured the transfer function of the locked feedback loop, which revealed a feedback bandwidth of 3.5 MHz (with a single integrator). Our data agrees with a simple model based on ideal components, which shows that the bandwidth is fundamentally limited by the signal delay. From this we suggested a modified design that should achieve a bandwidth exceeding 6 MHz with a near-causally limited feedback gain up to 4×10^7 at 1 kHz.

The low dissipation rates of our trampolines make them excellent candidates for studies of dissipation mechanisms. Although there was considerable gain in the understanding of limiting factors in high- Q_m Si_3N_4 resonators over recent years [151, 152, 93, 153, 92, 98, 57], there are open questions remaining. Among them is the relative contribution of bulk and surface defects to overall defect-induced losses [98, 57]. Also the influence of surface roughness, e.g. on the etched sidewalls of the devices, on Q_m is not fully understood; it has repeatedly been reported [105, 100, 1] (also this work) that subjecting patterned Si_3N_4 resonators to hydrofluoric acid solution, thereby removing few nanometers of material from all exposed surfaces, results in enhanced mechanical and optical quality factors. The underpinnings of this effect are yet unclear and it is speculated whether it is the removal of structural defects or chemical surface contaminants, e.g. oxygen or carbon [94], which causes the improvement. A possible route to diminishing surface roughness would be to optimize the dry etch process, used to write the trampoline shape into the Si_3N_4 device layer. This can be done by systematically investigating the sidewall roughness (e.g., with a scanning electron microscope) in dependency of etch parameters. To reduce surface contamination one could follow an approach described for silicon surfaces [154]. Here, a detailed surface analysis by means of X-ray photoelectron spectroscopy enabled identification of the contaminant (silicon dioxide) and surface passivation with an accordingly-chosen chemical (short-chain alkynes) significantly reduced contamination on newly-fabricated devices.

With regard to employing the trampolines in classical sensing applications, we envision in the simplest case capacitive [30, 155] or fiber [156] readout from within the silicon etch pit,

and a sharp tip (or other probe) fabricated upon the top surface. Alternatively, if high-finesse readout is required, one could position a probe at the edge of the central pad or upon the tethers, far from any light fields, employ a fiber cavity [157], and / or exploit the second order trampoline mode (where trampoline’s central pad twists around two resting (diagonal) tethers while the other two tethers oscillate out of phase, see Fig. 3.8(b)), which has the same force sensitivity but a larger tether displacement and spring constant. Furthermore, if Q_m follows the trend for nitride, namely increasing by a factor of 10-100 at low temperature [158, 155, 159], these devices could in principle achieve $\sim 14 \text{ zN/Hz}^{1/2}$ at 14 mK [155], a value approaching that of a carbon nanotube [160, 8], but with a significantly larger, stiffer platform amenable to the incorporation of additional circuitry and probes.

The compatibility of our trampolines with high-finesse optics, together with the long ring-down time of the fundamental trampoline mode, also provides access to parameter regimes of central interest in the field of optomechanics. Our measured parameters corresponds to a single-photon cooperativity $C_0 \sim 8$, which renders outstanding goals in the field feasible. For example, if the trampoline is simultaneously laser cooled to the back-action limit [23] and mechanically driven to an amplitude of $\sim 5 \text{ nm}$ (i.e. as in Fig. 3.8(a)), even the gentle quadratic optomechanical coupling found at a node or antinode [41] would be sufficient to perform a quantum nondemolition (QND) readout of the trampoline’s phonon shot noise [86] with a signal-to-noise ratio of ~ 170 . Importantly, such a scheme is inherently compatible with a single-port optical cavity such as the one employed in this work (see Sec. 4.2.2), as required by the theory [86]. This avoids the need to find clever ways to catch and recycle cavity light from one of the two ports found in other systems such as avoided crossings [43], wherein the requirements are significantly more stringent [161]. Finally, though these devices are not optimized to benefit from the Q_m -enhancement of partial levitation [81, 60, 80], the finite-element simulation of Sec. 4.3 predicts that Q_m can be boosted by a factor of ~ 2.5 when trapped to $\Omega_m \sim 2\pi \times 100 \text{ kHz}$, thereby achieving $Q_m > 10^8$. In this case, there would be an average of $\bar{n}_m = k_B T / \hbar \Omega_m \sim 6 \times 10^7$ thermal phonons in the mode at room temperature. This meets the requirement $\bar{n}_m < Q_m$ for laser cooling to the quantum mechanical ground state [88, 87].

A next step towards performing an optomechanics experiment with our setup would be to

achieve a stable frequency “lock” between an external laser and the cavity with incorporated trampoline. This would require optimizing our frequency stabilization technique, e.g., by implementing the suggested modifications to the feedback electronics (see Sec. 5.4), reducing the power of the incident laser, or locking to a cavity resonance with lower finesse. An interesting feature of our setup is, that the mechanical resonance frequency (40 kHz) is well within the feedback bandwidth (3.5 MHz), as this causes the feedback action to play an active role in the interaction between oscillating trampoline and electromagnetic cavity field. Recently it was demonstrated that exploiting this additional means of control in an optomechanical sideband cooling scheme enables cooling 7.5 dB beyond what is possible with sideband cooling alone [162]. Achieving a stable cavity lock for the setup discussed in this work would also be useful for employing more complex mechanical resonators comprising an array of coupled trampolines, e.g., to perform an experiment recently proposed by our group, where the geometry of the trampoline array, represented by its mechanical mode profile, is controlled by means of its interaction with the intra-cavity field [123].

Another aspect of future work could be the optimization of our setup with regard to enhanced cooperativity C_0 (Eq. 2.101). A straightforward approach would be to reduce the cavity length L_c ($C_0 \propto L_c^{-1}$) by incorporating a trampoline into one of our fiber cavities [163] ($L_c \sim 100 \mu\text{m}$), instead of the free-space cavity ($L_c \sim 5 \text{ cm}$) presented in Sec. 4.2.2. This would enable $C_0 \sim 1000$. Although striking, this increase would happen at the expense of operating in the “bad cavity limit”, where the optomechanical sidebands are located within the cavity resonance, thereby precluding efficient sideband cooling schemes. Increasing C_0 while remaining in the sideband-resolved regime could be realized by modifying the trampoline design; for example, using thinner trampolines would benefit C_0 directly by reducing mass m ($C_0 \propto m^{-1}$), and indirectly through an enhancement of the mechanical ringdown time τ_m ($C_0 \propto \tau_m$) [39]. This approach comes with a trade-off, since devices much thinner than $\sim 100 \text{ nm}$ suffer from reduced reflectivity $|r_d|^2$ ($C_0 \propto |r_d|^2$). This reduction can be compensated for by incorporating a photonic crystal reflector [52, 53, 54, 39, 55, 56] into the trampoline. Though, in order to achieve reflectivities $> 99 \%$, the nitride layer would have to be $\sim 200 \text{ nm}$ thick [39]. Therefore, in order to simultaneously optimize the trampoline’s mechanical and optical performance, one could follow the approach presented in [39], where the tethers are

thinned down with respect to the central pad, thereby optimizing mechanical and optical performance. In Addition, a photonic crystal reflector can significantly boost the quadratic optomechanical coupling [119] (Eq. 2.90) while still in principle maintaining a single-port cavity. This provides a promising route toward resolving individual quantum jumps between the phonon number states of the trampoline [41] at the expense of added optical losses that might limit the achievable finesse [119].

Appendix A

Theoretical Concepts

A.1 Reflection and Transmission Coefficient of a One-Dimensional Slab

We derive the reflection and transmission coefficient of a one-dimensional slab characterized by its thickness d and refractive index n_2 , which is surrounded by a medium with refractive index n_1 . The transfer matrix of the system is given by

$$M_d = \frac{1}{t_{12}} \begin{pmatrix} 1 & r_{12} \\ r_{12} & 1 \end{pmatrix} \begin{pmatrix} e^{ikn_2d} & 0 \\ 0 & e^{-ikn_2d} \end{pmatrix} \frac{1}{t_{21}} \begin{pmatrix} 1 & -r_{12} \\ -r_{12} & 1 \end{pmatrix} \\ \frac{1}{t_{12}t_{21}} \begin{pmatrix} e^{ikn_2d} - e^{-ikn_2d}r_{12}^2 & -2ir_{12}\sin(kn_2d) \\ 2ir_{12}\sin(kn_2d) & e^{-ikn_2d} - e^{ikn_2d}r_{12}^2 \end{pmatrix},$$

with wave number k , Fresnel coefficient r_{12} ($r_{21} = -r_{12}$) describing reflection when light impinges from the surrounding (slab) on the slab (surrounding), and Fresnel transmission coefficients t_{12} (t_{21}) describing light transmission from surrounding (slab) to slab (surrounding). Assuming light impinges only from one side, the reflection and transmission coefficients of the slab are given by (from Eqs. 2.47-2.48)

$$r_d = -\frac{(M_d)_{21}}{(M_d)_{22}} = \frac{r_{12}(-1 + e^{i2kn_2d})}{-1 + r_{12}^2 e^{i2kn_2d}} \quad (\text{A.1})$$

$$t_d = (M_d)_{11} - \frac{(M_d)_{12} (M_d)_{21}}{(M_d)_{22}} = \frac{(r_{12}^2 - 1)^2 e^{ikn_2 d}}{t_{12} t_{21} (-1 + r_{12}^2 e^{i2kn_2 d})}. \quad (\text{A.2})$$

In the case of a dielectric slab in air ($n_1 = 1$, $n_2 = n$) with normal incidence and lossless propagation of light in both materials, the Fresnel coefficients are given by (from Eqs. 2.39-2.40)

$$\begin{aligned} r_{12} &= \frac{1 - n}{1 + n} \\ t_{12} &= \frac{2}{1 + n} \\ t_{21} &= \frac{2n}{1 + n}. \end{aligned}$$

For the slab's reflection and transmission coefficients follows

$$r_{d\perp} = \frac{(1 - n^2) \sin(knd)}{(n^2 + 1) \sin(knd) + i2n \cos(knd)} \quad (\text{A.3})$$

$$t_{d\perp} = \frac{2in}{(n^2 + 1) \sin(knd) + i2n \cos(knd)}. \quad (\text{A.4})$$

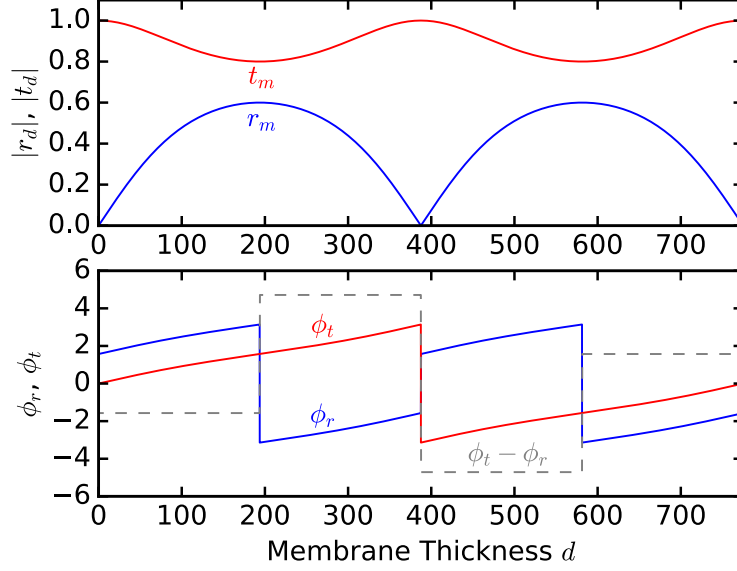


Figure A.1: Reflection and transmission coefficients r_d, t_d (Eqs. 2.39-2.40) of a dielectric slab with refractive index 2 (e.g. Si_3N_4 at wavelength 1550 nm) surrounded by air/vacuum with refractive index 1 as a function of slab thickness d . Respectively shown in blue and red are magnitudes $|r_d|, |t_d|$ and phases ϕ_r, ϕ_t . Gray dashed curve represents $\phi_t - \phi_r = \pm (2q + 1) \pi/2$ with $q \in \mathbb{N}$.

Figure A.1 shows reflection and transmission coefficients r_d, t_d (Eqs. 2.39-2.40) of a dielectric slab with refractive index 2 (e.g., Si_3N_4 at wavelength 1550 nm) surrounded by air/vacuum with refractive index 1 as a function of slab thickness d . Respectively plotted in blue and red are magnitudes $|r_d|, |t_d|$ and phases ϕ_r, ϕ_t . Gray dashed curve represents $\phi_t - \phi_r$, which, as a consequence of energy conservation is restricted to $\pm (2q + 1) \pi/2$ with $q \in \mathbb{N}$ (Eq. 2.43).

In the general case of oblique incidence, the reflection and transmission at an interface between two media depend on the polarization of the light. Typically, one distinguishes between perpendicular and parallel polarization, which are denoted in the following by superscripts s and p . In the former case, the electric field points in the direction perpendicular to the plane of incidence. In the latter case, the electric field is parallel to the plane of incidence. The polarization-dependent Fresnel coefficients describe reflection (r) and transmission (t) at the

interface between two media with refractive indices n_1, n_2 [70, 113]

$$\begin{aligned} r_{12}^s &= \frac{n_1 \cos \theta_1 - n_2 \cos \theta_2}{n_1 \cos \theta_1 + n_2 \cos \theta_2} = \frac{k_{1z} - k_{2z}}{k_{1z} + k_{2z}} \\ t_{12}^s &= \frac{2n_1 \cos \theta_1}{n_1 \cos \theta_1 + n_2 \cos \theta_2} = \frac{2k_{1z}}{k_{1z} + k_{2z}} \\ r_{12}^p &= \frac{n_1 \cos \theta_2 - n_2 \cos \theta_1}{n_2 \cos \theta_1 + n_1 \cos \theta_2} = \frac{n_1^2 k_{2z} - n_2^2 k_{1z}}{n_1^2 k_{2z} + n_2^2 k_{1z}} \\ t_{12}^p &= \frac{2n_1 \cos \theta_1}{n_2 \cos \theta_2 + n_1 \cos \theta_1} = \frac{2n_1 n_2 k_{1z}}{n_1^2 k_{2z} + n_2^2 k_{1z}}, \end{aligned}$$

where θ_1 and θ_2 are respectively the angles of incidence and refraction. The wave vector components along the direction of propagation are given by

$$\begin{aligned} k_{1z} &= \sqrt{k_0^2 - k_x^2 - k_y^2} = k_1 \cos \theta_1 = k_0 n_1 \cos \theta_1 \\ k_{2z} &= \sqrt{k_2^2 - k_x^2 - k_y^2} = k_2 \cos \theta_2 = k_0 n_2 \cos \theta_2. \end{aligned}$$

For both directions of polarization follows

$$\begin{aligned} r_{12} &= -r_{21} \\ 1 &= t_{12} t_{21} - r_{12} r_{21} \end{aligned}$$

We get the angle-dependent slab reflection coefficients by substituting $r_{12} \rightarrow r_{12}^s$ or $r_{12} \rightarrow r_{12}^p$, in r_d :

$$\begin{aligned} r_d^s &= \frac{(k_{1z}^2 - k_{2z}^2) (1 - e^{i2kn_2d})}{(k_{1z} + k_{2z})^2 - (k_{1z} - k_{2z})^2 e^{i2kn_2d}} \\ r_d^p &= \frac{(n_1^4 k_{2z}^2 - n_2^4 k_{1z}^2) (1 - e^{i2kn_2d})}{(n_1^2 k_{2z} + n_2^2 k_{1z})^2 - (n_1^2 k_{2z} - n_2^2 k_{1z})^2 e^{i2kn_2d}} \end{aligned}$$

which correspond to expressions (15a) and (16a) in Ref. [113].

A.2 Reflection and Transmission Coefficient of a DBR

An optical distributed Bragg reflector (DBR) is typically composed of a glass substrate with refractive index n_s and a coating formed by alternating dielectric layers with refractive indices n_1 and n_2 . This configuration acts as an efficient mirror for light with wavelength λ , if the portions reflected at each interface interfere constructively with each other. This is the case if the optical thickness (physical thickness multiplied with refractive index) of each layer is $\lambda/4$. The transfer matrix (TM) describing propagation through such a layer is given by (from TM in Table 2.1(column 1, row 3))

$$M_P = \begin{pmatrix} i & 0 \\ 0 & -i \end{pmatrix}. \quad (\text{A.5})$$

The transfer matrix describing reflection and transmission at the interface between layer a and b with $a, b \in \{1, 2\}$ is given by (see Sec. 2.2.1)

$$M_{ab} = \frac{1}{t_{ba}} \begin{pmatrix} 1 & -r_{ab} \\ -r_{ab} & 1 \end{pmatrix}. \quad (\text{A.6})$$

We start to assemble the transfer matrix describing the propagation through a DBR mirror M_{DBR} by writing down the matrix for a layer pair consisting of one layer made out of material 1 and one layer made out of material 2

$$M_{DL} = M_{21}M_P M_{12}M_P = \frac{1}{2} \begin{pmatrix} -\frac{n_1}{n_2} - \frac{n_2}{n_1} & -\frac{n_1}{n_2} + \frac{n_2}{n_1} \\ -\frac{n_1}{n_2} + \frac{n_2}{n_1} & -\frac{n_1}{n_2} - \frac{n_2}{n_1} \end{pmatrix}. \quad (\text{A.7})$$

For N consecutive double layers we have

$$M_{DL}^N = \frac{1}{2} \begin{pmatrix} \left(-\frac{n_1}{n_2}\right)^N + \left(-\frac{n_2}{n_1}\right)^N & \left(-\frac{n_1}{n_2}\right)^N - \left(-\frac{n_2}{n_1}\right)^N \\ \left(-\frac{n_1}{n_2}\right)^N - \left(-\frac{n_2}{n_1}\right)^N & \left(-\frac{n_1}{n_2}\right)^N + \left(-\frac{n_2}{n_1}\right)^N \end{pmatrix} \quad (\text{A.8})$$

and for a DBR where the coating starts and ends with material 1 follows

$$M_{\text{DBR}} = M_{1s} M_P M_{DL}^N M_{01}$$

$$= \frac{i}{2n_1 n_s} \begin{pmatrix} n_1^2 \left(-\frac{n_1}{n_2}\right)^N + n_s \left(-\frac{n_2}{n_1}\right)^N & n_1^2 \left(-\frac{n_1}{n_2}\right)^N - n_s \left(-\frac{n_2}{n_1}\right)^N \\ -n_1^2 \left(-\frac{n_1}{n_2}\right)^N + n_s \left(-\frac{n_2}{n_1}\right)^N & -n_1^2 \left(-\frac{n_1}{n_2}\right)^N - n_s \left(-\frac{n_2}{n_1}\right)^N \end{pmatrix}.$$

Here M_{01} describes the propagation from air (refractive index $n_0 \approx 1$) to the outer coating layer and M_{1s} describes the propagation from the substrate to the adjacent coating layer.

The reflection coefficient is given by (from Eq. 2.48)

$$r_{\text{DBR}} = -\frac{(M_{\text{DBR}})_{12}}{(M_{\text{DBR}})_{22}} = \frac{-n_1^{2N+2} + n_s n_2^{2N}}{n_1^{2N+2} + n_s n_2^{2N}} \quad (\text{A.9})$$

and the transmission coefficient is given by (from Eq. 2.47)

$$t_{\text{DBR}} = (M_{\text{DBR}})_{11} - \frac{(M_{\text{DBR}})_{12}(M_{\text{DBR}})_{21}}{(M_{\text{DBR}})_{22}} = \frac{i2n_1^{N+1}n_2^N}{n_1^{2N+2} + n_s n_2^{2N}}, \quad (\text{A.10})$$

with properties

$$t_{\text{DBR}} = i |t_{\text{DBR}}| \quad (\text{A.11})$$

and for $n_1 > n_2$, n_s

$$r_{\text{DBR}} = -|r_{\text{DBR}}|. \quad (\text{A.12})$$

For a lossless stack we have

$$|r_{\text{DBR}}|^2 + n_s |t_{\text{DBR}}|^2 = 1, \quad (\text{A.13})$$

where the transmission is scaled by n_s accounting for the change in intensity of an electromagnetic wave entering the stack from air and exiting it to the mirror substrate.

A.3 Derivation of Cavity Finesse

In Sec. 2.2.2 we have discussed, that in order for light to be amplified by a Fabry-Perot cavity with length L_c , its frequency needs to fulfill the resonance condition

$$\omega_N = N \frac{\pi c}{L_c} =: N \omega_{\text{FSR}} \quad (N \in \mathbb{N}_0), \quad (\text{A.14})$$

with speed of light c , and free spectral range ω_{FSR} . A commonly used figure of merit for the intra-cavity power enhancement is the cavity finesse, defined as

$$\mathcal{F} := \frac{\omega_{\text{FSR}}}{\Delta\omega}. \quad (\text{A.15})$$

The cavity linewidth $\Delta\omega$ is defined as the full width at half maximum

$$|E_c(\Delta\omega/2)|^2 = \frac{1}{2} \max(|E_c|^2). \quad (\text{A.16})$$

Plugging in the expression for the circulating field inside the cavity E_c (Eq. 2.56) yields

$$1 + r_1^2 r_2^2 - 2r_1 r_2 \cos(2kL) = 2 + 2r_1^2 r_2^2 - 4r_1 r_2. \quad (\text{A.17})$$

By making use of the dispersion relation $\omega = ck$, with wavenumber k , we express the phase factor as $\cos(2kL) = \cos(2\omega L/c)$. With $\omega = \omega_c + \Delta\omega/2$ follows $2\omega L/c = N2\pi + \Delta\omega L/c$ and applying the identity $\cos(x+y) = \cos(x)\cos(y) - \sin(x)\sin(y)$ gives $\cos(2kL) = \cos(\Delta\omega L/c)$. Plugging this into Eq. A.17 gives

$$\begin{aligned} 1 + r_1^2 r_2^2 - 2r_1 r_2 \cos(\Delta\omega L/c) &= 2 + 2r_1^2 r_2^2 - 4r_1 r_2 \\ 2r_1 r_2 \cos(\Delta\omega L/c) &= -1 - r_1^2 r_2^2 + 4r_1 r_2 \\ 2r_1 r_2 [1 - 2\sin^2(\Delta\omega L/2c)] &= -1 - r_1^2 r_2^2 + 4r_1 r_2 \\ \sin^2(\Delta\omega L/2c) &= \frac{(1 - r_1 r_2)^2}{4r_1 r_2}, \end{aligned}$$

with cavity mirror reflection coefficients r_1, r_2 . We apply definitions Eq. A.14-A.15 to the previous expression and get for the finesse

$$\mathcal{F} = \frac{\pi}{2 \arcsin\left(\frac{1-r_1 r_2}{2\sqrt{r_1 r_2}}\right)} \approx \frac{\pi}{1 - r_1 r_2}. \quad (\text{A.18})$$

The approximation, made in the last step, applies to the case of highly reflective cavity

mirrors $r_1, r_2 \approx 1$. Taylor expanding the denominator $1 - r_1 r_2$ yields $\mathcal{F} \approx 2\pi / (2 - r_1^2 - r_2^2)$.

A.4 Maxwell Stress Tensor

The classical coupling between an object containing charges and light is a consequence of the Lorentz force

$$\vec{F} = q \left(\vec{E} + \vec{v} \times \vec{B} \right), \quad (\text{A.19})$$

with charge q , velocity of charge \vec{v} , electric field \vec{E} , and magnetic field \vec{B} . By applying Maxwell's equations [72] one can replace q and $q\vec{v}$ in the Lorentz force in terms of \vec{E} and \vec{B} , resulting in the expression

$$\vec{f} + \varepsilon_0 \mu_0 \frac{\partial \vec{S}}{\partial t} = \nabla \cdot \overleftrightarrow{T}, \quad (\text{A.20})$$

where \vec{f} is the Lorentz force per unit volume, $\vec{S} = \vec{E} \times \vec{B} / \mu_0$ is the momentum per unit volume carried by the electromagnetic field, known as Poynting vector, and

$$\overleftrightarrow{T} = \varepsilon_0 \vec{E} \otimes \vec{E} + \frac{1}{\mu_0} \vec{B} \otimes \vec{B} - \frac{1}{2} (\varepsilon_0 E^2 + \mu_0 H^2) \overleftrightarrow{I}. \quad (\text{A.21})$$

is the Maxwell stress tensor, with vacuum permittivity ε_0 and vacuum permeability μ_0 . The double arrow indicates a second order tensor, which can be represented by a 3×3 matrix. \overleftrightarrow{I} corresponds to the identity matrix.

The mechanical force exerted by an electromagnetic field on a volume V of a medium follows from integrating Eq. A.20 over V

$$\vec{F} = \int_V dV \nabla \cdot \overleftrightarrow{T} - \varepsilon_0 \mu_0 \int_V dV \frac{\partial \vec{S}}{\partial t}. \quad (\text{A.22})$$

For a plane electromagnetic wave of the form

$$E_y = \text{Re} \left[E_0 e^{i(\pm kx - \omega t)} \right] \quad (\text{A.23})$$

$$B_z = \text{Re} \left[B_0 e^{i(\pm kx - \omega t)} \right], \quad (\text{A.24})$$

with wavenumber k , frequency ω , direction of propagation along the x -axis, and time t we have for the average force per cycle of oscillation

$$\langle F \rangle = \int_V dV \langle \nabla \cdot \vec{T} \rangle = \oint_{\mathcal{J}} d\mathcal{S} \langle \vec{T} \rangle \cdot \vec{n}, \quad (\text{A.25})$$

where the second expression follows from Stokes' theorem. The surface enclosing V is denoted by \mathcal{J} , which is characterized by its normal vector \vec{n} . The cycle average for the second term in Eq. A.22 vanishes. Expressing \vec{T} (Eq. A.21) element-wise

$$T_{ij} = \varepsilon_0 \left(E_i E_j - \frac{1}{2} \delta_{ij} E^2 \right) + \frac{1}{\mu_0} \left(B_i B_j - \frac{1}{2} \delta_{ij} B^2 \right) \quad (\text{A.26})$$

and substituting the plane wave expressions (Eq. A.23-A.24) gives

$$T_{xx} = -\frac{1}{2} \left(\varepsilon_0 E_y^2 + \frac{1}{\mu_0} B_z^2 \right). \quad (\text{A.27})$$

From Faraday's law [72]

$$\nabla \times \vec{E} = -\frac{\partial \vec{B}}{\partial t} \quad (\text{A.28})$$

together with the dispersion relation $\omega = ck$ follows

$$B_0 = \pm E_0/c, \quad (\text{A.29})$$

where positive (negative) sign holds for right (left) traveling wave. In the case of a stratified medium (see Sec. 2.2.1), the electromagnetic field at location x is given by

$$\begin{aligned} E_y &= \text{Re} \left[(A e^{ikx} + B e^{-ikx}) e^{-i\omega t} \right] \\ B_z &= \text{Re} \left[(A e^{ikx} - B e^{-ikx}) e^{-i\omega t} \right] / c. \end{aligned}$$

Here B_z follows from E_y by applying Eq. A.29. Plugging these expressions in Eq. A.27 and time averaging gives

$$\langle T_{xx} \rangle = -\frac{\varepsilon_0}{2} (A^2 + B^2), \quad (\text{A.30})$$

where we have made use of $c = 1/\sqrt{\varepsilon_0\mu_0}$. The mixed terms vanish due to the different signs of the left traveling components $\propto B$.

Let us consider the case of a dielectric membrane inside a cavity (see Sec. 2.2.3), where A and B are the right and left traveling field amplitudes on the left side of the membrane. Similarly, C and D are the right and left traveling field amplitudes on the right side of the membrane. The force acting on the membrane in this case is given by (from Eqs. A.25, A.30)

$$\langle F_x \rangle = \oint_{\mathcal{J}} d\mathcal{S} \langle T_{xx} \rangle n_x = \frac{\varepsilon_0 \mathcal{J}}{2} [A^2 + B^2 - C^2 - D^2] \quad (\text{A.31})$$

or in terms of optical power by

$$\langle F_x \rangle = \frac{1}{c} (P_A + P_B - P_C - P_D) \quad (\text{A.32})$$

with $P_A = c\varepsilon_0 \mathcal{J} A^2/2$ and so on.

Appendix B

Fabrication & Mechanical Characterization of Si₃N₄ Trampoline Resonators

B.1 Power Spectral Density Measurement with a Lock-In Amplifier

Here we present the analysis behind the spectral density measurement of a thermally driven trampoline resonator discussed in Sec. 3.3.2. The resonator's trajectory is given by [117, 164]

$$\begin{aligned}x(t) &= x_0(t) \cos [\Omega_m t + \phi(t)] \\x(t) &= x_0(t) \cos [\phi(t)] \cos (\Omega_m t) - x_0(t) \sin [\phi(t)] \sin (\Omega_m t) \\x(t) &\equiv X_1(t) \cos (\Omega_m t) - X_2(t) \sin (\Omega_m t),\end{aligned}\tag{B.1}$$

with time dependent amplitude $x_0(t)$ and phase $\phi(t)$, and oscillation frequency Ω_m . When measuring this signal with our lock-in amplifier (Zurich Instruments HF2, see Sec. 3.2), the output (once calibrated, see Sec. 3.2.2) are the two root-mean-square quadrature time traces $X_1(t)/\sqrt{2}$ and $X_2(t)/\sqrt{2}$, with

$$X_1(t) \equiv x_0(t) \cos[\phi(t)]$$

$$X_2(t) \equiv x_0(t) \sin[\phi(t)].$$

In order to see how we can extract the signal's power spectral density (PSD) from these two quantities, we evaluate the general expression of the double-sided PSD (see Sec. [2.1.2.1](#))

$$S_{xx}(\Omega) = \int_{-\infty}^{\infty} d\tau e^{-i\Omega\tau} \langle x(t)x^*(t-\tau) \rangle \quad (\text{B.2})$$

for the above given signal $x(t)$. Hereby, we make use of abbreviations

$$S_t := \sin(\Omega_m t)$$

$$C_t := \cos(\Omega_m t)$$

and trigonometric identities

$$\begin{aligned} S_a S_b &= \frac{1}{2} (C_{a-b} - C_{a+b}) \\ C_a C_b &= \frac{1}{2} (C_{a-b} + C_{a+b}) \\ S_a C_b &= \frac{1}{2} (S_{a-b} + S_{a+b}), \end{aligned}$$

with times a, b . For the autocorrelation function follows

$$\begin{aligned} \langle x(t)x^*(t-\tau) \rangle &= \langle [X_1(t) C_t - X_2(t) S_t] [X_1(t-\tau) C_{t-\tau} - X_2(t-\tau) S_{t-\tau}] \rangle \\ &= \frac{1}{2} \langle X_1(t) X_1(t-\tau) + X_2(t) X_2(t-\tau) \rangle C_\tau \\ &\quad + \frac{1}{2} \langle X_1(t) X_2(t-\tau) - X_1(t-\tau) X_2(t) \rangle S_\tau. \end{aligned}$$

Terms proportional to $S_{2t-\tau}$, $C_{2t-\tau}$ don't contribute since their time average is zero. This is because $\Omega_m \gg \Gamma_m$ (see Sec. [3.3.2](#)), where $1/\Gamma_m$ is the timescale on which $X_1(t)$, $X_2(t)$

change. For the double-sided PSD follows

$$\begin{aligned}
S_{xx}(\Omega) &= \frac{1}{4} \int_{-\infty}^{\infty} d\tau \left[e^{-i(\Omega-\Omega_m)\tau} + e^{-i(\Omega+\Omega_m)\tau} \right] \langle X_1(t) X_1(t-\tau) + X_2(t) X_2(t-\tau) \rangle \\
&\quad - \frac{i}{4} \int_{-\infty}^{\infty} d\tau \left[e^{-i(\Omega-\Omega_m)\tau} + e^{-i(\Omega+\Omega_m)\tau} \right] \langle X_1(t) X_2(t-\tau) - X_1(t-\tau) X_2(t) \rangle \\
&= \frac{1}{4} \int_{-\infty}^{\infty} d\tau \left[e^{-i(\Omega-\Omega_m)\tau} + e^{-i(\Omega+\Omega_m)\tau} \right] \langle [X_1(t) + iX_2(t)] [X_1(t-\tau) - iX_2(t-\tau)] \rangle
\end{aligned}$$

and for the single-sided PSD

$$S_x(\Omega) = \frac{1}{2} \int_{-\infty}^{\infty} d\tau e^{-i(\Omega-\Omega_m)\tau} \langle [X_1(t) + iX_2(t)] [X_1(t-\tau) - iX_2(t-\tau)] \rangle.$$

By defining $Y \equiv [X_1(t) + iX_2(t)] / \sqrt{2}$ we have

$$S_x(\Omega) = S_{YY}(\Omega - \Omega_m). \quad (\text{B.3})$$

From Parseval's theorem (Eq. 2.19)

$$\langle |x(t)|^2 \rangle = \int_0^\infty \frac{d\Omega}{2\pi} S_x(\Omega) = \int_{-\infty}^\infty \frac{d\Omega}{2\pi} S_{YY}(\Omega - \Omega_m) = \langle |Y(t)|^2 \rangle, \quad (\text{B.4})$$

follows the root mean square (rms) displacement, which is a measure for the average displacement amplitude

$$x_{\text{rms}} = \sqrt{\langle |x(t)|^2 \rangle} = \sqrt{\langle X_1^2(t) + X_2^2(t) \rangle / 2}. \quad (\text{B.5})$$

Alternatively, we can directly calculate this value based on its definition [68]

$$x_{\text{rms}}^2 := \lim_{T \rightarrow \infty} \frac{1}{T} \int_{-T/2}^{T/2} dt |x(t)|^2. \quad (\text{B.6})$$

Applying this to the signal given by Eq. B.1 yields

$$x_{\text{rms}}^2 = \lim_{T \rightarrow \infty} \frac{1}{T} \int_{-T/2}^{T/2} dt [X_1^2(t) \cos^2(\Omega_m t) + X_2^2(t) \sin^2(\Omega_m t)], \quad (\text{B.7})$$

where the term $\propto 2 \cos(\Omega_m t) \sin(\Omega_m t) = \sin(2\Omega_m t)$ was omitted, since its time average is zero. We can further evaluate the integral by exploiting the fact that the amplitudes $X_1(t)$, $X_2(t)$ change on vastly different time scales compared to the oscillatory terms $\sin(\Omega_m t)$, $\cos(\Omega_m t)$ (see Sec. 3.3.2); the former change on a characteristic time scale set by the mechanical ring-down time $\tau_m = 285$ s, and the latter oscillate with period $1/\Omega_m = 4$ μ s. Therefore, we can divide the time traces into shorter subsets of length $\Delta t = T/N$, with $1/\Omega_m \ll \Delta t \ll \tau_m$, during which the amplitudes are assumed to be constant. Applying this to the first integral in the above given expression yields

$$\begin{aligned} \int_{-T/2}^{T/2} dt X_1^2(t) \cos^2(\Omega_m t) &= \sum_{i=1}^N X_1^2(t_i) \int_{-T/2+(i-1)\Delta t}^{T/2-(N-i)\Delta t} dt \cos^2(\Omega_m t) \\ &= \frac{1}{2} \sum_{i=1}^N X_1^2(t_i) \Delta t \\ &= \frac{1}{2} \int_{-T/2}^{T/2} dt X_1^2(t) \end{aligned}$$

An equivalent relation holds for the second term in Eq. B.7, so that we have

$$x_{\text{rms}}^2 = \frac{1}{2} \lim_{T \rightarrow \infty} \frac{1}{T} \int_{-T/2}^{T/2} dt [X_1^2(t) + X_2^2(t)] = \frac{1}{2} \langle X_1^2(t) + X_2^2(t) \rangle, \quad (\text{B.8})$$

which is the same as Eq. B.5.

B.2 Gas Damping

At ambient pressure the mechanical performance (see Sec. 3.3.1) of our trampoline resonators is limited by gas damping. Here we give an estimate for the pressure dependent quality factor Q_m , based on a model including drag force gas damping [165, 166] and squeeze film gas damping [167, 168]. The former is a consequence of a pressure gradient created by the resonator in its environment while it oscillates¹. The latter occurs if the resonator's perimeter is comparable to its distance from a near by surface; in this case, the resonator might do work on the surrounding gas in two different ways: First, by compressing the gas and second, by shuttling gas in and out of the “thin film” area between resonator and neighboring surface.

The estimation presented in the following, applies to the free molecular flow regime, where the gas mean free path² λ_{gas} exceeds the characteristic length scale of the resonator b_c by ~ 10 [166, 169]. The ratio of these two length scales is known as the Knudsen number

$$\text{Kn} = \frac{\lambda_{\text{gas}}}{b_c} = \frac{k_B T}{b_c \sqrt{2\sigma P}}, \quad (\text{B.9})$$

with Boltzmann constant k_B , temperature T , scattering cross section of gas molecules σ , and gas pressure P .

Similar to the analysis presented in Sec. 2.1.1 for the intrinsic mechanical quality factor, we will estimate the quality factor resulting from gas damping. The mechanical energy of the resonator (average over cycle of oscillation $\propto \cos(\Omega_m t)$) is given by (Sec. 2.1.1)

$$U_m = \frac{1}{2} \rho_m \Omega_m^2 d \iint dx dy \zeta^2(x, y), \quad (\text{B.10})$$

with resonator material density ρ_m , mechanical resonance frequency $\Omega_m/2\pi$, resonator thickness d , and trampoline out-of-plane displacement $\zeta(x, y)$. The gas drag force per unit area is given by [166]

$$f(x, y) = k_m P \zeta(x, y) \frac{d}{dt} \cos(\Omega_m t), \quad (\text{B.11})$$

¹Alternatively, this can be seen as consequence of the different relative velocities between gas molecules and cantilever for the resonator side that moves towards the gas molecules and the side that moves away from them.

²To give an example, the mean free path of air with an ambient pressure of ~ 1 Torr is ~ 10 cm.

where under the assumption of elastic reflection of the gas molecules from the resonator and equal temperatures of gas and vacuum chamber wall, the damping coefficient is given by

$$k_m = \frac{4.2}{v_{\text{gas}}} = 4.2 \sqrt{\frac{m_{\text{gas}}}{2k_B T}}, \quad (\text{B.12})$$

with mean gas velocity v_{gas} and gas mass m_{gas} . The prefactor of 4.2 is a consequence of the rectangular cross section and a small thickness compared to the lateral extent of the resonator [166]. The work done by the resonator on the gas per cycle of oscillation³ is given by

$$\Delta U_{\text{dr}} = \pi k_m \Omega_m P \iint dx dy \zeta^2(x, y). \quad (\text{B.13})$$

For the quality factor purely limited by drag force gas damping we have

$$Q_{\text{dr}} = 2\pi \frac{U_m}{\Delta U_{\text{dr}}} = \frac{\rho_m \Omega_m d}{k_m P}. \quad (\text{B.14})$$

The quality factor, purely limited by squeeze film damping is related to the previous expression by [167, 168]

$$Q_{\text{sq}} = 16\pi \left(\frac{h}{u} \right) Q_{\text{dr}}, \quad (\text{B.15})$$

where h is the distance between resonator and neighboring surface and u is the resonator's perimeter.

In the absence of gas damping the resonator is limited by its intrinsic quality factor Q_0 . Therefore, we have for the overall mechanical quality factor

$$\frac{1}{Q_m} = \frac{1}{Q_0} + \frac{1}{Q_{\text{dr}}} + \frac{1}{Q_{\text{sq}}}. \quad (\text{B.16})$$

³Integrating the time dependency over one cycle of oscillation gives $\int_0^{2\pi/\Omega_m} dt \left[\frac{d}{dt} \cos(\Omega_m t) \right]^2 = \pi \Omega_m$.

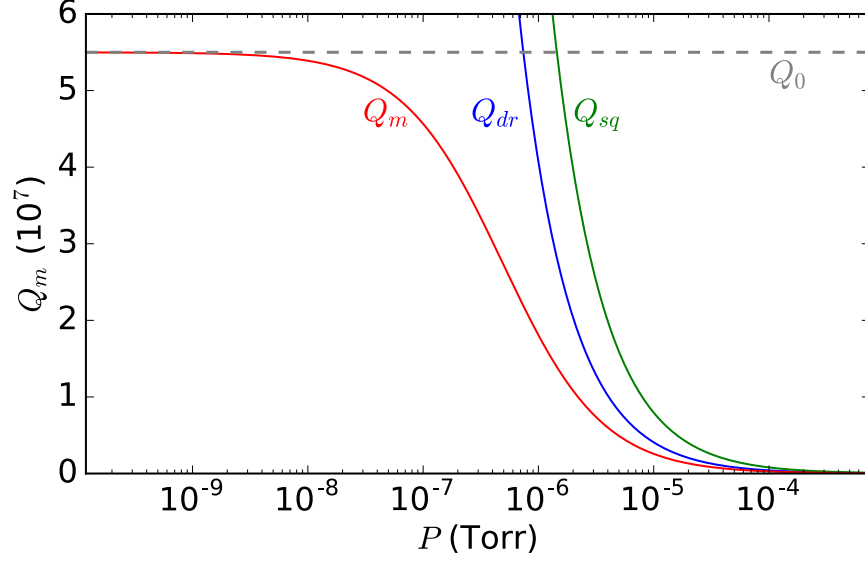


Figure B.1: Mechanical quality factor Q_m as a function of air pressure P for a trampoline resonator (see text for parameters). Gray curve shows an assumed intrinsic quality factor $Q_0 = 5.5 \times 10^7$ (absence of gas molecules). Green and blue curves show an estimate for respectively, Q_m purely limited by either squeeze film gas damping Q_{sq} or drag force gas damping Q_{dr} . Red curve shows the resulting mechanical quality factor $Q_m = 1 / (Q_0^{-1} + Q_{dr}^{-1} + Q_{sq}^{-1})$.

Figure B.1 shows Q_m (red curve) versus P (Eq. B.16) for a trampoline resonator (see Fig. 3.2) with window size $l = 3000 \mu\text{m}$, pad diameter $d = 100 \mu\text{m}$, tether width $a = 2.1 \mu\text{m}$, thickness $d = 80 \text{ nm}$, resonance frequency $\Omega_m / (2\pi) = 40.8 \text{ kHz}$ (fundamental out of plane mode), Si_3N_4 density $\rho_m = 2700 \text{ kg/m}^3$, trampoline perimeter $u \approx 4(\sqrt{2}l + d)$, and separation between trampoline and underlying support plate $h = 675 \mu\text{m}$. Furthermore, we consider temperature $T = 293 \text{ K}$, mass of air molecules $m_{\text{gas}} = 48.1 \times 10^{-27} \text{ kg}$ [166], and scattering cross section of air molecules $\sigma = 1.76 \times 10^{-19} \text{ m}^2$ [166]. The threshold set for the Q_m increase by the drag force gas damping (blue curve) and squeeze film gas damping (green curve) differ by less than a factor of two. In combination they cause Q_m to transition from 0 to an assumed intrinsic value $Q_0 = 5.5 \times 10^7$ in the range of $10^{-4} \text{ Torr} < P < 10^{-9} \text{ Torr}$. Note that $\text{Kn} \gg 10$ over the entire P range plotted in Fig. B.1, regardless of employing either d or a as critical dimension b_c in Eq. B.9.

The estimate presented in Fig. B.1 suggests, that the mechanical performance of the trampoline resonators presented in Sec. 3.3 might be limited by gas damping. In previous studies [169, 63, 96], similar models have been applied to successfully describe the measured

Q_m versus P dependency for Si_3N_4 nanobeam resonators with $\Omega_m/(2\pi)$ of a few MHz and $Q_m \sim 10^6$. In these studies Q_m was limited by gas damping down to pressures of $10^{-4} - 10^{-3}$ Torr. The difference of 10^4 for the limiting pressure between these studies and the here presented estimation is consistent with the trampoline's lower $\Omega_m/(2\pi)$, larger Q_m , and larger u . Studies of similar resonators as the one considered here [39, 57], mention slight influence of gas damping at $P \sim 10^{-7}$ Torr.

Appendix C

Vacuum Fabry-Perot Cavity with Incorporated Si_3N_4 Trampoline Resonator

C.1 Transverse Electromagnetic Cavity Modes

A symmetric spherical cavity formed by two spherical mirrors with identical radii of curvature R_c can stably confine light if the cavity length $L_c \leq 2R_c$. The resonant spectrum of complex electric field amplitudes in this case is given by the Hermite-Gaussian modes [109]

$$E_{mn}(r, z) = E_0 \frac{w_0}{w(z)} H_m \left(\frac{\sqrt{2}x}{w(z)} \right) H_n \left(\frac{\sqrt{2}y}{w(z)} \right) \exp \left[-\frac{r^2}{w^2(z)} \right] \exp [-j\varphi_{mn}(r, z)] \quad (\text{C.1})$$

with phase

$$\varphi_{mn}(r, z) = kz + k \frac{r^2}{2R(z)} + (m + n + 1) \zeta(z) \quad (\text{C.2})$$

and

$$\begin{aligned}
w_0 &= \sqrt{\frac{\lambda z_R}{\pi}} && \text{(mode waist)} \\
w(z) &= w_0 \sqrt{1 + \left(\frac{z}{z_R}\right)^2} && \text{(mode radius)} \\
R(z) &= z \left[1 + \left(\frac{z_R}{z}\right)^2 \right] && \text{(mode radius of curvature)} \\
\zeta(z) &= \arctan\left(\frac{z}{z_R}\right) && \text{(Gouy phase)}
\end{aligned}$$

The indices $m, n \in \mathbb{N}$ represent the transverse mode order which is equal to the number of field nodes along the two directions orthogonal to the cavity axis: x and y .

The Rayleigh range z_R can be calculated from the boundary condition

$$R_c \stackrel{!}{=} \frac{L_c}{2} \left[1 + \left(\frac{2z_R}{L_c} \right)^2 \right]. \quad (\text{C.3})$$

resulting in

$$z_R = \sqrt{\frac{L_c}{2} \left(R_c - \frac{L_c}{2} \right)} \quad (\text{C.4})$$

and the cavity waist

$$w_0 = \sqrt{\frac{\lambda}{\pi} \sqrt{\frac{L_c}{2} \left(R_c - \frac{L_c}{2} \right)}}. \quad (\text{C.5})$$

The cavity resonance condition requires that $\varphi_{mn}(r, z)$ is constant across the mirror surfaces and that the wave is invariant under translations of $2L_c$ (cavity roundtrip) which can be expressed as

$$\varphi_{mn}(0, z) = 2kL_c + 4(m+n+1)\zeta\left(\frac{L_c}{2}\right) \stackrel{!}{=} l \times 2\pi \quad (\text{C.6})$$

where $l \in \mathbb{N}$ is the longitudinal mode order giving the number of field antinodes along the cavity axis. With the above found expression for z_R follows

$$L_{lmn} = \frac{1}{k} \left[l\pi + 2(m+n+1) \arctan\left(\frac{1}{\sqrt{2R_c/L_c - 1}}\right) \right] \quad (\text{C.7})$$

which resembles the spectrum of cavity resonance lengths. To characterize the modes of our cavity (see Sec. 4.2) we periodically compress its length by a small amount ΔL_c which enables us to observe modes of a few consecutive longitudinal mode orders. In the identification of these modes we are interested only in the relative change of l with respect to its initial value $l_0 = \text{Round}(kL_c/\pi) =: kL_0/\pi$. By replacing $l \rightarrow l_0 + l$ we can write $L_{lmn} = L_0 - \Delta L_{lmn}$ where ΔL_{lmn} is given by Eq. C.7. For a homogeneous and isotropic cavity the spectrum is degenerate in m, n and we can replace $\Delta L_{lmn} \rightarrow \Delta L_{lm+n}$ where only a change in the added transverse mode indices results in a length change. This degeneracy is lifted for example in the case of slightly elliptic cavity mirrors or birefringent mirror or cavity materials [43].

Beam Diameter

The beam diameter is defined as the diameter where the optical power is reduced to $1/e^2$ from its peak level. For a Gaussian beam (TEM₀₀) with intensity distribution

$$I(r, z) = E_0^2 \frac{w_0^2}{w^2(z)} \exp \left[-\frac{2r^2}{w^2(z)} \right] \quad (\text{C.8})$$

the beam diameter is therefore given by $2w(z)$.

C.2 Cavity Finesse Tuning by Mirror Etching

Mirrors formed by a thin metal (e.g. silver) film deposited onto a glass slab or polished substrate, are omnipresent in everyday life and an important constituent of optical setups. When it comes to precisely engineered reflection and transmission spectra in combination with low optical losses (as required for optical cavities), the component of choice commonly is a dielectric distributed Bragg reflector (DBR). The typical composition of a DBR is sketched in Fig. C.1(a) where alternating layers of two different dielectric materials (here Ta₂O₅ and SiO₂) are deposited on top of a glass substrate. This structure forms an efficient mirror for light of wavelength λ if the following requirements are met: the optical thickness (physical thickness multiplied by the material's refractive index n) of each layer equals $\lambda/4$, which results in constructive interference between the portions of light reflected at each interface.

Here the reflected fraction is bigger for higher contrast in the materials' refractive indices. The overall reflection increases for a larger number of dielectric layers. Furthermore, the penetration depth of light into the mirror is reduced when the stack is terminated with the high index material, which in turn minimizes optical loss. The expression for the DBR's reflectivity in this case is given by (see Appendix [A.2](#))

$$R_N = |r_{\text{DBR}}|^2 = \left(\frac{-n_1^{2N+2} + n_s n_2^{2N}}{n_1^{2N+2} + n_s n_2^{2N}} \right)^2 \quad (\text{C.9})$$

where n_1 , n_2 (with $n_1 > n_2$) are the refractive indices of the dielectrics, n_s is the refractive index of the glass substrate and N is the number of dielectric double layers. Two additional and important requisites are low optical material losses and low scattering losses at interfaces and at the DBR surface, which demand good material quality, a deposition process that yields smooth layers, and a superpolished substrate (roughness ~ 0.1 nm). The DBRs forming our cavity (designed for $\lambda = 1550$ nm) are manufactured by Advanced Thin Films (ATFilms) and comprise $N=20$ double layers of Ta_2O_5 ($n_1 = 2.10$, thickness 184.5 nm) and SiO_2 ($n_2 = 1.47$, thickness 263.6 nm) and an additional Ta_2O_5 layer (which terminates the stack). During fabrication the dielectric layers are deposited by ion beam sputtering onto a fused silica substrate ($\varnothing=0.3$ inch) which was previously superpolished [[170](#)]. The resulting optical losses per mirror are specified by ATFilms to be 2 ppm.

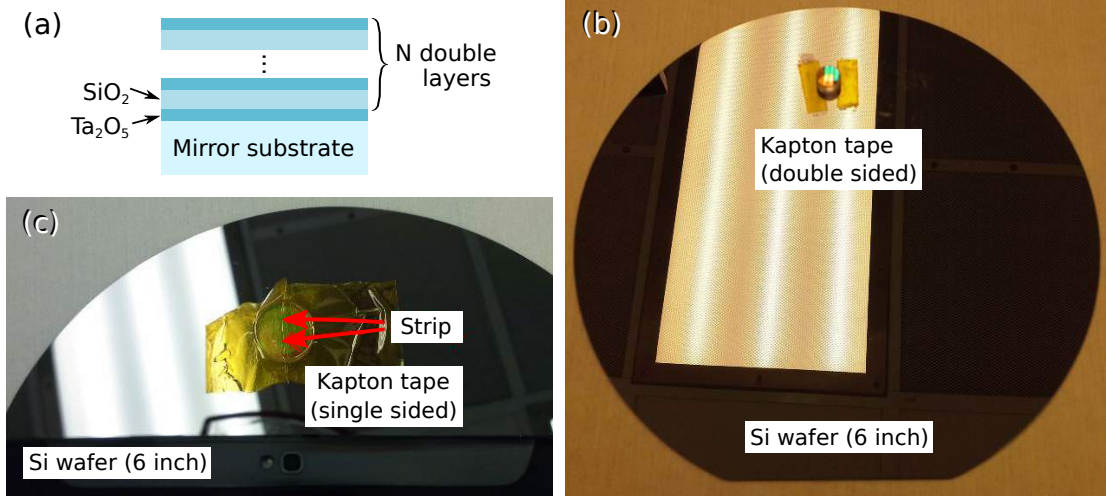


Figure C.1: Schematic layer structure of a distributed Bragg reflector (DBR) and mounting of a DBR on a 6 inch Si wafer for reactive ion etching. (a) Sketch of a DBR comprising N alternating double layers of Ta₂O₅ and SiO₂ and an additional Ta₂O₅ layer deposited onto a glass substrate. The optical thickness of each layer (physical thickness times the material's refractive index) is $\lambda/4$ which causes the portions of light reflected at each interface to interfere constructively. (b) A DBR is attached to a Si wafer by double sided Kapton tape for loading into a reactive ion etch chamber. (c) Etch rate estimation on a test mirror by covering most of the mirror surface by Kapton tape and exposing only a stripe of $\approx 200 \mu\text{m}$ width to the etch plasma. This enables measuring the etched profile by a contact profilometer.

In an initial step of characterization, we assembled a cavity from two of the above described mirrors with radius of curvature $R_c = 2.5 \text{ cm}$, cavity length $L_c = 3 \text{ cm}$, resulting TEM₀₀ mode field diameter at the cavity center $2w_0 = 156 \mu\text{m}$, and mode diameter at each mirror $2w_c = 246 \mu\text{m}$. Right after the assembly we measured a ringdown time $\tau_c = 29 \mu\text{s}$ corresponding to cavity finesse $\mathcal{F} = \pi c \tau_c / L_c = 910,000$ (see Sec. 4.2.1 for method), which, over a few days, dropped to $\mathcal{F} = 470,000$, where it remained until the disassembly of the cavity¹.

While higher finesse enables stronger interaction between photons and objects, such as one of our Si₃N₄ structures, it entails more challenging working conditions. This is mainly due to the reduced resonance linewidth (see Sec. A.3) which makes it both harder to align the cavity²

¹The cavity was not encapsulated for periods of time (minutes to hours) and exposed to the ambient lab environment. This might have caused a single or multiple dust particle(s) to stuck to the mirrors in the region of the cavity mode.

²During alignment we sweep the cavity length to scan for optical resonances (see Sec. 4.2.1). Hereby, the sweep rate should be slow enough to enable a measurable amount of light to be transferred to the cavity mode. For a narrower resonance this requires a slower sweep rate. This in turn results in an increased exposure of

and to permanently stabilize (or lock) the laser frequency and the cavity resonance with respect to each other (see Chapter 5). For a cavity formed by two mirrors with reflectivities R_1 and R_2 the finesse is given by $\mathcal{F} = 2\pi/(2 - R_1 - R_2)$ (lossless case, see Sec. (Sec. A.3)). Together with Eq. C.9 this suggests to reduce the number of dielectric layer pairs N as a means to reduce \mathcal{F} . This is realized by etching away dielectric layers from the cavity DBR's [171].

Similar to the method presented in Ref. [171] we remove one double layer from the dielectric coating by starting with reactive ion etching (RIE) of the Ta_2O_5 layer and then removing the SiO_2 layer in hydrofluoric acid (HF). This approach is well suited since the Ta_2O_5 acts as etch stop material for the HF etch and therefore enables the controlled removal of individual layer pairs.

Before etching the DBR in the reactive ion etcher (Applied Precision 5000) of the McGill Nanotool - Microfab cleanroom we perform an O_2 plasma clean of the etch chamber (see Table. 3.1 for recipe). Figure C.1(b) shows the DBR attached by double-sided Kapton tape to a 6 inch silicon wafer (necessary in order to insert the mirror into the etch chamber). Due to the overall thickness of 4.2 mm the Si wafer with attached DBR can not be loaded from a cassette through the front of our RIE machine (as is standard procedure), instead it has to be inserted manually into the loadlock chamber by opening the chamber's top³. From there, the wafer is transferred automatically to the etch chamber (a bigger mirror of thickness 6.4 mm didn't fit through the loading port of the etch chamber) and etched.

Figure C.1(b) shows a DBR, similarly mounted as described in the previous paragraph, which is mostly covered by Kapton tape except a $\approx 200\ \mu\text{m}$ wide strip that is exposed to the etch plasma. This enables us to determine the etch rate by means of a mechanical profiler (Ambios XP-200) that we use to scan across the etch profile. Our RIE recipe (based on Ref. [172]), wet etch recipe, and measured etch rates are presented in Table C.1. Here it can be seen that the RIE etches the SiO_2 about four times faster than the Ta_2O_5 . We accordingly chose an etch time of 11 min, which removes all the Ta_2O_5 and $\approx 20\ \text{nm}$ of the underlying

the system to environmental noise (e.g. mechanical vibrations, thermal drift), which is more pronounced on longer time scales and causes fluctuations in the resonance length of the cavity. Therefore, it is harder to meet the resonance condition of a higher finesse/narrower linewidth cavity. In addition, the amount of light reflected from and transmitted through the cavity is more sensitive to optical loss.

³Thanks to Don Berry for doing this over and over and over again!

SiO₂ layer. Subsequently, we rinse the mirror in DI water and transfer it to HF 10:1 where we leave it for 6 min. This ensures complete removal of the SiO₂. We transfer the mirror to a beaker filled with DI water, from which we take it out while rinsing first with isopropanol then methanol. Finally, we dry the mirror in a stream of nitrogen. The procedure is then repeated until the desired mirror reflectivity and cavity finesse is realized.

	RIE recipe	Wet etch recipe
	Ar 25 sccm CHF3 25 sccm CF4 15 sccm RF Power 200 W Pressure 30 mtorr	HF 10:1
Etch time	11 min	6 min
Ta ₂ O ₅ etch rate	18 nm/min	X
SiO ₂ etch rate	65 nm/min	> 43 nm/min

Table C.1: Etch recipes and etch rates for reactive ion etching [172] and wet etching of dielectric mirror layers.

Table C.2 shows parameters for 4 cavity configurations which are formed by mirrors that have different numbers of dielectric layers (N_1 : input mirror layer number, N_2 : output mirror layer number) in consequence of repeated etching.

	Cavity 1	Cavity 2	Cavity 3	Cavity 4
N_1	20	17	15	14
N_2	20	17	15	19
\mathcal{F}	470,000	86,000	24,000	20,000
L_c	3 cm	3 cm	3 cm	4.7 cm
R_c	2.5 cm	2.5 cm	2.5 cm	2.5 cm
$2w_0$	156 μ m	156 μ m	156 μ m	110 μ m
$2w_c$	246 μ m	246 μ m	246 μ m	446 μ m

Table C.2: Parameters of cavities comprising DBR mirrors with different number of dielectric layer pairs as a result of etching: Number of double layers of input and backstop mirror N_1 and N_2 , measured cavity finesse \mathcal{F} , cavity length L_c , radius of curvature of cavity mirrors R_c , TEM₀₀ mode field diameter at the cavity center $2w_0$, and TEM₀₀ mode field diameter on the mirror surface w_c .

The cavity finesse characterization presented in the following two sections employs a “single port cavity” (Table C.2, Cavity 4) where mainly the reflectivity of the input mirror is

reduced, resulting in $\approx 98\%$ of light exiting through to input mirror which, e.g., can benefit the detection efficiency in the context of quantum limited sensing.

Appendix D

Simple Delay-Limited Sideband Locking with Heterodyne Readout

D.1 Reflection from an Asymmetric Cavity

Consider a cavity of length L with mirrors that are not identical, having field transmission coefficients it_1 and it_2 and reflection coefficients $-r_1$ and $-r_2$ (where t_i and r_i are real positive and $|t_i|^2 + |r_i|^2 \leq 1$). If the first mirror is driven by a field of amplitude E_{in} and angular frequency ω , the steady-state reflected field – a sum of the prompt reflection and all subsequent paths leaking from the input mirror – can be calculated from the resulting geometric series:

$$\frac{E_r}{E_{in}} = -r_1 + t_1^2 r_2 e^{-2i\omega L/c} + t_1^2 r_2 e^{-2i\omega L/c} (r_1 r_2 e^{-2i\omega L/c}) \quad (\text{D.1})$$

$$\begin{aligned} &+ t_1^2 r_2 e^{-2i\omega L/c} (r_1 r_2 e^{-2i\omega L/c})^2 + \dots \\ &= -r_1 + \frac{t_1^2 r_2 e^{-2i\omega L/c}}{1 - r_1 r_2 e^{-2i\omega L/c}} \end{aligned} \quad (\text{D.2})$$

In the high-finesse limit, this can be expanded in terms of the small transmission $t_i \ll 1$ and loss $\rho_i \equiv \sqrt{1 - r_i^2} \ll 1$, such that the overall reflection coefficient

$$r(\delta) \equiv \frac{E_r}{E_{in}} \approx \frac{t_1^2 \tau c / L}{1 + i2\tau\delta} - 1, \quad (\text{D.3})$$

where $\tau = \frac{2L/c}{\rho_1^2 + \rho_2^2}$ is the power ringdown time and $\delta = \omega - \omega_r$ is the detuning from the n^{th} resonance frequency $\omega_r = nc/2L$ (δ is also assumed small compared to the mode spacing $c/2L$).

D.2 Transfer Function from Laser Noise to Error Signal

D.2.1 Shorthand Notation

To save space and avoid typos, we adopt the following shorthand notation.

$$C_a, S_a \equiv \cos(\omega_a t), \sin(\omega_a t) \quad (\text{D.4})$$

$$C_{a\pm b}, S_{a\pm b} \equiv \cos(\omega_a t \pm \omega_b t), \sin(\omega_a t \pm \omega_b t) \quad (\text{D.5})$$

$$C_{a\pm b\psi}, S_{a\pm b\psi} \equiv \cos(\omega_a t \pm (\omega_b t + \psi)), \sin(\omega_a t \pm (\omega_b t + \psi)) \quad (\text{D.6})$$

$$C_{a\pm 2b\psi}, S_{a\pm 2b\psi} \equiv \cos(\omega_a t \pm (2\omega_b t + \psi)), \sin(\omega_a t \pm (2\omega_b t + \psi)) \quad (\text{D.7})$$

The diode and mixer steps discussed below involve nonlinear operations, and so (as a matter of algebraic taste) we save complex notation for the end of the calculation.

D.2.2 Propagating Laser Noise Through the Readout System

We proceed by adding a small “noise” term to the field from a laser, and then propagate this through the electro-optical modulator (EOM), cavity, photodiode, and mixers to determine the readout’s overall transfer function. Suppose the laser has a “noise” component at frequency ω , with amplitude and frequency modulation

$$\epsilon(t) = \epsilon_n \cos(\omega t) \quad (\text{D.8})$$

$$\Omega(t) = \Omega_n \cos(\omega t) \quad (\text{D.9})$$

for constants ϵ_n and Ω_n . In this case, the field (nominally of the noiseless form $\sqrt{P_l} \cos(\omega_l t)$ for laser frequency ω_l and power P_l) is $E(t) = \sqrt{P_l}(1 + \epsilon_n C_n) \cos(\omega_l t + \phi_n S_n)$, where $\phi_n \equiv \Omega_n/\omega$ is the phase modulation amplitude. If this passes through an electro-optical modulator (EOM)

driven by a voltage-controlled oscillator (VCO) output of the form $V_{VCO}(t) = V_e \sin(\omega_e t)$ (for constant V_e and frequency ω_e), E is further modified to

$$E(t) = \sqrt{P_l}(1 + \epsilon_n C_n + \epsilon_e S_e) \cos(\omega_l t + \phi_n S_n + \phi_e S_e), \quad (\text{D.10})$$

where $\phi_e = \eta_{EOM} V_{VCO}$ is the phase excursion for a “flat” EOM conversion efficiency η_{EOM} (units of rad/V), and we have included a small amount of “accidental” amplitude modulation ϵ_e due to imperfections in the EOM optics for generality. If we assume the modulations are small ($\epsilon_n, \epsilon_e, \phi_n, \phi_e \ll 1$), the field can be expanded to second order and rewritten in terms of a carrier at ω_l plus 12 sidebands:

$$\begin{aligned} \frac{E(t)}{\sqrt{P_l}} \approx & \left(1 - \frac{1}{4}\phi_e^2 - \frac{1}{4}\phi_n^2\right) \textcolor{red}{C}_l \\ & + \frac{1}{2}\epsilon_n (\textcolor{red}{C}_{l+n} + \textcolor{red}{C}_{l-n}) + \frac{1}{2}\phi_n (\textcolor{red}{C}_{l+n} - \textcolor{red}{C}_{l-n}) \\ & + \frac{1}{2}\epsilon_e (S_{l+e} - S_{l-e}) + \frac{1}{2}\phi_e (C_{l+e} - C_{l-e}) \\ & + \frac{1}{8}\phi_n^2 (\textcolor{red}{C}_{l+2n} + \textcolor{red}{C}_{l-2n}) + \frac{1}{4}\phi_n \epsilon_n (\textcolor{red}{C}_{l+2n} - \textcolor{red}{C}_{l-2n}) \\ & + \frac{1}{8}\phi_e^2 (C_{l+2e} + C_{l-2e}) + \frac{1}{4}\phi_e \epsilon_e (-2S_l + S_{l+2e} + S_{l-2e}) \\ & + \frac{1}{4}\phi_e \phi_n (\textcolor{blue}{C}_{l+e+n} - \textcolor{blue}{C}_{l+e-n} - C_{l-e+n} + C_{l-e-n}) \\ & + \frac{1}{4}\phi_n \epsilon_e (\textcolor{blue}{S}_{l+e+n} - \textcolor{blue}{S}_{l+e-n} - S_{l-e+n} + S_{l-e-n}) \\ & + \frac{1}{4}\phi_e \epsilon_n (\textcolor{blue}{C}_{l+e+n} + \textcolor{blue}{C}_{l+e-n} - C_{l-e+n} - C_{l-e-n}). \end{aligned} \quad (\text{D.11})$$

Now suppose these beams land on a cavity with either a resonance “ A ” tuned to the *carrier* at ω_l or a resonance “ B ” tuned to the *upper sideband* at $\omega_l + \omega_e$ (we track both options through the calculation, allowing the choice of scenarios afterward). In the limit of “large” VCO frequency ($\omega_e \gg \omega, 1/\tau$), only the red terms in Eq. (D.11) interact with resonance A and only the blue terms interact with resonance B , so the field reflected from

the cavity becomes

$$\begin{aligned}
\frac{-E(t)}{r_1\sqrt{P_l}} = & \left(1 - \frac{1}{4}\phi_e^2 - \frac{1}{4}\phi_n^2\right) \rho_{A0} C_l \\
& + \frac{1}{2}\epsilon_n (\rho_{An} C_{l+n\psi_A} + \rho_{An} C_{l-n\psi_A}) + \frac{1}{2}\phi_n (\rho_{An} C_{l+n\psi_A} - \rho_{An} C_{l-n\psi_A}) \\
& + \frac{1}{2}\epsilon_e (\rho_{B0} S_{l+e} - \alpha S_{l-e}) + \frac{1}{2}\phi_e (\rho_{B0} C_{l+e} - \alpha C_{l-e}) \\
& + \frac{1}{8}\phi_n^2 (\rho_{A2n} C_{l+2n\phi_A} + \rho_{A2n} C_{l-2n\phi_A}) \\
& + \frac{1}{4}\phi_n \epsilon_n (\rho_{A2n} C_{l+2n\phi_A} - \rho_{A2n} C_{l-2n\phi_A}) \\
& + \frac{1}{8}\phi_e^2 (C_{l+2e} + C_{l-2e}) + \frac{1}{4}\phi_e \epsilon_e (-2S_l + S_{l+2e} + S_{l-2e}) \\
& + \frac{1}{4}\phi_e \phi_n (\rho_{Bn} C_{l+e+n\psi_B} - \rho_{Bn} C_{l+e-n\psi_B} - \alpha C_{l-e+n} + \alpha C_{l-e-n}) \\
& + \frac{1}{4}\phi_n \epsilon_e (\rho_{Bn} S_{l+e+n\psi_B} - \rho_{Bn} S_{l+e-n\psi_B} - \alpha S_{l-e+n} + \alpha S_{l-e-n}) \\
& + \frac{1}{4}\phi_e \epsilon_n (\rho_{Bn} C_{l+e+n\psi_B} + \rho_{Bn} C_{l+e-n\psi_B} - \alpha C_{l-e+n} - \alpha C_{l-e-n}).
\end{aligned} \tag{D.12}$$

where we define

$$\rho_N(\delta) \equiv 1 - \frac{t_1^2 \tau c / L}{1 + i2\tau\delta} \tag{D.13}$$

$$\rho_{N0} \equiv \rho_N(0) \tag{D.14}$$

$$\rho_{Nn} \equiv |\rho_N(\omega)| \tag{D.15}$$

$$\psi_N \equiv \arg[\rho(\omega)] = -\arg[\rho(-\omega)] \tag{D.16}$$

$$\rho_{N2n} \equiv |\rho_N(2\omega)| \tag{D.17}$$

$$\phi_N \equiv \arg[\rho(2\omega)] = -\arg[\rho(-2\omega)] \tag{D.18}$$

for cavity resonance $N \in (A, B)$, and we have attached a prefactor $\alpha = 1$ to the *lower* sidebands to track their effect on the demodulated signal (see below).

When all of this light lands on a photodiode, the resulting signal comprises all frequencies generated by the quantity $E^2(t)$ that are within the diode's electronic bandwidth (a few GHz in our case), which includes *many* frequency components. Anticipating the subsequent demodulation at ω_e and our eventual interest in the noise term at ω , we can ignore the

vast majority, however. Assuming a constant photodiode conversion efficiency η_{PD} (units of V/W) and again keeping only terms up to second order in $\epsilon_n, \epsilon_e, \phi_n, \phi_e$, the photodiode's output $V_{PD}(t)$ is then given by

$$\begin{aligned}
\frac{4V_{PD}(t)}{\eta_{PD}r_1^2P_l} \approx & \dots + \rho_{A0}\phi_e\phi_n (\rho_{Bn}C_{e+n\psi_B} - \rho_{Bn}C_{e-n\psi_B} + \alpha C_{e+n} - \alpha C_{e-n}) \quad (D.19) \\
& + \rho_{A0}\epsilon_e\phi_n (\rho_{Bn}S_{e+n\psi_B} - \rho_{Bn}S_{e-n\psi_B} + \alpha S_{e-n} - \alpha S_{e+n}) \\
& + \rho_{A0}\phi_e\epsilon_n (\rho_{Bn}C_{e+n\psi_B} + \rho_{Bn}C_{e-n\psi_B} - \alpha C_{e-n} - \alpha C_{e+n}) \\
& + \rho_{An}\epsilon_e\epsilon_n (\rho_{B0} + \alpha) (S_{e-n\psi_A} + S_{e+n\psi_A}) \\
& + \rho_{An}\phi_e\epsilon_n (\rho_{B0} - \alpha) (C_{e-n\psi_A} + C_{e+n\psi_A}) \\
& + \rho_{An}\epsilon_e\phi_n (\rho_{B0} - \alpha) (S_{e-n\psi_A} - S_{e+n\psi_A}) \\
& + \rho_{An}\phi_e\phi_n (\rho_{B0} + \alpha) (C_{e-n\psi_A} - C_{e+n\psi_A})
\end{aligned}$$

At this point, we can demodulate this signal with the VCO output $\propto \sin(\omega_e t)$ to produce the “classic” Pound-Drever-Hall (PDH) error signal quadrature V_Y , and we can simultaneously demodulate with a phase-shifted VCO output $\propto \cos(\omega_e t)$ to produce the other quadrature V_X . Assuming a “flat” mixer efficiency η_M , (i.e. $V_Y = \eta_M V_{PD} S_e$ and $V_X = \eta_M V_{PD} C_e$) and keeping only terms at ω , the two quadratures simplify to

$$\begin{aligned}
\frac{4V_Y(t)}{\eta_M \eta_{PD} r_1^2 P_l} \approx & -\phi_e\phi_n \rho_{A0} (\rho_{Bn} S_{n\psi_B} + \alpha S_n) + \phi_e\phi_n (\rho_{B0} + \alpha) \rho_{An} S_{n\psi_A} \quad (D.20) \\
& + \epsilon_e\epsilon_n (\rho_{B0} + \alpha) \rho_{An} C_{n\psi_A}
\end{aligned}$$

$$\begin{aligned}
\frac{4V_X(t)}{\eta_M \eta_{PD} r_1^2 P_l} \approx & \epsilon_e\phi_n \rho_{A0} (\rho_{Bn} - \alpha) S_{n\psi_B} + \phi_e\epsilon_n \rho_{A0} (\rho_{Bn} C_{n\psi_B} - \alpha C_n) \quad (D.21) \\
& + \phi_e\epsilon_n \rho_{An} (\rho_{B0} - \alpha) C_{n\psi_A} - \epsilon_e\phi_n \rho_{An} (\rho_{B0} - \alpha) S_{n\psi_A}.
\end{aligned}$$

These expressions can be applied to many situations, and we now consider those relevant to the main text.

D.2.3 Case 1: Frequency Noise only, Ideal EOM, Cavity Resonant with Carrier

If we consider only frequency noise, an ideal EOM, and the cavity resonant with the carrier, $\epsilon_e \rightarrow 0$, $\epsilon_n \rightarrow 0$, $\rho_{Bn} \rightarrow 1$, $\rho_{B0} \rightarrow 1$ and $\psi_B \rightarrow 0$, so the quadratures (Eqs. (D.20)–(D.21)) become

$$V_Y(t) \rightarrow \sqrt{\frac{P_l P_e}{8}} \eta_M \eta_{PD} r_1^2 \phi_n (1 + \alpha) (\rho_{An} S_{n\psi_A} - \rho_{A0} S_n) \quad (\text{D.22})$$

$$V_X(t) \rightarrow 0. \quad (\text{D.23})$$

where we have used Eq. (D.11) to rewrite the power in each EOM-driven sideband $\sqrt{P_e} \approx \sqrt{\frac{1}{2} P_l} \phi_e$. The “amplitude” quadrature V_X is zero to lowest order, which is sensible considering the laser is exactly on resonance and we are only modulating its frequency. With both sidebands present ($\alpha = 1$), the “phase” quadrature V_Y also provides the dynamic response of the classic PDH error signal

$$V_Y = \sqrt{\frac{P_l P_e}{2}} \eta_M \eta_{PD} r_1^2 \phi_n (\rho_{An} S_{n\psi_A} - \rho_{A0} S_n). \quad (\text{D.24})$$

If the lower sideband is *not* present, the signal is simply a factor of 2 smaller; the “classic” PDH error signal receives a contribution from both sidebands in proportion to the frequency noise.

Now that all the nonlinear operations (photodiode, mixer) are complete, we have a linear mapping from the original noise $\Omega(t)$ to the error signal V_Y . We can convert this into a complex transfer function by noting that Ω is the real part of $\tilde{\Omega} = \Omega_n e^{i\omega t}$, and that V_Y is the real part of

$$\tilde{V}_Y \equiv -i \sqrt{\frac{P_l P_e}{2}} \eta_M \eta_{PD} r_1^2 \phi_n (\rho_A(\omega) e^{i\omega t} - \rho_A(0) e^{i\omega t}). \quad (\text{D.25})$$

The complex transfer function is then the ratio

$$\frac{\tilde{V}_Y}{\tilde{\Omega}} = \frac{\sqrt{2 P_l P_e} \eta_M \eta_{PD} r_1^2 t_1^2 c \tau^2 / L}{1 + i 2 \tau \omega} = \frac{2 \phi_e E_l^2 \beta \tau^2}{1 + i 2 \tau \omega}. \quad (\text{D.26})$$

where we have used the definitions of $\phi_n = \Omega_n / \omega$ and ρ_A (Eq. (D.13)) and defined the

constant $\beta = \eta_M \eta_{PD} r_1^2 t_1^2 c / 2L$. The cavity acts as a low-pass filter.

D.2.4 Case 2: Frequency Noise only, Ideal EOM, Cavity Resonant with Upper Sideband

If the cavity is instead resonant with the upper sideband, $\rho_{An} \rightarrow 1$, $\rho_{A0} \rightarrow 1$ and $\psi_A \rightarrow 0$, and the quadratures (Eqs. (D.20)-(D.21)) become

$$V_Y(t) \rightarrow -\sqrt{\frac{P_l P_e}{8}} \eta_M \eta_{PD} r_1^2 \phi_n (\rho_{Bn} S_{n\psi_B} - \rho_{B0} S_n) \quad (\text{D.27})$$

$$V_X(t) \rightarrow 0. \quad (\text{D.28})$$

Following the same analysis as Case 1,

$$\frac{\tilde{V}_Y}{\tilde{\Omega}} = -\sqrt{\frac{P_l P_e}{2}} \frac{\eta_M \eta_{PD} c \tau^2 r_1^2 t_1^2 / L}{1 + i2\tau\omega} = -\frac{\phi_e E_l^2 \beta \tau^2}{1 + i2\tau\omega}. \quad (\text{D.29})$$

The error signal behaves exactly the same, but is half as large and inverted. The lower sideband does not play a role.

D.2.5 Case 3: Amplitude Noise only, Ideal EOM, Cavity Resonant with Carrier

If we now consider only amplitude noise, an ideal EOM, and the cavity resonant with the carrier, $\epsilon_e, \phi_n \rightarrow 0$, $\rho_{Bn} \rightarrow 1$, $\rho_{B0} \rightarrow 1$, $\psi_B \rightarrow 0$, and the quadratures (Eqs. (D.20)-(D.21)) become

$$V_Y(t) \rightarrow 0 \quad (\text{D.30})$$

$$V_X(t) \rightarrow \sqrt{\frac{P_l P_e}{8}} \eta_M \eta_{PD} r_1^2 \epsilon_n (1 - \alpha) (\rho_{A0} C_n + \rho_{An} C_{n\psi_A}) \quad (\text{D.31})$$

The “phase” quadrature V_Y is zero, as expected, regardless of the presence of the lower sideband; this is consistent with the notion that changing the laser’s amplitude will not affect location of the error signal’s zero-crossing. Following the analysis of the previous cases,

$$\frac{\tilde{V}_X}{\tilde{\epsilon}} = \sqrt{\frac{P_l P_e}{2}} \eta_M \eta_{PD} r_1^2 (1 - \alpha) \left(1 - \frac{c\tau t_1^2}{L} \left(\frac{1 + i\tau\omega}{1 + i2\tau\omega} \right) \right). \quad (\text{D.32})$$

This signal is only nonzero if the lower sideband is either missing or is otherwise not identical to the upper sideband (i.e. $\alpha \neq 1$ and/or the EOM is not ideal).

D.2.6 Case 4: Amplitude noise only, ideal EOM, cavity resonant with upper sideband

If the cavity is instead resonant with the upper sideband, $\epsilon_e, \phi_n \rightarrow 0$, $\rho_{An} \rightarrow 1, \rho_{A0} \rightarrow 1$, $\psi_A \rightarrow 0$, and

$$V_Y(t) \rightarrow 0 \quad (\text{D.33})$$

$$V_X(t) \rightarrow \sqrt{\frac{P_l P_e}{8}} \eta_M \eta_{PD} r_1^2 \epsilon_n (\rho_{Bn} C_{n\psi_B} + \rho_{B0} C_n - 2\alpha C_n) \quad (\text{D.34})$$

meaning

$$\frac{\tilde{V}_X}{\tilde{\epsilon}} = \sqrt{\frac{P_l P_e}{2}} \eta_M \eta_{PD} r_1^2 \left(1 - \alpha - \frac{c\tau t_1^2}{L} \left(\frac{1 + i\tau\omega}{1 + i2\tau\omega} \right) \right) \quad (\text{D.35})$$

with an overall offset determined by the lower sideband α . The presence of the lower sideband ($\alpha = 1$) produces a PI-like behavior (see Eq. 5.5).

$$\frac{\tilde{V}_X}{\tilde{\epsilon}} = -\phi_e E_l^2 \beta \tau \left(\frac{1 + i\tau\omega}{1 + i2\tau\omega} \right). \quad (\text{D.36})$$

D.3 Error Signal for Wider Range of VCO Outputs

Figure D.1 shows the two quadrature amplitudes of the photodiode signal, taken with a shorter cavity of $L = 5$ cm and for a wider range of VCO tune voltages than that of Fig. 5.2(c) in the main text. Over this range, the non-ideal response of the system components is visible. Note in particular the peaks of $V_X(\delta)$, systematically vary with ω_e by a factor of ~ 2 , arising from a combination of VCO and EOM nonidealities (they are not “flat”). Large frequency noise will therefore produce amplitude noise even if it is perfectly tracked by a sideband, highlighting the fact that, while a large headroom is desirable to remain locked in the presence

of large fluctuations, it is always preferable to engineer a stable, vibration-isolated cavity.

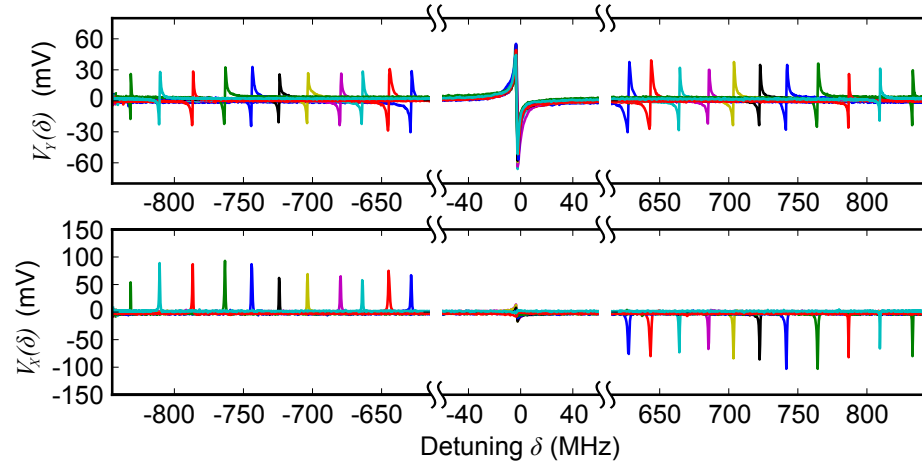


Figure D.1: Quadrature amplitudes of the photodiode signal for 11 different VCO voltages.

Bibliography

- [1] C. Reinhardt, T. Müller, A. Bourassa, and J. C. Sankey, “Ultralow-Noise SiN Trampoline Resonators for Sensing and Optomechanics,” *Physical Review X*, vol. 6, no. 2, p. 21001, apr 2016. [Online]. Available: <http://dx.doi.org/10.1103/PhysRevX.6.021001> viii, x, 4, 56, 58, 91, 123, 139
- [2] C. Reinhardt, T. Müller, and J. C. Sankey, “Simple delay-limited sideband locking with heterodyne readout,” *Opt. Express*, vol. 25, no. 2, pp. 1582–1597, jan 2017. [Online]. Available: <http://www.opticsexpress.org/abstract.cfm?URI=oe-25-2-1582> viii, ix, x, 6, 106
- [3] M. Poot and H. S. van der Zant, “Mechanical systems in the quantum regime,” *Physics Reports*, vol. 511, no. 5, pp. 273–335, 2012. 1, 4
- [4] K. Y. Yasumura, T. D. Stowe, E. M. Chow, T. Pfafman, T. W. Kenny, B. C. Stipe, and D. Rugar, “Quality factors in micron- and submicron-thick cantilevers,” *Journal of Microelectromechanical Systems*, vol. 9, no. 1, pp. 117–125, mar 2000. [Online]. Available: <http://ieeexplore.ieee.org/lpdocs/epic03/wrapper.htm?arnumber=825786> 1, 4
- [5] Y. Tao, J. M. Boss, B. A. Moores, and C. L. Degen, “Single-crystal diamond nanomechanical resonators with quality factors exceeding one million.” *Nature communications*, vol. 5, p. 3638, jan 2014. [Online]. Available: <http://www.nature.com/ncomms/2014/140408/ncomms4638/abs/ncomms4638.html> 1, 4
- [6] J. M. Nichol, E. R. Hemesath, L. J. Lauhon, and R. Budakian, “Displacement detec-

- tion of silicon nanowires by polarization-enhanced fiber-optic interferometry,” *Applied Physics Letters*, vol. 93, no. 19, p. 193110, 2008. 1, 4
- [7] K. Jensen, K. Kim, and A. Zettl, “An atomic-resolution nanomechanical mass sensor,” *Nature nanotechnology*, vol. 3, no. 9, pp. 533–537, 2008. 1, 4
- [8] J. Moser, A. Eichler, J. Güttinger, M. I. Dykman, and A. Bachtold, “Nanotube mechanical resonators with quality factors of up to 5 million.” *Nature nanotechnology*, vol. 9, no. 12, pp. 1007–1011, oct 2014. [Online]. Available: <http://dx.doi.org/10.1038/nnano.2014.234> 1, 140
- [9] D. Rugar, R. Budakian, H. J. Mamin, and B. W. Chui, “Single spin detection by magnetic resonance force microscopy.” *Nature*, vol. 430, no. 6997, pp. 329–332, 2004. 1
- [10] C. L. Degen, M. Poggio, H. J. Mamin, C. T. Rettner, and D. Rugar, “Nanoscale magnetic resonance imaging.” *Proceedings of the National Academy of Sciences of the United States of America*, vol. 106, no. 5, pp. 1313–1317, feb 2009. [Online]. Available: <http://www.pubmedcentral.nih.gov/articlerender.fcgi?artid=2628306&tool=pmcentrez&rendertype=abstract> 1
- [11] M. A. Castellanos-Beltran, D. Q. Ngo, W. E. Shanks, A. B. Jayich, and J. G. E. Harris, “Measurement of the full distribution of persistent current in normal-metal rings.” *Physical review letters*, vol. 110, no. 15, p. 156801, apr 2013. [Online]. Available: <http://www.ncbi.nlm.nih.gov/pubmed/25167295> 1
- [12] T. P. Purdy, R. W. Peterson, and C. A. Regal, “Observation of Radiation Pressure Shot Noise on a Macroscopic Object,” *Science*, vol. 339, no. 6121, pp. 801–804, feb 2013. [Online]. Available: <http://dx.doi.org/10.1126/science.1231282> 2, 4, 91
- [13] A. Nunnenkamp, K. Børkje, J. G. E. Harris, and S. M. Girvin, “Cooling and squeezing via quadratic optomechanical coupling,” *Physical Review A*, vol. 82, no. 2, pp. 021 806+, aug 2010. [Online]. Available: <http://dx.doi.org/10.1103/physreva.82.021806> 2

- [14] J. D. Teufel, T. Donner, D. Li, J. W. Harlow, M. S. Allman, K. Cicak, A. J. Sirois, J. D. Whittaker, K. W. Lehnert, and R. W. Simmonds, “Sideband cooling of micromechanical motion to the quantum ground state,” *Nature*, vol. 475, no. 7356, pp. 359–363, jul 2011. [Online]. Available: <http://dx.doi.org/10.1038/nature10261> 2, 48, 50
- [15] J. Chan, T. M. Alegre, A. H. Safavi-Naeini, J. T. Hill, A. Krause, S. Gröblacher, M. Aspelmeyer, and O. Painter, “Laser cooling of a nanomechanical oscillator into its quantum ground state,” *Nature*, vol. 478, no. 7367, pp. 89–92, 2011. 2, 48, 50
- [16] A. H. Safavi Naeini, J. Chan, J. T. Hill, T. P. Mayer Alegre, A. Krause, and O. Painter, “Observation of Quantum Motion of a Nanomechanical Resonator,” *Physical Review Letters*, vol. 108, pp. 033602+, jan 2012. [Online]. Available: <http://dx.doi.org/10.1103/physrevlett.108.033602> 2, 122
- [17] T. P. Purdy, P.-L. Yu, N. S. Kampel, R. W. Peterson, K. Cicak, R. W. Simmonds, and C. A. Regal, “Optomechanical Raman-ratio thermometry,” *Physical Review A*, vol. 92, no. 3, p. 31802, sep 2015. [Online]. Available: <http://link.aps.org/doi/10.1103/PhysRevA.92.031802> 2, 122, 124
- [18] M. Underwood, D. Mason, D. Lee, H. Xu, L. Jiang, A. B. Shkarin, K. Børkje, S. M. Girvin, and J. G. E. Harris, “Measurement of the motional sidebands of a nanogram-scale oscillator in the quantum regime,” *Physical Review A*, vol. 92, no. 6, p. 61801, dec 2015. [Online]. Available: <http://journals.aps.org/pr/abstract/10.1103/PhysRevA.92.061801> 2, 122, 124
- [19] S. M. Meenehan, J. D. Cohen, G. S. MacCabe, F. Marsili, M. D. Shaw, and O. Painter, “Pulsed excitation dynamics of an optomechanical crystal resonator near its quantum ground state of motion,” *Phys. Rev. X*, vol. 5, p. 041002, Oct 2015. [Online]. Available: <https://link.aps.org/doi/10.1103/PhysRevX.5.041002> 2
- [20] V. Sudhir, D. J. Wilson, R. Schilling, H. Schütz, S. A. Fedorov, A. H. Ghadimi, A. Nunnenkamp, and T. J. Kippenberg, “Appearance and disappearance of quantum corre-

- lations in measurement-based feedback control of a mechanical oscillator,” *Physical Review X*, vol. 7, no. 1, p. 011001, 2017. [2](#)
- [21] M. Aspelmeyer, T. J. Kippenberg, and F. Marquardt, “Cavity optomechanics,” *Reviews of Modern Physics*, vol. 86, no. 4, pp. 1391–1452, dec 2014. [Online]. Available: <http://link.aps.org/doi/10.1103/RevModPhys.86.1391> [2](#), [31](#), [32](#), [44](#), [49](#), [52](#), [59](#), [86](#), [122](#)
- [22] V. B. Braginsky and A. B. Manukin, “Ponderomotive Effects of Electromagnetic Radiation,” *Soviet Physics Journal of Experimental and Theoretical Physics*, vol. 52, pp. 986+, 1967. [2](#)
- [23] R. W. Peterson, T. P. Purdy, N. S. Kampel, R. W. Andrews, P.-L. Yu, K. W. Lehnert, and C. A. Regal, “Laser Cooling of a Micromechanical Membrane to the Quantum Backaction Limit,” *Physical Review Letters*, vol. 116, no. 6, p. 63601, feb 2016. [Online]. Available: <http://journals.aps.org/prl/abstract/10.1103/PhysRevLett.116.063601> [2](#), [140](#)
- [24] J. B. Clark, F. Lecocq, R. W. Simmonds, J. Aumentado, and J. D. Teufel, “Sideband cooling beyond the quantum backaction limit with squeezed light,” *Nature*, vol. 541, no. 7636, pp. 191–195, 2017. [2](#), [51](#)
- [25] S. Weis, R. Rivière, S. Deléglise, E. Gavartin, O. Arcizet, A. Schliesser, and T. J. Kippenberg, “Optomechanically Induced Transparency,” *Science*, vol. 330, no. 6010, pp. 1520–1523, dec 2010. [Online]. Available: <http://dx.doi.org/10.1126/science.1195596> [2](#)
- [26] A. H. Safavi-Naeini, T. P. Mayer Alegre, J. Chan, M. Eichenfield, M. Winger, Q. Lin, J. T. Hill, D. E. Chang, and O. Painter, “Electromagnetically induced transparency and slow light with optomechanics.” *Nature*, vol. 472, no. 7341, pp. 69–73, apr 2011. [Online]. Available: <http://dx.doi.org/10.1038/nature09933> [2](#)
- [27] J. T. Hill, A. H. Safavi-Naeini, J. Chan, and O. Painter, “Coherent optical wavelength conversion via cavity optomechanics.” *Nature communications*, vol. 3, p. 1196, jan 2012. [Online]. Available: <http://dx.doi.org/10.1038/ncomms2201> [2](#)

- [28] Y. Liu, M. Davanço, V. Aksyuk, and K. Srinivasan, “Electromagnetically Induced Transparency and Wideband Wavelength Conversion in Silicon Nitride Microdisk Optomechanical Resonators,” *Physical Review Letters*, vol. 110, no. 22, p. 223603, may 2013. [Online]. Available: <http://link.aps.org/doi/10.1103/PhysRevLett.110.223603> **2**
- [29] J. Bochmann, A. Vainsencher, D. D. Awschalom, and A. N. Cleland, “Nanomechanical coupling between microwave and optical photons,” *Nat Phys*, vol. 9, no. 11, pp. 712–716, nov 2013. [Online]. Available: <http://dx.doi.org/10.1038/nphys2748> **2**
- [30] R. W. Andrews, R. W. Peterson, T. P. Purdy, K. Cicak, R. W. Simmonds, C. A. Regal, and K. W. Lehnert, “Bidirectional and efficient conversion between microwave and optical light,” *Nature Physics*, vol. 10, no. 4, pp. 321–326, mar 2014. [Online]. Available: <http://dx.doi.org/10.1038/nphys2911> **2, 4, 91, 139**
- [31] T. Bağcı, A. Simonsen, S. Schmid, L. G. Villanueva, E. Zeuthen, J. Appel, J. M. Taylor, A. Sørensen, K. Usami, A. Schliesser *et al.*, “Optical detection of radio waves through a nanomechanical transducer,” *Nature*, vol. 507, no. 7490, pp. 81–85, 2014. **2**
- [32] A. H. Safavi-Naeini, S. Gröblacher, J. T. Hill, J. Chan, M. Aspelmeyer, and O. Painter, “Squeezed light from a silicon micromechanical resonator.” *Nature*, vol. 500, no. 7461, pp. 185–189, aug 2013. [Online]. Available: <http://dx.doi.org/10.1038/nature12307> **2**
- [33] T. P. Purdy, P.-L. Yu, R. W. Peterson, N. S. Kampel, and C. A. Regal, “Strong Optomechanical Squeezing of Light,” *Physical Review X*, vol. 3, no. 3, p. 31012, sep 2013. [Online]. Available: <http://link.aps.org/doi/10.1103/PhysRevX.3.031012> **2, 4, 91**
- [34] E. E. Wollman, C. Lei, A. Weinstein, J. Suh, A. Kronwald, F. Marquardt, A. Clerk, and K. Schwab, “Quantum squeezing of motion in a mechanical resonator,” *Science*, vol. 349, no. 6251, pp. 952–955, 2015. **2**
- [35] H. Xu, D. Mason, L. Jiang, and J. G. E. Harris, “Topological energy transfer in an optomechanical system with exceptional points,” *Nature*, vol. 537, no. 7618, pp. 80–83, Sep 2016, letter. [Online]. Available: <http://dx.doi.org/10.1038/nature18604> **2, 4**

- [36] K. Fang, J. Luo, A. Metelmann, M. H. Matheny, F. Marquardt, A. A. Clerk, and O. Painter, “Generalized non-reciprocity in an optomechanical circuit via synthetic magnetism and reservoir engineering,” *Nat Phys*, vol. 13, no. 5, pp. 465–471, May 2017, article. [Online]. Available: <http://dx.doi.org/10.1038/nphys4009> 2
- [37] A. Jöckel, A. Faber, T. Kampschulte, M. Korppi, M. T. Rakher, and P. Treutlein, “Sympathetic cooling of a membrane oscillator in a hybrid mechanical atomic system,” *Nat Nano*, vol. 10, no. 1, pp. 55–59, Jan 2015, letter. [Online]. Available: <http://dx.doi.org/10.1038/nnano.2014.278> 2, 4
- [38] C. B. Møller, R. A. Thomas, G. Vasilakis, E. Zeuthen, Y. Tsaturyan, M. Balabas, K. Jensen, A. Schliesser, K. Hammerer, and E. S. Polzik, “Quantum back-action-evading measurement of motion in a negative mass reference frame,” *Nature*, vol. 547, no. 7662, pp. 191–195, Jul 2017, letter. [Online]. Available: <http://dx.doi.org/10.1038/nature22980> 2, 4
- [39] R. A. Norte, J. P. Moura, and S. Groblacher, “Mechanical Resonators for Quantum Optomechanics Experiments at Room Temperature,” *Physical Review Letters*, vol. 116, no. 14, p. 147202, apr 2016. [Online]. Available: <http://link.aps.org/doi/10.1103/PhysRevLett.116.147202> 4, 5, 48, 56, 58, 85, 91, 123, 141, 160
- [40] M. Kumar and H. Bhaskaran, “Ultrasensitive room-temperature piezoresistive transduction in graphene-based nanoelectromechanical systems,” *Nano letters*, vol. 15, no. 4, pp. 2562–2567, 2015. 4
- [41] J. D. Thompson, B. M. Zwickl, A. M. Jayich, F. Marquardt, S. M. Girvin, and J. G. E. Harris, “Strong dispersive coupling of a high-finesse cavity to a micromechanical membrane,” *Nature*, vol. 452, no. 7183, pp. 72–75, mar 2008. [Online]. Available: <http://dx.doi.org/10.1038/nature06715> 4, 61, 91, 138, 140, 142
- [42] D. J. Wilson, C. A. Regal, S. B. Papp, and H. J. Kimble, “Cavity Optomechanics with Stoichiometric SiN Films,” *Physical Review Letters*, vol. 103, no. 20, pp. 207 204+, nov

2009. [Online]. Available: <http://dx.doi.org/10.1103/physrevlett.103.207204> 4, 57, 90, 91, 110
- [43] J. C. Sankey, C. Yang, B. M. Zwickl, A. M. Jayich, and J. G. E. Harris, “Strong and tunable nonlinear optomechanical coupling in a low-loss system,” *Nature Physics*, vol. 6, no. 9, pp. 707–712, jun 2010. [Online]. Available: <http://dx.doi.org/10.1038/nphys1707> 4, 7, 91, 92, 98, 106, 110, 114, 115, 140, 163
- [44] A. Jayich, J. Sankey, K. Børkje, D. Lee, C. Yang, M. Underwood, L. Childress, A. Petrenko, S. Girvin, and J. Harris, “Cryogenic optomechanics with a Si_3N_4 membrane and classical laser noise,” *New Journal of Physics*, vol. 14, no. 11, p. 115018, 2012. 4
- [45] T. P. Purdy, R. W. Peterson, P. L. Yu, and C. A. Regal, “Cavity optomechanics with Si_3N_4 membranes at cryogenic temperatures,” *New Journal of Physics*, vol. 14, no. 11, pp. 115021+, nov 2012. [Online]. Available: <http://dx.doi.org/10.1088/1367-2630/14/11/115021> 4
- [46] Y. Tsaturyan, A. Barg, A. Simonsen, L. G. Villanueva, S. Schmid, A. Schliesser, and E. S. Polzik, “Demonstration of suppressed phonon tunneling losses in phononic bandgap shielded membrane resonators for high-q optomechanics,” *Optics Express*, vol. 22, no. 6, pp. 6810–6821, 2014. 4, 57
- [47] P.-L. Yu, K. Cicak, N. Kampel, Y. Tsaturyan, T. Purdy, R. Simmonds, and C. Regal, “A phononic bandgap shield for high-q membrane microresonators,” *Applied Physics Letters*, vol. 104, no. 2, p. 023510, 2014. 4, 57
- [48] M. J. Weaver, B. Pepper, F. Luna, F. M. Buters, H. J. Eerkens, G. Welker, B. Peck, K. Heeck, S. de Man, and D. Bouwmeester, “Nested trampoline resonators for optomechanics,” *Applied Physics Letters*, vol. 108, no. 3, p. 033501, 2016. 4
- [49] D. Kleckner and D. Bouwmeester, “Sub-kelvin optical cooling of a micromechanical resonator,” *Nature*, vol. 444, no. 7115, pp. 75–78, nov 2006. [Online]. Available: <http://dx.doi.org/10.1038/nature05231> 4, 50, 91

- [50] S. Groblacher, J. B. Hertzberg, M. R. Vanner, G. D. Cole, S. Gigan, K. C. Schwab, and M. Aspelmeyer, “Demonstration of an ultracold micro-optomechanical oscillator in a cryogenic cavity,” *Nature Physics*, vol. 5, no. 7, pp. 485–488, jun 2009. [Online]. Available: <http://dx.doi.org/10.1038/nphys1301> 4, 61, 91
- [51] D. Kleckner, B. Pepper, E. Jeffrey, P. Sonin, S. M. Thon, and D. Bouwmeester, “Optomechanical trampoline resonators,” *Optics Express*, vol. 19, no. 20, p. 19708, 2011. 4, 5, 57, 61, 91
- [52] C. H. Bui, J. Zheng, S. W. Hoch, L. Y. T. Lee, J. G. E. Harris, and C. Wei Wong, “High-reflectivity, high-Q micromechanical membranes via guided resonances for enhanced optomechanical coupling,” *Applied Physics Letters*, vol. 100, no. 2, p. 21110, jan 2012. [Online]. Available: <http://scitation.aip.org/content/aip/journal/apl/100/2/10.1063/1.3658731> 4, 48, 91, 141
- [53] U. Kemiktarak, M. Durand, M. Metcalfe, and J. Lawall, “Cavity optomechanics with sub-wavelength grating mirrors,” *New Journal of Physics*, vol. 14, no. 12, p. 125010, 2012. 4, 91, 141
- [54] K. Makles, T. Antoni, A. Kuhn, S. Deléglise, T. Briant, P.-F. Cohadon, R. Braive, G. Beaudoin, L. Pinard, C. Michel *et al.*, “2d photonic-crystal optomechanical nanoresonator,” *Optics letters*, vol. 40, no. 2, pp. 174–177, 2015. 4, 91, 141
- [55] S. Bernard, C. Reinhardt, V. Dumont, Y.-A. Peter, and J. C. Sankey, “Precision resonance tuning and design of sin photonic crystal reflectors,” *Optics Letters*, vol. 41, no. 24, pp. 5624–5627, 2016. 4, 48, 91, 141
- [56] X. Chen, C. Chardin, K. Makles, C. Caër, S. Chua, R. Braive, I. Robert-Philip, T. Briant, P.-F. Cohadon, A. Heidmann *et al.*, “High-finesse fabry–perot cavities with bidimensional si₃n₄ photonic-crystal slabs,” *Light: Science & Applications*, vol. 6, no. 1, p. e16190, 2017. 4, 48, 91, 141
- [57] Y. Tsaturyan, A. Barg, E. S. Polzik, and A. Schliesser, “Ultracoherent nanomechanical resonators via soft clamping and dissipation dilution,” *Nature*

- Nanotechnology*, vol. advance online publication, Jun 2017, article. [Online]. Available: <http://dx.doi.org/10.1038/nnano.2017.101> 5, 56, 58, 123, 139, 160
- [58] R. W. P. Drever, J. L. Hall, F. V. Kowalski, J. Hough, G. M. Ford, A. J. Munley, and H. Ward, “Laser phase and frequency stabilization using an optical resonator,” *Applied Physics B Photophysics and Laser Chemistry*, vol. 31, no. 2, pp. 97–105, jun 1983. [Online]. Available: <http://link.springer.com/10.1007/BF00702605> 6, 7, 122, 125, 127, 128, 129
- [59] D. J. Wilson, *Cavity optomechanics with high-stress silicon nitride films*. California Institute of Technology, 2012. 7, 55, 56, 90
- [60] D. E. Chang, K.-K. Ni, O. Painter, and H. J. Kimble, “Ultrahigh- Q mechanical oscillators through optical trapping,” *New Journal of Physics*, vol. 14, no. 4, p. 45002, apr 2012. [Online]. Available: <http://stacks.iop.org/1367-2630/14/i=4/a=045002?key=crossref.29c8cf6b5ec26bac42abcbe56a4c041e> 7, 42, 92, 103, 115, 116, 117, 138, 140
- [61] H. B. Callen and T. A. Welton, “Irreversibility and generalized noise,” *Physical Review*, vol. 83, no. 1, p. 34, 1951. 9, 16
- [62] P. R. Saulson, “Thermal noise in mechanical experiments,” *Physical Review D*, vol. 42, no. 8, pp. 2437–2445, oct 1990. [Online]. Available: <http://link.aps.org/doi/10.1103/PhysRevD.42.2437> 9, 10, 12, 87
- [63] S. Fedorov, V. Sudhir, R. Schilling, H. Schütz, D. Wilson, and T. Kippenberg, “Evidence for structural damping in a high-stress silicon nitride nanobeam and its implications for quantum optomechanics,” *arXiv preprint arXiv:1703.07134*, 2017. 9, 159
- [64] A. S. Nowick, *Anelastic relaxation in crystalline solids*. Elsevier, 2012, vol. 1. 10
- [65] M. Imboden and P. Mohanty, “Dissipation in nanoelectromechanical systems,” *Physics Reports*, vol. 534, no. 3, pp. 89–146, 2014. [Online]. Available: <http://linkinghub.elsevier.com/retrieve/pii/S0370157313003475> 11

- [66] A. A. Clerk, M. H. Devoret, S. M. Girvin, F. Marquardt, and R. J. Schoelkopf, “Introduction to quantum noise, measurement, and amplification,” *Reviews of Modern Physics*, vol. 82, no. 2, p. 1155, 2010. 12, 13, 14, 52
- [67] A. Einstein, *Investigations on the Theory of the Brownian Movement*. Courier Corporation, 1956. 12
- [68] P. F. Dunn, *Measurement and data analysis for engineering and science*. CRC press, 2014. 14, 155
- [69] T. Fließbach, *Statistische Physik, Lehrbuch zur Theoretischen Physik IV*. Spektrum Akademischer Verlag, Heidelberg/Berlin,, 2007, vol. 4. 18
- [70] “Lecture notes on optical transfer matrix method,” accessed: 2017-03-29. [Online]. Available: <https://people.ifm.liu.se/boser/elma/Lect13.pdf> 19, 146
- [71] M. Born and E. Wolf, “Principles of optics, 7-th ed,” *Cambridge University, Cambridge*, 1999. 19, 23
- [72] J. D. Jackson and R. F. Fox, “Classical electrodynamics,” *American Journal of Physics*, vol. 67, no. 9, pp. 841–842, 1999. 19, 150, 151
- [73] F. Elste, S. M. Girvin, and A. A. Clerk, “Quantum Noise Interference and Backaction Cooling in Cavity Nanomechanics,” *Physical Review Letters*, vol. 102, no. 20, p. 207209, may 2009. [Online]. Available: <http://link.aps.org/doi/10.1103/PhysRevLett.102.207209> 32, 40, 50
- [74] M. Li, W. H. P. Pernice, and H. X. Tang, “Reactive Cavity Optical Force on Microdisk-Coupled Nanomechanical Beam Waveguides,” *Physical Review Letters*, vol. 103, no. 22, pp. 223 901+, 2009. [Online]. Available: <http://dx.doi.org/10.1103/physrevlett.103.223901> 32, 40, 50
- [75] A. Xuereb, R. Schnabel, and K. Hammerer, “Dissipative optomechanics in a michelson-sagnac interferometer,” *Phys. Rev. Lett.*, vol. 107, p. 213604, Nov 2011. [Online]. Available: <https://link.aps.org/doi/10.1103/PhysRevLett.107.213604> 32, 40, 50

- [76] M. Wu, A. C. Hryciw, C. Healey, D. P. Lake, H. Jayakumar, M. R. Freeman, J. P. Davis, and P. E. Barclay, “Dissipative and Dispersive Optomechanics in a Nanocavity Torque Sensor,” *Physical Review X*, vol. 4, no. 2, p. 21052, jun 2014. [Online]. Available: <http://link.aps.org/doi/10.1103/PhysRevX.4.021052> 32, 40, 50
- [77] A. Sawadsky, H. Kaufer, R. M. Nia, S. P. Tarabrin, F. Y. Khalili, K. Hammerer, and R. Schnabel, “Observation of Generalized Optomechanical Coupling and Cooling on Cavity Resonance,” *Physical Review Letters*, vol. 114, no. 4, p. 43601, jan 2015. [Online]. Available: <http://link.aps.org/doi/10.1103/PhysRevLett.114.043601> 32, 40, 50
- [78] M. Cotrufo, A. Fiore, and E. Verhagen, “Coherent atom-phonon interaction through mode field coupling in hybrid optomechanical systems,” *Physical Review Letters*, vol. 118, no. 13, p. 133603, 2017. 32
- [79] A. M. Jayich, J. C. Sankey, B. M. Zwickl, C. Yang, J. D. Thompson, S. M. Girvin, A. A. Clerk, F. Marquardt, and J. G. E. Harris, “Dispersive optomechanics: a membrane inside a cavity,” *New Journal of Physics*, vol. 10, no. 9, pp. 095008+, sep 2008. [Online]. Available: <http://dx.doi.org/10.1088/1367-2630/10/9/095008> 32, 114
- [80] T. Müller, C. Reinhardt, and J. C. Sankey, “Enhanced optomechanical levitation of minimally supported dielectrics,” *Phys. Rev. A*, vol. 91, p. 053849, May 2015. [Online]. Available: <https://link.aps.org/doi/10.1103/PhysRevA.91.053849> 42, 98, 140
- [81] K. K. Ni, R. Norte, D. J. Wilson, J. D. Hood, D. E. Chang, O. Painter, and H. J. Kimble, “Enhancement of Mechanical Q Factors by Optical Trapping,” *Physical Review Letters*, vol. 108, pp. 214302+, may 2012. [Online]. Available: <http://dx.doi.org/10.1103/physrevlett.108.214302> 42, 45, 62, 116, 121, 140
- [82] U. Kemiktarak, M. Metcalfe, M. Durand, and J. Lawall, “Mechanically compliant grating reflectors for optomechanics,” *Applied Physics Letters*, vol. 100, no. 6, p. 61124, feb 2012. [Online]. Available: <http://scitation.aip.org/content/aip/journal/apl/100/6/10.1063/1.3684248> 48

- [83] I. Favero, S. Stapfner, D. Hunger, P. Paulitschke, J. Reichel, H. Lorenz, E. M. Weig, and K. Karrai, “Fluctuating nanomechanical system in a high finesse optical microcavity,” *Optics express*, vol. 17, no. 15, pp. 12813–12820, 2009. 48
- [84] N. E. F. Jacobs, S. W. Hoch, J. C. Sankey, A. Kashkanova, A. M. Jayich, C. Deutsch, J. Reichel, and J. G. E. Harris, “Fiber-cavity-based optomechanical device,” *Applied Physics Letters*, vol. 101, no. 22, pp. 221109+, 2012. [Online]. Available: <http://dx.doi.org/10.1063/1.4768779> 48, 92
- [85] H. Zhong, G. Fläschner, A. Schwarz, R. Wiesendanger, P. Christoph, T. Wagner, A. Bick, C. Staarmann, B. Abeln, K. Sengstock *et al.*, “A millikelvin all-fiber cavity optomechanical apparatus for merging with ultra-cold atoms in a hybrid quantum system,” *Review of Scientific Instruments*, vol. 88, no. 2, p. 023115, 2017. 48
- [86] A. A. Clerk, F. Marquardt, and J. G. E. Harris, “Quantum Measurement of Phonon Shot Noise,” *Physical Review Letters*, vol. 104, no. 21, pp. 213603+, may 2010. [Online]. Available: <http://dx.doi.org/10.1103/physrevlett.104.213603> 48, 140
- [87] I. Wilson-Rae, N. Nooshi, W. Zwerger, and T. J. Kippenberg, “Theory of Ground State Cooling of a Mechanical Oscillator Using Dynamical Backaction,” *Physical Review Letters*, vol. 99, no. 9, p. 93901, aug 2007. [Online]. Available: <http://link.aps.org/doi/10.1103/PhysRevLett.99.093901> 49, 121, 140
- [88] F. Marquardt, J. P. Chen, A. A. Clerk, and S. M. Girvin, “Quantum Theory of Cavity-Assisted Sideband Cooling of Mechanical Motion,” *Physical Review Letters*, vol. 99, no. 9, pp. 093902+, aug 2007. [Online]. Available: <http://dx.doi.org/10.1103/physrevlett.99.093902> 49, 121, 140
- [89] D. Wilson, V. Sudhir, N. Piro, R. Schilling, A. Ghadimi, and T. J. Kippenberg, “Measurement-based control of a mechanical oscillator at its thermal decoherence rate,” *Nature*, vol. 524, no. 7565, pp. 325–329, 2015. 50
- [90] M. Pinard, Y. Hadjar, and A. Heidmann, “Effective mass in quantum effects of radiation

- pressure,” *The European Physical Journal D-Atomic, Molecular, Optical and Plasma Physics*, vol. 7, no. 1, pp. 107–116, 1999. 55, 117
- [91] S. S. Verbridge, J. M. Parpia, R. B. Reichenbach, L. M. Bellan, and H. Craighead, “High quality factor resonance at room temperature with nanostrings under high tensile stress,” *Journal of Applied Physics*, vol. 99, no. 12, p. 124304, 2006. 55, 61, 62, 85
- [92] S. Chakram, Y. Patil, L. Chang, and M. Vengalattore, “Dissipation in Ultrahigh Quality Factor SiN Membrane Resonators,” *Physical Review Letters*, vol. 112, no. 12, p. 127201, mar 2014. [Online]. Available: <http://link.aps.org/doi/10.1103/PhysRevLett.112.127201> 55, 56, 57, 90, 139
- [93] Q. P. Unterreithmeier, T. Faust, and J. P. Kotthaus, “Damping of nanomechanical resonators,” *Physical review letters*, vol. 105, no. 2, p. 027205, 2010. 55, 139
- [94] S. Schmid, K. D. Jensen, K. H. Nielsen, and A. Boisen, “Damping mechanisms in high- Q micro and nanomechanical string resonators,” *Physical Review B*, vol. 84, pp. 165307+, oct 2011. [Online]. Available: <http://dx.doi.org/10.1103/physrevb.84.165307> 55, 56, 62, 85, 90, 139
- [95] A. G. Krause, T. D. Blasius, and O. Painter, “Optical read out and feedback cooling of a nanostring optomechanical cavity,” *arXiv preprint arXiv:1506.01249*, 2015. 55
- [96] A. H. Ghadimi, D. J. Wilson, and T. Kippenberg, “Dissipation engineering of high-stress silicon nitride nanobeams,” *arXiv preprint arXiv:1603.01605*, 2016. 56, 85, 159
- [97] E. Gavartin, P. Verlot, and T. J. Kippenberg, “A hybrid on-chip optomechanical transducer for ultrasensitive force measurements.” *Nature nanotechnology*, vol. 7, no. 8, pp. 509–514, aug 2012. [Online]. Available: <http://dx.doi.org/10.1038/nnano.2012.97> 56
- [98] L. G. Villanueva and S. Schmid, “Evidence of Surface Loss as Ubiquitous Limiting Damping Mechanism in SiN Micro- and Nanomechanical Resonators,” *Physical Review Letters*, vol. 113, no. 22, p. 227201, nov 2014. [Online]. Available: <http://link.aps.org/doi/10.1103/PhysRevLett.113.227201> 56, 57, 139

- [99] T. Faust, J. Rieger, M. J. Seitner, J. P. Kotthaus, and E. M. Weig, “Signatures of two-level defects in the temperature-dependent damping of nanomechanical silicon nitride resonators,” *Phys. Rev. B*, vol. 89, p. 100102, Mar 2014. [Online]. Available: <https://link.aps.org/doi/10.1103/PhysRevB.89.100102> 56
- [100] R. Zhang, C. Ti, M. I. Davanco, Y. Ren, V. Aksyuk, Y. Liu, and K. Srinivasan, “Integrated tuning fork nanocavity optomechanical transducers with high f mqm product and stress-engineered frequency tuning,” *Applied Physics Letters*, vol. 107, no. 13, p. 131110, 2015. 58, 139
- [101] D. Rugar, H. Mamin, and P. Guethner, “Improved fiber-optic interferometer for atomic force microscopy,” *Applied Physics Letters*, vol. 55, no. 25, pp. 2588–2590, 1989. 59, 69
- [102] R. A. Norte, “Nanofabrication for on-chip optical levitation, atom-trapping, and superconducting quantum circuits,” Ph.D. dissertation, California Institute of Technology, 2015. 61, 120
- [103] K. F. Graff, *Wave motion in elastic solids*. Courier Corporation, 2012. 62, 84
- [104] I. Zubel and M. Kramkowska, “Etch rates and morphology of silicon (h k l) surfaces etched in KOH and KOH saturated with isopropanol solutions,” *Sensors and Actuators A: Physical*, vol. 115, no. 2-3, pp. 549–556, 2004. [Online]. Available: <http://www.sciencedirect.com/science/article/pii/S0924424703006435> 66
- [105] K. E. Grutter, M. Davanco, and K. Srinivasan, “Si₃N₄ Nanobeam Optomechanical Crystals,” *IEEE Journal of Selected Topics in Quantum Electronics*, vol. 21, no. 4, pp. 61–71, jul 2015. [Online]. Available: <http://ieeexplore.ieee.org/lpdocs/epic03/wrapper.htm?arnumber=6975027> 66, 139
- [106] B. P. Abbott, R. Abbott, T. Abbott, M. Abernathy, F. Acernese, K. Ackley, C. Adams, T. Adams, P. Addesso, R. Adhikari *et al.*, “Observation of gravitational waves from a binary black hole merger,” *Physical review letters*, vol. 116, no. 6, p. 061102, 2016. 69, 122
- [107] *HF2 User Manual*, Zurich Instruments, 4 2014. 71

- [108] E. R. Abraham and E. A. Cornell, “Teflon feedthrough for coupling optical fibers into ultrahigh vacuum systems,” *Applied Optics*, vol. 37, no. 10, pp. 1762–1763, 1998. 72
- [109] B. E. A. Saleh and M. C. Teich, *Fundamentals of Photonics*, 1st ed. John Wiley & Sons, 1991. 77, 78, 161
- [110] L. Novotny and B. Hecht, *Principles of nano-optics*. Cambridge university press, 2012. 77
- [111] R. St-Gelais, A. Poulin, and Y.-A. Peter, “Advances in modeling, design, and fabrication of deep-etched multilayer resonators,” *Journal of Lightwave technology*, vol. 30, no. 12, pp. 1900–1908, 2012. 77
- [112] G. B. Arfken and H. J. Weber, “Mathematical methods for physicists,” 1999. 77
- [113] Q. Li and R. J. Vernon, “Theoretical and experimental investigation of gaussian beam transmission and reflection by a dielectric slab at 110 ghz,” *IEEE transactions on antennas and propagation*, vol. 54, no. 11, pp. 3449–3457, 2006. 79, 146
- [114] W. B. Joyce and B. C. DeLoach, “Alignment of Gaussian beams,” *Appl. Opt.*, vol. 23, no. 23, pp. 4187–4196, dec 1984. [Online]. Available: <http://ao.osa.org/abstract.cfm?URI=ao-23-23-4187> 79
- [115] “Comsol Documentation: Vibrating Membrane.” [Online]. Available: https://www.comsol.com/model/download/285161/models.sme.vibrating_membrane.pdf 84
- [116] S. S. Verbridge, H. G. Craighead, and J. M. Parpia, “A megahertz nanomechanical resonator with room temperature quality factor over a million,” *Applied Physics Letters*, vol. 92, no. 1, p. 013112, 2008. 85
- [117] J. Rutman and F. Walls, “Characterization of frequency stability in precision frequency sources,” *Proceedings of the IEEE*, vol. 79, no. 7, pp. 952–960, 1991. 86, 153
- [118] A. Schwarz, R. Wiesendanger, P. Christoph, T. Wagner, and A. Bick, “A millikelvin all-fiber cavity optomechanical apparatus for merging with ultra-cold atoms in a

- hybrid quantum system,” *arXiv:1611.03406v2*, no. MiM, pp. 1–12, 2017. [Online]. Available: <https://arxiv.org/abs/1611.03406> 92
- [119] C. Stambaugh, H. Xu, U. Kemiktarak, J. Taylor, and J. Lawall, “From membrane-in-the-middle to mirror-in-the-middle with a high-reflectivity sub-wavelength grating,” *Annalen der Physik*, vol. 527, no. 1-2, pp. 81–88, jan 2015. [Online]. Available: <http://doi.wiley.com/10.1002/andp.201400142> 92, 142
- [120] Y. He and B. J. Orr, “Optical heterodyne signal generation and detection in cavity ringdown spectroscopy based on a rapidly swept cavity,” *Chemical Physics Letters*, vol. 335, no. 3-4, pp. 215–220, feb 2001. [Online]. Available: <http://www.sciencedirect.com/science/article/pii/S0009261401000318> 97, 107
- [121] V. Jain, J. Gieseler, C. Moritz, C. Dellago, R. Quidant, and L. Novotny, “Direct measurement of photon recoil from a levitated nanoparticle,” *Physical Review Letters*, vol. 116, no. 24, p. 243601, 2016. 116
- [122] T. Müller, C. Reinhardt, and J. C. Sankey, “Enhanced optomechanical levitation of minimally supported dielectrics,” *Physical Review A*, vol. 91, no. 5, pp. 1–10, 2015. [Online]. Available: <http://link.aps.org/doi/10.1103/PhysRevA.91.053849> 116, 117, 121
- [123] A. Z. Barasheed, T. Müller, and J. C. Sankey, “Optically defined mechanical geometry,” *Physical Review A*, vol. 93, no. 5, p. 053811, 2016. 116, 141
- [124] L. Landau and E. Lifshitz, “Mechanics, vol. 1,” *Course of theoretical physics*, pp. 84–93, 1976. 117
- [125] J. Bechhoefer, “Feedback for physicists: A tutorial essay on control,” *Reviews of Modern Physics*, vol. 77, no. 3, pp. 783–836, aug 2005. [Online]. Available: <http://link.aps.org/doi/10.1103/RevModPhys.77.783> 122, 123, 125
- [126] K. Dschao, M. Glaser, and J. Helmcke, “I2 Stabilized He-Ne Lasers at 612 nm,” *IEEE Transactions on Instrumentation and Measurement*, vol. 29, no. 4, pp.

- 354–357, 1980. [Online]. Available: <http://ieeexplore.ieee.org/lpdocs/epic03/wrapper.htm?arnumber=4314953> 122
- [127] P. Cerez, A. Brillet, C. N. Man-Pichot, and R. Felder, “He-ne lasers stabilized by saturated absorption in iodine at 612 nm,” *IEEE Transactions on Instrumentation and Measurement*, vol. 29, no. 4, pp. 352–354, 1980. 122
- [128] T. Kessler, C. Hagemann, C. Grebing, T. Legero, U. Sterr, F. Riehle, M. J. Martin, L. Chen, and J. Ye, “A sub-40-mHz-linewidth laser based on a silicon single-crystal optical cavity,” *Nature Photonics*, vol. 6, no. 10, pp. 687–692, sep 2012. [Online]. Available: <http://www.nature.com/doifinder/10.1038/nphoton.2012.217> 122, 123
- [129] D. Leibfried, R. Blatt, C. Monroe, and D. Wineland, “Quantum dynamics of single trapped ions,” *Reviews of Modern Physics*, vol. 75, no. 1, pp. 281–324, mar 2003. [Online]. Available: <http://link.aps.org/doi/10.1103/RevModPhys.75.281> 122
- [130] T. Rosenband, D. B. Hume, P. O. Schmidt, C. W. Chou, A. Brusch, L. Lorini, W. H. Oskay, R. E. Drullinger, T. M. Fortier, J. E. Stalnaker, S. A. Diddams, W. C. Swann, N. R. Newbury, W. M. Itano, D. J. Wineland, and J. C. Bergquist, “Frequency Ratio of Al⁺ and Hg⁺ Single-Ion Optical Clocks; Metrology at the 17th Decimal Place,” *Science*, vol. 319, no. 5871, 2008. 122
- [131] C. Chou, D. Hume, J. Koelemeij, D. Wineland, and T. Rosenband, “Frequency Comparison of Two High-Accuracy Al⁺ Optical Clocks,” *Physical Review Letters*, vol. 104, no. 7, p. 070802, feb 2010. [Online]. Available: <http://link.aps.org/doi/10.1103/PhysRevLett.104.070802> 122
- [132] J. Ye, L. S. Ma, and J. L. Hall, “Ultrasensitive detections in atomic and molecular physics: demonstration in molecular overtone spectroscopy,” *Journal of the Optical Society of America B*, vol. 15, no. 1, p. 6, 1998. 122
- [133] A. Schoof, J. Grunert, S. Ritter, and A. Hemmerich, “Reducing the linewidth of a diode laser below 30 Hz by stabilization to a reference cavity with a finesse

- above 10^5 ,” *Optics Letters*, vol. 26, no. 20, p. 1562, oct 2001. [Online]. Available: <https://www.osapublishing.org/abstract.cfm?URI=ol-26-20-1562> 123
- [134] T. C. Briles, D. C. Yost, A. Cingoz, J. Ye, and T. R. Schibli, “Simple piezoelectric-actuated mirror with 180 kHz servo bandwidth,” *Optics Express*, vol. 18, no. 10, p. 9739, may 2010. [Online]. Available: <https://www.osapublishing.org/oe/abstract.cfm?uri=oe-18-10-9739> 123, 129
- [135] J. F. S. Brachmann, H. Kaupp, T. W. Hansch, and D. Hunger, “Photothermal effects in ultra-precisely stabilized tunable microcavities,” *Optics Express*, vol. 24, no. 18, p. 21205, sep 2016. [Online]. Available: <https://www.osapublishing.org/abstract.cfm?URI=oe-24-18-21205> 123
- [136] J. L. Hall and T. W. Hansch, “External dye-laser frequency stabilizer,” *Optics Letters*, vol. 9, no. 11, p. 502, nov 1984. [Online]. Available: <https://www.osapublishing.org/abstract.cfm?URI=ol-9-11-502> 123
- [137] R. Houtz, C. Chan, and H. Muller, “Wideband, efficient optical serrodyne frequency shifting with a phase modulator and a nonlinear transmission Line,” *Optics Express*, vol. 17, no. 21, p. 19235, oct 2009. [Online]. Available: <https://www.osapublishing.org/oe/abstract.cfm?uri=oe-17-21-19235> 124
- [138] R. Kohlhaas, T. Vanderbruggen, S. Bernon, A. Bertoldi, A. Landragin, and P. Bouyer, “Robust laser frequency stabilization by serrodyne modulation,” *Optics Letters*, vol. 37, no. 6, p. 1005, mar 2012. [Online]. Available: <https://www.osapublishing.org/abstract.cfm?URI=ol-37-6-1005> 124
- [139] D. Gatti, R. Gotti, T. Sala, N. Coluccelli, M. Belmonte, M. Prevedelli, P. Laporta, and M. Marangoni, “Wide-bandwidth Pound-Drever-Hall locking through a single-sideband modulator,” *Optics Letters*, vol. 40, no. 22, p. 5176, nov 2015. [Online]. Available: <https://www.osapublishing.org/abstract.cfm?URI=ol-40-22-5176> 124
- [140] V. V. Protopopov, *Laser Heterodyning*, ser. Springer Series in Optical Sciences.

- Berlin, Heidelberg: Springer Berlin Heidelberg, 2009, vol. 149. [Online]. Available: <http://link.springer.com/10.1007/978-3-642-02338-5> 124, 127
- [141] R. V. Pound, “Electronic Frequency Stabilization of Microwave Oscillators,” *Review of Scientific Instruments*, vol. 17, no. 11, p. 490, 1946. [Online]. Available: <http://scitation.aip.org/content/aip/journal/rsi/17/11/10.1063/1.1770414> 125, 127
- [142] E. D. Black, “An introduction to Pound-Drever-Hall laser frequency stabilization,” *American Journal of Physics*, vol. 69, no. 1, pp. 79–87, jan 2001. [Online]. Available: <http://dx.doi.org/10.1119/1.1286663> 125, 127, 128, 129
- [143] R. L. Barger, “Frequency stabilization of a cw dye laser,” *Applied Physics Letters*, vol. 22, no. 11, p. 573, 1973. [Online]. Available: <http://scitation.aip.org/content/aip/journal/apl/22/11/10.1063/1.1654513> 127
- [144] S. L. Danilishin and F. Y. Khalili, “Quantum measurement theory in gravitational-wave detectors,” *Living Reviews in Relativity*, vol. 15, no. 1, pp. 1–147, 2012. 127
- [145] M. Heurs, I. R. Petersen, M. R. James, and E. H. Huntington, “Homodyne locking of a squeezer,” *Lasers and Electro-Optics (CLEO) and Quantum Electronics and Laser Science Conference (QELS), 2010 Conference on*, vol. 34, no. 16, pp. 1–2, 2010. 127
- [146] T. W. Hansch and B. Couillaud, “Laser frequency stabilization by polarization spectroscopy of a reference cavity,” *Optics Communications*, vol. 35, no. 3, pp. 441–444, 1980. 127
- [147] C. E. Wieman and S. L. Gilbert, “Laser-frequency stabilization using mode interference from a reflecting reference interferometer.” *Optics letters*, vol. 7, no. 10, pp. 480–2, 1982. [Online]. Available: <https://www.osapublishing.org/ol/abstract.cfm?uri=ol-7-10-480> 127
- [148] D. A. Shaddock, M. B. Gray, and D. E. McClelland, “Frequency locking a laser to an optical cavity by use of spatial mode interference,” *Optics Letters*, vol. 24, no. 21, p. 1499, nov 1999. [Online]. Available: <https://www.osapublishing.org/abstract.cfm?URI=ol-24-21-1499> 127

- [149] M. Rakhmanov, R. Savage, D. Reitze, and D. Tanner, “Dynamic resonance of light in Fabry-Perot cavities,” *Physics Letters A*, vol. 305, no. 5, pp. 239–244, 2002. 127, 128
- [150] M. J. Lawrence, B. Willke, M. E. Husman, E. K. Gustafson, and R. L. Byer, “Dynamic response of a Fabry-Perot interferometer,” *Journal of the Optical Society of America B*, vol. 16, no. 4, p. 523, apr 1999. [Online]. Available: <https://www.osapublishing.org/abstract.cfm?URI=josab-16-4-523> 132
- [151] I. Wilson-Rae, “Intrinsic dissipation in nanomechanical resonators due to phonon tunneling,” *Physical Review B - Condensed Matter and Materials Physics*, vol. 77, no. 24, pp. 1–31, 2008. 139
- [152] I. Wilson-Rae, R. A. Barton, S. S. Verbridge, D. R. Southworth, B. Ilic, H. G. Craighead, and J. M. Parpia, “High- q nanomechanics via destructive interference of elastic waves,” *Phys. Rev. Lett.*, vol. 106, p. 047205, Jan 2011. [Online]. Available: <https://link.aps.org/doi/10.1103/PhysRevLett.106.047205> 139
- [153] P.-L. Yu, T. Purdy, and C. Regal, “Control of material damping in high- q membrane microresonators,” *Physical review letters*, vol. 108, no. 8, p. 083603, 2012. 139
- [154] Y. Tao, R. Hauert, and C. L. Degen, “Exclusively gas-phase passivation of native oxide-free silicon (100) and silicon (111) surfaces,” *ACS applied materials & interfaces*, vol. 8, no. 20, pp. 13 157–13 165, 2016. 139
- [155] M. Yuan, M. A. Cohen, and G. Steele, “Silicon nitride membrane resonators at millikelvin temperatures with quality factors exceeding 10^8 ,” pp. 1–10, 2015. [Online]. Available: <http://arxiv.org/abs/1510.07468> 139, 140
- [156] H. I. Rasool, P. R. Wilkinson, A. Z. Stieg, and J. K. Gimzewski, “A low noise all-fiber interferometer for high resolution frequency modulated atomic force microscopy imaging in liquids.” *The Review of scientific instruments*, vol. 81, no. 2, p. 23703, feb 2010. [Online]. Available: <http://scitation.aip.org/content/aip/journal/rsi/81/2/10.1063/1.3297901> 139

- [157] N. Flowers-Jacobs, S. Hoch, J. Sankey, A. Kashkanova, A. Jayich, C. Deutsch, J. Reichel, and J. Harris, “Fiber-cavity-based optomechanical device,” *Applied Physics Letters*, vol. 101, no. 22, p. 221109, 2012. 140
- [158] B. M. Zwickl, W. E. Shanks, A. M. Jayich, C. Yang, A. C. B. Jayich, J. D. Thompson, and J. G. E. Harris, “High quality mechanical and optical properties of commercial silicon nitride membranes,” *Applied Physics Letters*, vol. 92, no. 10, pp. 103 125+, 2008. [Online]. Available: <http://aip.scitation.org/doi/full/10.1063/1.2884191> 140
- [159] R. Fischer, N. Kampel, G. Assumpção, P.-L. Yu, K. Cicak, R. Peterson, R. Simmonds, and C. Regal, “Optical probing of mechanical loss of a si_3n_4 membrane below 100 mk,” *arXiv preprint arXiv:1611.00878*, 2016. 140
- [160] J. Moser, J. Güttinger, A. Eichler, M. J. Esplandiu, D. E. Liu, M. I. Dykman, and A. Bachtold, “Ultrasensitive force detection with a nanotube mechanical resonator,” *Nature Nanotechnology*, vol. 8, no. 7, pp. 493–496, 2013. [Online]. Available: <http://www.nature.com/doifinder/10.1038/nnano.2013.97> 140
- [161] H. Miao, S. Danilishin, T. Corbitt, and Y. Chen, “Standard Quantum Limit for Probing Mechanical Energy Quantization,” *Physical Review Letters*, vol. 103, no. 10, p. 100402, sep 2009. [Online]. Available: <http://link.aps.org/doi/10.1103/PhysRevLett.103.100402> 140
- [162] M. Rossi, N. Kralj, S. Zippilli, R. Natali, A. Borrielli, G. Pandraud, E. Serra, G. Di Giuseppe, and D. Vitali, “Enhancing sideband cooling by feedback-controlled light,” *arXiv preprint arXiv:1704.04556*, 2017. 141
- [163] E. Janitz, M. Ruf, M. Dimock, A. Bourassa, J. Sankey, and L. Childress, “Fabry-Perot microcavity for diamond-based photonics,” *Physical Review A*, vol. 92, no. 4, p. 43844, oct 2015. [Online]. Available: <http://link.aps.org/doi/10.1103/PhysRevA.92.043844> 141
- [164] K. Y. Fong, W. H. Pernice, and H. X. Tang, “Frequency and phase noise of ultrahigh

- q silicon nitride nanomechanical resonators,” *Physical Review B*, vol. 85, no. 16, p. 161410, 2012. 153
- [165] R. Christian, “The theory of oscillating-vane vacuum gauges,” *Vacuum*, vol. 16, no. 4, pp. 175–178, 1966. 157
- [166] M. J. Martin, B. H. Houston, J. W. Baldwin, and M. K. Zalalutdinov, “Damping models for microcantilevers, bridges, and torsional resonators in the free-molecular-flow regime,” *Journal of Microelectromechanical Systems*, vol. 17, no. 2, pp. 503–511, 2008. 157, 158, 159
- [167] M. Bao, H. Yang, H. Yin, and Y. Sun, “Energy transfer model for squeeze-film air damping in low vacuum,” *Journal of Micromechanics and Microengineering*, vol. 12, no. 3, p. 341, 2002. 157, 158
- [168] M. Bao and H. Yang, “Squeeze film air damping in mems,” *Sensors and Actuators A: Physical*, vol. 136, no. 1, pp. 3–27, 2007. 157, 158
- [169] S. S. Verbridge, R. Ilic, H. Craighead, and J. M. Parpia, “Size and frequency dependent gas damping of nanomechanical resonators,” *Applied Physics Letters*, vol. 93, no. 1, p. 013101, 2008. 157, 159
- [170] “Advanced Thin Films, manufacturing.” [Online]. Available: <http://advancedthinfilms.com/Capabilities/Manufacturing> 164
- [171] T. P. Purdy, “Cavity QED with Ultracold Atoms on an Atom Chip,” Ph.D. dissertation, University of California, Berkeley, 2009. 166
- [172] M. S. Ilango, M. D. Charlton, and C. C. Vidyasagar, “Etch Process Development of Tantalum Pentoxide (Ta_2O_5) Using Photoresist (S1813),” *Nanoscience and Nanotechnology: An International Journal*, vol. 3, no. 2, pp. 36–40, 2013. 166, 167